

Important Notice

This copy may be used only for the purposes of research and private study, and any use of the copy for a purpose other than research or private study may require the authorization of the copyright owner of the work in question. Responsibility regarding questions of copyright that may arise in the use of this copy is assumed by the recipient.

THE UNIVERSITY OF CALGARY

Prestack Depth Imaging and Velocity Analysis for P-P and P-S Data with
Nonstationary Integral Extrapolators

by

Yanpeng Mi

A THESIS

SUBMITTED TO THE FACULTY OF GRADUATE STUDIES
IN PARTIAL FULFILLMENT OF THE REQUIREMENTS FOR THE
DEGREE OF DOCTOR OF PHILOSOPHY

DEPARTMENT OF GEOLOGY AND GEOPHYSICS

CALGARY, ALBERTA

August, 2001

© Yanpeng Mi 2001

THE UNIVERSITY OF CALGARY

FACULTY OF GRADUATE STUDIES

The undersigned certify that they have read and recommended to the Faculty of Graduate Studies for acceptance a thesis entitled “Prestack Depth Imaging and Velocity Analysis for P-P and P-S Data with Nonstationary Integral Extrapolators” submitted by Yanpeng Mi in partial fulfillment of the requirements for the degree of Doctor of Philosophy.

Supervisor, Dr. G. F. Margrave
Department of Geology and Geophysics

Dr. D.C. Lawton
Department of Geology and Geophysics

Dr. L. R. Lines
Department of Geology and Geophysics

Dr. R. J. Brown
Department of Geology and Geophysics

Dr. J.A. R. Blais
Department of Geomatics Engineering

Dr. M. D. Sacchi
Department of Physics, University of Alberta

Date

ABSTRACT

Practical parallel implementation of the nonstationary integral wavefield extrapolators is presented. Two approaches, the windowed split-step algorithm and full integral algorithm, were implemented. The integral extrapolators are suitable for large-step wavefield extrapolation, even when lateral velocity variations are strong, provided that the static phase-shift and the focusing phase-shift velocities are replaced by time-average and depth-average velocities, respectively. Linear vertical wavefield interpolation between reference wavefields produced by large-step extrapolation algorithms can be used to compute the intermediate depth image. This dual algorithm significantly reduces the run time of the integral wavefield extrapolators.

Nonstationary extrapolators are found to be very capable of imaging shallow events at large dipping angles as well as at deep events, even when severe topography variations and high near-surface velocity is present. The Marmousi synthetic data set and the Alberta Foothills synthetic data set were migrated and superior depth images were achieved.

P-P prestack depth imaging techniques can be conveniently applied to converted-wave data based on the primary-only P-S wave propagation model. Prestack P-S shot gather migration with the dual algorithm produced a very good depth image for the 1997 Blackfoot 3C-2D survey.

The concept of downward-continuation migration velocity analysis (DMVA) is proposed. It can be used to partially eliminate the assumption of laterally invariant velocity in the established migration velocity analysis techniques and hence provide a better velocity estimation.

ACKNOWLEDGMENTS

This thesis would not have been possible without the continual and generous support of the CREWES Project and the sponsors. I would like to sincerely thank my supervisor, Dr. Gary F. Margrave, for his support, guidance and encouragement throughout the entire enriching project. Many of his comments and suggestions kept me on the right track when navigating the fascinating frontier of exploration geophysics. Additional thanks are owed to committee members, Dr. D. Lawton, Dr. L. Lines and Dr. R. J. Brown, who provided very useful discussions and suggested revisions to this thesis.

I also would like to extend my thanks to the many people who have offered help since the day I began my Ph.D. project. Unfortunately, space does not permit the long list of names. Special thanks to Dr. Zhengsheng Yao for his beneficial academic advice and suggestions, and to Ms. Hanxing Lu, for the time she spent generously with me in discussing seismic data processing issues. I would also like to acknowledge D. Phillips of the MACI project at the University of Calgary for his kind help in many parallel-computing issues.

DEDICATION

For my family.

TABLE OF CONTENTS

Approval page	ii
Abstract	iii
Acknowledgments	iv
Dedication	v
Table of Contents	vi
List of Figures	ix
List of Tables	xiii
Symbols and Acronyms	xiv

CHAPTER 1

INTRODUCTION

1.1 Introduction	1
1.2 Introduction to the theory of nonstationary filtering	8
1.3 Application of nonstationary filtering theory in Fourier-domain depth imaging ..	11
1.4 Thesis structure	12

CHAPTER 2

IMPLEMENTATION OF INTEGRAL WAVEFIELD EXTRAPOLATORS 15

2.1 Sign definition in Fourier transform and wavefield extrapolation	15
2.2 Wavefield extrapolation by phase-shift-plus-interpolation	17
2.3 Integral wavefield extrapolators	20
2.4 Imaging condition for prestack depth migration	24
2.5 Review of split-step Fourier algorithm	26

2.6 Derivation of split-step extrapolator from nonstationary phase-shift operator	30
2.7 Approximation of PSPI, NSPS and SNPS as windowed split-step Fourier algorithms.....	32
2.8 Parallel implementation on the MACI Alpha cluster	38
2.9 Computing issues.....	43
2.10 Chapter summary.....	48
CHAPTER 3	
LARGE-STEP WAVEFIELD EXTRAPOLATION AND THE DUAL ALGORITHM.....	54
3.1 Introduction.....	54
3.2 Static and focusing phase shift in complex media.....	55
3.3 Large-step formulae for PSPI and NSPS	58
3.4 The dual algorithm.....	67
3.5 Depth imaging of Marmousi with the dual algorithm	72
3.6 Large-step extrapolation by eigenvalue decomposition	75
3.7 Large-step extrapolation with Padé approximation to matrix exponential.....	78
3.8 Numerical examples for large-step extrapolation with the Padé approximation.....	81
3.9 Comparison of speed and limitations of algorithms	84
3.10 Chapter summary.....	86
CHAPTER 4	
DEPTH IMAGING FROM TOPOGRAPHY WITH NSPS AND PSPI	87
4.1 Introduction.....	87
4.2 PSPI extrapolation from topography	88
4.3 NSPS extrapolation from topography.....	95
4.4 A velocity model of Canadian Rocky mountain region and synthetic data	98

4.5 Depth imaging of the Foothills synthetic data	99
4.6 Chapter summary	101
CHAPTER 5	
FOURIER DOMAIN CONVERTED WAVE PRESTACK DEPTH IMAGING. 107	
5.1 Introduction.....	107
5.2 Conventional converted-wave processing.....	109
5.3 P-S wave reflection at a solid-solid boundary	111
5.4 Introduction to the 1997 Blackfoot 3C-2D surevey	115
5.5 Prestack depth imaging from topography of the vertical and radial component .	120
5.6 Correlation of P-P and P-S depth images.....	128
5.7 Chapter summary	129
CHAPTER 6	
DOWNWARD-CONTINUATION MIGRATION VELOCITY ANALYSIS..... 142	
6.1 Introduction.....	142
6.2 Prestack migration velocity analysis as a tool of velocity analysis.....	144
6.3 Downward-continuation velocity analysis (DCVA)	147
6.4 An example – DCVA applied to the Marmousi synthetic	150
6.5 Downward-continuation migration velocity analysis (DCMVA)	163
6.6 Chapter summary	169
CHAPTER 7	
CONCLUSIONS..... 170	
REFERENCES 174	

LIST OF FIGURES

Figure 1.1	Creation of a synthetic trace with nonstationary convolution.....	10
Figure 1.2	Deconvolution test with NSD.....	11
Figure 2.1	Computational steps of the SNPS depth imaging algorithm.....	25
Figure 2.2	Marmousi shot-gather 120 located in the middle of the velocity model.....	37
Figure 2.3	Marmousi P-wave velocity model.....	38
Figure 2.4	Marmousi CIG stack with two kinds of slowness correction	39
Figure 2.5	Network configuration of the MACI Alpha Cluster	41
Figure 2.6	Photographs of three types of Alpha workstations	42
Figure 2.7	The general topology of the parallel algorithm.....	43
Figure 2.8	Number of unrepeated velocities in the Marmousi model after application of velocity blocking factors.....	49
Figure 2.9	CIG gather at 6200 m computed by split-step Fourier method and SNPS with two velocity blocking factors	51
Figure 2.10	Reflectivity of the Marmousi model.....	51
Figure 2.11	Marmousi depth image computed by the local split-step Fourier algorithm.....	52
Figure 2.12	Marmousi depth image computed by recursive SNPS with a 75 m/s velocity blocking factor	52
Figure 2.13	Marmousi depth image computed by recursive SNPS with a 5 m/s velocity blocking factor	53
Figure 3.1	Two velocity zones in the Mamrousi model with different lateral velocity gradients	62
Figure 3.2	160-m-thick average and mean velocity in the two velocity zones.....	63
Figure 3.3	Extrapolation test in velocity zone 1	64
Figure 3.4	Extrapolation test in velocity zone 2	65

Figure 3.5	Inverse extrapolation extrapolator with recursive PSPI integral.....	66
Figure 3.6	Zero-offset wavefields at 760 m of Marmousi model produced by recursive PSPI and large-step PSPI	66
Figure 3.7	The dual algorithm	68
Figure 3.8	Zero-offset wavefield extrapolation of 11 impulses to 560 m and 600 m of the Marmousi model.....	70
Figure 3.9	Intermediate wavefields between 560 m and 600 m computed by vertical linear wavefield interpolation.....	71
Figure 3.10	Inverse extrapolation of the intermediate wavefields with recursive PSPI.....	73
Figure 3.11	Marmousi CIG image computed with a 40 m dual-algorithm and two kinds of interpolation algorithms.....	74
Figure 3.12	Marmousi CIG image computed with a 16 m dual-algorithm	75
Figure 3.13	Two-block model used to test Padé approximation.....	82
Figure 3.14	Forward and inverse extrapolation of an impulse through the two-block velocity model.....	83
Figure 3.15	Test of the eigenvalue decomposition algorithm and the Padé approximation algorithm through a media of randomly varying velocity	84
Figure 4.1	Wave equation redatuming	89
Figure 4.2	Single-step Fourier domain redatuming with nonstationary wavefield extrapolator.....	90
Figure 4.3	Zero-offset forward extrapolation from topography with recursive PSPI integral.....	93
Figure 4.4	Accuracy comparison of inverse extrapolation with different step sizes	94
Figure 4.5	Zero-offset extrapolation from topography with large-step NSPS.....	97
Figure 4.6	A velocity model representing typical geology of the northeastern British Columbia	99
Figure 4.7	A shot-gather located in the middle of the Foothills model.....	102

Figure 4.8	Figure 4.7 after migration from topography with the dual algorithm..	102
Figure 4.9	Result of prestack depth imaging from topography with large-step PSPI algorithm.....	104
Figure 4.10	Result of prestack depth imaging of the Foothills synthetic by other authors.....	106
Figure 5.1	Conventional P-S data processing flow.....	112
Figure 5.2	Wave modes at a solid-solid boundary.....	113
Figure 5.3	The $W_P CW_S$ model for P-S wave.....	114
Figure 5.4	Location of the Blackfoot oil field.....	116
Figure 5.5	The sedimentary sequence of southern Alberta and the blocked V_p and V_s from well L0908.....	117
Figure 5.6	Isopach of the Blackfoot Galuconitic.....	118
Figure 5.7	Acquisition geometry of the 1997 Blackfoot survey.....	119
Figure 5.8	Topography variation along the acquisition line.....	119
Figure 5.9	V_p - V_s cross-plots of well log 09-08.....	122
Figure 5.10	P and S velocity model for prestack depth imaging.....	122
Figure 5.11	Source location adjustment by spatial linear phase-shift.....	124
Figure 5.12	Vertical and radial components of shot 75.....	126
Figure 5.13	Pre-processing flow for the vertical and radial components.....	127
Figure 5.14	Vertical components of three shots before and after migration.....	130
Figure 5.15	Radial components of three shots before and after migration.....	133
Figure 5.16	Three vertical-component CIGs.....	136
Figure 5.17	Three radial-component CIGs.....	138
Figure 5.18	Vertical component depth image.....	140
Figure 5.19	Radial component depth image.....	140
Figure 5.20	Correlation analysis of the P-P image and the P-S image.....	141

Figure 6.1	Three velocity analysis panels for data recorded at the surface	153
Figure 6.2	0-600 m velocity model derived from DCVA.....	154
Figure 6.3	Shot-gather 120 before and after being downward continued to 200 m.....	154
Figure 6.4	Three velocity analysis panels for data recorded at 200 m depth.....	155
Figure 6.5	200 – 800 m velocity model derived from DCVA	156
Figure 6.6	Three velocity analysis panels for data recorded at 400 m depth.....	157
Figure 6.7	400 – 1000 m velocity model derived from DCVA	158
Figure 6.8	Three velocity analysis panels for the data recorded at 600 m depth.....	159
Figure 6.9	600 – 1200 m velocity model derived from DCVA	160
Figure 6.10	The shot-gather 120 after downward-continued to 400 m and 600 m	160
Figure 6.11	Velocity models of the 0-1200 m of the Mamousi derived from DCVA.....	161
Figure 6.12	0-1200 m depth image of the Marmousi migrated with three velocity models	162
Figure 6.13	CIG at 3300 m generated with 80%-120% of the DCVA velocity model.....	165
Figure 6.14	The velocity model scaling factors	166
Figure 6.15	The velocity model after application of the scaling factors.....	167
Figure 6.16	The CIG at 3300 m migrated with the true and adjusted velocity models	167
Figure 6.17	The depth image migrated with the adjusted velocity model.....	168

LIST OF TABLES

Table 3.1 Summary of the performance of Fourier-domain imaging techniques.....	86
---	----

SYMBOLS AND ACRONYMS

C	P-to-S conversion coefficients.
D	Seismic receiver-array response.
e	2.71827...
f, F	Frequency.
H	Primary-only subsurface filter, including downgoing wavefield propagation, reflection and upgoing wavefield propagation.
h	Topographic function.
k, k_x, k_z	Wavenumber, horizontal wavenumber and vertical wavenumber.
P	General expression of Fourier-domain wavefield. The wavefield can be either in (ω, x) domain or in (ω, k_x) domain.
p	General expression of (t, x) -domain wavefield.
R	P-to-P reflection coefficients.
\tilde{r}	Reflection coefficient computed with imaging condition.
S	Seismic source-array response.
s	Slowness.
t, τ	Time.
v	Velocity.
W	Wavefield propagator.
W_p	Compressional wavefield propagator.
W_s	Shear wavefield propagator.
x	Lateral coordinate.
z	Depth or topographic function.
α	Nonstationary phase-shift.

β	(ω, x) -domain static phase-shift.
λ	Wavelength.
π	3.14159...
ψ	(ω, x) -domain wavefield.
φ	(ω, k_x) -domain wavefield.
ω	Angular frequency.
Φ	Phase.
Ω	Window function.
<i>PSPI</i>	Phase-shift-plus-interpolation.
<i>NSPS</i>	Nonstationary phase-shift.
<i>SNPS</i>	Symmetric nonstationary phase-shift.

CHAPTER 1

INTRODUCTION

1.1 INTRODUCTION

Prestack depth-imaging in regions of complex geology requires accurate migration algorithms. Modern seismic acquisition can produce large amounts of data that require high-speed algorithms. A fast and accurate algorithm is often hard to achieve due either to the limitation of the approximation embedded in the algorithm or to inadequate computing resources. Selecting a practical algorithm often requires a trade-off between accuracy and speed. Conventional Kirchhoff migration algorithms are fast; however, they often have difficulty handling caustics, multiple arrivals, shadow zones and extreme lateral velocity variation that leads to chaotic rays (Fei et al., 1996; Audebert et al., 1997). More accurate ray tracing methods that take into account multi-pathing and computes correct amplitudes for each arrival are computationally expensive and more difficult to implement. Although theoretically the Kirchhoff migration algorithms allow “true amplitude,” the theory is often difficult to enact. Normally, Kirchhoff algorithms compute traveltimes by solving the eikonal equation with ray tracing. Amplitude scaling factors are applied to correct the amplitude loss due to geometric spreading. For a

true-amplitude algorithm, the energy-transport equation must be solved (Hubral, 1983). Methods based on full wave equation are capable of providing solutions for arbitrarily complex media since all reflections including all multiples are involved in computing (Baysal et al., 1985; Wapenaar et al., 1987). Steep reflections can be imaged very well. Unfortunately, such approaches are extremely time-consuming and a high degree of migration noise is inevitable. The Fourier-domain one-way wave-equation migration algorithm is exact and as fast as the Kirchhoff migration algorithms in constant-velocity media (Stolt, 1978); however it becomes slower in laterally varying media. However, one-way wave-equation migration techniques allow energy to propagate along all possible ray paths and are less problematic in complex velocity models.

Seismic migration can be conceptually perceived as a spatial deconvolution that removes wave propagation effects. The wavefield at depth z_0 , normally at the Earth's surface, in response to the wavefield at depth level z_N , can be written as

$$P(z_0) = S(z_0)H(z_0, z_N)D(z_0), \quad (1.1)$$

where $P(z_0)$ is the wavefield response at depth z_0 , $S(z_0)$ is the source response and $D(z_0)$ is the receiver-array response. $H(z_0, z_N)$ is the operator that includes the downward-propagation effects from z_0 to z_N , reflection response $R(z_N)$ and the upward propagation effects from z_N to z_0 . $H(z_0, z_N)$ can be written as

$$H(z_0, z_N) = W(z_0, z_N)R(z_N)W(z_N, z_0), \quad (1.2)$$

where $W(z_0, z_N)$ and $W(z_N, z_0)$ are propagation operators from z_0 to z_N and from z_N back to z_0 . Equation (1.2) can be formulated as a spatial convolution and the inverse problem, which removes the propagation effects $W(z_0, z_N)$ and $W(z_N, z_0)$, can be formulated as a spatial deconvolution (Berkhout, 1980). When the medium is inhomogeneous, both the forward and inverse filters become dependent on the spatial coordinates.

The concept of downward continuation is evident in Fourier-domain depth migration algorithms. Recorded seismic wavefields at the surface or a seismic source signature can be recursively extrapolated backward to the surface or forward into the Earth's interior with a known velocity model. The extrapolation process is based on a one-way wave equation and can be explicitly expressed as 'filtering' (Berkhout, 1981). Varying approximations to the scalar wave equation result in filters of different accuracy and speed. These filters are called extrapolators. Seismic reflectivity can then be estimated by the ratio between the backward-extrapolated receiver wavefield and the forward-extrapolated source wavefield immediately above a certain depth level, where the traveltimes becomes zero. This is called an 'imaging condition' (Claerbout, 1971).

In media of extreme lateral velocity gradients, a highly accurate wavefield extrapolator is required in order to carry the wavefield at one depth to another. Typical wavefield-extrapolation techniques, such as phase-shift-plus-interpolation (PSPI) (Gazdag and Sguazzero, 1984), split-step (Freire and Stoffa, 1986; Stoffa et al., 1990) and phase-screen (Wu and Huang, 1992), use approximate solution and small

extrapolation steps to achieve efficiency and acceptable accuracy. For example, Gazdag's PSPI uses a set of constant reference velocities to compute reference wavefields using constant-velocity phase-shift and the extrapolated wavefield is computed by (ω, x) domain interpolation between the reference wavefields. The split-step extrapolator decomposes the slowness field into a constant reference field and a scattering field. This method was developed based on the perturbation theory and is not very capable of handling strong lateral velocity variations. Instead of decomposing the slowness field, Jin and Wu (1998) proposed the phase-screen algorithm that decomposes the velocity field into a constant reference field and a perturbation field. This method, too, is not capable of adequately handling large lateral velocity variations.

In the extreme form, when all velocities are used to compute the extrapolator, Gazdag's PSPI becomes a nonstationary combination filter (Margrave, 1998) that performs an inverse Fourier transform simultaneously with wavefield extrapolation (Margrave and Ferguson, 1999a). This limiting form is also called PSPI to emphasize the relation to Gazdag's original PSPI concept. NSPS is a transpose form of PSPI that performs a simultaneous forward Fourier transform with wavefield extrapolation. A natural combination of NSPS and PSPI leads to a symmetric phase-shift extrapolator (SNPS) of higher accuracy and better stability (Margrave and Ferguson, 1999b). The three above-noted integral algorithms were implemented by Ferguson and Margrave (1999) with a windowed split-step Fourier approach.

Explicit solutions to the one-way wavefield extrapolators in laterally varying media have recently been recognized as pseudo-differential operators (Margrave and Ferguson, 1997; 1999a; Grimbergen et al., 1998). Pseudo-differential operators are generalization

of translation-invariant (stationary) operators to approximately translation-variant (nonstationary) operators (Stein, 1993: 231). Generalizing a stationary operator, such as the constant velocity phase-shift method of Gazdag (1978), to a nonstationary operator allows extrapolation of seismic wavefields through strongly heterogeneous media. This is especially advantageous for the imaging problems in regions of complex geology, such as the Canadian Rockies.

A small extrapolation step is required when the wavefield is extrapolated through laterally varying media. The wavefield propagation can thus be locally treated as homogeneous within a lateral distance comparable to the extrapolation step size. A piece-wise-constant-velocity model is often used in Fourier-domain wavefield extrapolation. The eigenvalue decomposition algorithm (Yao and Margrave, 2000) is accurate when the extrapolation step is large, but is too slow for practical application. Mi et al. (2000) show that large-step extrapolation with Padé approximation is slightly less accurate but a much faster algorithm, compared with the eigenvalue decomposition algorithm. However, the lack of speed is unsatisfactory. Mi and Margrave (2001a) have shown that a relatively large extrapolation step can be taken by the nonstationary integral extrapolators as long as appropriate replacement velocities are used for the static phase-shift and the focusing phase-shift. The large-step algorithm allows a much faster Fourier-domain wavefield extrapolation and can be used to generate reference wavefields at depth levels coarser than imaging steps. The wavefields at each imaging step can be computed with vertical linear interpolation between adjacent reference wavefields. This approach significantly reduces the run time of integral extrapolators without a significant loss of image quality.

The Alberta Foothills region is important to the Canadian oil and gas industry. Topographic variation often exceeds several hundred meters. High near-surface velocities in addition to these topographic variations present great difficulty for conventional statics correction that is based on the assumption of near-surface vertical raypaths. Though wave-equation redatuming (Berryhill, 1979; Shtivelman and Canning, 1988) is often very effective, correction to any artificial migration datum below the topography results in a loss of near-surface images. Imaging from topography thus becomes advantageous in such a case of severely varying topography (Gray and Marfurt, 1995; Lines et al., 1996). Kirchhoff-type migration-from-topography algorithms can be implemented by computing traveltimes from topography; however, difficulties previously discussed endure. Fourier-domain imaging techniques have many advantages over Kirchhoff algorithms; however, these methods require that seismic data be acquired on a flat datum so that plane wave decomposition can be performed with a double Fourier transform. One common way to perform Fourier-domain imaging from topography is by continuously muting the energy above the topography and including data recorded on the topography in each imaging step. Another method is to directly incorporate the laterally varying extrapolation step size into the nonstationary wavefield extrapolator (Margrave and Yao, 2000).

Converted-wave (P-S) exploration is often effective in areas where the P wave methods encounter difficulties. Converted-wave depth-imaging also produces shear-wave velocity information that is often crucial in determining physical properties of rock. The elastic wavefield-extrapolation theory has existed for more than a decade (Haime and Wapenaar, 1989; Wapenaar and Haime, 1990, 1991; Haime and Wapenaar, 1991);

however, it is not yet popularly used in seismic processing. This is due to the fact that acquisition techniques that highlight converted shear waves have not existed for long enough to prove worthiness and the cost is often prohibitively high. Converted-wave data processing is fundamentally different from conventional P-P wave data processing. Algorithms found to be effective and simple on P-P data, such as the DMO, become quite complex with P-S data. An advantage of Fourier-domain wavefield extrapolation is that P-P algorithms can be conveniently applied to converted wave data without significant complications.

Prestack depth-imaging is sensitive to velocity errors. Migration velocity analysis (MVA) utilizes this sensitivity and often provides better estimations of velocity than conventional velocity analysis techniques. The core technology in any MVA algorithm is the update method of the velocity model. Well established MVA methods include 1) **iterative profile migration**, which updates the model parameter by minimizing the event curvature in common-image-gathers (CIG) (Al Yahya, 1989), 2) **stacking power optimization**, which is analogous to conventional velocity analysis in that it uses a variety of subsurface models to migrate and stack the data to obtain a semblance spectrum (Tieman, 1984) and 3) **focusing analysis**, which utilizes the best focusing point as a criterion to judge the velocity model (Yilmaz and Chambers, 1984; MacKay and Abma, 1992). The aforementioned methods, however, assume that velocity is laterally invariant. The most appropriate means is tomographic inversion, which performs traveltimes inversions for each event. Lateral velocity variation is allowed and handled well with this method. It is, however, much slower than other non-inversion methods due to intensive involvement of human interpretation.

1.2 INTRODUCTION TO THE THEORY OF NONSTATIONARY FILTERING

The concept of nonstationary convolution and time-variant filtering was first formulated by Pann and Shin (1976) and Sheuer and Oldenburg (1988). Margrave (1998) used a more complete formulation and showed two fundamental types of nonstationary filters: nonstationary convolution and nonstationary combination. A time-domain nonstationary convolution can be written as

$$g(t) = \int_{-\infty}^{+\infty} a(t - \tau, \tau)h(\tau)d\tau , \quad (1.3)$$

where $a(t - \tau, \tau)$ is the time-variant impulse response with t symbolizing the time of a particular impulse response and τ denoting time tracking the variation of the impulse form, $h(\tau)$ is the stationary time series; for example, reflectivity sequences, to be convolved and $g(t)$ is the nonstationary convolution result. The Fourier-domain counterpart can be written as

$$G(f) = \int_{-\infty}^{+\infty} H(F)A(f, f - F)dF , \quad (1.4)$$

where $G(f)$ and $H(F)$ are the ordinary Fourier spectra of $g(t)$ and $h(\tau)$ respectively.

They are given by

$$G(f) = \int_{-\infty}^{+\infty} g(t) e^{-2\pi i f t} dt$$

and

$$H(F) = \int_{-\infty}^{+\infty} h(\tau) e^{-2\pi i F \tau} d\tau .$$

Also in equation (1.4), $A(f, f - F)$ is the frequency connection function, a 2D Fourier transform of $a(t - \tau, \tau)$. It is written as

$$A(p, q) = \int \int_{-\infty}^{+\infty} a(u, v) e^{-2\pi i p u} e^{-2\pi i q v} dudv ,$$

with $u = t - \tau$, $v = \tau$, $p = f$ and $q = f - F$.

The time-domain nonstationary combination and its Fourier counterpart can be written as

$$\bar{g}(t) = \int_{-\infty}^{+\infty} a(t - \tau, t) h(\tau) d\tau , \quad (1.5)$$

and

$$\bar{G}(f) = \int_{-\infty}^{+\infty} H(F) A(F, f - F) dF . \quad (1.6)$$

The symbols are similar to those defined in the nonstationary convolution. An overhead bar denotes nonstationary combination. Margrave (1998) showed that a time-domain nonstationary convolution is equivalent to a Fourier-domain nonstationary combination, and vice versa. The nonstationary convolution corresponds to a

windowing-then-filtering process and the nonstationary combination corresponds to a filtering-then-windowing process (Margrave, 1998).

The nonstationary filtering concept can be easily illustrated with the construction of a seismic trace with a minimum phase Q attenuation effect. Figure 1.1 shows the nonstationary convolution between a random reflectivity series and a time-variant wavelet. The wavelet experiences a $Q=40$ anelastic attenuation as it propagates. Each column of the matrix on the left of the graphic equation is a wavelet at time τ after attenuation. The nonstationary convolution is merely a replacement of each spike at time τ with with the wavelet at time τ scaled by the amplitude of the spike.

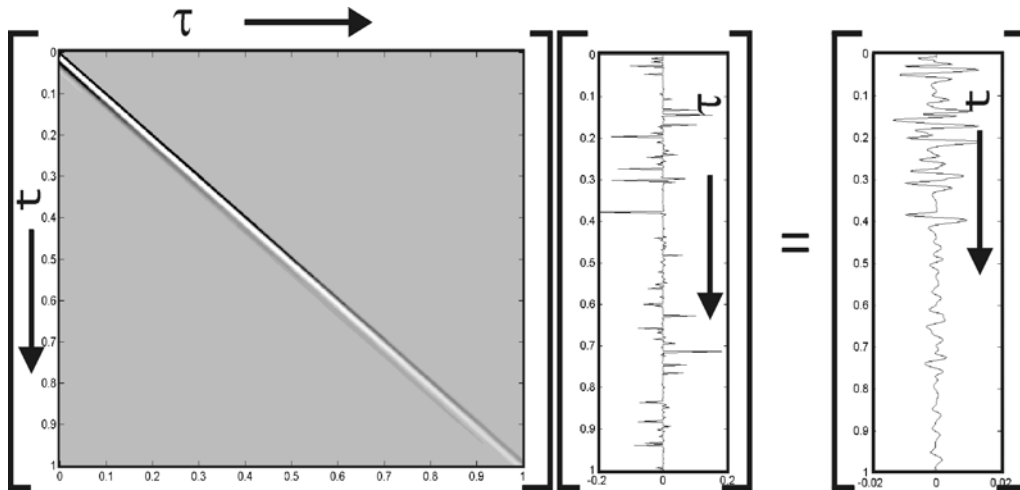


Figure 1.1 A synthetic seismic trace is created by nonstationary convolution. The nonstationary convolution can be implemented by multiplication of a time-variant wavelet matrix with stationary reflectivity vector (Margrave, 1998).

Margrave (1998) applied the nonstationary filtering theory in the context of 1D time-variant deconvolution. Schoepp (1998) presented more technical details of the nonstationary deconvolution (NSD) algorithm and Mi and Margrave (1999) further combined the homomorphic deconvolution and the nonstationary deconvolution

algorithm for better estimation of the reflectivity. Details of the homomorphic nonstationary deconvolution technique can be found in Mi and Margrave (1999).

Figure 1.2 compares the (a) original reflectivity, (b) synthetic seismic trace, (c) band-limited reflectivity (5-10-75-80 Hz Butterworth) and (d) the trace deconvolved by the homomorphic nonstationary deconvolution algorithm. Note the similarity between the band-limited reflectivity and the deconvolution results.

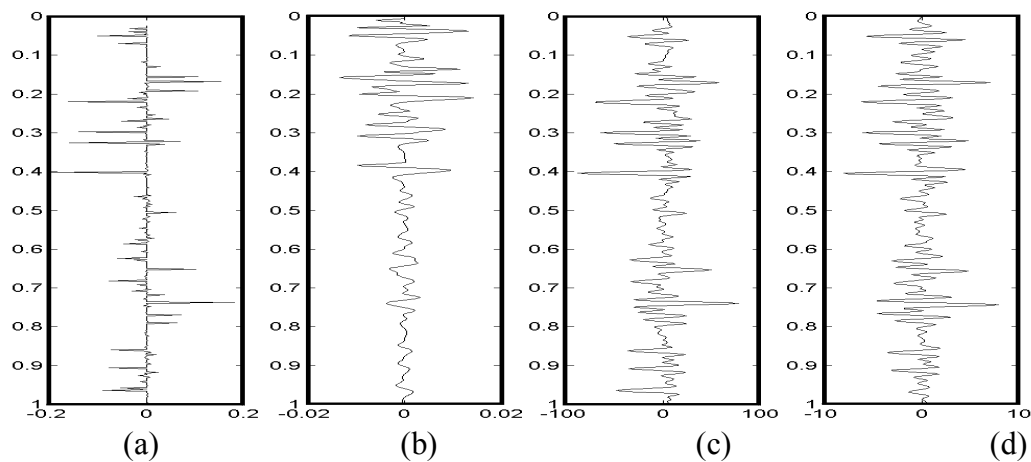


Figure 1.2 An example of the homomorphic nonstationary deconvolution algorithm. (a) reflectivity, (b) synthetic trace with $Q=40$ attenuation, (c) band-limited reflectivity by convolving a 5-10-70-85 (same bandwidth as the deconvolved trace) Ormsby wavelet with the reflectivity and (d) deconvolved trace.

1.3 APPLICATION OF NONSTATIONARY FILTERING THEORY IN FOURIER-DOMAIN PRESTACK DEPTH IMAGING

Margrave (1998) suggested a natural extension of the nonstationary filtering theory to seismic imaging to best handle large lateral velocity variation. Margrave and Ferguson (1997; 1999a) developed the combinational extrapolator (PSPI) and the convolutional extrapolator (NSPS). They recognized that these extrapolators are pseudo-differential

operator solutions to the wave equation with variable coefficients. These two extrapolators were applied to depth-imaging using a windowed split-step Fourier method approach. The relative computational efficiency of the two extrapolators was examined by Ferguson and Margrave (1997) and found to be equivalent. A Taylor-series derivation of the PSPI and the NSPS extrapolators showed that first-order error terms opposed each other and a symmetric extrapolator (SNPS) can be formed by combining the two (Margrave and Ferguson, 2000). This combination has higher accuracy and stability than either PSPI and NSPS alone.

Black et al. (1984) and Fishman and McCoy (1985) provided similar analysis of Fourier-domain algorithms, which accommodate lateral velocity variations. However, Black et al. (1984) provided little insight into the nature of their extrapolator and Fishman and McCoy (1985) didn't recognize theirs as Gazdag's PSPI in nonstationary limitations.

1.4 THESIS STRUCTURE

The objective of this thesis is to further develop theoretical and practical aspects of integral nonstationary wavefield extrapolators. Chapter 2 reviews three types of integral nonstationary wavefield extrapolators (PSPI, NSPS and SNPS) and provides full integral implementation as well as an approximate implementation of windowed, split-step Fourier algorithm. Various computing issues relating to the full integral implementation are discussed since the volume of data requiring computation has been the factor most deterring the practical implementation. Details on parallel implementation of these

algorithms on the Compaq Alpha cluster workstation at the University of Calgary is also given. The parallel environment provided by the Multimedia Advanced Computational Infrastructure (MACI) at the University of Calgary is the primary facility used to compute most of the results of this thesis.

Chapter 3 discusses the dual algorithm, which utilizes the integral nonstationary wavefield extrapolator to computing reference wavefields at coarse depth levels and vertical interpolation to compute the wavefields at imaging steps. A key issue in the dual algorithm is selection of appropriate replacement velocities for the static and focusing phase-shift terms. Both zero-offset extrapolation tests and prestack depth-imaging examples are provided.

Chapter 4 presents the algorithm for prestack depth-imaging from topography with the nonstationary wavefield extrapolators. A comparison between the images generated by other algorithms and the dual algorithm is given.

Chapter 5 reviews the elastic wavefield extrapolation theory and gives the dual algorithm solution to the P-S shot gather prestack depth-imaging problem. The Blackfoot 1997 3C-2D data set was used for testing the algorithm. Both the vertical and radial components are migrated with the dual algorithm for correlation analysis.

There has been significant interest in wave-equation migration and development of computationally efficient 3D prestack depth migration algorithms based on the scalar wave equation (Biondi and Palacharla, 1996; Biondi, 1997; Mosher et al., 1997). Corresponding progress in the development of wave equation migration velocity analysis (MVA), however, has been little. Since most established MVA algorithms assume

laterally invariant velocity, when velocity varies laterally, good estimations of velocity can only be provided when the following two conditions hold true: 1) analysis aperture is small and 2) the wavefield is recorded close to the reflector. Chapter 6 discusses an innovative MVA method that utilizes downward continuation of the wavefields to reduce the analysis aperture and the distance to the reflectors.

CHAPTER 2

IMPLEMENTATION OF INTEGRAL WAVEFIELD EXTRAPOLATORS

2.1 SIGN DEFINITION IN FOURIER TRANSFORMS AND WAVEFIELD EXTRAPOLATION

The ‘signs’ of kernel function in the time- and spatial-Fourier transform must be defined before delineating the direction of wavefield extrapolation. The convention of Fourier transforms used in this thesis is as follows

- I. Time-to-frequency transform

$$G(\omega) = \int_{-\infty}^{+\infty} g(t) e^{-i\omega t} dt .$$

- II. Frequency-to-time transform

$$g(t) = \frac{1}{2\pi} \int_{-\infty}^{+\infty} G(f) e^{i\omega t} d\omega.$$

$g(t)$ and $G(\omega)$ are the signal and the corresponding Fourier transform, where ω is the circular frequency defined as $\omega = 2\pi f$.

III. Spatial-coordinate-to-wavenumber transform

$$H(k_x) = \int_{-\infty}^{+\infty} h(x) e^{ik_x x} dx.$$

IV. Wavenumber-to-spatial-coordinate transform

$$h(x) = \frac{1}{2\pi} \int_{-\infty}^{+\infty} H(k_x) e^{-ik_x x} dk_x.$$

Functions $h(x)$ and $H(k_x)$ are the signal and the corresponding Fourier transform, where k_x is the spatial wavenumber defined as $k_x = 2\pi/\lambda_x$. λ_x is the apparent horizontal wavelength. Only the 1D case is considered. Note that the signs in the spatial transform are opposite to those used in time-frequency transforms.

According to the foregoing sign convention, a time function $g(t)$ after advancing Δt in time can be written as

$$g(t + \Delta t) = \frac{1}{2\pi} \int_{-\infty}^{+\infty} G(\omega) e^{i\omega(t+\Delta t)} d\omega.$$

This corresponds to a linear phase-shift in the frequency domain.

In seismic migration, the z -axis points downward. Downward extrapolation from z to $z + \Delta z$ of a mono-frequency wavefield, $\phi(k_x, \omega, z)$, in a constant-velocity medium can be written as

$$\phi(k_x, \omega, z + \Delta z) = \phi(k_x, \omega, z) e^{ik_z \Delta z},$$

where $\phi(k_x, \omega, z)$ is transformed with 2D Fourier transform, following the sign convention defined before. ω is the angular frequency as defined before and k_z is the vertical wavenumber defined as $k_z = \pm \sqrt{\frac{\omega^2}{v^2} - k_x^2}$, where v is the medium velocity, '+' denotes downward extrapolation and '-' denotes upward extrapolation.

2.2 WAVEFIELD EXTRAPOLATION BY PHASE-SHIFT-PLUS - INTERPOLATION

Considering only the 2D case, the derivation of the phase-shift-plus-interpolation (PSPI) algorithm (Gazdag and Sguazzero, 1984) begins with the scalar wave equation

$$\frac{\partial^2 p}{\partial^2 z} + \frac{\partial^2 p}{\partial^2 x} = \frac{1}{v^2(x, z)} \frac{\partial^2 p}{\partial t^2}, \quad (2.1)$$

where $p = p(x, z, t)$ is the pressure wavefield field and $v = v(x, z)$ denotes the earth velocity field.

The pressure field $p(x,z,t)$ can be expressed as a double Fourier transform of its (ω, k_x) -domain counterpart

$$p(x, z, t) = \frac{1}{(2\pi)^2} \int_{-\infty}^{+\infty} \int_{-\infty}^{+\infty} P(k_x, z, \omega) e^{i(k_x x - \omega t)} dk_x d\omega. \quad (2.2)$$

Substituting equation (2.2) into equation (2.1) leads to

$$\frac{1}{(2\pi)^2} \int_{-\infty}^{+\infty} \int_{-\infty}^{+\infty} \left[\frac{\partial^2 P(k_x, z, \omega)}{\partial z^2} - k_x^2 P(k_x, z, \omega) + \frac{\omega^2}{v^2(x, z)} P(k_x, z, \omega) \right] e^{i(k_x x - \omega t)} dk_x d\omega = 0. \quad (2.3)$$

When $v(x,z)$ is set to constant, the terms outside the square parentheses can be stripped off so that equation (2.3) becomes

$$\frac{\partial^2 P(k_x, z, \omega)}{\partial z^2} = \left(k_x^2 - \frac{\omega^2}{v^2} \right) P(k_x, z, \omega). \quad (2.4)$$

For a constant velocity, the vertical wavenumber is written as

$$k_z = \pm \sqrt{\frac{\omega^2}{v^2} - k_x^2}. \quad (2.5)$$

Equation (2.4) is an ordinary differential equation

$$\frac{\partial^2 P}{\partial z^2} = -k_z^2 P, \quad (2.6)$$

whose analytical solution includes waves propagating in both positive and negative directions,

$$P(k_x, z + \Delta z, \omega) = P_+(k_x, z, \omega)e^{ik_z \Delta z} + P_-(k_x, z, \omega)e^{-ik_z \Delta z}. \quad (2.7)$$

This is the theoretical basis on which phase-shift migration algorithms are established. For laterally variant media, Gazdag and Sguazzero (1984) proposed to extrapolate the wavefield, one depth-interval at a time with several reference velocities, then, to inverse Fourier transform the extrapolated wavefields to the space domain and interpolate for each point along the x -axis. In other words, starting with equation (2.4), consider several constant velocities (v_1, v_2, \dots) in the intervals $[v_{\min}, v_{\max}]$ and downward extrapolate the wavefield $P(k_x, z, \omega)$ to $P(k_x, z + dz, \omega)$ with each velocity. The resulting wavefields are

$$(P_1(k_x, z + dz, \omega), P_2(k_x, z + dz, \omega), \dots).$$

They are then inversely transformed to the (ω, x) domain

$$(P_1(x, z + dz, \omega), P_2(x, z + dz, \omega), \dots).$$

The wavefield at each spatial location is then computed by interpolating the two reference wavefields of closest reference velocity values. For example, using spatial location x with velocity $v(x)$, $v_1 < v(x) < v_2$, the amplitude and phase of the wavefield at this location can be computed as

$$|P_x(x, z + dz, \omega)| = \frac{v(x) - v_1}{v_1 + v_2} |P_2(x, z + dz, \omega)| + \frac{v_2 - v(x)}{v_1 + v_2} |P_1(x, z + dz, \omega)| \quad (2.8)$$

and

$$\Phi_x(x, z + dz, \omega) = \frac{v(x) - v_1}{v_1 + v_2} \Phi_2(x, z + dz, \omega) + \frac{v_2 - v(x)}{v_1 + v_2} \Phi_1(x, z + dz, \omega). \quad (2.9)$$

The resulting wavefield shifted by $v(x)$ can then be approximated as

$$P_x(x, z + dz, \omega) = |P_x(x, z + dz, \omega)| e^{i\Phi_x}. \quad (2.10)$$

All locations with velocity $v(x)$ can then be extracted from $P_x(x, z + dz, \omega)$ by a windowing process.

2.3 INTEGRAL WAVEFIELD EXTRAPOLATORS

With the use of a complete velocity set, the PSPI algorithm becomes an integral over horizontal wavenumber k_x , which performs wavefield extrapolation simultaneously with an inverse Fourier transform. It can be written as (Margrave and Ferguson, 1999b)

$$\psi(x, z, \omega) = \frac{1}{2\pi} \int_{-\infty}^{+\infty} \alpha(x, k_x, z, \omega) \varphi(k_x, 0, \omega) e^{-ik_x x} dk_x, \quad (2.11)$$

where $\alpha(x, k_x, z, \omega)$ is the nonstationary wavefield extrapolator that carries the wavefields from depth 0 to z or vice-versa. This is provided by

$$\alpha(x, k_x, z, \omega) = e^{\pm iz \sqrt{\frac{\omega^2}{v^2(x)} - k_x^2}}, \quad (2.12)$$

where $\psi(x, z, \omega)$ is the (ω, x) -domain expression of the wavefield at depth z and $\varphi(k_x, 0, \omega)$ is its (ω, k_x) -domain expression. Instead of using P to represent the wavefield in both (ω, k_x) and (ω, x) domains, ψ and φ will be used consistently throughout the rest of this thesis to represent the wavefields in (ω, x) and (ω, k_x) domains, respectively. The plus and minus signs denote downward and upward extrapolation.

Equation (2.11) has a transposed form, called nonstationary phase-shift (NSPS), which performs wavefield extrapolation simultaneously with a forward Fourier transform

$$\varphi(k_x, z, \omega) = \int_{-\infty}^{+\infty} \alpha(x, k_x, z, \omega) \psi(x, 0, \omega) e^{ik_x x} dx, \quad (2.13)$$

where $\alpha(x, k_x, z, \omega)$ is expressed by equation (2.12).

Equation (2.11) can be computed using matrix-vector multiplication when the velocity field is piece-wise constant

$$\underline{\underline{\psi}}_z = \underline{\underline{A}} \underline{\underline{\varphi}}_0, \quad (2.14)$$

where a single underscore represents vectors and a double underscore denotes the matrix. $\underline{\underline{\varphi}}_0$ and $\underline{\underline{\psi}}_z$ are, therefore, column vectors representing a mono-frequency wavefield in the (ω, k_x) domain at depth 0 and the extrapolated wavefield in the (ω, x) domain at depth z , respectively. Both $\underline{\underline{\varphi}}_0$ and $\underline{\underline{\psi}}_z$ are referred as “frequency slices” in this thesis.

Matrix $\underline{\underline{A}}$ is the array product of the PSPI wavefield extrapolator matrix and the inverse Fourier-transform kernel matrix

$$\underline{\underline{A}} = \begin{pmatrix} e^{i\left(\pm z \sqrt{\frac{\omega^2}{v_1^2} - k_{x1}^2} - x_1 k_{x1}\right)} & \cdot & \cdot & \cdot & e^{i\left(\pm z \sqrt{\frac{\omega^2}{v_1^2} - k_{xn}^2} - x_1 k_{xn}\right)} \\ \cdot & \cdot & \cdot & \cdot & \cdot \\ \cdot & \cdot & \cdot & \cdot & \cdot \\ \cdot & \cdot & \cdot & \cdot & \cdot \\ e^{i\left(\pm z \sqrt{\frac{\omega^2}{v_n^2} - k_{x1}^2} - x_n k_{x1}\right)} & \cdot & \cdot & \cdot & e^{i\left(\pm z \sqrt{\frac{\omega^2}{v_n^2} - k_{xn}^2} - x_n k_{xn}\right)} \end{pmatrix}. \quad (2.15)$$

Similarly, equation (2.13) can also be written in a matrix-vector product form

$$\underline{\varphi}_z = \underline{\underline{B}} \underline{\psi}_0, \quad (2.16)$$

where $\underline{\psi}_0$ and $\underline{\varphi}_z$ are column vectors representing a mono-frequency wavefield in the (ω, x) domain at depth 0 and the extrapolated wavefield in the (ω, k_x) domain at depth z , respectively. Matrix $\underline{\underline{B}}$ is the array product of the NSPS wavefield extrapolator matrix and the forward Fourier-transform kernel matrix

$$\underline{\underline{B}} = \begin{pmatrix} e^{i\left(\pm z \sqrt{\frac{\omega^2}{v_1^2} - k_{x1}^2} + x_1 k_{x1}\right)} & \cdot & \cdot & \cdot & e^{i\left(\pm z \sqrt{\frac{\omega^2}{v_n^2} - k_{xn}^2} + x_n k_{xn}\right)} \\ \cdot & \cdot & \cdot & \cdot & \cdot \\ \cdot & \cdot & \cdot & \cdot & \cdot \\ \cdot & \cdot & \cdot & \cdot & \cdot \\ e^{i\left(\pm z \sqrt{\frac{\omega^2}{v_1^2} - k_{xn}^2} + x_1 k_{xn}\right)} & \cdot & \cdot & \cdot & e^{i\left(\pm z \sqrt{\frac{\omega^2}{v_n^2} - k_{xn}^2} + x_n k_{xn}\right)} \end{pmatrix}. \quad (2.17)$$

The plus and minus signs in both equation (2.15) and (2.17) denote downward and upward extrapolation.

When $z=0$, matrix $\underline{\underline{A}}$ becomes the forward spatial Fourier-transform kernel and matrix $\underline{\underline{B}}$ becomes the inverse spatial Fourier-transform kernel. They are transposed to each other.

Margrave and Ferguson (1999b) showed that the NSPS and PSPI can be naturally combined into a symmetric wavefield extrapolator (SNPS) by first performing NSPS for the upper half z and PSPI for the lower half z within an extrapolation step. A Taylor-series derivation of PSPI and NSPS and related error analysis show that the first-order errors of PSPI and NSPS oppose one another; thus, that SNPS has a smaller error and higher stability than either PSPI or NSPS alone (Margrave and Ferguson, 2000).

2.4 IMAGING CONDITION FOR PRESTACK DEPTH MIGRATION

Prestack depth-imaging requires that both the recorded wavefield on the Earth's surface and the seismic source impulse be extrapolated downward into the Earth, utilizing a velocity model. The sign convention for source extrapolation adheres to that defined in section 2.1, while that of receiver extrapolation needs be reversed. Estimation of reflectivity from wavefields at a certain depth level is called an imaging condition, of which there are two types:

I. The deconvolution imaging condition estimates reflectivity by the ratio between the receiver and source wavefields. This process involves both phase- and amplitude-correction. Geometric-spreading energy-loss from both the source and the receiver are automatically corrected. Each frequency slice produces a frequency-dependent estimation of the reflectivity and all are averaged to eliminate frequency-dependence. The deconvolution imaging condition can be written as (Claerbout, 1971)

$$\tilde{r}_{\text{decon}}(x,z) = \frac{1}{[\omega_{\text{max}} - \omega_{\text{min}}]} \int_{\omega_{\text{min}}}^{\omega_{\text{max}}} \frac{|\psi_R(x,z,\omega)|}{|\psi_S(x,z,\omega)|} e^{i(\Phi_R(x,z,\omega) - \Phi_S(x,z,\omega))} d\omega, \quad (2.18)$$

where ω_{max} and ω_{min} are the maximum and minimum frequencies used in migration.

II. The crosscorrelation imaging condition sets the amplitude of the source wavefield to a constant value, normally 1.0, which leads to the crosscorrelation imaging condition. This process involves only the phase- and geometric-spreading corrections to the receiver wavefield. Source-side geometric spreading loss is ignored. It can be written as (Claerbout, 1971)

$$\tilde{r}_{\text{corr}}^*(x, z) = \frac{1}{[\omega_{\text{max}} - \omega_{\text{min}}]} \int_{\omega_{\text{min}}}^{\omega_{\text{max}}} |\psi_R(x, z, \omega)| e^{i(\Phi_R(x, z, \omega) - \Phi_S(x, z, \omega))} d\omega. \quad (2.19)$$

The frequency-dependent reflectivity is averaged to eliminate frequency dependency.

The deconvolution imaging condition is a true-amplitude algorithm and, theoretically, more appropriate in terms of true-amplitude processing. It is, however, unstable for real seismic evaluations due to the embedded noise and is often accompanied by a very noisy background. The crosscorrelation imaging condition is more stable and the image quality can be superior to the deconvolution imaging condition. All depth images in this thesis have been computed with the crosscorrelation imaging condition. A prestack shot gather depth-imaging algorithm with SNPS is shown in **Figure 2.1**.

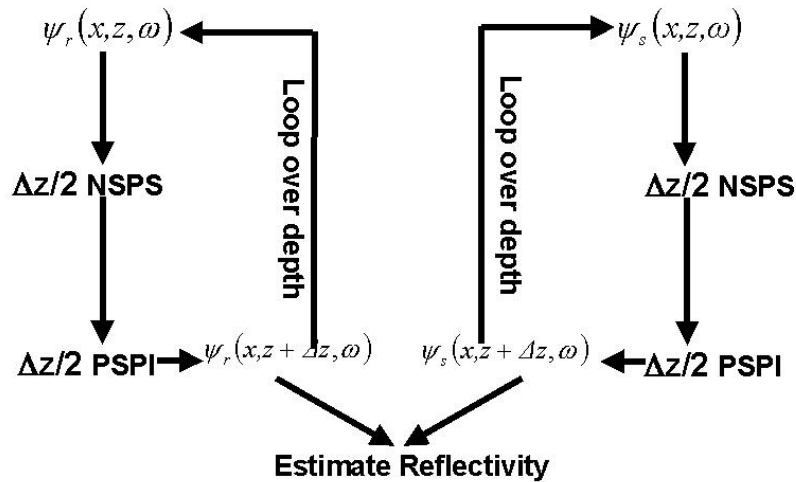


Figure 2.1 Computational steps of the SNPS prestack depth-imaging algorithm.

2.5 REVIEW OF SPLIT-STEP FOURIER ALGORITHM

A precise solution to the one-way scalar wave equation exists only in a medium of constant velocity. The split-step Fourier method provides an accurate numerical solution to the variable-coefficient wave equation in weakly inhomogeneous media (Hardin and Tappert, 1973). This is based on the perturbation theory and has been widely used in studies of acoustic wave propagation in oceans (for example, McDaniel, 1975). Stoffa et al. (1990) introduced this method to seismic imaging. Several variations, such as the phase-screen and pseudo-screen methods (Wu and Huang, 1992; de Hoop and van Stralen, 1997), were developed in later literatures. A brief review of the split-step algorithm is given below.

The 2D propagation of acoustic waves in a constant-density medium can be expressed by the wave equation

$$\nabla^2 p - s^2 \frac{\partial^2 p}{\partial t^2} = 0, \quad (2.20)$$

where $p(x,z,t)$ is the pressure field and $s = s(x,z)$ is the slowness field of the media, which is defined as the inverse of half the propagation velocity $s(x,z) = 2/(v(x,z))$. This consideration is mandated by the exploding reflector model when zero-offset or post-stack data are migrated. For prestack depth-imaging, since both the source and receivers are extrapolated downward, this slowness field should be defined as the inverse of the true propagation velocity.

Taking the Fourier transform of equation (2.20) gives the frequency-domain expression

$$\nabla^2 P + \omega^2 s^2 P = 0, \quad (2.21)$$

where

$$P(x, z, \omega) = \int_{-\infty}^{+\infty} p(x, z, t) e^{-i\omega t} dt. \quad (2.22)$$

The slowness field can be decomposed to a constant component and a perturbation component

$$s(x, z) = s_0(x, z) + \Delta s(x, z). \quad (2.23)$$

The constant reference slowness field $s_0(x, z)$ is normally specified as the mean of $s(x, z)$ and the perturbation slowness field $\Delta s(x, z)$ accommodates all velocity field variations. Thus, the homogeneous wave equation is transformed into an inhomogeneous, constant-slowness wave equation

$$\nabla^2 P + \omega^2 s_0^2 P = -S(x, z, \omega), \quad (2.24)$$

where P denotes the Fourier-transformed wavefield and $S(x, z, \omega)$ is a source-like term given by

$$S(x, z, \omega) = \omega^2 \left[2s_0 \Delta s(x, z, \omega) + \Delta s^2(x, z, \omega) \right] P(x, z, \omega). \quad (2.25)$$

Ignoring the second-order term $\Delta s^2(x, z, \omega)$ in the square brackets, the split-step Fourier method can be performed with the following three steps,

- I. Spatial Fourier-transform the previously extrapolated wavefield at depth z_n to the wavenumber domain

$$\bar{P}(k_x, z_n, \omega) = \int_{-\infty}^{+\infty} P(x, z_n, \omega) e^{ik_x x} dx. \quad (2.26)$$

The overhead bar indicates that the wavefield is in wavenumber domain.

- II. Apply phase-shift based on the vertical wavenumber, computed using the reference slowness for all frequencies and wavenumbers

$$\bar{P}_r(k_x, z_n, \Delta z, \omega) = \bar{P}(k_x, z_n, \omega) e^{ik_{z_0} \Delta z}, \quad (2.27)$$

where

$$k_{z_0} = \sqrt{\omega^2 s_0^2 - k_x^2} = \omega s_0 \sqrt{1 - (k_x / \omega s_0)^2}. \quad (2.28)$$

s_0 is the mean slowness within the extrapolation step.

- III. Inverse Fourier-transform the phase-shifted data to the space domain

$$P_r(x, z_n, \Delta z, \omega) = \frac{1}{2\pi} \int_{-\infty}^{+\infty} P_r(k_x, z_n, \Delta z, \omega) e^{ik_x x} dk_x, \quad (2.29)$$

then apply a static phase-shift to correct for slowness perturbation in the extrapolation interval

$$P(x, z_{n+1}, \omega) = P_r(x, z_n, \Delta z, \omega) e^{i\omega \Delta s(x, z) \Delta z}. \quad (2.30)$$

Integrate $P(x, z_{n+1}, \omega)$ over all the frequencies of interest to obtain the migrated data

$$p(x, z_{n+1}, 0) = \frac{1}{2\pi} \int_{-\infty}^{+\infty} P(x, z_{n+1}, \omega) d\omega. \quad (2.31)$$

To be consistent with derivations in later sections, replace the wavefield symbol P in equation (2.21) with a general symbol ψ that can be any of a pressure field, a displacement field or a velocity field, the extrapolation from depth z to $z + \Delta z$ with split-step Fourier method can be written as

$$\psi(x, z + \Delta z, \omega) = e^{i\omega \Delta s(x, z) \Delta z} \int_{-\infty}^{+\infty} \left(\int_{-\infty}^{+\infty} \psi(x', z, \omega) e^{ik_x x'} dx' \right) e^{ik_{z0} \Delta z} dk_x. \quad (2.32)$$

The integrals in the above equation correspond to the (ω, k_x) -domain constant-velocity extrapolation while the term outside the integrals corresponds to a (ω, x) -domain slowness-perturbation correction. k_{z0} is the vertical wavenumber of the wave propagating at background velocity v_0 . The resulting wavefield is exact in vertical traveltime while approximately focused.

2.6 DERIVATION OF SPLIT-STEP EXTRAPOLATOR FROM NONSTATIONARY PHASE-SHIFT OPERATOR

As expressed in the nonstationary filter (2.12), the vertical wavenumber k_z in heterogeneous media can be written as

$$k_z(k_x, x) = \sqrt{\frac{\omega^2}{v^2(x)} - k_x^2}, \quad (2.33)$$

which in the discrete case can be written as a matrix with k_x and x as coordinates. For

simplicity's sake, only the positive sign is considered. Add, then subtract $\frac{\omega^2}{v_0^2}$ under the

square root, and then extract $k_{z_0} = \sqrt{\frac{\omega^2}{v_0^2} - k_x^2}$ which produces

$$k_z(k_x, x) = k_{z_0} \sqrt{1 + \frac{\omega^2}{k_{z_0}^2} \left(\frac{1}{v^2(x)} - \frac{1}{v_0^2} \right)}. \quad (2.34)$$

The second term under the square root in (2.34) can be much smaller than 1 when $v(x)$ is close to v_0 , a binomial expansion and truncation of the higher-order terms of equation (2.34) leads to

$$k_z(k_x, x) \approx k_{z_0} + \frac{\omega^2}{2k_{z_0}} \left(\frac{1}{v^2(x)} - \frac{1}{v_0^2} \right). \quad (2.35)$$

Note that the first term on the right side of equation (2.35) is a (ω, k_x) -domain homogeneous phase-shift. Similar to the computation of integral extrapolators, the second term can also be written as a matrix with x and k_x as coordinates. By approximating k_{z_0} with $\frac{\omega}{v_0}$ in the second term on the right of equation (2.35), the sequence becomes a (ω, x) -domain static phase-shift that is independent of wavenumbers. Equation (2.35) can thus be written as

$$k_z \approx k_{z_0} + \frac{\omega v_0}{2} \left(\frac{1}{v(x)} + \frac{1}{v_0} \right) \left(\frac{1}{v(x)} - \frac{1}{v_0} \right). \quad (2.36)$$

Using the approximation $\frac{v_0}{2} \left(\frac{1}{v(x)} + \frac{1}{v_0} \right) \approx 1$ since $v(x)$ is close to v_0 , a split-step operator can be obtained

$$k_z \approx k_{z_0} + \omega \left(\frac{1}{v(x)} - \frac{1}{v_0} \right). \quad (2.37)$$

The wavefield extrapolation from z to $z + \Delta z$ can then be written as

$$\psi(x, z + \Delta z, \omega) = \int_{-\infty}^{+\infty} \left(\int_{-\infty}^{+\infty} \psi(x', z, \omega) e^{ik_x x'} dx' \right) e^{i \left[k_{z_0} + \omega \left(\frac{1}{v(x)} - \frac{1}{v_0} \right) \right] \Delta z} dk_x. \quad (2.38)$$

The term in the parentheses is a forward spatial Fourier-transform. Since

$\Delta s = \left(\frac{1}{v(x)} - \frac{1}{v_0} \right)$ is independent of k_x , the above equation can be written as

$$\psi(x, z + \Delta z, \omega) = e^{i\omega \Delta s(x, z) z} \int_{-\infty}^{+\infty} \left(\int_{-\infty}^{+\infty} \psi(x', z, \omega) e^{ik_x x'} dx' \right) e^{ik_{z_0} \Delta z} dk_x. \quad (2.39)$$

This equation is the same as equation (2.32).

By direct using equation (2.36), equation 2.38 becomes

$$\psi(x, z + \Delta z, \omega) = \int_{-\infty}^{+\infty} \left(\int_{-\infty}^{+\infty} \psi(x', z, \omega) e^{ik_x x'} dx' \right) e^{i \left[k_{z_0} + \frac{1}{2} \omega \left(\frac{1}{v(x)} - \frac{1}{v_0} \right) \left(\frac{1}{v(x)} + \frac{1}{v_0} \right) \right] \Delta z} dk_x. \quad (2.40)$$

This gives a slightly more accurate form of split-step method

$$\psi(x, z + \Delta z, \omega) = e^{i \frac{1}{2} \omega \left(\frac{1}{v(x)} - \frac{1}{v_0} \right) \left(\frac{1}{v(x)} + \frac{1}{v_0} \right) \Delta z} \int_{-\infty}^{+\infty} \left(\int_{-\infty}^{+\infty} \psi(x', z, \omega) e^{ik_x x'} dx' \right) e^{ik_{z_0} \Delta z} dk_x. \quad (2.41)$$

2.7 APPROXIMATION OF PSPI, NSPS AND SNPS AS WINDOWED SPLIT-STEP FOURIER ALGORITHMS

The PSPI integral extrapolator is written as

$$\psi(x,z,\omega) = \frac{1}{2\pi} \int_{-\infty}^{+\infty} \alpha(x,k_x,z,\omega) \varphi(k_x,0,\omega) e^{-ik_x x} dk_x. \quad (2.42)$$

but is generally too slow for practical application. A faster while less accurate approximation is to break the lateral velocity function into small windows $(1,2,\dots,j)$, in which the velocity variation is small in term of percentage of the local mean value (for example, no more than 15%), so that the split-step Fourier method remains accurate locally. The percentage velocity variation within a spatial window is defined as

$$percentage = \frac{v_{\max} - v_{\min}}{v_{\text{mean}}}. \quad (2.43)$$

Considering that the PSPI integral is a nonstationary combination filter, which corresponds to a filtering-then-windowing process, the extrapolation of the overall wavefield can be written as a combination of all wavefield extrapolations within each lateral window. Reducing the window size to a single, spatial location leads to the exact PSPI integral. Considering extrapolation from $z = 0$ to depth z , the PSPI integral can be approximated by a localized split-step algorithm (Ferguson and Margrave, 1999)

$$\psi(x,z,\omega) = \sum_j \Omega_j(x) \frac{1}{2\pi} \int_{-\infty}^{+\infty} \alpha'_j(k_x,z,\omega) \varphi(k_x,0,\omega) e^{-ik_x x} dk_x, \quad (2.44)$$

where $\alpha'_j(k_x,z,\omega)$ is the local wavefield extrapolator applied to the overall wavefield so that the wavefield in spatial window j can be best approximated. $\varphi(k_x,0,\omega)$ is the (ω,k_x) -domain wavefield at depth 0. The windowing function is

$$\Omega_j(x) = \begin{cases} 1, & \text{within window} \\ 0, & \text{outside of window} \end{cases}. \quad (2.45)$$

Following the split-step Fourier method, $\alpha_j(k_x, z, \omega)$ can be written as a constant reference based on the mean velocity with the addition of a slowness-perturbation factor due to the velocity variation within the spatial windows. The overall extrapolated wavefield can be written as

$$\psi(x, z, \omega) = \sum_j \beta_j(x, \omega) \Omega_j(x) \frac{1}{2\pi} \int_{-\infty}^{+\infty} \alpha_j(k_x, z, \omega) \rho(k_x, 0, \omega) e^{-ik_x x} dk_x, \quad (2.46)$$

where $\alpha_j(k_x, z, \omega)$ and $\beta_j(x, \omega)$ are wavefield extrapolators with constant velocity, relevant to a (ω, k_x) -domain focusing phase-shift and a (x, ω) -domain vertical traveltime correction, respectively. These can be written as

$$\alpha_j(k_x, z, \omega) = \exp\left(iz \sqrt{\left(\frac{\omega}{v_j}\right)^2 - k_x^2}\right), \quad (2.47)$$

and

$$\beta_j(\omega, x) = \exp\left(i\omega z \left(\frac{1}{v(x)} - \frac{1}{v_j}\right)\right). \quad (2.48)$$

Similarly, the NSPS integral can be approximated as

$$\varphi(k_x, z, \omega) = \sum_j \alpha_j(k_x, z, \omega) \int_{-\infty}^{+\infty} \psi(x, 0, \omega) \Omega_j \beta_j(x, \omega) e^{ik_x x} dx, \quad (2.49)$$

which first performs a (ω, x) -domain windowing and slowness correction based on the reference velocities in each window and then a (ω, k_x) -domain constant velocity wavefield extrapolation.

Kessinger (1992) gave an extended split-step Fourier method similar to equation (2.46) to accommodate large lateral velocity variation. However, he did not realize the existence of the the NSPS form of the windowed split-step Fourier method, which is roughly a transposed form of the algorithm he proposed.

A recursive, symmetric and windowed wavefield extrapolator can be formulated by combining equations (2.46) and (2.49).

Computing equations (2.46) and (2.49) is much faster than the corresponding integral operators when the number of spatial windows is small. The performance of both algorithms is discussed in section 3.9. A Matlab version of the localized split-step Fourier algorithm expressed in equation (2.39) for prestack shot gather depth-imaging was implemented by Ferguson (2000) and rewritten by the present author in Fortran 90 (Mi and Margrave, 2000a). The Fortran 90 version is stand-alone software that accepts data in standard IEEE SEG-Y format. The split-step Fourier algorithm expressed in equation (2.41) was also implemented. An in-depth and detailed description of this software can be found in Mi and Margrave (2000a).

Figure 2.2 shows the migration of shot gather 120 from the Marmousi synthetic data set (Bourgeois et al., 1991) with localized split-step Fourier algorithm using a set of reference velocities 100 m/s apart. Each original shot gather contains 96 traces with 25-m receiver spacing. The nearest offset is 200 m. The geometry simulates typical, one-sided, marine data acquisition. In consideration of the complexity of the velocity model, each of the shot gathers was padded to 256 traces of split-spread geometry in order to accommodate the migrated energy on both sides of the source. Each trace has 512 samples at a 4-ms sampling interval. Migration of each shot produced local images of the subsurface; and overlapping all migrated shot gathers produces a complete subsurface image. The overlapping process is equivalent to common-image-gather (CIG) sorting and stacking, a procedure in which all traces belonging to a certain receiver location are gathered and stacked. **Figure 2.3** shows the Marmousi velocity model. **Figure 2.4** shows the CIG-stack section produced with a set of reference velocities 100 m/s apart and with the (ω, x) -domain slowness corrections described in equation (2.39) and equation (2.41), respectively. Both structures in the middle of the model and the flat spot at depth 2550 m from the CIG at 6000 m to the CIG at 7500 m are slightly better imaged with equation (2.41).

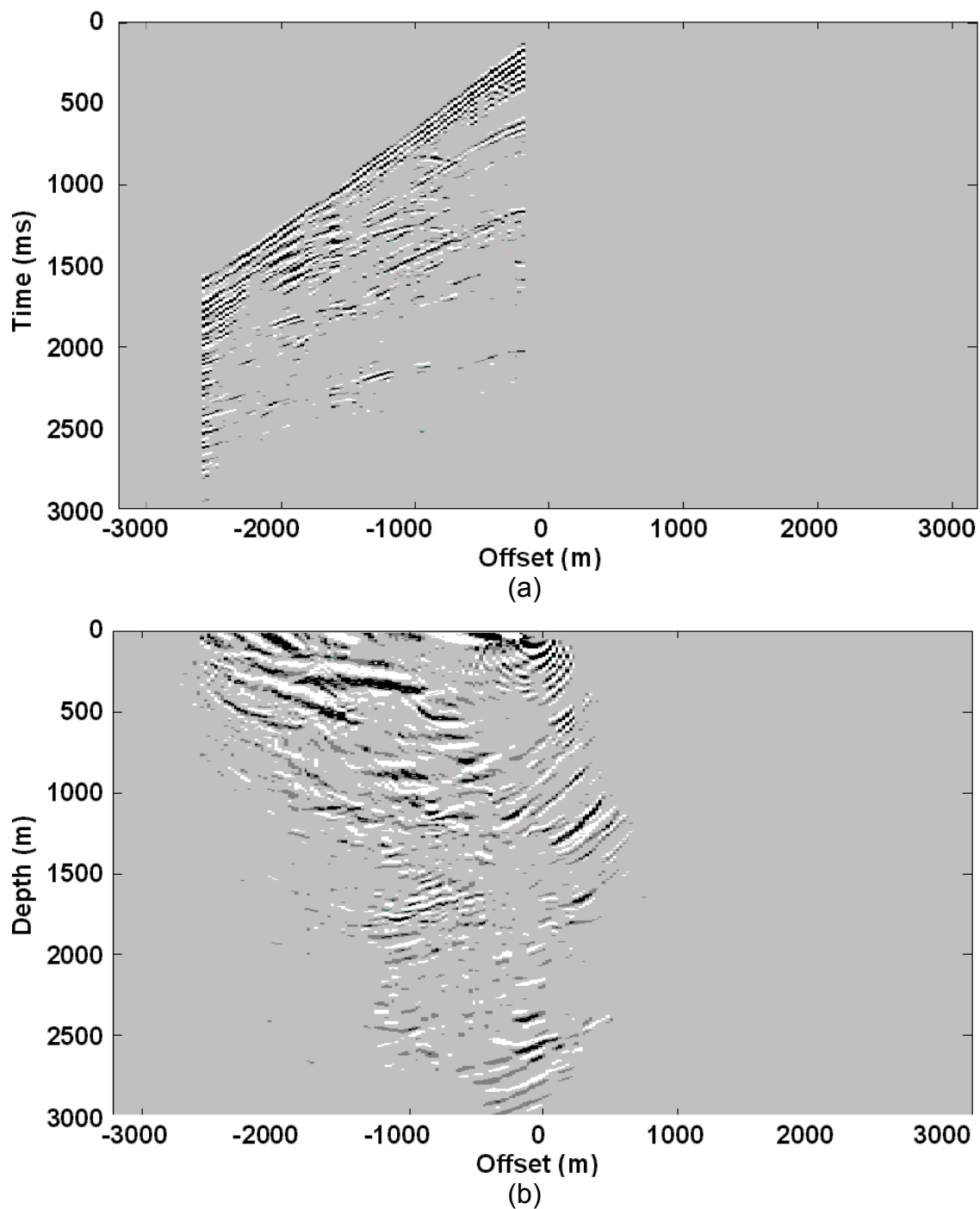


Figure 2.2 Marmousi synthetic shot gather 120 located at the middle of the velocity model (a) before and (b) after migration. The migration is performed with the localized split-step Fourier algorithm as an approximation of the SNPS integral algorithm. Reference velocities of 100 m/s apart and slowness correction described in equation (2.39) were used.

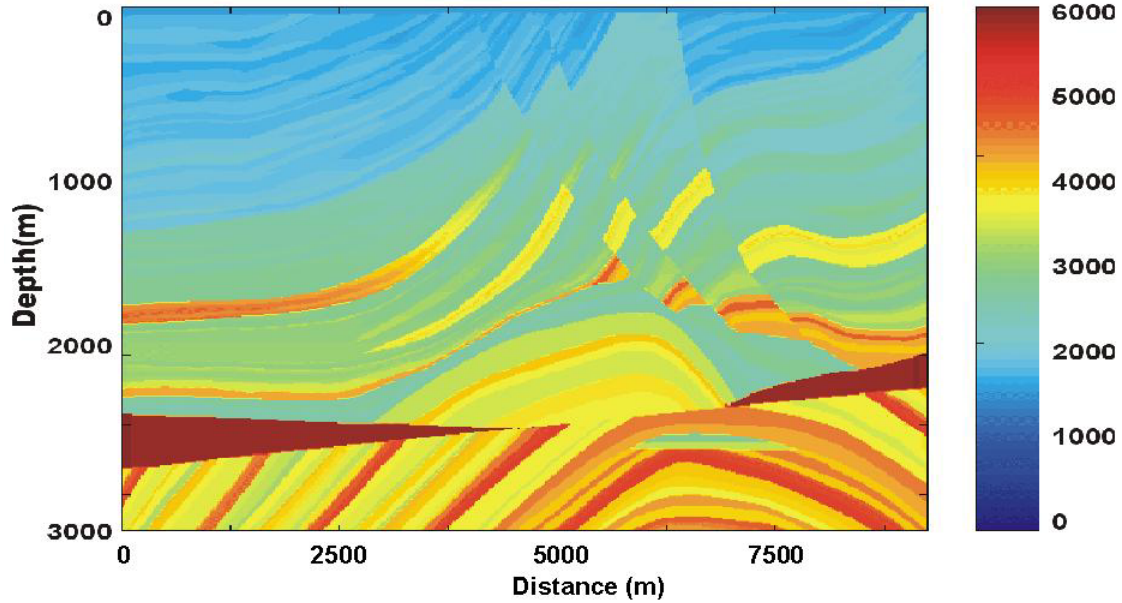
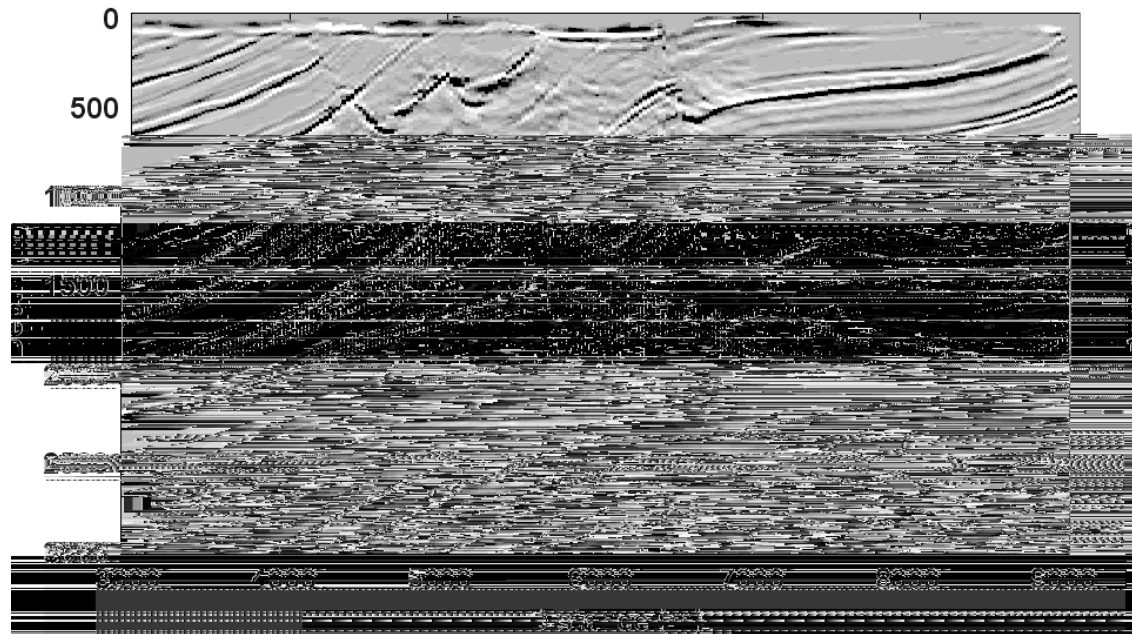


Figure 2.3 Marmousi P-wave velocity model.

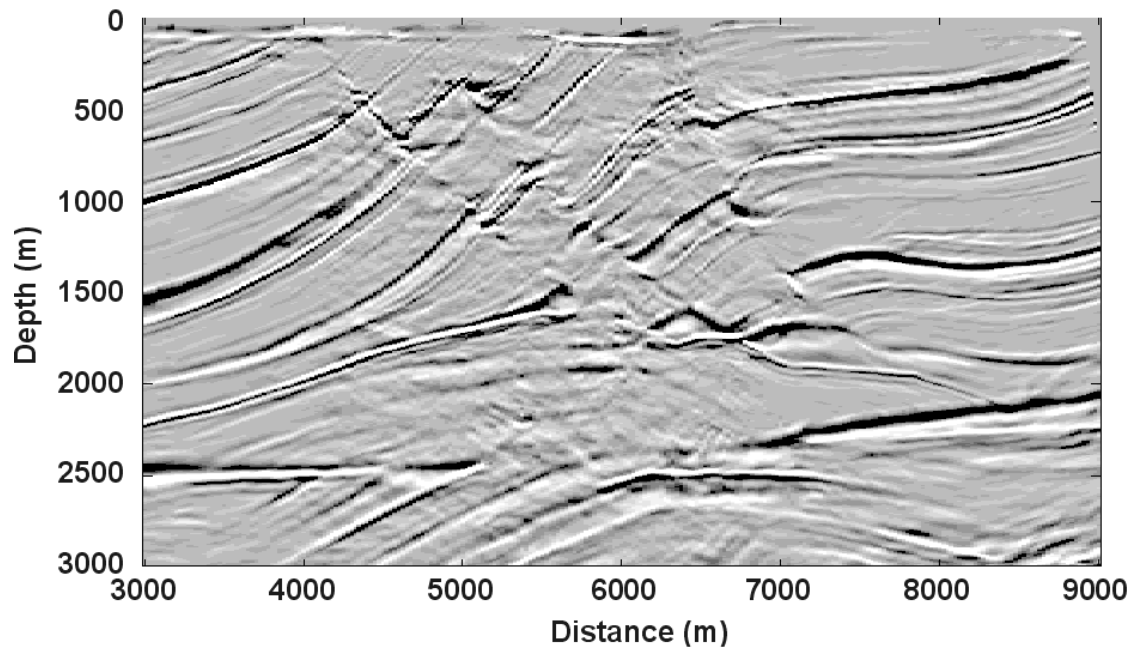
2.8 PARALLEL IMPLEMENTATION ON THE MACI ALPHA CLUSTER

Computing each frequency with matrix-vector multiplication is an $O(N^2)$ algorithm, where N is the number of traces in a shot gather. Assuming that the number of frequencies to be computed, N_ω , is of the same order as N , each step of SNPS is an N^3 algorithm. If the number of depth steps is N_z and the number of shots is N_s , the total computation required for imaging is of the order $N_s N_z N^3$. Computing equations (2.39) and (2.41) is much faster than the integral operators, since the N^2 -order matrix-vector multiplication for each frequency is replaced by a Fourier transform of order $N \log N$. If only one reference velocity is used, the total computation becomes the order of $N_s N_z N \log N$. For large lateral velocity gradients, more than one reference velocity must be used; so

that the total computation becomes an algorithm of order $N_s N_z N_v N \log N$, where N_v is the average number of reference velocities within each depth step.



(a)



(b)

Figure 2.4 Marmousi CIG stacks (a) with slowness correction described in equation (2.39) and (b) with slowness correction described in equation (2.41). The structures and the flat spot are imaged slightly better in (b).

Both the integral nonstationary operators and the localized split-step Fourier algorithm were implemented on the Multimedia Advanced Computational Infrastructure (MACI) Alpha Cluster at the University of Calgary (Mi and Margrave, 2001c). MACI is a collaborative project of the Universities of Alberta, Calgary, Lethbridge and of Manitoba to provide high-performance computing resources to researchers and educators. The Alpha Cluster at the University of Calgary is part of the high-performance computing facility of the MACI project. The Cluster consists of approximately 117 Compaq Alpha workstations; the total number of CPUs was 173 at the time this thesis was written. A general network configuration of the Alpha Cluster is shown in **Figure 2.5**. Photographs of the three major machine types are shown in **Figure 2.6**.

The two types of parallel implementation used include the Message Passing Interface (MPI). MPI is a programming library that consists of communication functions mainly written in C language and callable by FORTRAN programs. Each computing node was assigned a single shot-gather migration task. The master C++ main program performs data I/O and parallel message distribution and collection operations. The shot-gather imaging kernel function was written in FORTRAN 90 to achieve high performance. Messages passing from the master node to the slave nodes included a shot gather and the corresponding velocity model, as well as migration parameters. Messages returned from the slave nodes contain only the migrated shot gather. **Figure 2.7** shows a general topology of the parallel program.

MACI Alpha Cluster Hardware and Networking

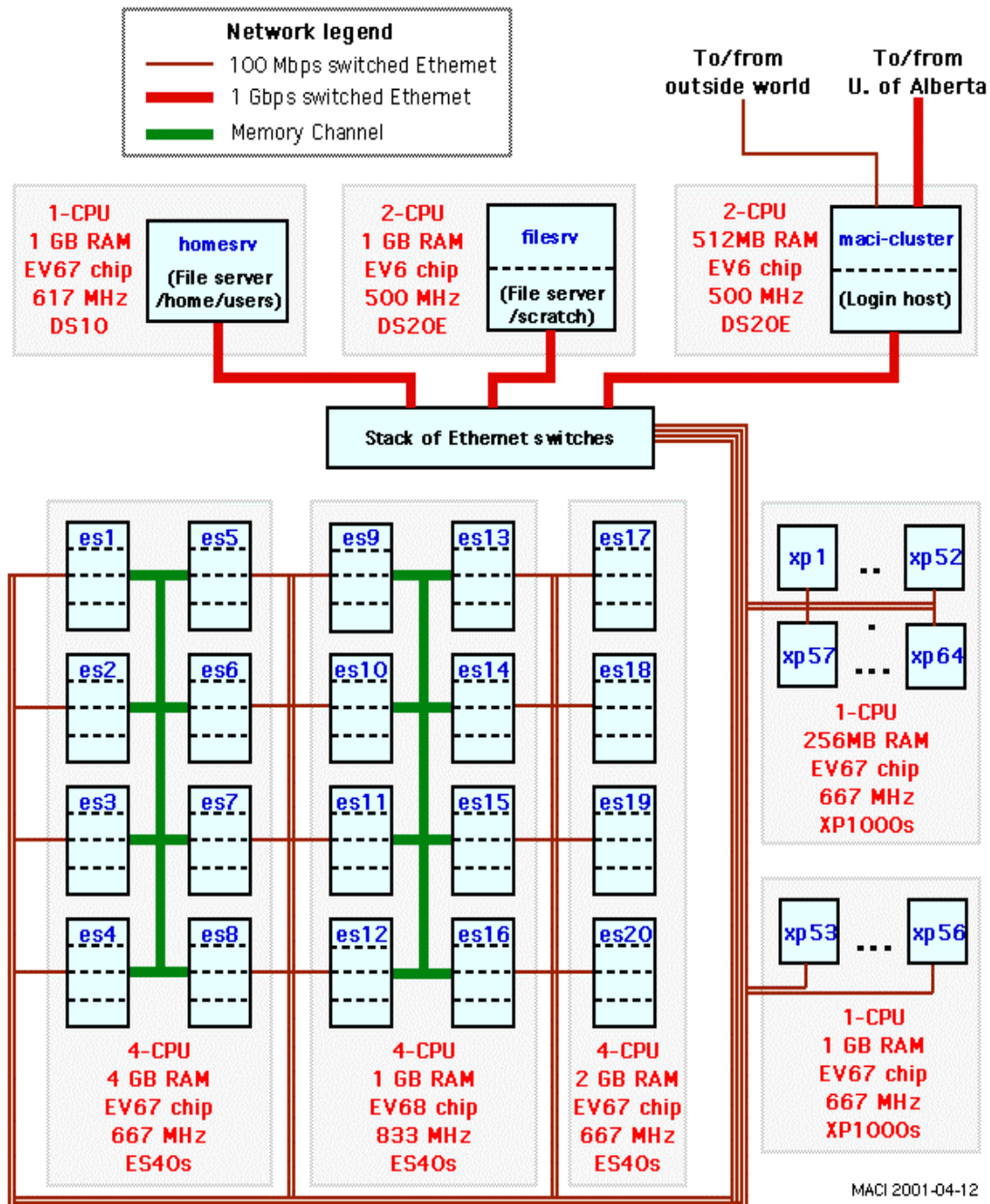


Figure 2.5. The general network configuration of the Alpha Cluster computer at the University of Calgary (Courtesy of MACI, University of Calgary).

The second is a pseudo-parallel implementation that assigns a multi-shot-gather migration task to each computing node. Each node performs its own data I/O and the actual computing. The output from each node is written onto separate disk files and assembled before post-migration processing. The first approach is user friendlier while the second approach is more flexible and especially useful for testing purposes. Most of the imaging done for this thesis used the latter approach since intensive algorithm testing was carried out.



(a)



(b)



(c)

Figure 2.6 Photographs of the three types of Alpha workstations (a) XP1000, (b) PWS 500 and (c) ES40 machines (Courtesy of MACI, University of Calgary).

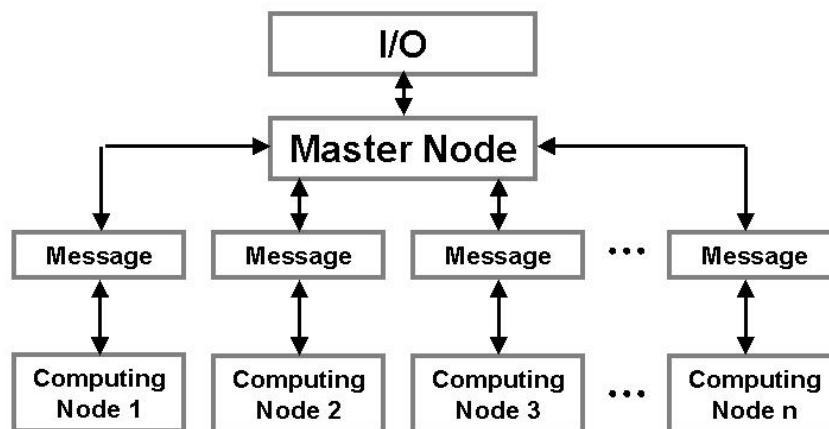


Figure 2.7 The general topology of the parallel program. Black lines denote data flow between the master node and the slave nodes.

2.9 COMPUTING ISSUES

As mentioned beforehand, the shot gathers in the Marmousi synthetic data were padded to 256 traces of split-spread acquisition geometry to accommodate migrated energy. Each trace has 512 samples, at a sample rate of 4 ms. Three hours were required to migrate a single shot gather on a 128 Mb memory XP1000 Alpha workstation with direct computation of equations (2.14) and (2.16). Such lack of speed is unacceptable for production purposes. Several processes exist with which to make algorithms perform considerably faster:

- 1) The square matrices in both equation (2.14) and (2.16) can be expressed by array-products of the extrapolation matrices and the inverse and forward Fourier transform kernel matrices. The exponential of large imaginary numbers, which results from large offsets in the transform kernel, would consume substantial

computing time if equations (2.14) and (2.16) were to be computed at each depth step. Precomputation of the inverse and forward Fourier transform matrices significantly reduces the run time.

- 2) The wavefield extrapolation matrix is symmetric about column $N/2+1$, if the horizontal wavenumber is arranged in such a way as to vary from 0 to $k_{x_{nyq}}$ and then from $-k_{x_{nyq}}$ to $-dk_x$ with the first element ($k_x=0$) excluded, where $k_{x_{nyq}}$ is the Nyquist wavenumber. Computing time of the wavefield extrapolation matrix can then be further reduced by 50% since the values of the corresponding negative wavenumbers are duplicates of the corresponding positive wavenumbers.
- 3) Computation of the scalar exponential function is a heavily involved process. The intrinsic exponential function in FORTRAN 90 is accurate, but slow. The Padé approximation to the scalar exponential function is much faster but slightly less accurate. The accuracy can be adjusted by selecting appropriate expansion parameters to fit the requirement of wavefield extrapolation. The Padé approximation to the scalar function e^z is defined by Golub and Van Loan (1989) as

$$e^z \approx R_{pq}(z) = D_{pq}(z)^{-1} N_{pq}(z), \quad (2.50)$$

where

$$N_{pq} = \sum_{k=0}^p \frac{(p+q-k)! p!}{(p+q)! k! (p-k)!} z^k, \quad (2.51)$$

and

$$D_{pq} = \sum_{k=0}^q \frac{(p+q-k)!q!}{(p+q)!k!(q-k)!} (-z)^k \quad (2.52)$$

Note that when q is zero, equation (2.50) reduces to the p th order Taylor-series expansion

$$R_{p0}(z) = 1 + z + \dots + z^p / p! \quad (2.53)$$

Compared with the Taylor-series expansion, the Padé-approximation converges more quickly and more accurately at the same order. The choice of $p = q = 2$ is capable producing sufficiently accurate and fast results when z is a small number close to zero. This can be written as

$$R_{p=2,q=2}(z) = D_{p=2,q=2}(z)^{-1} N_{p=2,q=2}(z), \quad (2.54)$$

where

$$D_{p=2,q=2}(z) = 1 - \frac{1}{2}z + \frac{1}{12}z^2, \quad (2.55)$$

and

$$N_{p=2,q=2}(z) = 1 + \frac{1}{2}z + \frac{1}{12}z^2. \quad (2.56)$$

The Padé approximation is only accurate near the origin and the computing procedure should be altered to $e^z = (e^{z/m})^m$, where m is a power of 2, for a high degree of efficiency. $e^{z/m}$ is the first step in the computation. Golub and Van

Loan (1989) showed that error can be minimized by choosing equal p and q values and an appropriate m value (Golub and Van Loan, 1989).

- 4) In cases where velocities repeat in a model layer, which is generally true even for a model as complicated as the Marmousi, the extrapolation portion of the array elements in equations (2.15) and (2.17) need not be recomputed for repeated velocities. Blocking the velocity field with a small velocity value, 10 m/s, for example, can significantly increase the number of repeated velocity values without causing noticeable error. It will be shown that a 75 m/s blocking factor has very little impact on the image quality; however, the computing time can be further reduced by 75%. **Figures 2.8a** and **b** show the number of velocities at each depth step when using 1) a 10 m/s velocity blocking factor and 2) a 75 m/s velocity blocking factor. Velocities would number 256 at each depth step without blocking. Note that numbers have been significantly reduced.

A more reasonable procedure would be to use a dynamic velocity-blocking factor determined as a percentage of the minimum velocity within each depth step. **Figures 2.8c** and **d** show the number of velocities requiring computing in each layer when the blocking factors are 1% and 2% of the minimum velocity. This approach produces roughly the same number of velocity values, but in a more reasonable manner.

Figure 2.9 shows the CIG at 6200 m of the migrated Marmousi data set, computed by (a) the localized split-step Fourier algorithm discussed in section 2.7, (b) integral SNPS extrapolator with a 75-m/s velocity-blocking factor and (c) integral SNPS extrapolator

with a 5-m/s velocity-blocking factor. The integral SNPS extrapolator dramatically improved the CIGs. Apparent improvements are:

- II. Shallow events have clearer expression across the gather. The events from 400 m to 1200 m were confined between the shot point (middle of the shot gather) and channel 159 in the localized split-step algorithm, while between channel 89 and channel 159 with the integral SNPS approach. These results are to be expected since waves propagating at large angles can be more accurately computed using the SNPS integral operator. Also, note that the vertical resolution of the shallow events has improved.
- III. There is less residual moveout. Note that about 50 m of residual moveout remains for the event at 1250 m in the localized split-step Fourier algorithm approach; this residual moveout eventually degrades image quality. These events are nicely aligned in the integral SNPS extrapolator approach, even when the blocking velocity is as large as 75 m/s.
- IV. There is greater continuity of the deeper events: for example, the events at 1700 m and 2500 m, have improved.

Figure 2.10 shows the reflectivity of the Marmousi P-wave velocity model. The reflectivity function was smoothed with a 0-20 Hz zero-phase bandpass wavelet so that it is comparable with a depth image. The challenges presented by the Marmousi data set to depth imaging technologies are 1) shallow events throughout the section, 2) high-angle faults in the middle of the model and 3) images of flat spots at depths of 2550 m from 6000 m to 7500 m. **Figures 2.11-2.13** show the images computed by the localized split-

step Fourier algorithm approach with a group of reference velocities 100 m/s apart, the images computed by the SNPS extrapolator with 75 m/s and 5 m/s velocity blocking factors, respectively. In comparing the band-limited reflectivity and the computed image, it is clearly evident that the foregoing imaging problems are easily resolved using the SNPS integral extrapolator. Shallow events are generally better imaged and the vertical resolution is improved. Fault planes are clearer, and the reservoir flat spot is especially well imaged. The localized split-step Fourier algorithm approach produced slightly inferior images; for example, the upper boundary of the wedge on the left at depth 2400 m.

2.10 CHAPTER SUMMARY

In this chapter, two forms of windowed split-step Fourier algorithms were introduced as an approximation to the PSPI and NSPS integral extrapolators. The approximation to PSPI integral extrapolator is similar to that proposed by Kessinger (1992). A better slowness-correction algorithm for perturbation was discussed and produced a better image than the standard split-step slowness correction. The integral SNPS extrapolator, though slow, significantly improved image quality. Several means to speed up computation were presented; these included utilizing symmetric properties of the matrices, precomputation of the Fourier transform kernel matrices, the Padé approximation to scalar exponential function and velocity-field blocking. Application of all the above techniques significantly reduces the run time. The imaging test also showed

that a fairly large velocity-blocking factor (75 m/s) could be used to produce reliable depth images. This is especially valuable for larger data sets, such as the Foothills synthetic data used in Chapter 4.

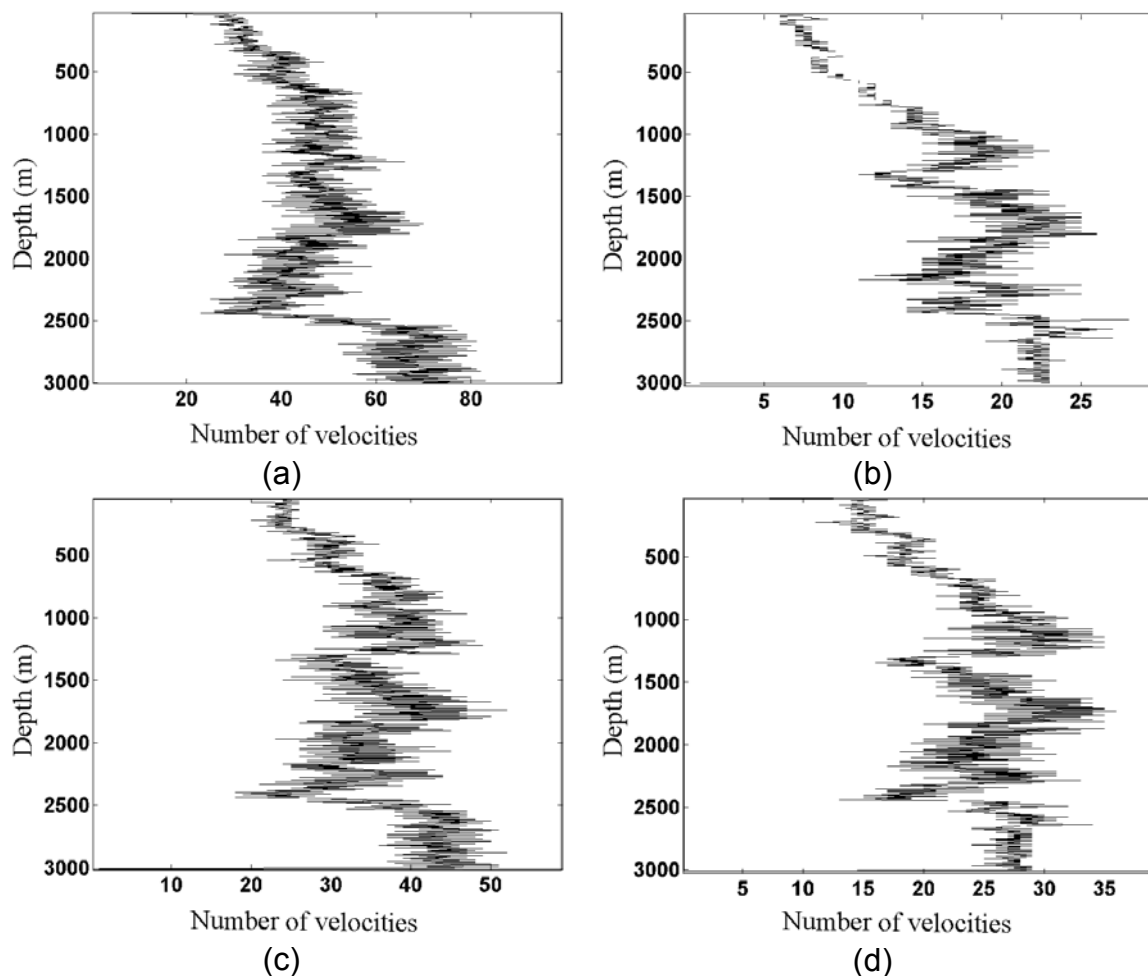
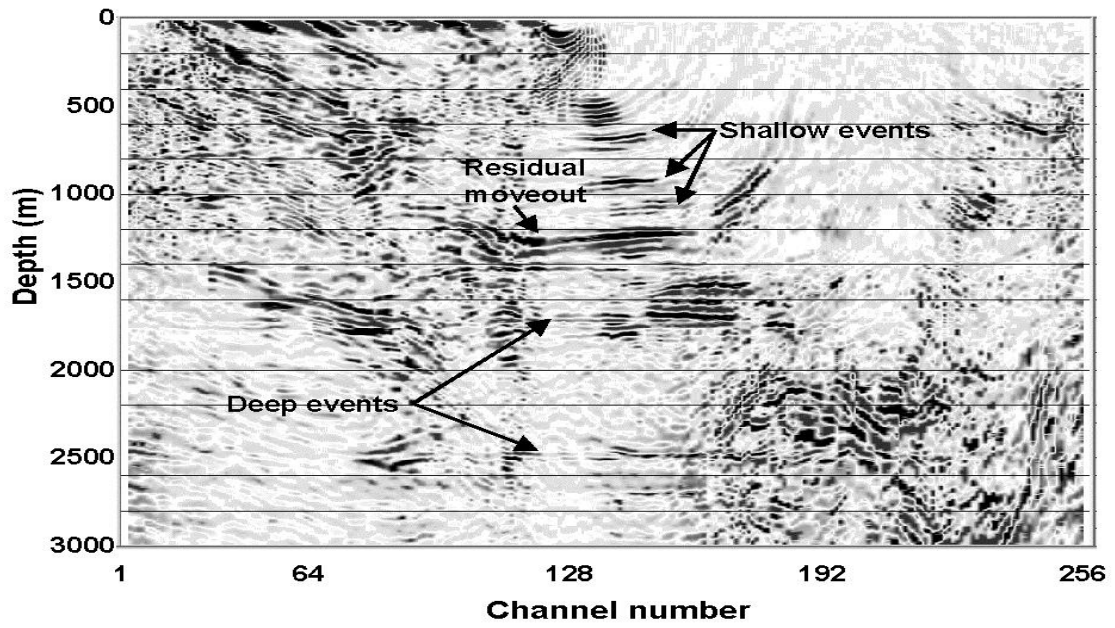
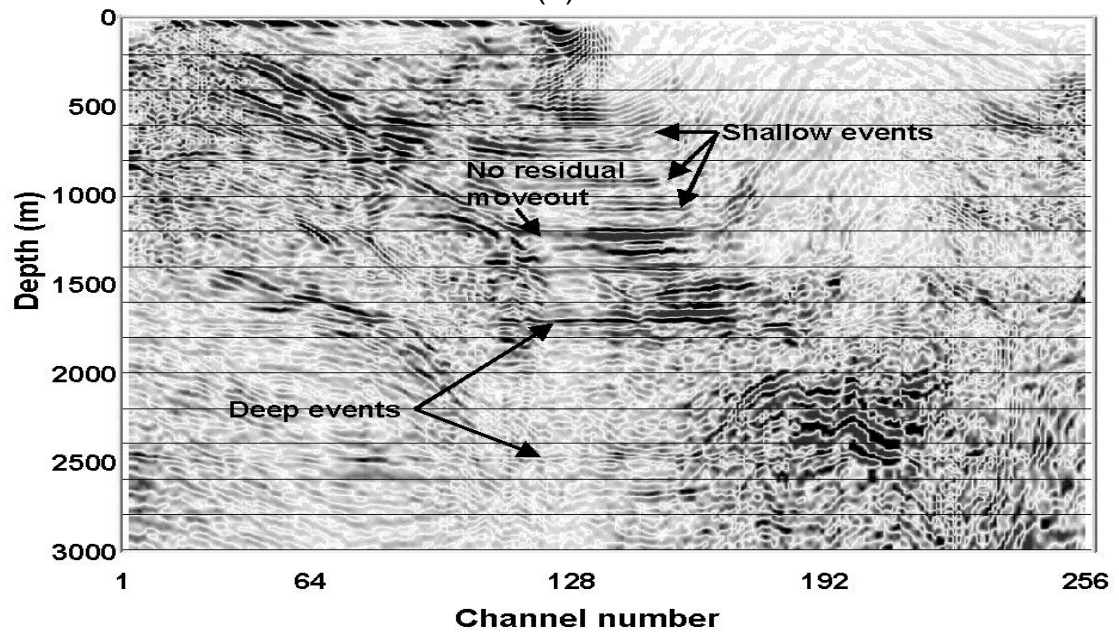


Figure 2.8 The number of velocity values need to be computed at each depth step when the blocking factor is (a) 10 m/s, (b) 20 m/s, (c) 1% of minimum velocity within layer and (d) 2% of minimum velocity within layer.

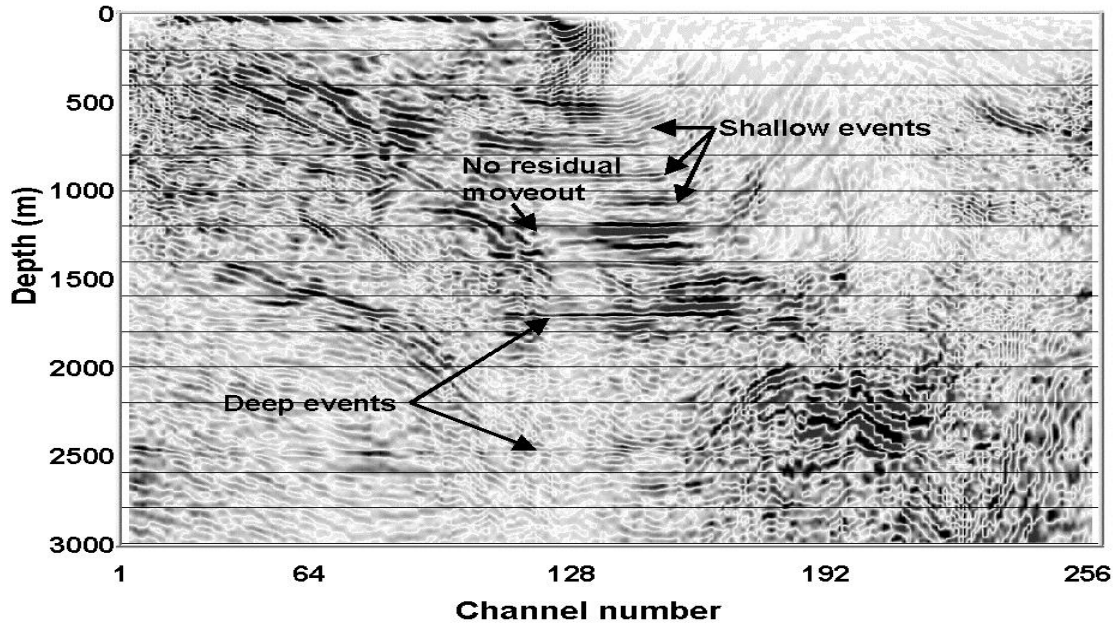


(a)



(b)

Figure 2.9 (Continues)



(c)

Figure 2.9 CIG at 6200 m (a) CIG computed by the localized split-step Fourier algorithm approach, (b) CIG computed by the SNPS integral extrapolator with a blocking factor of 75 m/s and (c) CIG computed by the SNPS integral extrapolator with a blocking factor of 5 m/s.

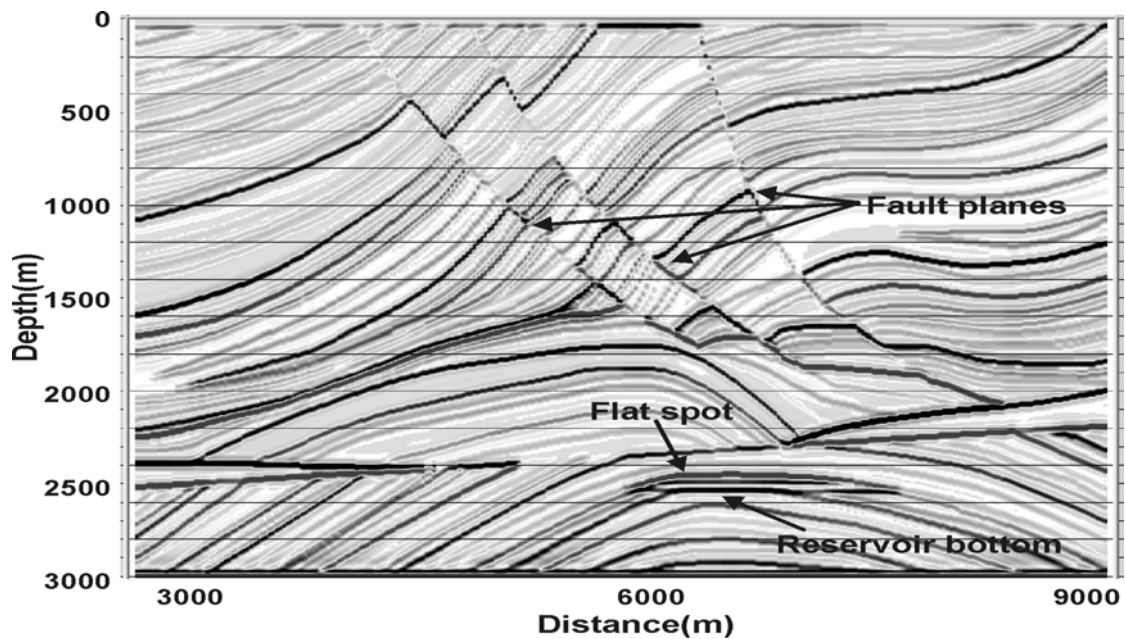


Figure 2.10 Reflectivity of the Marmousi model from 2500 m to 9100 m. The reflectivity is filtered to 0-20 Hz by treating depth as time to highlight the benchmark reflectors.

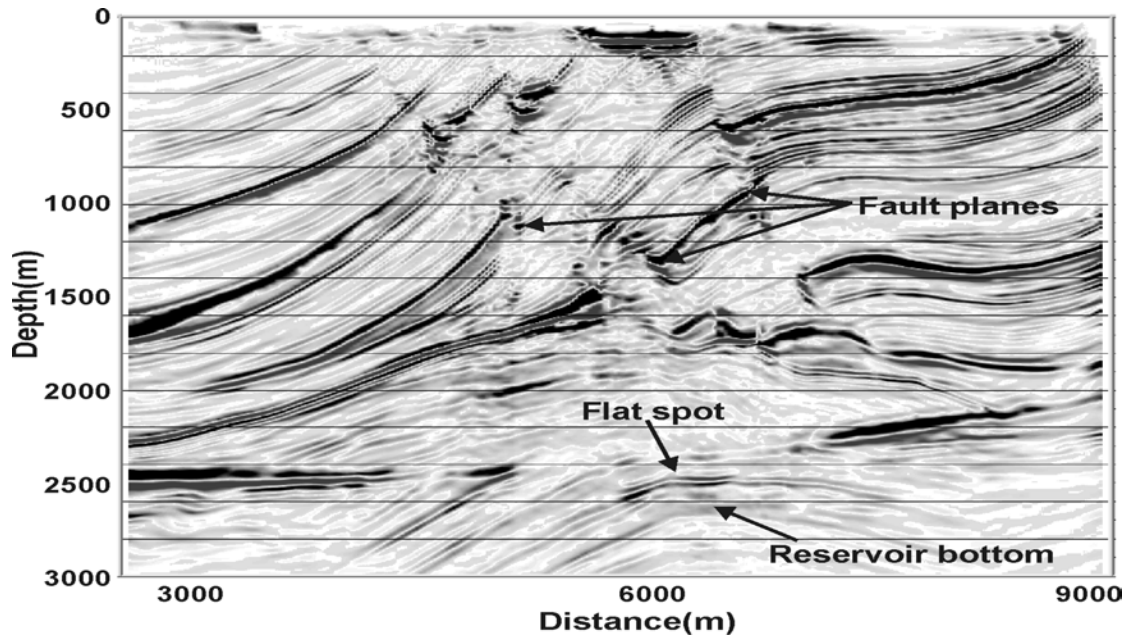


Figure 2.11 Marmousi image from 2500 m to 9100 m, computed by the localized split-step Fourier algorithm.

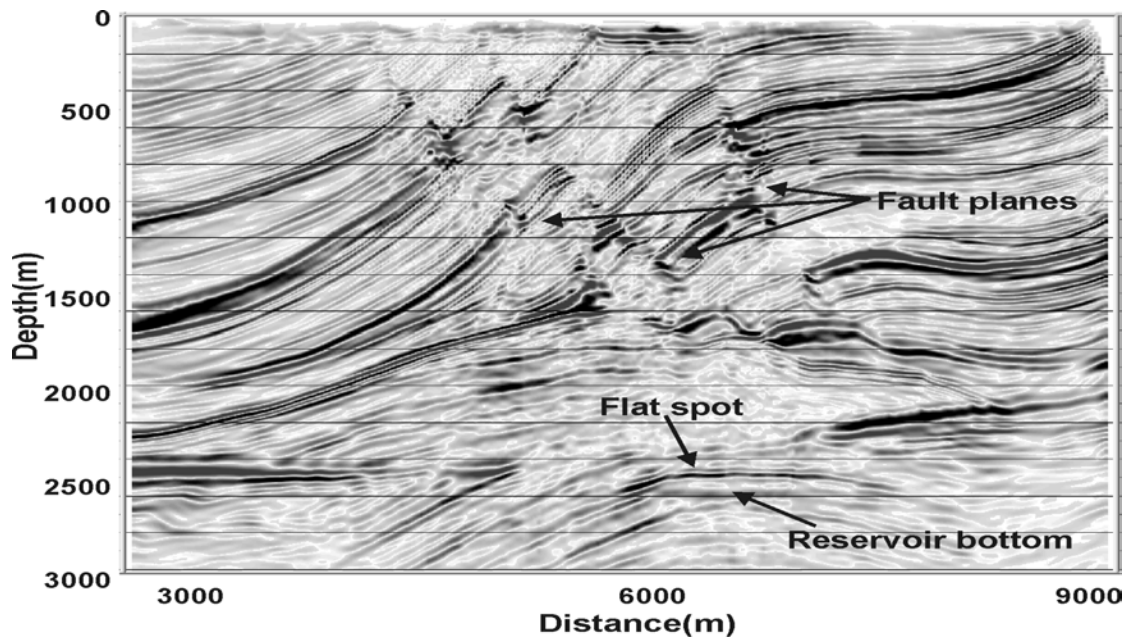


Figure 2.12 Marmousi image from 2500 m to 9100 m, computed by recursive SNPS integral extrapolator with a blocking velocity of 75 m/s.

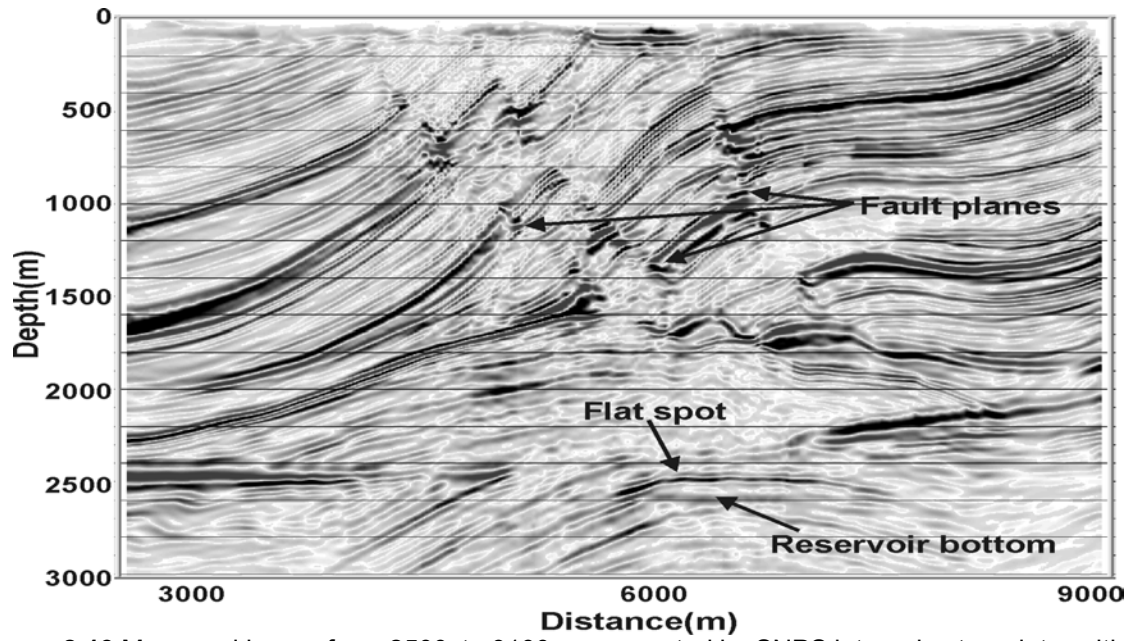


Figure 2.13 Marmousi image from 2500 to 9100 m, computed by SNPS integral extrapolator with a blocking velocity of 5 m/s.

CHAPTER 3

LARGE-STEP WAVEFIELD EXTRAPOLATION AND THE DUAL ALGORITHM

3.1 INTRODUCTION

Complex geology requires increasing the number of reference velocities for Gazdag's PSPI and the number of windows for the localized split-step Fourier algorithm. This significantly increases the amount of computing time required. As mentioned in Chapter 2, the full integral algorithms are of the order $N_s N_z N^3$ and the localized split-step Fourier approach is an $N_s N_z N_v N^2 \log N$ algorithm. N , N_s , N_z and N_v represent the number of traces in a shot gather, the number of shot gathers in a data set, the number of extrapolation steps and the average number of reference velocities in each velocity layer, respectively. When the number of reference velocities exceeds the limit $N_{v_{lim}} = N / \log N$, the full integral algorithm becomes faster. In practice, $N_{v_{lim}}$ is often less than $N / \log N$, due to other windowing-related computational costs in the localized split-step approximation.

In regions of complex geology, the lateral velocity gradient often exceeds the vertical velocity gradient, especially in regions adjacent to faults of large throw. More accurate

algorithms, such as integral extrapolators, are required at every imaging step for proper wavefield propagation. However, they are too costly to perform.

With small vertical and lateral velocity gradients, the extrapolation step can be large without resulting in noticeable errors. Ng (1994) demonstrated that a large time step could be used in PSPI time migration. In this Chapter, a dual algorithm is developed to demonstrate that a large extrapolation step can be used to speed up the nonstationary integral extrapolators for depth imaging. The resulting wavefields are accurate as long as proper replacement velocities are used. The intermediate wavefields for imaging can be produced by interpolation between the reference wavefields computed with large-step extrapolation.

3.2 STATIC AND FOCUSING PHASE-SHIFT IN COMPLEX MEDIA

In media of constant velocity, considering only downward extrapolation, the overall phase-shift that carries the wavefield from 0 to z can be split into the sum of a static phase-shift in the (ω, x) domain and a focusing phase-shift in the (ω, k_x) domain

$$\begin{aligned}
\Phi &= z \sqrt{\frac{\omega^2}{v^2} - k_x^2} = \Phi_{\text{static}} + \Phi_{\text{focus}} \\
\Phi_{\text{static}} &= \frac{\omega z}{v} \\
\Phi_{\text{focus}} &= \frac{\omega z}{v} \left(\sqrt{1 - \frac{k_x^2 v^2}{\omega^2}} - 1 \right),
\end{aligned} \tag{3.1}$$

where Φ_{static} is applied in (ω, x) domain, and the focusing term Φ_{focus} is applied in the (ω, k_x) domain.

Equation (3.1) is exact for homogeneous media. It is also approximately applicable for $v(z)$ media by replacement of the focusing velocity with a root-mean-square (RMS) velocity. Equation (3.1) can be generalized to media with lateral velocity variation. Both the static and the focusing phase-shift become a function of spatial location, that is,

$$\begin{aligned}
\Phi(x) &= z \sqrt{\frac{\omega^2}{v^2(x)} - k_x^2} = \Phi(x)_{\text{static}} + \Phi(x)_{\text{focus}} \\
\Phi(x)_{\text{static}} &= \frac{\omega z}{v(x)} \\
\Phi(x)_{\text{focus}} &= \frac{\omega z}{v(x)} \left(\sqrt{1 - \frac{k_x^2 v(x)^2}{\omega^2}} - 1 \right)
\end{aligned} \tag{3.2}$$

Similar to the case of constant velocity, the static phase-shift $\Phi(x)_{\text{static}}$ is applied in the (ω, x) domain, which corresponds to a spatially varying vertical traveltime. The focusing phase-shift $\Phi(x)_{\text{focus}}$ is applied in the (ω, k_x) domain, which handles the propagating energy at all possible angles.

In the case of forward extrapolation, substitution of equation (3.1) into equation (2.2) gives a split nonstationary operator

$$\alpha(x, k_x, z, \omega) = e^{-i(\Phi(x)_{\text{static}} + \Phi(x)_{\text{focus}})}. \quad (3.3)$$

The PSPI and NSPS integral extrapolators can then be written as

$$\psi_{\text{PSPI}}(x, z, \omega) = e^{-i\Phi(x)_{\text{static}}} \left[\frac{1}{(2\pi)^2} \int_{-\infty}^{+\infty} \alpha'(x, k_x, z, \omega) \varphi(k_x, 0, \omega) e^{-ik_x x} dk_x \right] \quad (3.4)$$

and

$$\varphi_{\text{NSPS}}(k_x, z, \omega) = \int_{-\infty}^{+\infty} \alpha'(x, k_x, z, \omega) [\psi(x, 0, \omega) e^{-i\Phi(x)_{\text{static}}}] e^{ik_x x} dx, \quad (3.5)$$

respectively. $\alpha'(x, k_x, z, \omega)$ is the nonstationary focusing operator

$$\alpha'(x, k_x, z, \omega) = e^{-i \frac{\omega z}{v(x)} \left(\sqrt{1 - \frac{k_x^2 v(x)^2}{\omega^2}} - 1 \right)}. \quad (3.6)$$

Equations (3.4) and (3.5) can be written, approximately, in the form of matrix-vector multiplication with the (ω, x) -domain static phase-shift applied before (for NSPS) and after (for PSPI) application of the nonstationary focusing term.

3.3 LARGE-STEP FORMULAE FOR PSPI AND NSPS

For $v(z)$ media, both the static and focusing phase-shifts are independent of spatial location and can be accumulated over depth. The accumulated static phase-shift is written as

$$\Phi_{\text{static}} = \int_0^z \frac{\omega}{v(z')} dz' = \frac{\omega z}{v_{\text{ave}}(z)}. \quad (3.7)$$

The accumulated focusing term can be written as

$$\Phi_{\text{focus}} = \int_0^z \frac{\omega}{v(z')} \left(\sqrt{1 - \frac{k_x^2 v(z')^2}{\omega^2}} - 1 \right) dz'. \quad (3.8)$$

Note that equations (3.7) and (3.8) together give a **WKBJ** solution for $v(z)$ media. For media with lateral velocity variation, equation (3.7) remains valid, while equation (3.8) does not, since PSPI and NSPS integrals do not perform exact inverse- or forward- spatial Fourier transforms. PSPI and NSPS thus become local integral operators that do not directly accumulate over depth. However, for weak lateral-velocity variation, the focusing phase-shift accumulates approximately, and equation (3.8) can be generalized to

$$\Phi_{\text{focus}} = \int_0^z \frac{\omega}{v(x, z')} \left(\sqrt{1 - \frac{k_x^2 v(x, z')^2}{\omega^2}} - 1 \right) dz'. \quad (3.9)$$

The static phase-shift remains an exact accumulation

$$\Phi_{\text{static}} = \int_0^z \frac{\omega}{v(x, z')} dz' = \frac{\omega z}{v_{\text{ave}}(x, z)}. \quad (3.10)$$

Binomial expansion of the square-root term in equation (3.9) leads to

$$\Phi_{\text{focus}} = -\frac{k_x^2 z}{2\omega} \frac{1}{z} \int_0^z v(x, z') dz' - \frac{k_x^4 z}{8\omega^3} \frac{1}{z} \int_0^z v(x, z')^3 dz' + \frac{k_x^6 z}{16\omega^5} \frac{1}{z} \int_0^z v(x, z')^5 dz' - \dots \quad (3.11)$$

Note that the depth-average velocity (mean velocity) is defined as

$$v_{\text{mean}} = \frac{1}{z} \int_0^z v(z') dz' \quad (3.12)$$

Bringing equation (3.12) in to (3.11) suggests that equation (3.11) can be approximated by

$$\Phi'_{\text{focus}} = \frac{\omega z}{v_{\text{mean}}(x, z)} \left(\sqrt{1 - \frac{k_x^2 v_{\text{mean}}(x, z)^2}{\omega^2}} - 1 \right). \quad (3.13)$$

Binomial expansion of equation (3.13) then subtraction of equation (3.11) lead to the error term of the focusing phase-shift

$$\Phi_{\text{error}} = \frac{k_x^4 z}{8\omega^3} \left(\frac{1}{z} \int_0^z v(x, z')^3 dz' - v_{\text{mean}}(x, z)^3 \right) + \frac{k_x^6 z}{16\omega^5} \left(\frac{1}{z} \int_0^z v(x, z')^5 dz' - v_{\text{mean}}(x, z)^5 \right) + \dots \quad (3.14)$$

This error can generally be ignored when 1) the propagation angle is small or 2) the depth step z is small or 3) the lateral-velocity gradient is small.

Defined the average velocity as $v_{\text{ave}}(z) = z / \int_0^z \frac{1}{v(z')} dz'$. For large-step extrapolation,

equations (3.4) and (3.5) become

$$\psi(x, z, \omega) = e^{-i \frac{\omega z}{v_{\text{ave}}(x)}} \left[\frac{1}{(2\pi)^2} \int_{-\infty}^{+\infty} \alpha'_{\text{mean}}(x, k_x, z, \omega) \phi(k_x, 0, \omega) e^{-ik_x x} dk_x \right] \quad (3.15)$$

and

$$\phi(k_x, z, \omega) = \int_{-\infty}^{+\infty} \alpha'_{\text{mean}}(x, k_x, z, \omega) \left[\psi(x, 0, \omega) e^{-i \frac{\omega z}{v_{\text{ave}}(x)}} \right] e^{ik_x x} dx, \quad (3.16)$$

where $\alpha'_{\text{mean}}(x, k_x, z, \omega)$ is now the mean nonstationary focusing operator

$$\alpha'_{\text{mean}}(x, k_x, z, \omega) = e^{-i \frac{\omega z}{v_{\text{mean}}(x)} \left(\sqrt{1 - \frac{k_x^2 v_{\text{mean}}(x)^2}{\omega^2}} - 1 \right)}. \quad (3.17)$$

Similar to the recursive SNPS algorithm (Ferguson and Margrave, 1999b), equations (3.15) and (3.16) can also be naturally combined to provide a symmetric wavefield extrapolator. For example, a one-step symmetric large-step extrapolation from depth 0 to z can be formulated as

$$\psi(x, z, \omega) = e^{-i \frac{\omega z}{2v_{\text{ave}}(z/2 \rightarrow z)(x)}} \left[\frac{1}{(2\pi)^2} \int_{-\infty}^{+\infty} \alpha'_{\text{mean}(z/2 \rightarrow z)}(x, k_x, z, \omega) \phi(k_x, z/2, \omega) e^{-ik_x x} dk_x \right], \quad (3.18)$$

where

$$\varphi(k_x, z/2, \omega) = \int_{-\infty}^{+\infty} \alpha'_{\text{mean}(0 \rightarrow z/2)}(x, k_x, z/2, \omega) \left[\psi(x, 0, \omega) e^{-i \frac{\omega z}{2v_{\text{ave}}(0 \rightarrow z/2)(x)}} \right] e^{ik_x x} dx. \quad (3.19)$$

The symbols $(0 \rightarrow z/2)$ and $(z/2 \rightarrow z)$ denote depth intervals from 0 to $z/2$ and $z/2$ to z .

Equations (3.18) and (3.19) require the same amount of computational effort as the recursive PSPI and NSPS integrals described before. They allow, however, a much larger extrapolation step. The maximum allowable depth-step under certain phase-error conditions is dependent upon the complexity of the velocity field and the maximum angle to be imaged.

A simple test of accuracy involves inverting the accurately modeled data with the large-step algorithm and examining the quality of the focal points. **Figure 3.1** shows the Marmousi model of a 4-m (vertical) by 25-m (lateral) grid. The testing velocity zones are highlighted: zone 1 (0-160 m) and zone 2 (1200-1360 m). **Figure 3.2** shows the overall average and mean velocities of these two velocity zones. Note that the maximum-percentage average-velocity variation is about 20% for velocity zone 1, and about 50% for velocity zone 2.

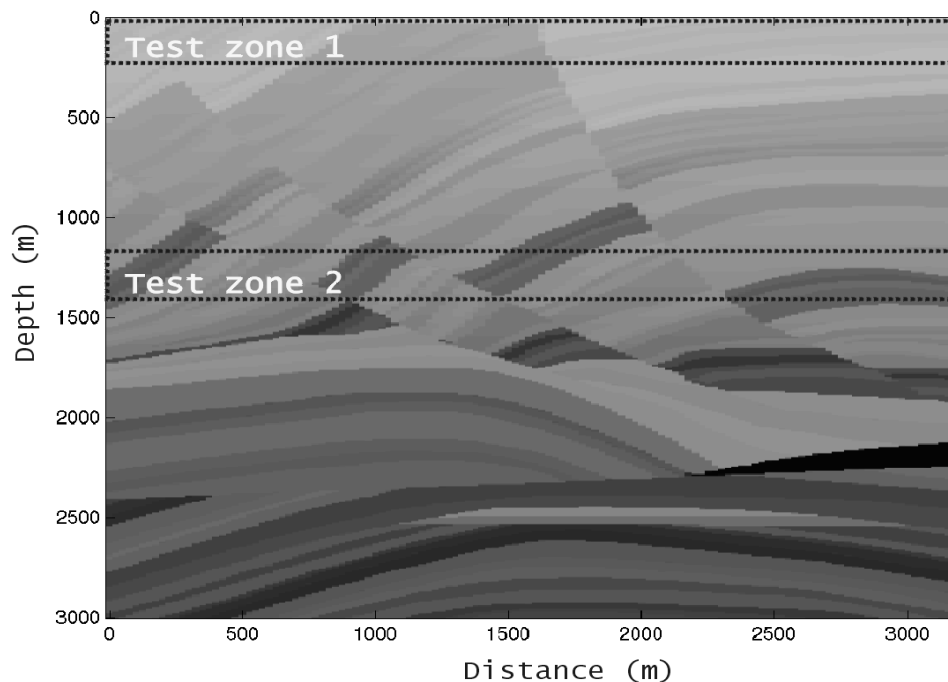


Figure 3.1 Two velocity zones with different lateral velocity variations are chosen to test the large-step PSPI integral wavefield extrapolator.

Zero-offset forward modeling was performed with recursive application of the PSPI integral to produce accurate synthetic data. For each velocity zone, 11 impulses were recursively forward extrapolated through 20, 30 and 40 steps at 4 m each. The quality of the inverse extrapolation with the large-step PSPI integral [equation (3.18)] of the three synthetic data sets indicates how robust the algorithm is when different lateral velocity variations are present.

Figure 3.3 shows the extrapolation test in velocity zone 1. 11 impulses are forward extrapolated through the velocity model with 4-m step size recursive PSPI integral, to the depth of 80 m (20 layers) (**Figure 3.3a**), 120 m (30 layers) (**Figure 3.3b**) and 160 m (40 layers) (**Figure 3.3c**). Inverse extrapolation with a 40-m step size PSPI large-step extrapolator show that the impulses are very well focused in all the three cases. This suggests that even larger extrapolation steps can be used.

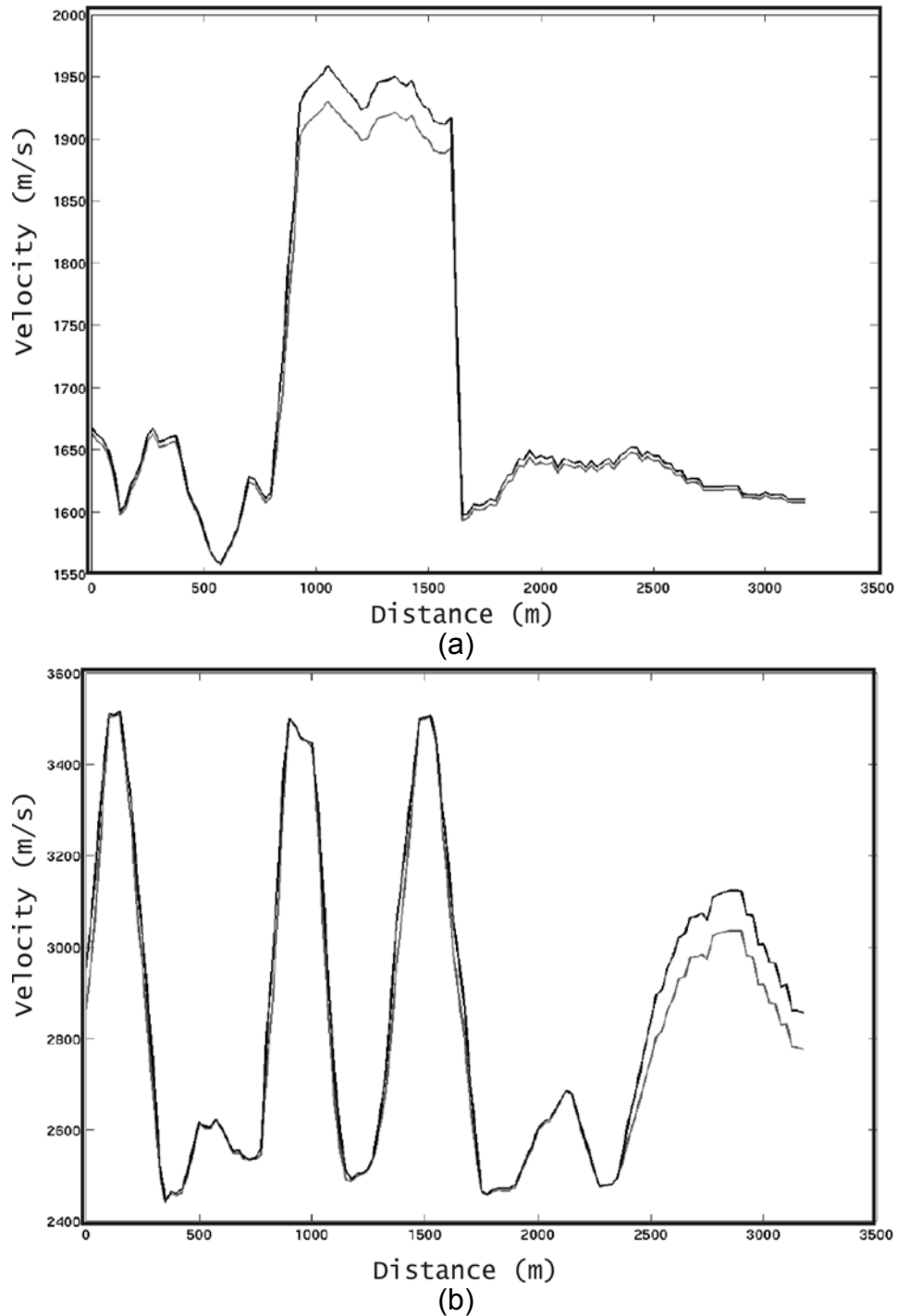


Figure 3.2 The mean-velocity and average-velocity in a 160-m depth interval within velocity zones 1 (a) and 2 (b). Solid black lines denote average velocities and gray lines denote mean velocities.

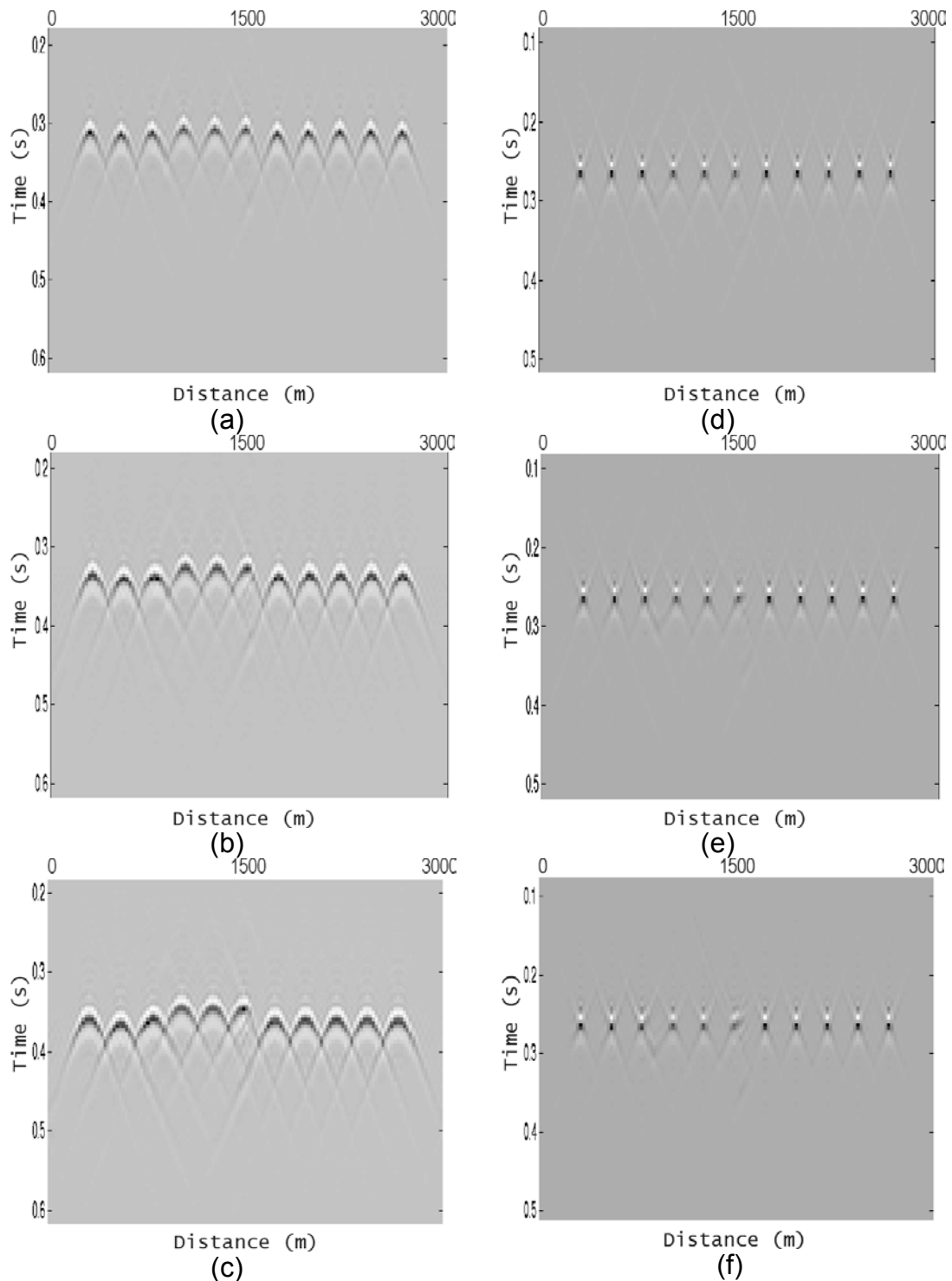


Figure 3.3 Extrapolation test in velocity zone 1. (a), (b) and (c) are results of forward modeling by recursive PSPI integral through 20, 30 and 40 layers. The step size is 4 m. (d), (e) and (f) are inverse extrapolation of (a), (b) and (c) using a 40-m PSPI large-step extrapolation.

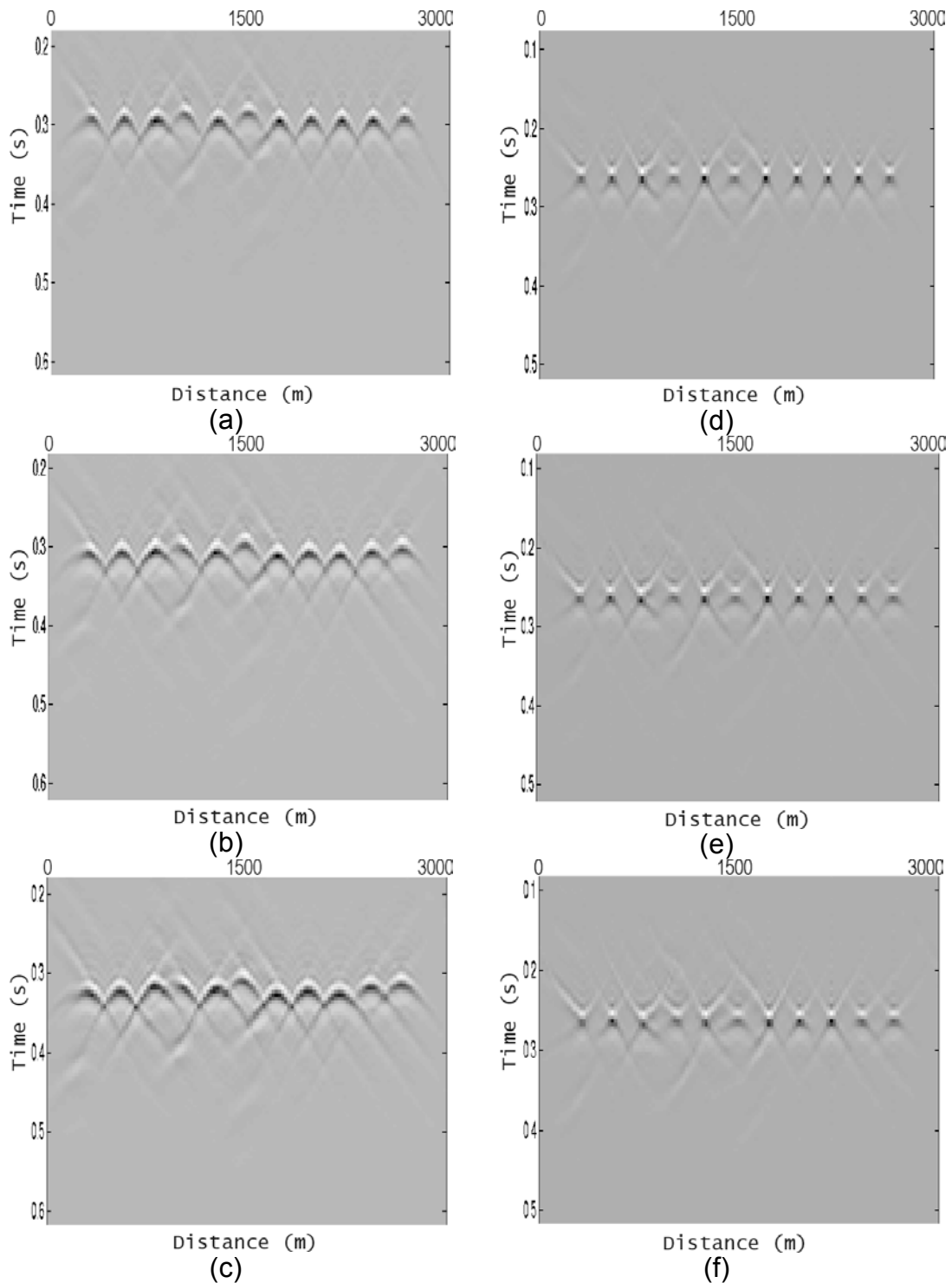


Figure 3.4 Extrapolation test in velocity zone 2. (a), (b) and (c) are forward modeling by recursive PSPI integral through 20, 30 and 40 layers. The step size is 4 m. (d), (e) and (f) are inverse extrapolation of (a), (b) and (c) using a 40-m step PSPI large-step extrapolation.

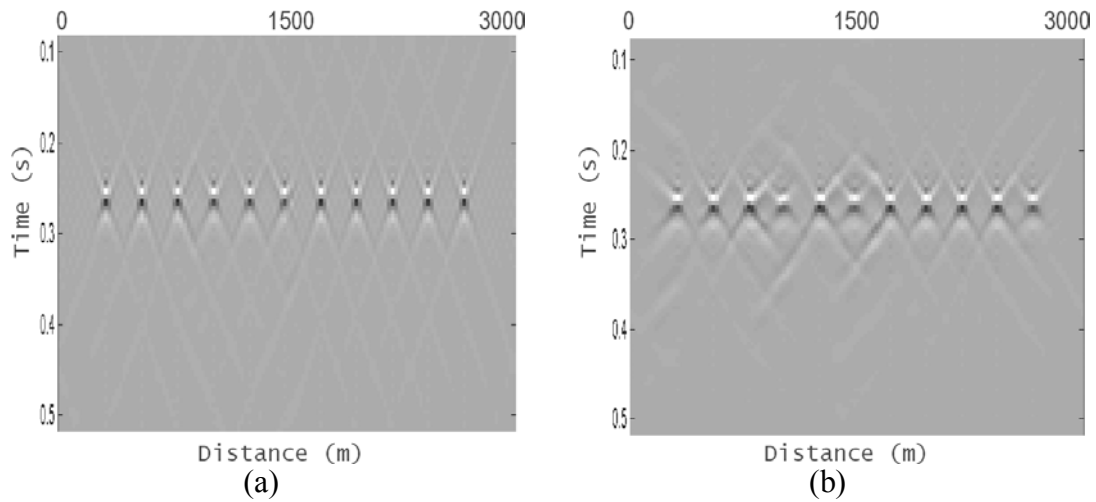


Figure 3.5 Inverse extrapolation of **Figure 3.3c** and **Figure 3.4c** with 4-m-step recursive PSPI integral.

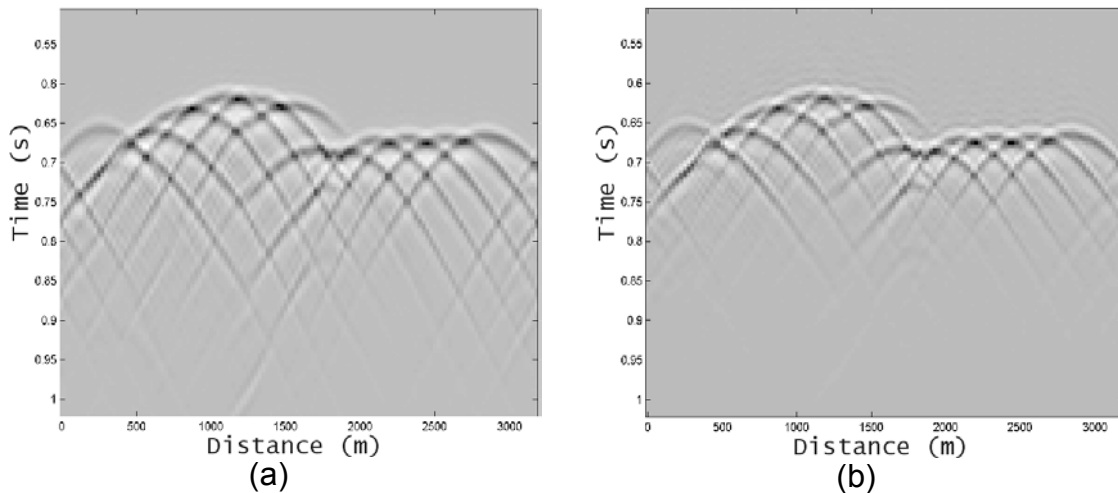


Figure 3.6 Zero-offset wavefields at 760 m of Marmousi model. (a) extrapolation with a 40-m large-step PSPI integral extrapolator and (b) extrapolation by recursive PSPI integral of 4-m step size.

Figure 3.4 shows the extrapolation test in velocity zone 2 and similar conclusions can be drawn. **Figure 3.5** shows the results of inverse extrapolation of **Figure 3.3c** and **Figure 3.4c** with recursive PSPI integral extrapolator. Note that the inverse extrapolation with large-step PSPI integral extrapolator in both the shallow and deep parts of the model produces very similar results to that of the 4-m PSPI integral extrapolator.

Figure 3.6 shows the comparison of zero-offset extrapolation of 11 impulses to 760-m depth of the Marmousi model with a 40-m step size large-step PSPI integral extrapolator. The wavefields are very similar to each other; however, computation for **Figure 3.6a** is 10 times faster than that for **Figure 3.6b**.

3.4 THE DUAL ALGORITHM

For recursive Fourier-domain imaging algorithms, the error caused by approximation to the theory accumulates at every depth step. The integral wavefield extrapolators are accurate, but computationally quite costly. One means of increasing computation speed is to compute relatively accurate reference wavefields over a depth grid coarser than the imaging depth grid and computing intermediate wavefields from these reference wavefields. A linear interpolation between these reference wavefields, with proper vertical traveltimes correction applied, can produce an intermediate wavefield with correct vertical traveltimes, though slightly misfocused when the distance and the velocity variation between the reference wavefields are small. **Figure 3.7** depicts a schematic of the dual algorithm.

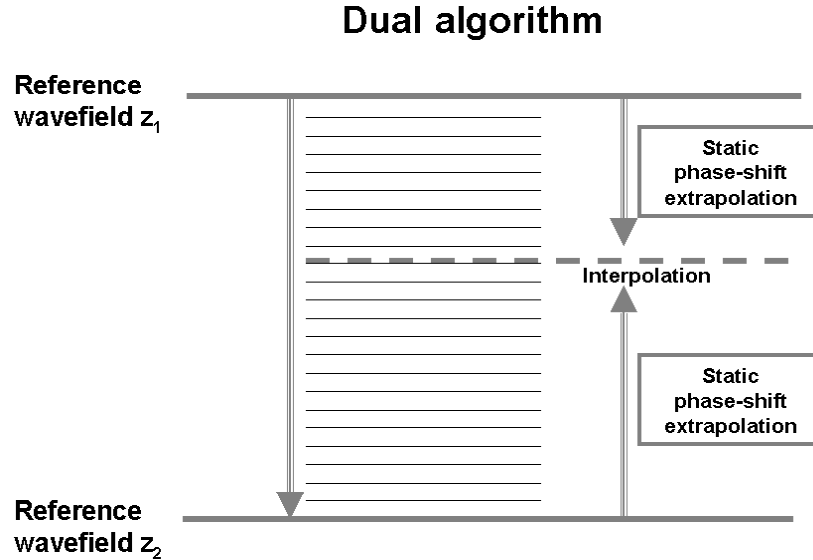


Figure 3.7 The dual algorithm uses accurate nonstationary integral extrapolators to produce relatively accurate reference wavefields over a depth grid coarser than the imaging depth grid. Intermediate wavefields can then be computed by quick interpolation.

Consider two (ω, x) -domain mono-frequency reference wavefields at z_1 and z_2 , $\psi(x, z_1, \omega)$, $\psi(x, z_2, \omega)$, computed by the large-step PSPI integral extrapolator. An intermediate wavefield between z_1 and z_2 , $\psi(x, z, \omega)$, can be computed by either forward extrapolation from the wavefield at z_1 or by inverse extrapolation from the wavefield at z_2 . Computation of the focusing term is, however, time-consuming; it requires the same computing effort as that of a normal PSPI or NSPS integral extrapolator. Since the velocity variation and distance between the upper and lower reference wavefields are small, the upper reference wavefield becomes an underfocused version of the intermediate wavefield and the lower reference wavefield becomes an overfocused version, after the vertical traveltimes correction. The error in focusing terms can be roughly cancelled if appropriate weighting factors are applied.

Vertical traveltimes correction of the upper and lower reference wavefields produces two approximations to the intermediate wavefield $\psi(x, z, \omega)$. They can be written as

$$\psi'_1(x, z, \omega) = \psi(x, z_1, \omega) e^{-\frac{i(z-z_1)\omega}{v_{\text{ave1}}(x)}} \quad (3.20)$$

and

$$\psi'_2(x, z, \omega) = \psi(x, z_2, \omega) e^{\frac{i(z-z_2)\omega}{v_{\text{ave2}}(x)}}, \quad (3.21)$$

where v_{ave1} and v_{ave2} are average velocities from z_1 to z and z to z_2 .

Equation (3.20) and (3.21) are merely vertical time corrections. Another approach, though slightly slower, is to use a single-reference-velocity split-step Fourier algorithm to approximately correct for the focusing error.

The intermediate wavefield can be computed by linear interpolation between $\psi'_1(x, z, \omega)$ and $\psi'_2(x, z, \omega)$. If the difference between v_{ave1} and v_{ave2} is small, this roughly cancels the focusing error, so that

$$\psi(x, z, \omega) \approx \frac{z_2 - z}{z_2 - z_1} \psi'_1(x, z, \omega) + \frac{z - z_1}{z_2 - z_1} \psi'_2(x, z, \omega). \quad (3.22)$$

The weight of the reference wavefields in the intermediate wavefield decreases linearly as the distance increases. For a larger difference between v_{ave1} and v_{ave2} , correction for the focusing term is required. This can be achieved with a single-reference-velocity split-step Fourier algorithm.

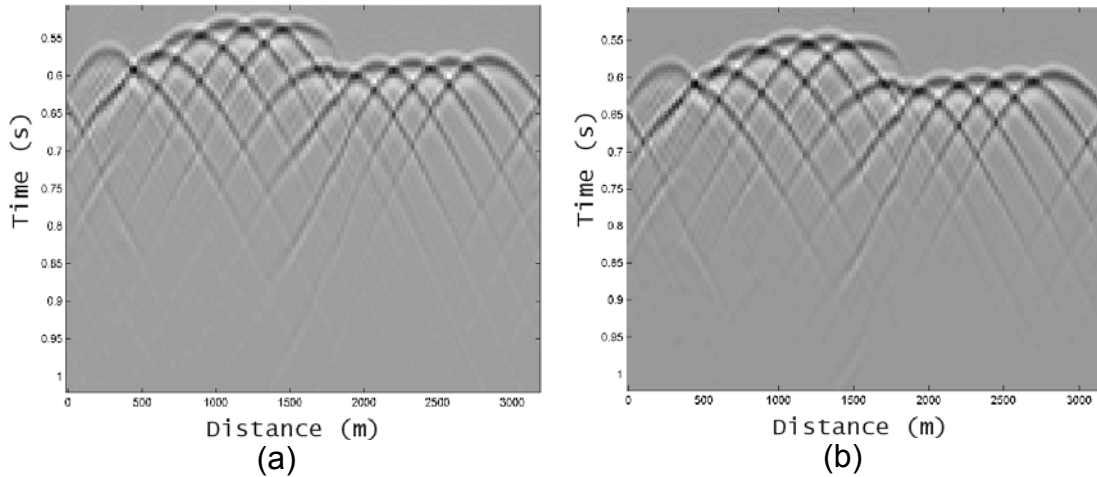


Figure 3.8 Zero-offset wavefield extrapolation of 11 impulses to depths of both (a) 560 m and (b) 600 m of the Marmousi model.

Figure 3.8 and **Figure 3.9** show the zero-offset forward-extrapolation of 11 impulses, starting at 0.25 s through the shallow part of the Marmousi model, using the dual algorithm. Two reference wavefields, at 560 m and 600 m, were computed utilizing the large-step PSPI integral extrapolator with a 40-m step size (**Figure 3.8**). The intermediate wavefields at 564 m, 572 m, 580 m, 588 m and 596 m were computed using equation (3.22).

The quality of the intermediate wavefield degrades slightly as the wavefield approaches the middle of the interval. The inverse of these intermediate wavefields using the accurate 4-m step size integral algorithm indicates the accuracy of these intermediate wavefields. The inverse of **Figure 3.9**, from **a** through **e** inclusive, with a 4-m recursive PSPI integral extrapolator is shown in **Figure 3.10**. The slight differences between the focal images indicate that these wavefields are accurate.

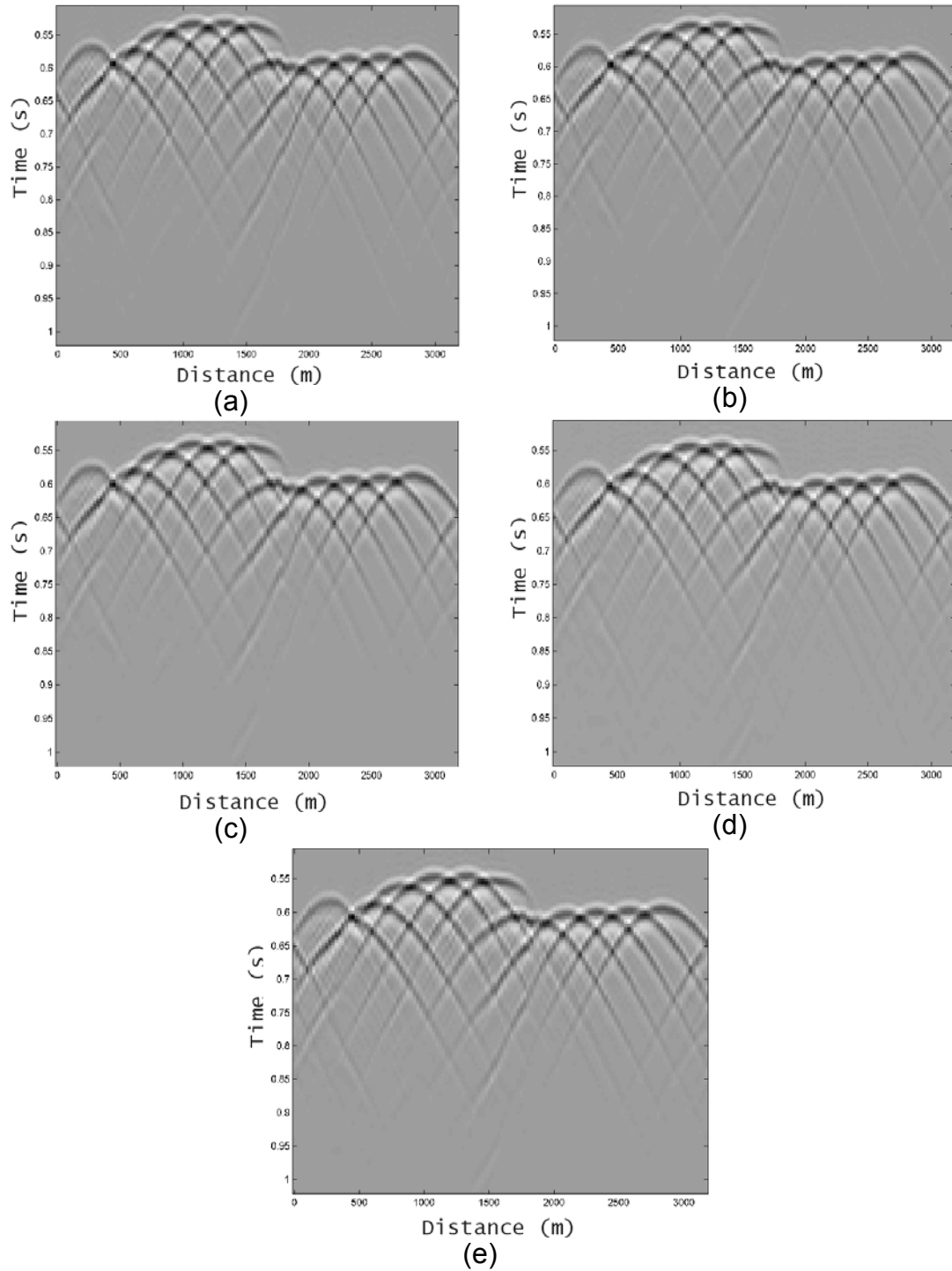


Figure 3.9 Intermediate wavefields at (a) 564 m, (b) 572 m, (c) 580 m, (d) 588 m and (e) 596 m were computed by linear interpolation between the reference wavefields at 560 m and 600 m.

3.5 DEPTH IMAGING OF MARMOUSI WITH THE DUAL ALGORITHM

Figure 3.11 shows the imaging test with a 40-m step size PSPI dual algorithm. Phase corrections with both the vertical traveltimes correction and the single-reference-velocity split-step Fourier algorithm are tested. Note that the split-step corrections produce a better image [**Figure 3.11(b)**]. **Figure 3.12** shows a Marmousi depth-image computed with a 16-m PSPI dual algorithm with vertical traveltimes correction before interpolation. As a result of the focusing phase error introduced by the large-step extrapolation and linear interpolation, the events on the middle left of the image of **Figure 3.11 a**, marked as ‘poor image,’ are discontinuous. The quality of the image produced with the 16-m dual algorithm is, however, quite comparable with that generated by the recursive SNPS algorithm (**Figure 2.12**). The computational cost of achieving **Figure 3.12** is about 1/4 that of **Figure 2.12**. Only three minutes were required to migrate a shot gather using a single-CPU Alpha XP1000 workstation.

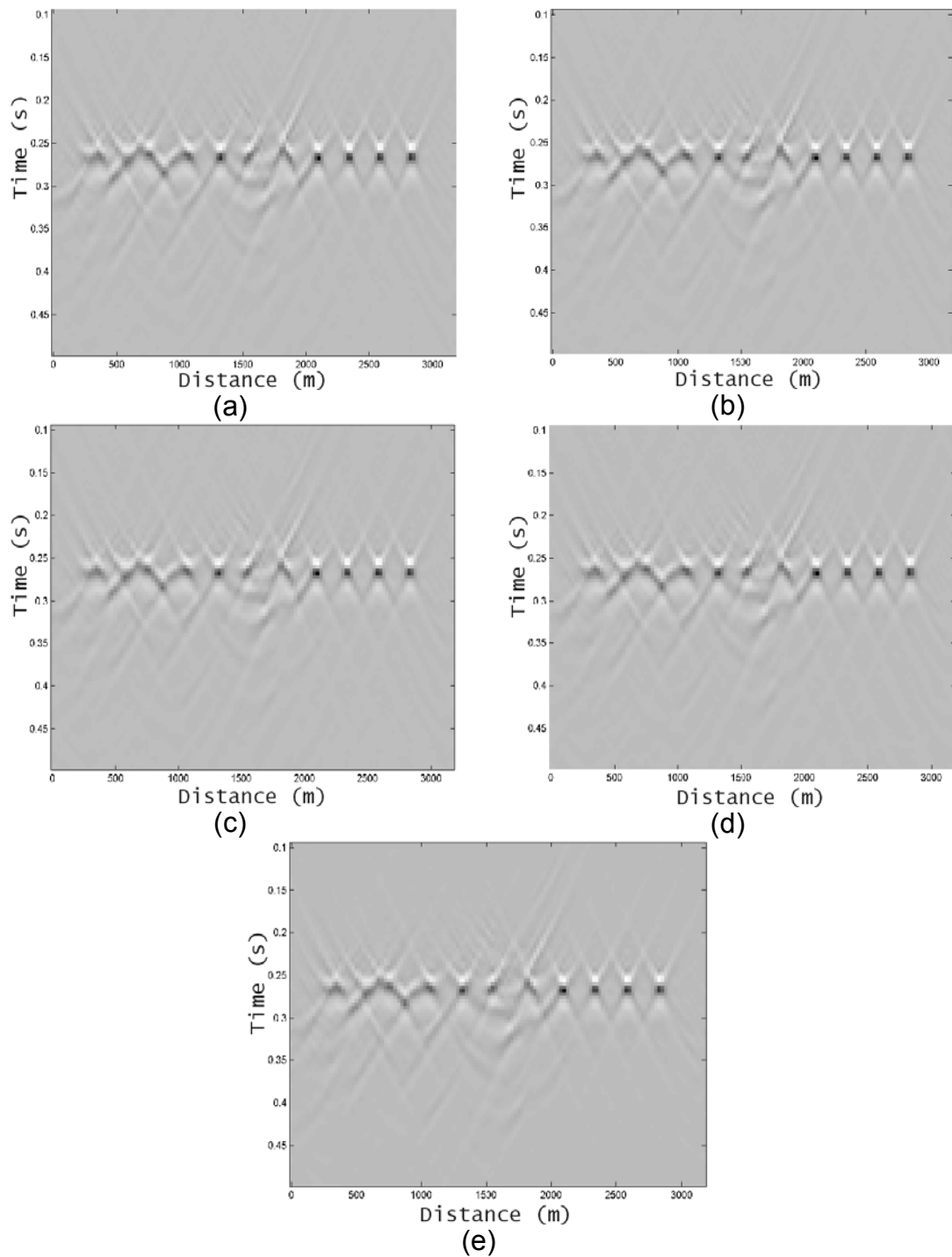
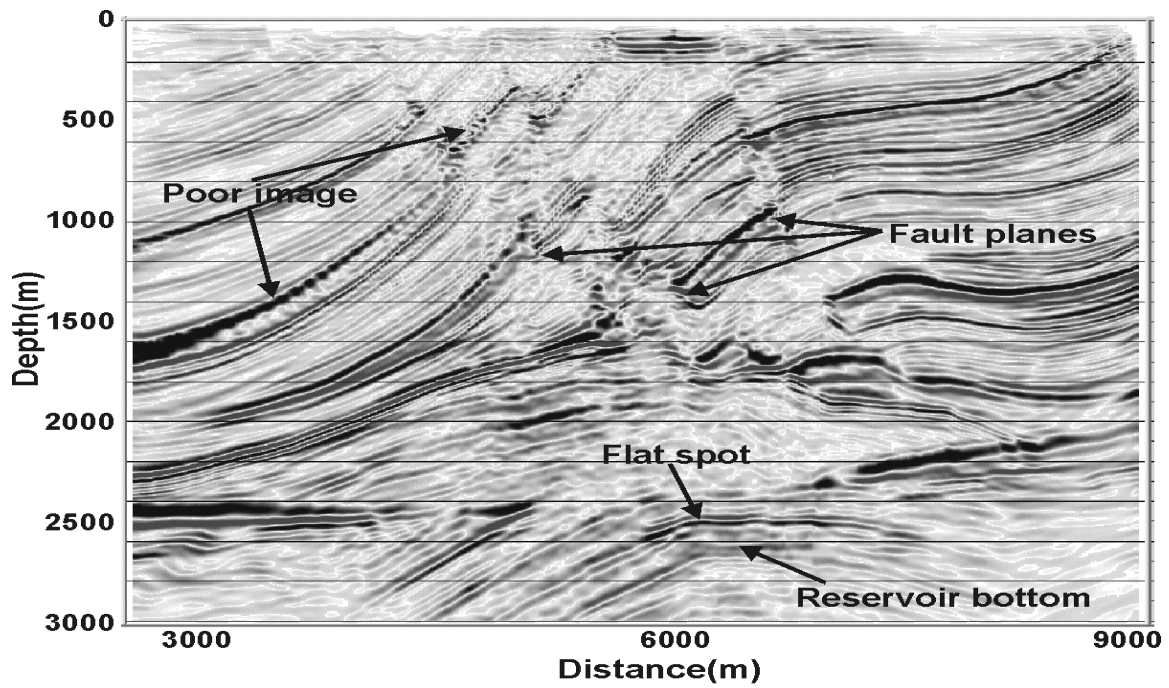
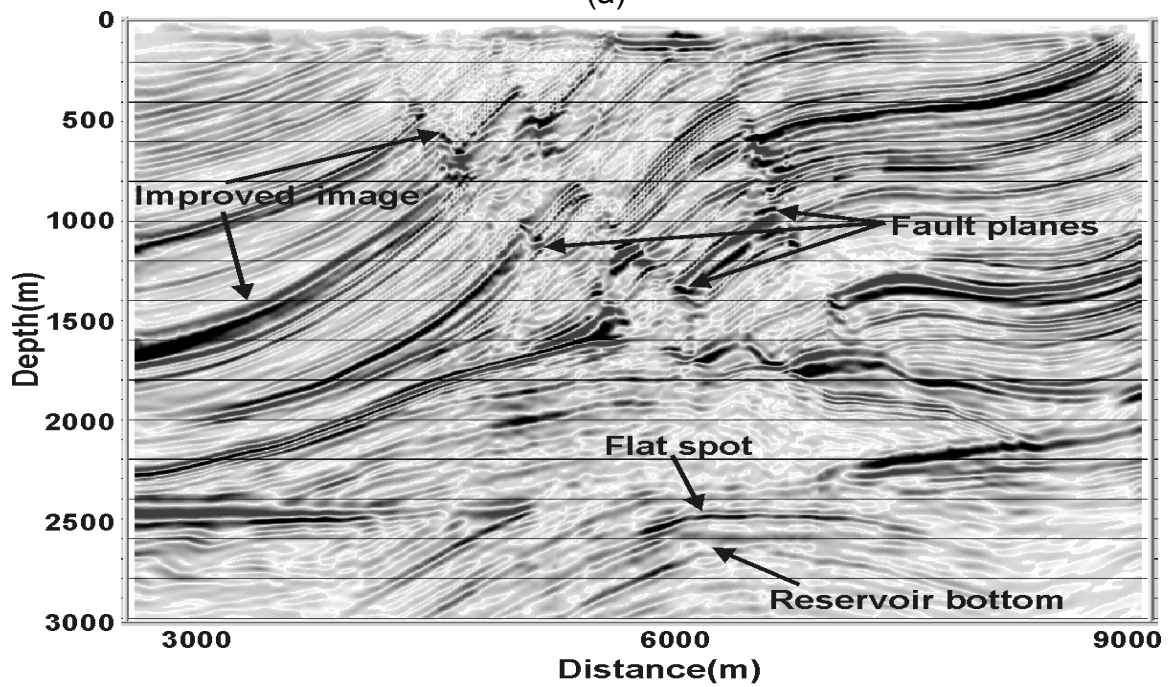


Figure 3.10 Inverse extrapolation of the intermediate wavefields at (a) 564 m, (b) 572 m, (c) 580 m, (d) 588 m and (e) 596 m with the 4-m step recursive PSPI integral operator.



(a)



(b)

Figure 3.11 Marmousi CIG image computed with a 40-m dual algorithm by (a) linear interpolation of static phase-shift-corrected wavefield and (b) linear interpolation of wavefields corrected with the single-reference-velocity split-step algorithm. Note: the phase error generated by the large-step extrapolation on high-angle reflections in (a) and the improvement in (b).

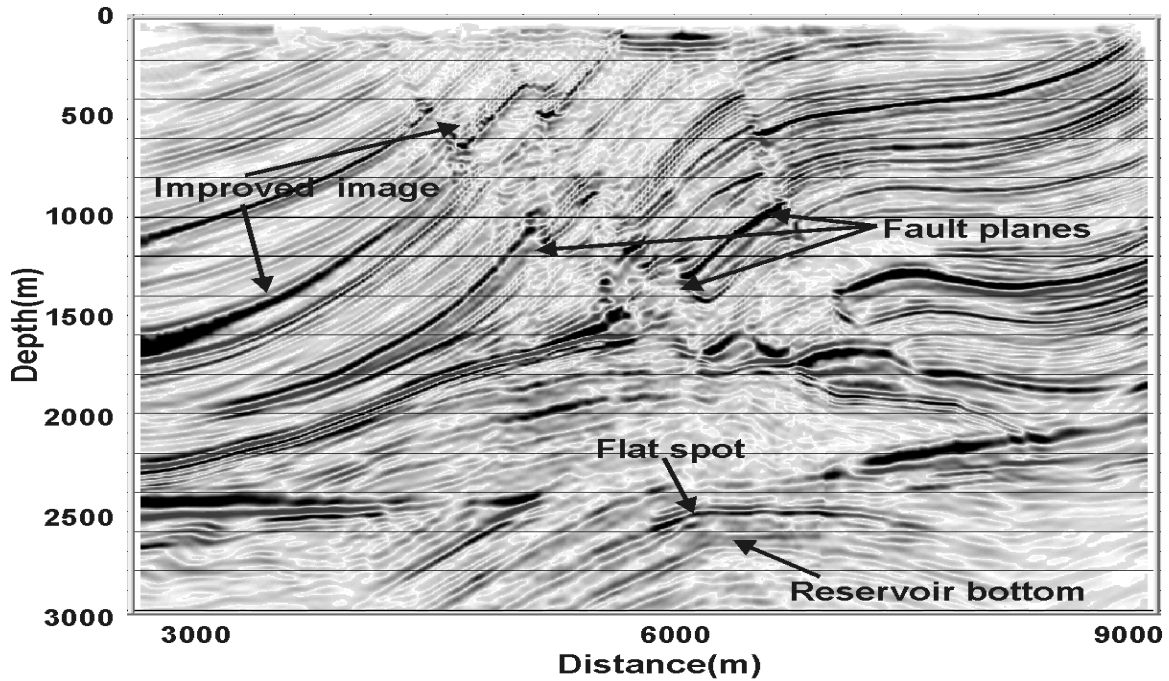


Figure 3.12 Marmousi CIG image computed with a 16-m dual algorithm. The image is very comparable to **Figure 2.12**, computed with recursive SNPS algorithm.

3.6 LARGE-STEP EXTRAPOLATION BY EIGENVALUE DECOMPOSITION

Although the integral wavefield extrapolators are accurate, their dip limit is determined by the downward-continuation step and by the lateral velocity-block size of the piece-wise velocity model. Waves propagating travel through the boundary between velocity blocks do not comply with isotropic wave propagation theory. For the recursive PSPI algorithm with $\Delta x = 25$ m and $\Delta z = 4$ m, the dip limit is about $\tan^{-1}\left(\frac{25}{4}\right) \approx 80^\circ$. In

this section, an eigenvalue-decomposition algorithm that provides a more accurate solution to wavefield propagation across the velocity-block boundaries, is discussed.

The 2D wave equation can be written in the Fourier-domain as the Helmholtz equation

$$\left(\frac{\partial^2}{\partial x^2} + \frac{\partial^2}{\partial z^2} + \frac{\omega^2}{v(x)^2} \right) \underline{\psi}(x, z, \omega) = 0, \quad (3.23)$$

where $v(x)$ is the laterally varying velocity field and $\underline{\psi}(x, z, \omega)$ is a mono-frequency wavefield. The boundary condition for the wavefield extrapolation problem is $\underline{\Psi}(x, z, \omega)|_{z=0} = \underline{\Psi}_0(x, \omega)$, where $\underline{\Psi}_0(x, \omega)$ is assumed to consist of the upgoing wavefield only.

Yao and Margrave (2000) showed that the extrapolated wavefield at depth z could be written as

$$\underline{\underline{\psi}}(x, z, \omega) = \underline{\underline{F}}_x^{-1} \left[e^{\pm iz \sqrt{\underline{\underline{C}}^2 - \underline{\underline{K}}^2}} \underline{\underline{F}}_x \underline{\underline{\psi}}(x, z=0, \omega) \right]. \quad (3.24)$$

Symbols with a single underscore are vectors and those doubly underscored are matrices.

$\underline{\underline{C}}^2$ is a Toeplitz matrix defined as

$$\underline{\underline{C}}^2 = \omega^2 \begin{pmatrix} s_0 & \cdot & \cdot & s_{-(n-1)} \\ \cdot & & & \\ \cdot & & & \\ s_{(n-1)} & \cdot & \cdot & s_0 \end{pmatrix}. \quad (3.25)$$

In the above matrix, s_n in the above matrix is defined as the forward spatial Fourier

transform of $\frac{1}{v(x)^2}$, such that

$$s_n = \frac{1}{L} \int v^{-2}(x) e^{in\Delta k_x x} dx. \quad (3.26)$$

In a laterally varying velocity field, it contains off-diagonal components. In the constant-velocity field, the matrix is diagonal.

$\underline{\underline{K}}^2$ is a diagonal matrix with the square of horizontal wavenumbers populating the main diagonal

$$\underline{\underline{K}}^2 = \begin{pmatrix} k_x^2(1) & & & \\ & \cdot & & \\ & & \cdot & \\ & & & k_x^2(n) \end{pmatrix}. \quad (3.27)$$

With eigenvalue decomposition, equation (3.24) can be written as

$$\underline{\underline{\psi}}(x, z, \omega) = \underline{\underline{F}}_x^{-1} \left[\underline{\underline{D}} e^{-i\Lambda^{1/2} z} \underline{\underline{D}}^{-1} \underline{\underline{F}}_x \underline{\underline{\psi}}(x, z=0, \omega) \right]. \quad (3.28)$$

$\underline{\underline{C}}^2 - \underline{\underline{K}}^2$ can be decomposed as

$$\underline{\underline{C}}^2 - \underline{\underline{K}}^2 = \underline{\underline{D}} \underline{\underline{\Lambda}} \underline{\underline{D}}^{-1}, \quad (3.29)$$

where $\underline{\underline{\Lambda}}$ is a diagonal matrix with eigenvalues of the matrix $\underline{\underline{C}}^2 - \underline{\underline{K}}^2$ populating the main diagonal. $\underline{\underline{D}}$ is a matrix whose columns are corresponding eigenvectors.

3.7 LARGE-STEP EXTRAPOLATION WITH PADÉ APPROXIMATION TO MATRIX EXPONENTIAL

The direct solution of the wave equation discussed above involves computing the matrix exponential with eigenvalue decomposition. The resulting reference wavefields are more accurate than those generated by the large-step nonstationary integral extrapolators. By using the direct solution, waves propagating through velocity-block boundaries can be accurately computed and a velocity-field approximation is the only source of error. This resolution is suitable for both practical forward seismic modeling and depth imaging, as long as computation can be quickly performed. In the case of depth-imaging, if the step size is too small, the algorithm is no faster than the recursive integral algorithm. Computing the matrix exponential and the square-root functions in equation (3.28) is significantly slower than computing the integral operators.

Matrix exponential computing techniques are well described in the literature of mathematics (Golub and Van Loan, 1989, for example). The eigenvalue decomposition approach and Padé approximation algorithms are typical. In large-step wavefield extrapolation, an approximate wavefield extrapolator such as the Padé approximation can be used. The Padé approximation is slightly less accurate than the eigenvalue decomposition algorithm but is sufficiently accurate to map the wavefield to the next depth through a laterally varying velocity field.

Matrix exponential function and its Padé approximation

A matrix function $f(\underline{A})$ can be defined from a scalar function $f(z)$ by simply replacing the variable z with matrix \underline{A} . A matrix exponential function is defined as

$$f(\underline{A}) = e^{\underline{A}}. \quad (3.30)$$

In our case, \underline{A} is the phase-shift and wavenumber-mixing matrix defined in equation (3.24), $\underline{A} = \pm iz \sqrt{\underline{C}^2 - \underline{K}^2}$. All approximation rules applicable to the scalar function e^z can be applied to function $e^{\underline{A}}$, directly.

Similar to the Padé approximation to a scalar exponential function as described in Chapter 2, the Padé approximation to the matrix exponential function can be conveniently written as

$$e^{\underline{A}} \approx R_{pq}(\underline{A}) = D_{pq}(\underline{A})^{-1} N_{pq}(\underline{A}), \quad (3.31)$$

where

$$N_{pq} = \sum_{k=0}^p \frac{(p+q-k)! p!}{(p+q)! k! (p-k)!} \underline{A}^k, \quad (3.32)$$

and

$$D_{pq} = \sum_{k=0}^q \frac{(p+q-k)!q!}{(p+q)!k!(q-k)!} (-\underline{\underline{A}})^k, \quad (3.33)$$

Note that when q is zero, equation (3.31) reduces to the p th-order Taylor-series expansion

$$R_{p0}(\underline{\underline{A}}) = 1 + \underline{\underline{A}} + \dots + \underline{\underline{A}}^p / p!. \quad (3.34)$$

For a commonly used case $p = q = 2$, equations (3.32) and (3.33) can be written as

$$D_{p=2,q=2}(\underline{\underline{A}}) = I - \frac{1}{2}\underline{\underline{A}} + \frac{1}{12}\underline{\underline{A}}\underline{\underline{A}}, \quad (3.35)$$

and

$$N_{p=2,q=2}(\underline{\underline{A}}) = I + \frac{1}{2}\underline{\underline{A}} + \frac{1}{12}\underline{\underline{A}}\underline{\underline{A}}. \quad (3.36)$$

Similar to that of the Padé approximation to the scalar exponential function, the computing procedure should be altered as $e^{\underline{\underline{A}}} \Rightarrow \left(e^{\underline{\underline{A}}/m}\right)^m$, where m is a power of 2, in order to achieve efficiency (Golub and Van Loan, 1989).

Padé approximation to the wavefield-extrapolation matrix

Equation (3.24) can also be written as

$$\underline{\underline{\psi}}(z, \omega) = \underline{\underline{F}}_x^{-1} e^{\underline{\underline{A}}} \underline{\underline{F}}_x \underline{\underline{\psi}}(z=0, \omega), \quad (3.37)$$

where $\underline{\underline{A}}$ is the wavefield extrapolation matrix defined by $\underline{\underline{A}} = \pm iz \underline{\underline{B}}$ and $\underline{\underline{B}}$ is defined as the square root of the matrix $\underline{\underline{C}}^2 - \underline{\underline{K}}^2$, such that

$$\underline{\underline{B}}^{1/2} \underline{\underline{B}}^{1/2} = \underline{\underline{C}}^2 - \underline{\underline{K}}^2. \quad (3.38)$$

The wavefield extrapolation matrix $e^{\underline{\underline{A}}}$ can then be computed with the Padé approximation. Computation of the matrix square-root function is also time-consuming, though much faster than the matrix exponential functions; it is thus not discussed in this context.

3.8 NUMERICAL EXAMPLES FOR LARGE-STEP EXTRAPOLATION WITH THE PADÉ APPROXIMATION

Figure 3.13 shows a two-block velocity model used for the zero-offset forward/inverse extrapolation test with the eigenvalue decomposition algorithm and the Padé approximation algorithm. The forward synthetic by eigenvalue decomposition can be accurately inverted by the Padé approximation algorithm and vice versa (**Figure 3.14**).

Random lateral velocity variation and a large extrapolation step present a significant challenge to wavefield extrapolation algorithms. **Figure 3.15** shows an extreme test. The lateral velocity variation of adjacent velocity blocks exceeds 75%. Forward modeling is performed with the eigenvalue-decomposition algorithm and the synthetic

data can be perfectly inverted by the Padé-approximation algorithm. The sizes of the focal points are directly related to the velocity of the block in which they reside.

Compared to the direct eigenvalue decomposition algorithm, the Padé approximation solution is about three times faster, though still slow for practical application.

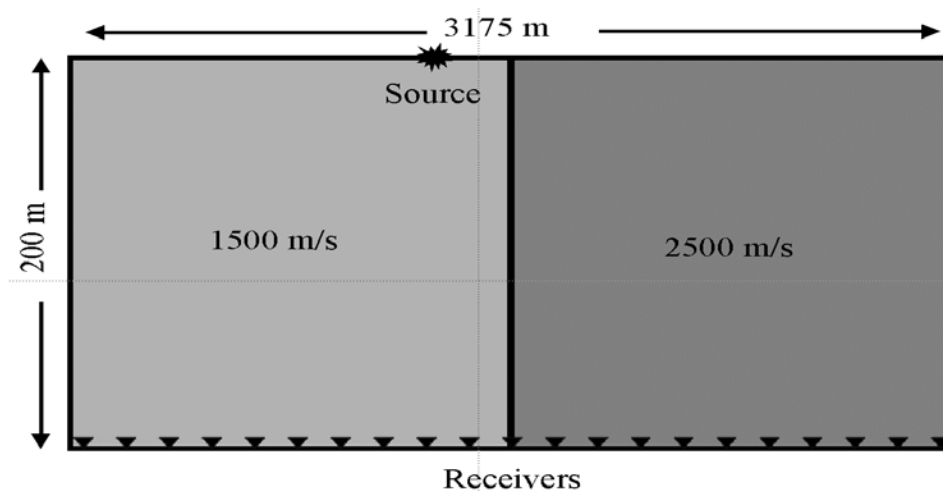


Figure 3.13 Two-block model to test zero-offset extrapolation with Padé approximation. The star indicates the position of the source and black triangles are receiver locations.

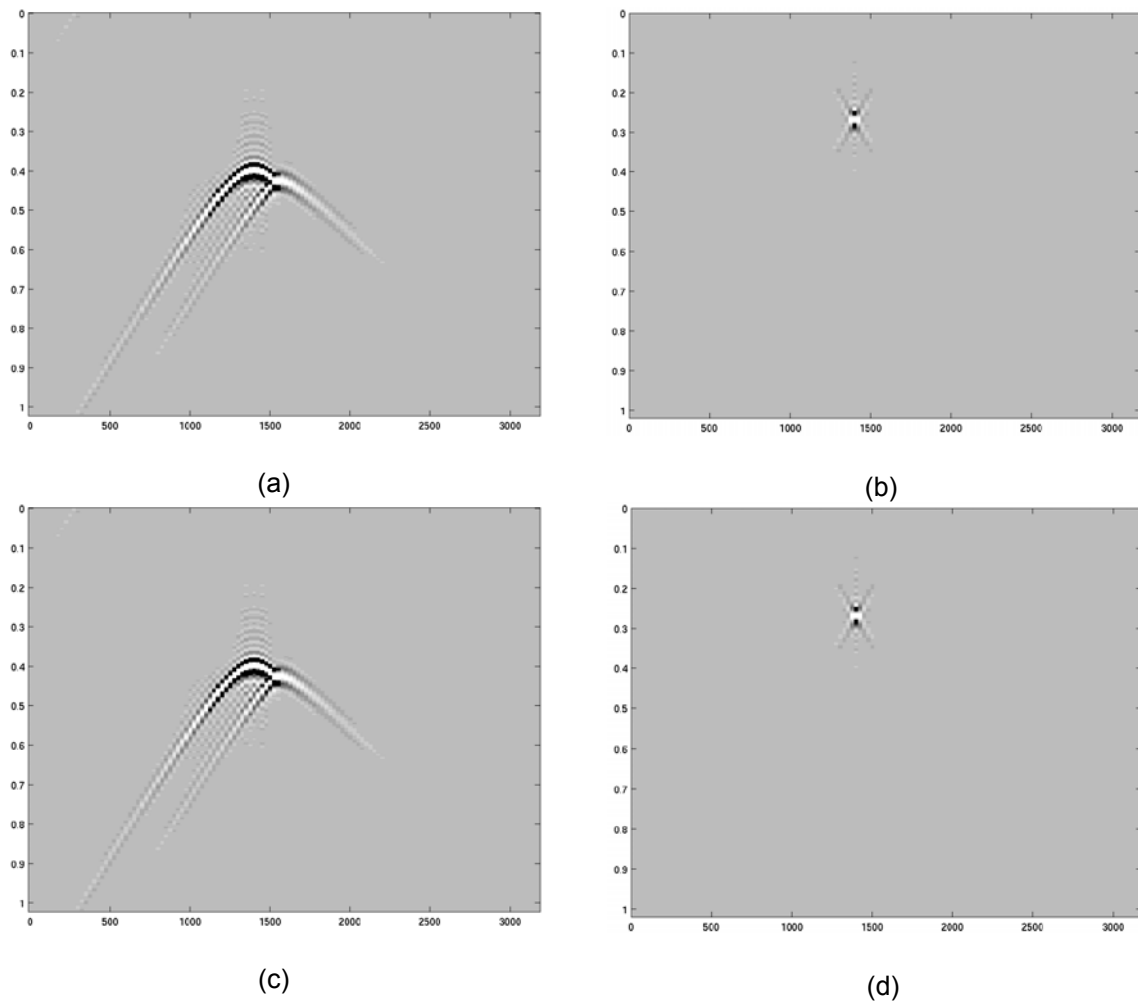


Figure 3.14 Forward and backward extrapolation of an impulse through a two-block model as shown in **Figure 3.13**. (a) The forward extrapolation of a single spike computed with the Padé approximation; (b) The inverse extrapolation of (a) with the eigenvalue decomposition algorithm; (c) The forward extrapolation a single spike computed with eigenvalue decomposition; (d) The inverse extrapolation of (c) computed the Padé approximation algorithm.

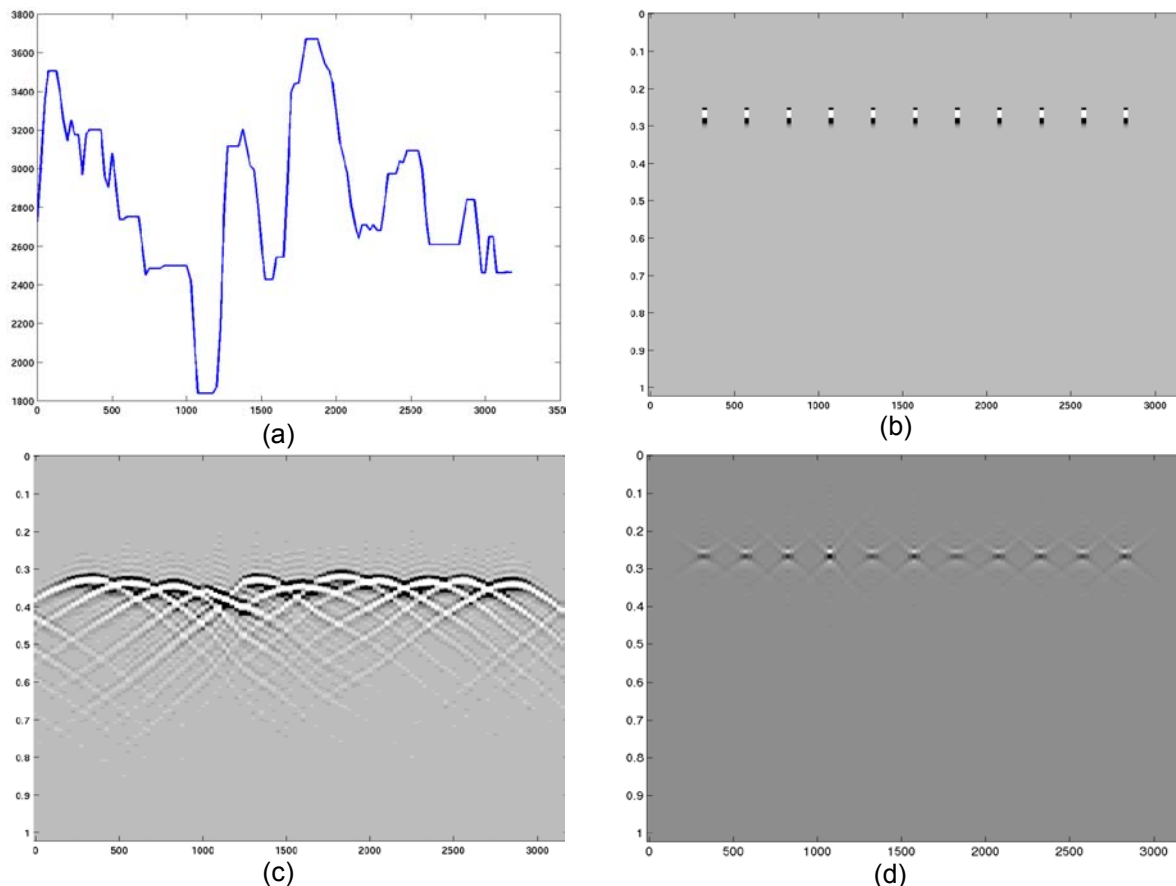


Figure 3.15 Zero-offset forward extrapolation with the eigenvalue decomposition algorithm and inverse extrapolation with the Padé approximation algorithm through a randomly varying velocity media. (a) Random velocity model. The thickness of the model is 400 m; (b) 11 impulses, starting at 0.25 s; (c) Forward extrapolation of the 11 impulses in (b) with eigenvalue decomposition; (d) Inverse extrapolation of (c) computed with the Padé approximation algorithm.

3.9 COMPARISON OF SPEED AND LIMITATIONS OF ALGORITHMS

The NSPS, PSPI and SNPS are $N_s N_z N^3$ algorithms. The order of other Fourier-domain prestack depth-imaging methods can be computed in a similar way. For the single-reference-velocity split-step Fourier method or phase-screen method, ignoring the computation time for vertical traveltime correction (since computing the focusing term consumes most of the computer time), the cost function can generally be written as $N_s N_z N^2 \log N$. For a localized split-step approach, the computer time-cost function can be

written as $N_s N_z N_w N^2 \log N$, where N_w is the number of spatial windows. Gazdag's PSPI approach is roughly in the same order of a localized split-step Fourier method and the computing cost function can be written as $N_s N_z N_v N^2 \log N$, where N_v is the number of reference velocities. For the dual algorithm, the cost function can be written as $N_s N_z N^3 / N_L$, where N_L is the number of intermediate steps in a large-step extrapolation. When the condition $N_v \log N > N / N_L$ is satisfied, the dual algorithm becomes faster than the localized split-step Fourier method and Gazdag's PSPI approach. Numerical tests on zero-offset synthetic data showed that the eigenvalue-decomposition method is significantly slower than the integral operators are and not at all practical. The Padé approximation is about three times as fast as the eigenvalue-decomposition method; however, more research is required before implementation would be practical. The cost functions of these two methods are not examined here.

Table 3.1 shows the relative performance and capability of different Fourier-domain wavefield extrapolators. This is a rough estimation only and should only be considered in a relative sense.

Algorithms	Ability to Handle Large Lateral Velocity Gradient	Order of Algorithm	Relative Speed
NSPS, PSPI and SNPS integrals	Strong	$N_s N_z N^3$	Slow.
Dual algorithm	Strong	$N_s N_z N^3 / N_L$	Very fast.
Split-step / Phase-screen	Weak	$N_s N_z N^2 \log N$	Very fast.
Localized split-step / Phase-screen	Strong when sufficient numbers of windows are used.	$N_s N_z N_w N^2 \log N$	Slow when the number of windows exceeds $N/\log N$.
Gazdag's PSPI	Strong when sufficient number of reference velocities is used.	$N_s N_z N_v N^2 \log N$	Slow when number of reference velocities exceeds $N/\log N$.
Eigenvalue decomposition	Very strong	N/A	Very slow.
Padé approximation	Very strong.	N/A	Slow, but three times faster than Eigenvalue decomposition.

Table 3.1 Summary of the performance of Fourier-domain imaging techniques.

3.10 CHAPTER SUMMARY

A dual algorithm is presented in this chapter and is an efficient way to speed up integral extrapolation algorithms. The size of the large step is directly related to the lateral velocity variation. Less lateral velocity variation permits a relatively large step and, hence, a more efficient algorithm. In dealing with a more rapid lateral velocity variation with a large-step extrapolation, an accurate algorithm such as the eigenvalue decomposition, though very slow, should be used. As an alternative, the Padé approximation algorithm can be used to produce results sufficiently accurate for our purposes.

CHAPTER 4

PRESTACK DEPTH IMAGING FROM TOPOGRAPHY WITH NSPS AND PSPI

4.1 INTRODUCTION

Fourier-domain imaging algorithms require that seismic data be corrected to a flat datum. Statics correction, assuming near-surface vertical ray-paths, is often not sufficiently accurate to produce correct wavefields at the datum when near-surface geology is complicated. Wave-equation redatuming is often required (Berryhill, 1979, 1984; Shtivelman and Canning, 1988). In mountainous areas such as the Canadian Rockies, topographic variation often exceeds several hundred meters and redatuming inevitably results in the loss of near-surface image, which is often important for correlation analysis between a seismic image and actual geological outcrops. Direct imaging from topography improves this situation. The problem in this specific region has been addressed by several authors (Gray and Marfurt, 1995; Lines et al., 1996).

Imaging from topography with wave-equation methods is a natural extension of wave-equation redatuming techniques in that both are established on the wavefield

extrapolation theory. This chapter addresses the issue, with the nonstationary phase-shift theory.

4.2 PSPI EXTRAPOLATION FROM TOPOGRAPHY

Figure 4.1 shows the basics of wave-equation redatuming. In place of applying a vertical time-shift to the traces, the energy at each receiver location is allowed to propagate at all possible angles. For a complex velocity model, Fourier-domain redatuming requires recursive wavefield extrapolation, continuous muting of energy above the topography as the result of extrapolation and inclusion of data recorded at current depth levels. The final datum is often flat below the lowest point of topography.

For less complex media and with relatively small topographic variation, recursive wavefield extrapolation can be approximately replaced by a single-step nonstationary wavefield extrapolation with both velocity and extrapolation step sizes varying with spatial location (Margrave and Yao, 2000) (**Figure 4.2**). For example, a PSPI nonstationary redatuming algorithm can be formulated as,

$$\psi(x, z, \omega) = \frac{1}{2\pi} \int_{-\infty}^{+\infty} \alpha(x, k_x, z, \omega) \varphi(k_x, 0, \omega) e^{-ik_x x} dk_x, \quad (4.1)$$

with the nonstationary redatuming wavefield extrapolator $\alpha(x, k_x, z, \omega)$ written as

$$\alpha(x, k_x, z, \omega) = e^{\pm ih(x) \sqrt{\frac{\omega^2}{v_{ave}^2(x)} - k_x^2}} \quad (4.2)$$

Note that both the velocity and the extrapolation step size are now x -dependent. Plus and minus signs denote backward and forward extrapolation.

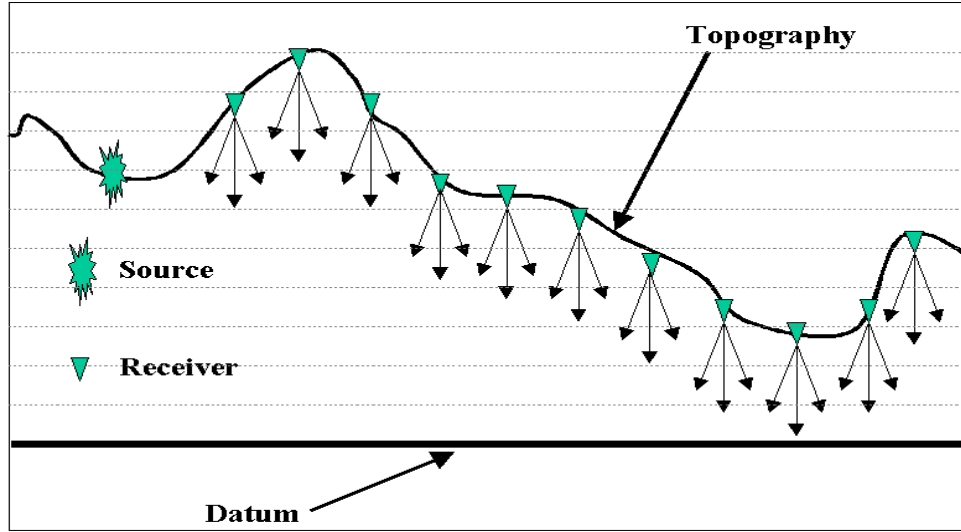


Figure 4.1 Wave-equation redatuming allows the energy at each receiver location to propagate along all possible angles. Dotted grid lines denote depth steps.

Note that equation (4.1) is a large-step algorithm; however, different from that in Chapter 3. The average velocity is used to compute both static phase-shift and focusing phase-shift terms. According to the large-step-extrapolation algorithm in Chapter 3, equation (4.2) can be split into static-phase-shift and focusing-phase-shift terms. The extrapolation can be written as

$$\psi(x, z, \omega) = e^{-i\Phi(x)_{static}} \left[\frac{1}{2\pi} \int_{-\infty}^{+\infty} \alpha'(x, k_x, z, \omega) \phi(k_x, z, \omega) e^{-ik_x x} dk_x \right], \quad (4.3)$$

where Φ_{static} is the static phase-shift defined as

$$\Phi_{\text{static}} = \frac{\omega h(x)}{v_{\text{ave}}}. \quad (4.4)$$

The nonstationary, focusing phase-shift operator can be written as

$$\alpha'_{\text{mean}}(x, k_x, z, \omega) = e^{-i \frac{\omega h(x)}{v_{\text{mean}}(x)} \left(\sqrt{1 - \frac{k_x^2 v_{\text{mean}}(x)^2}{\omega^2}} - 1 \right)}, \quad (4.5)$$

where both the average and the mean velocities are computed from the topography to the flat datum. Note that only the forward-extrapolation case is considered.

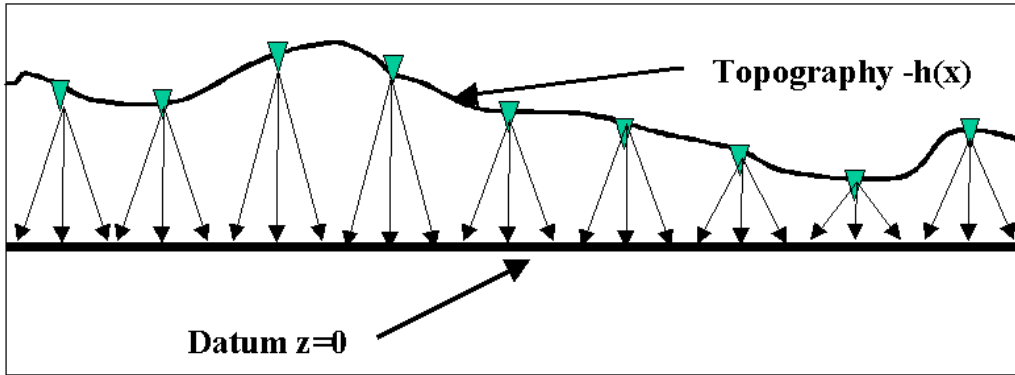


Figure 4.2 Single-step Fourier-domain redatuming with nonstationary wavefield extrapolator. Both the extrapolation step size and the velocity are functions of spatial location.

For more severe topographic variation and strong lateral-velocity variation, an accurate large-angle propagator is desirable. Equation (4.3) can be applied recursively with the x -dependent depth-step function being a slice of the overall topography $z(x)$ in each step; however, a spatial mute function must be applied in order to eliminate the extrapolated wavefield above the topography. Data recorded at the current depth-step is included for the next phase of extrapolation. For a large-step PSPI implementation, the thinner the slice, the more accurate the algorithm. For a PSPI implementation, each step of extrapolation can be written as

$$\begin{aligned} \psi(x, z_0 + \Delta z, \omega) = & PSPI[\varphi(k_x, z_0, \omega)]W(x, z_0) \\ & + \psi_{z(x)}(x, z_0 \leq z < z_0 + \Delta z, \omega), \end{aligned} \quad (4.6)$$

where PSPI denotes the PSPI integral algorithm. $\varphi(k_x, z_0, \omega)$ and $\psi(x, z_0 + \Delta z, \omega)$ denote the (ω, k_x) -domain wavefield at depth z_0 and the (ω, x) -domain wavefield at depth $z_0 + \Delta z$, respectively. $W(x, z_0)$ represents the spatial-windowing function, defined as

$$W = \begin{cases} 1 & z_0 > h(x) \\ 0 & z_0 \leq h(x) \end{cases}. \quad (4.7)$$

$\psi_{z(x)}$ denotes the wavefield recorded on the topography $z(x)$. The extrapolation depth-step function in the nonstationary phase-shift operator (equation 4.5) is now defined as

$$h(x) = h_2(x) - h_1(x), \quad (4.8)$$

where $h_1(x)$ and $h_2(x)$ are the x -dependent topographic functions at z_0 and $z_0 + \Delta z$ is defined as

$$\begin{aligned} h_1(x) &= \max[z(x), z_0] \\ h_2(x) &= \max[z(x), z_0 + \Delta z], \end{aligned} \quad (4.9)$$

and $z(x)$ is the topography.

Figure 4.3 shows a zero-offset forward extrapolation of 11 impulses through a complex velocity model. The impulses are placed uniformly at the bottom of the model and receivers are placed at each spatial location on the topography. Forward modeling is

done by recursive application of the PSPI integral extrapolator with a step size of 4 m. The velocity model has a maximum 100% lateral velocity variation and roughly 110 m of topographic relief, within a distance of 750 m. Comparison of the downward extrapolation with large-step PSPI extrapolation algorithm against the recursive PSPI integral algorithm highlights the robustness of the large-step algorithm. **Figure 4.4** depicts the inverse extrapolation with the recursive 4-m step-size PSPI integral and large-step algorithm with various step sizes. Note that the quality of the focal points degrades only slightly when the step size is increased to 80 m.

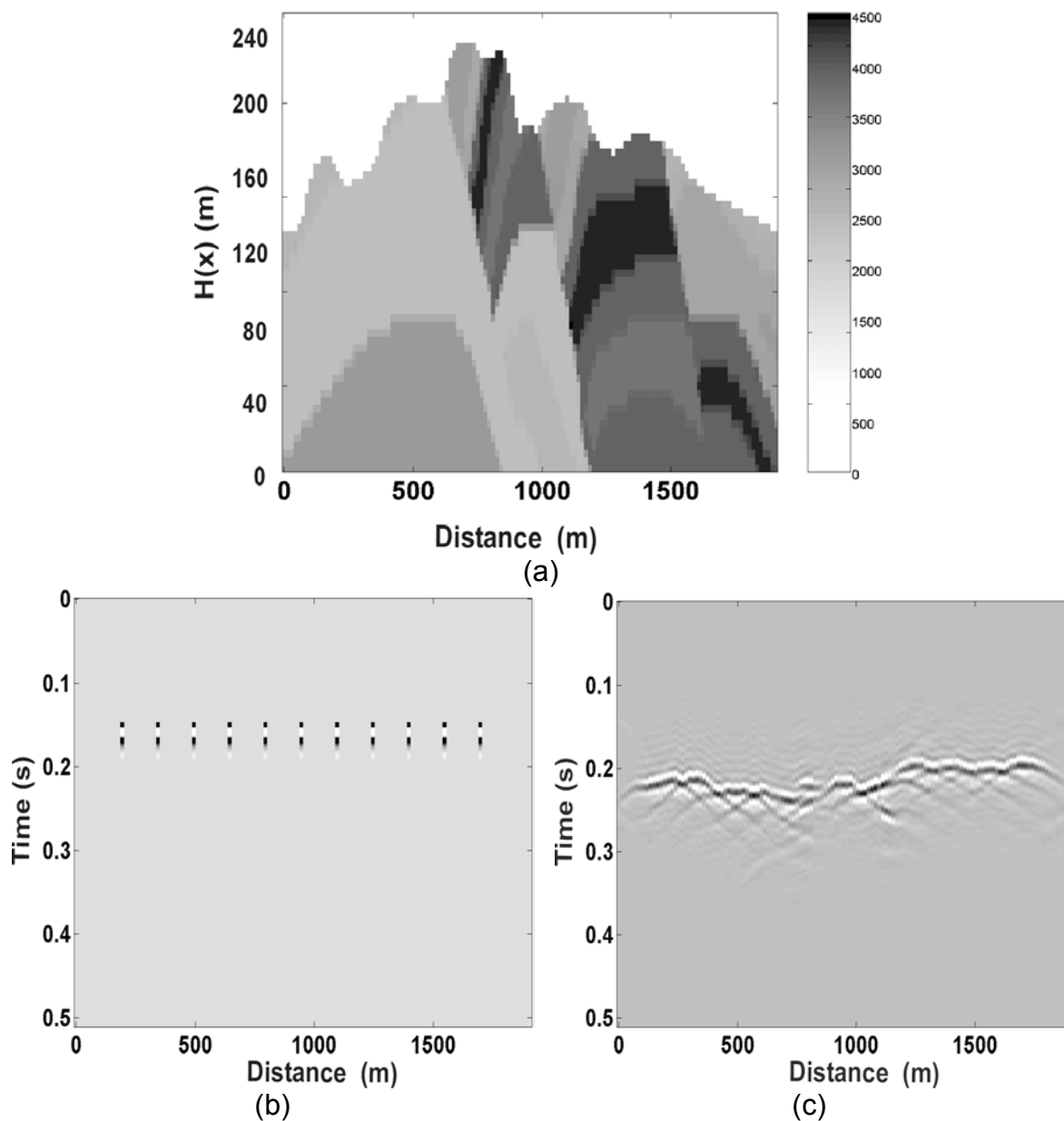


Figure 4.3. Zero-offset forward extrapolation with recursive PSPI integral of 4-m step size. (a) the velocity model, (b) the 11 impulses and (c) the zero-offset synthetic.

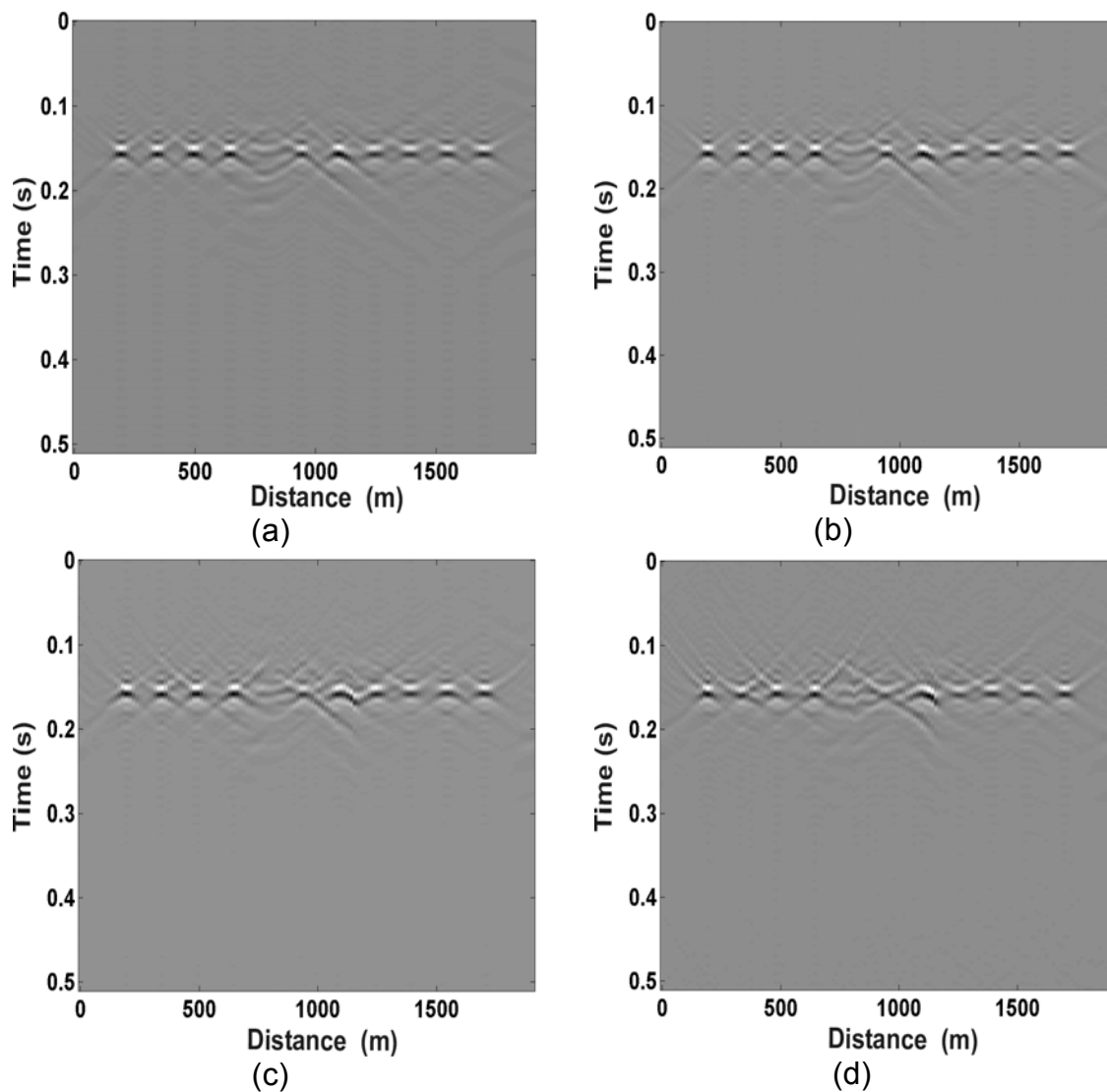


Figure 4.4 Accuracy comparison of inverse extrapolation: (a) Recursive PSPI integral extrapolator with 4-m step size, (b) inverse extrapolation with 20-m PSPI integral extrapolator, (c) inverse extrapolation with 80-m PSPI integral extrapolator and (d) inverse extrapolation with 120-m integral extrapolator.

4.3 NSPS EXTRAPOLATION FROM TOPOGRAPHY

The NSPS counterparts of equation (4.1) can be written as

$$\varphi(k_x, z, \omega) = \int_{-\infty}^{+\infty} \alpha(x, k_x, z, \omega) \psi(x, 0, \omega) e^{ik_x x} dx, \quad (4.10)$$

with the nonstationary wavefield extrapolator $\alpha(x, k_x, z, \omega)$ expressed in equation (4.2).

Similarly, the NSPS counterpart of equation (4.3) can be written as,

$$\varphi(k_x, z, \omega) = \int_{-\infty}^{+\infty} \alpha'(x, k_x, z, \omega) \psi(x, z, \omega) e^{-i\Phi(x)_{\text{static}}} e^{ik_x x} dx, \quad (4.11)$$

where Φ_{static} is the static phase-shift defined as in equation (4.4) and the focusing phase-shift $\alpha'(x, k_x, z, \omega)$ is defined as in equation (4.5). For multi-step extrapolation through topography, the extrapolated process involves similar muting of the extrapolated wavefield above topography and inclusion of recorded data at current depth levels.

The spatial Fourier transform requires that the seismic data be recorded on a flat datum. Both equations (4.1) and (4.3) violate this assumption in that they require the wavefield recorded on a non-flat datum be transformed from x coordinate to k_x coordinate. The same discrepancy exists with equation (4.10). Equation (4.11) is advantageous in that the wavefield is first vertically shifted to a flat datum with an

average interval velocity equivalent to a standard statics correction and then extrapolated and forward-transformed to the k_x domain.

Figure 4.5 shows forward- and inverse-extrapolation tests similar to those shown in **Figure 4.4**. Note that the difference between modeled data with the PSPI integral (**Figure 4.3c**) and the NSPS integral (**Figure 4.5a**) is minor; however, the energy of the events around $x = 750$ m, corresponding to the highest point of the topography and greatest lateral-velocity contrast, is more complete. **Figure 4.5b-d** depict large-step inverse extrapolation of **Figure 4.5a** with 80-m, 120-m and 160-m NSPS integral extrapolators. The source impulse at $x=750$ m is missing in the PSPI extrapolation test (**Figure 4.4**) due to severe topographic variation and high lateral velocity contrast; however, NSPS quite ably recovers the source impulse, even when the extrapolation step size is increased to 160 m.

For depth imaging, the wavefield at each depth-step within the topography can be computed by either recursive extrapolation or the dual algorithm, with the spatial muting function W (equation 4.7) applied and field data recorded at the current depth-level, added.

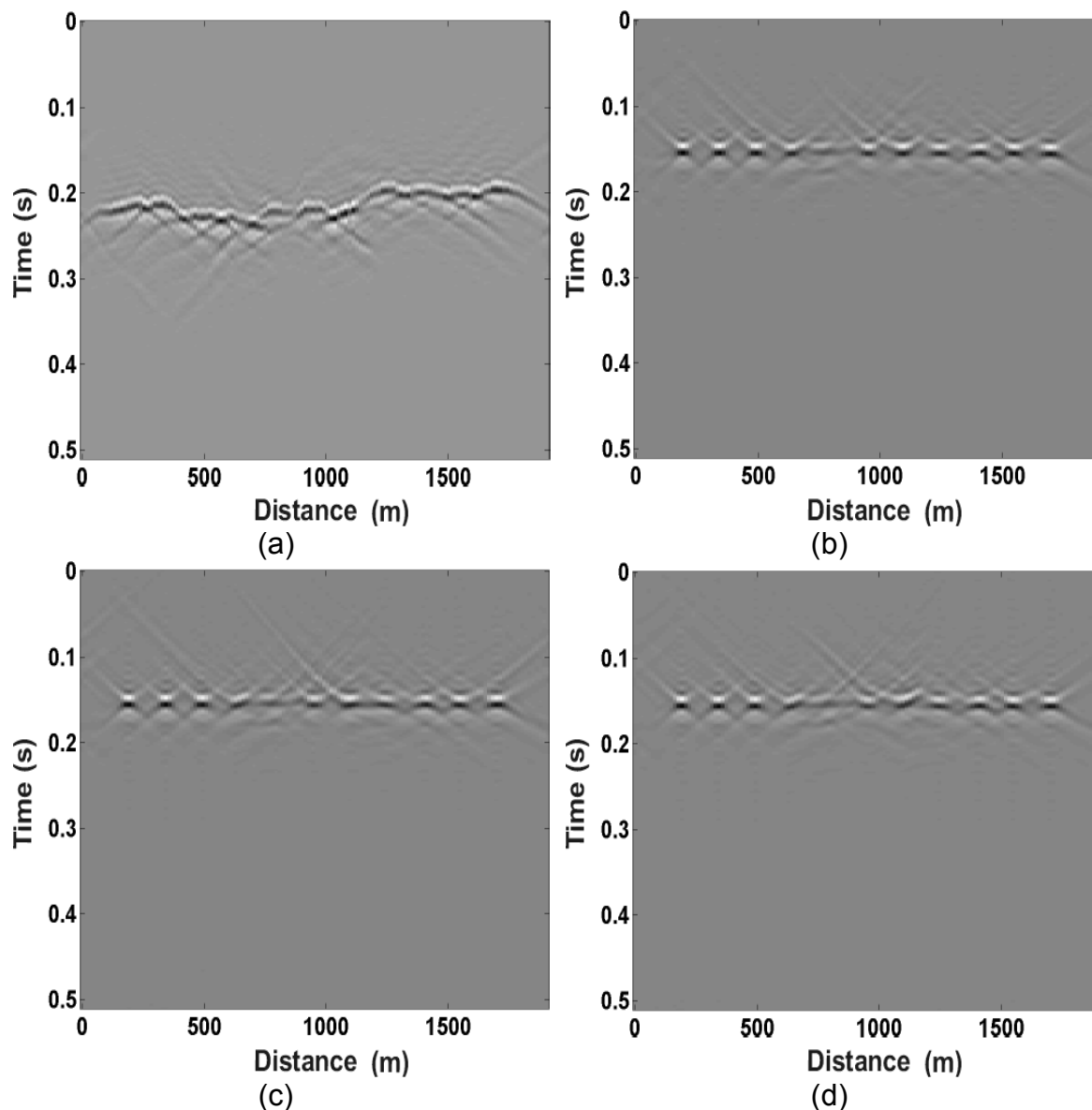


Figure 4.5 Zero-offset extrapolation test with large-step NSPS. (a) Recursive NSPS with 4-m step-size, (b) inverse extrapolation with 80-m step-size NSPS, (c) inverse extrapolation with 120 m NSPS and (d) inverse extrapolation with 160 m NSPS.

4.4 A VELOCITY MODEL OF THE CANADIAN ROCKY MOUNTAIN REGION AND SYNTHETIC DATA

Figure 4.6 shows a geologic cross-section representation of northeastern British Columbia, where large topographic variation and high-angle thrust faults are common. The model contains a number of faults and folded layers, as well as about 1600 m of elevation relief typical to the Canadian Rockies. High near-surface velocity presents an additional challenge to depth imaging algorithms. The model is 25 km long. The highest topography is approximately 2 km above sea level and the deepest about 8 km below sea level. The model has P-wave velocity variation from 3600 m/s near the surface to 5900 m/s near the bottom. The depth-model sample rate is 10 m. A total of 278 2D synthetic shot gathers were computed with finite-difference modeling. The data were recorded to 5 s by a split spread of 480 receivers with offsets ranging from 15 m to 3600 m on both sides of the shot points. The shot spacing is 90 m and the original sample rate is 4 ms. The 2D cylindrical-spreading loss is proportional to $t^{-1/2}$. A geometrical spreading correction should be applied before processing.

Figure 4.7 shows a shot gather in the middle of the model. Rapid topographic variation, high velocities near the surface and complex structures present significant challenges to depth-imaging algorithms.

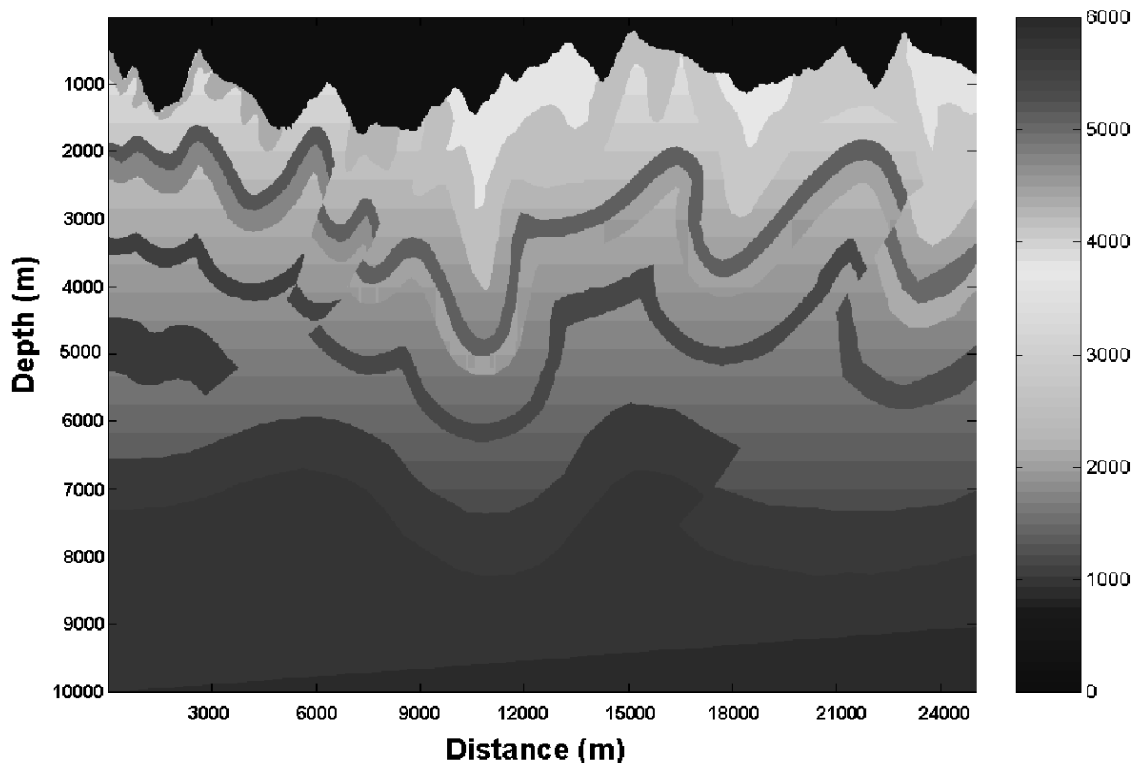


Figure 4.6 A velocity/depth model representation of northeastern British Columbia (after Gray and Marfurt, 1995).

4.5 DEPTH IMAGING OF THE FOOTHILLS SYNTHETIC DATA

The dominant frequency content of the original synthetic data ranges from 5 to 40 Hz and allows resampling to a 6-ms rate to facilitate computing. Each shot gather was padded to 7.5 s in order to accommodate the energy wrapped around by the extrapolation and Fourier transform, which becomes background noise if not properly handled. A more efficient approach is to pad only small amounts of time to the traces and mute the padded region after one or several large-step extrapolations, as long as the vertical travelt ime shift in the extrapolation does not exceed the padded time. Each shot gather was padded to 512 traces, with the source located in the middle, so that 15 padded traces

(225 m) on both sides accommodate the energy wrapped around by extrapolation and spatial Fourier transforms. The padded traces are muted after each large-step extrapolation. For a step size of 50 m, the padding accommodate a design dip of 78° . This is often sufficient for most complex geology settings.

The algorithm was implemented on the MACI cluster workstation (Mi and Margrave, 2001b). A total of 14 computing nodes were used and migration of the data set required about 8 hours. **Figure 4.8** shows the shot gather in **Figure 4.7** after migration and **Figure 4.9** shows a CIG at the middle of the line and the final CIG stack. A zoomed near-surface section is also shown. **Figure 4.10** shows two images produced by other authors, a prestack Kirchhoff migration by Gray and Marfurt (1995) and a 75° finite-difference prestack migration by H. Lu of the CREWES Project (unpublished), with the prestack finite-difference depth-migration module in ProMAX. The parts corresponding to **Figure 4.9(c)** are also zoomed for more detailed comparison. The image produced by the large-step PSPI integral algorithm (**Figure 4.9b**) has several improvements, not only in terms of near-surface events, but also in terms of migration noise level and image resolution. The Kirchhoff algorithm fails to recover both flanks of the syncline located in the middle of the model, at depths from 7000 m to 8000 m (**Figure 4.10 (a)**). The major near-surface events are clear; however, the degree of migration noise is obvious. The 75° finite-difference algorithm produced a less noisy section; the image depth, however, is slightly incorrect. This is apparent in that the left end of the section: basement reflection should be at 10000 m instead of 10300 m. The quality of the dominant fault planes on the right of the section, as well as the strata on both sides, indicates the algorithm's ability

to image high-angle events. Apparently, the large-step PSPI integral algorithm produced the best result.

4.6 CHAPTER SUMMARY

A Fourier-domain migration-from-topography based on the nonstationary phase-shift theory was developed. Details of both the PSPI and NSPS extrapolation from topography were given. The test on zero-offset synthetic data over a complex-velocity model shows that both algorithms are capable of handling extreme lateral-velocity and topographic variations. NSPS is more suitable for large-step extrapolation. However, given the typical large-step size in depth imaging, the difference between the two algorithms is minimal. Prestack algorithms were developed and the Foothills synthetic data set was used for testing. Comparisons between the image produced by the PSPI algorithm against those generated with Kirchhoff and finite-difference algorithms indicate that the nonstationary phase-shift algorithm is more capable of recovering the near-surface image and high-angle fault planes.

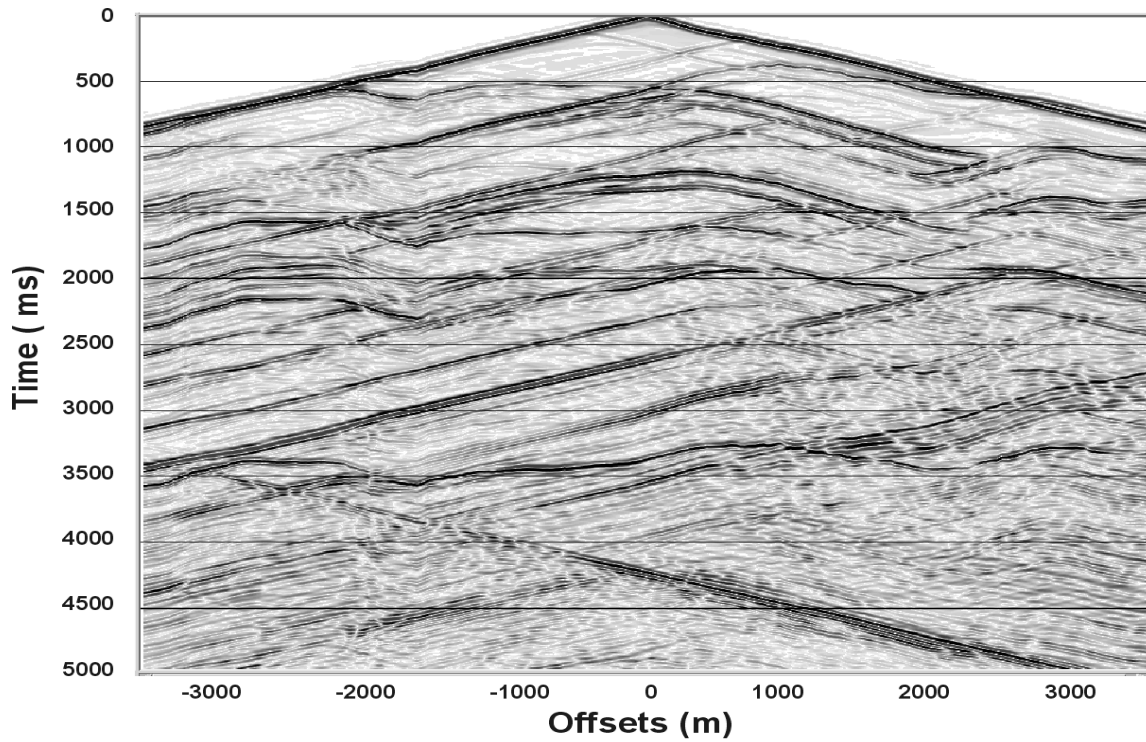


Figure 4.7 A shot gather located in the middle of the model.

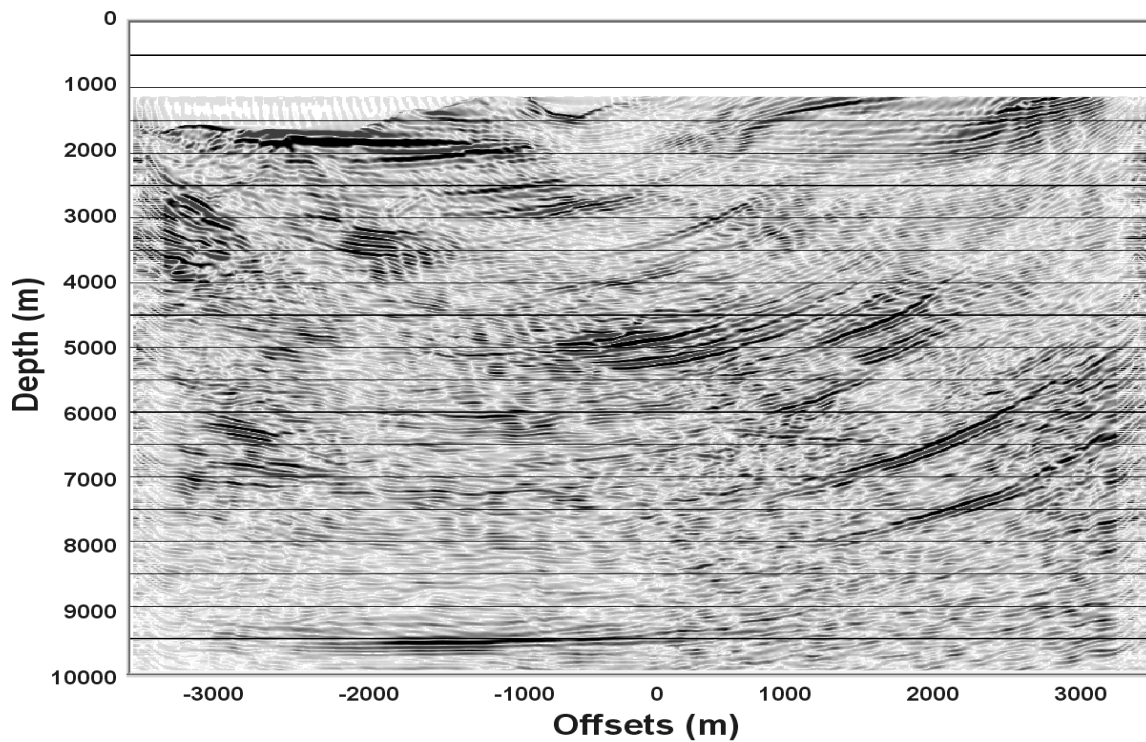


Figure 4.8 Shot gather of **Figure 4.7** after migration from topography with the dual algorithm. The extrapolation step is 50 m.

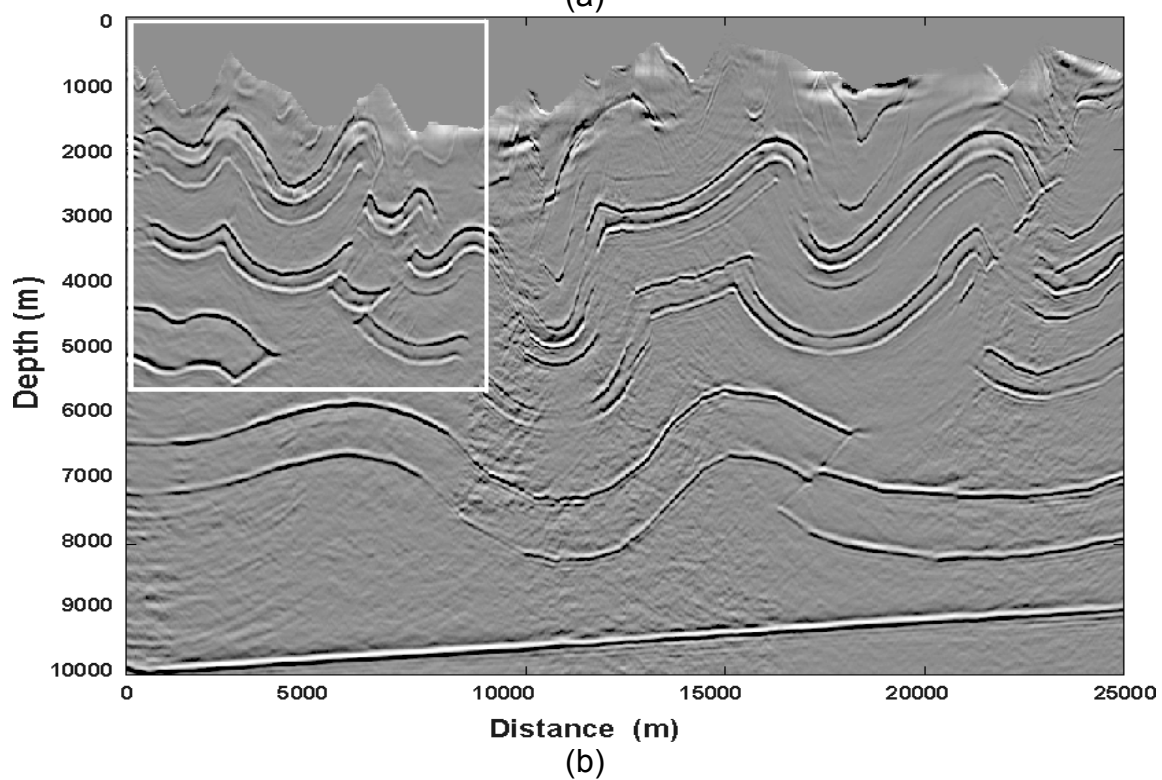
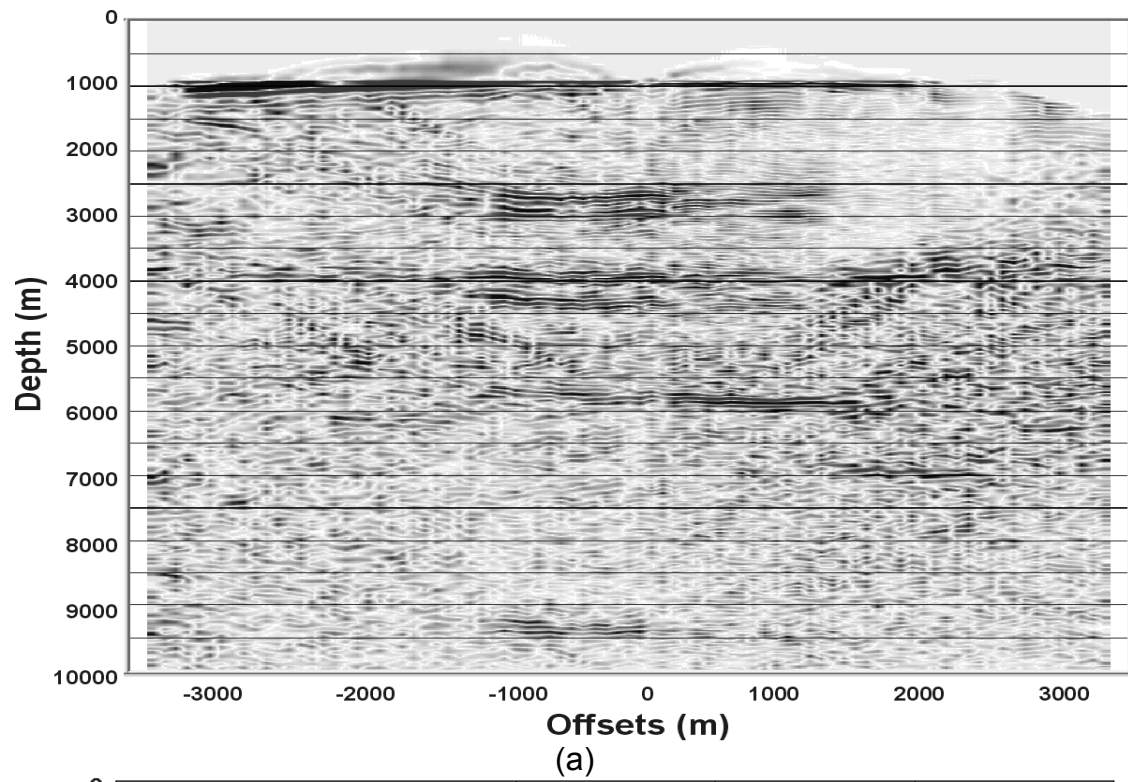


Figure 4.9 (continues)

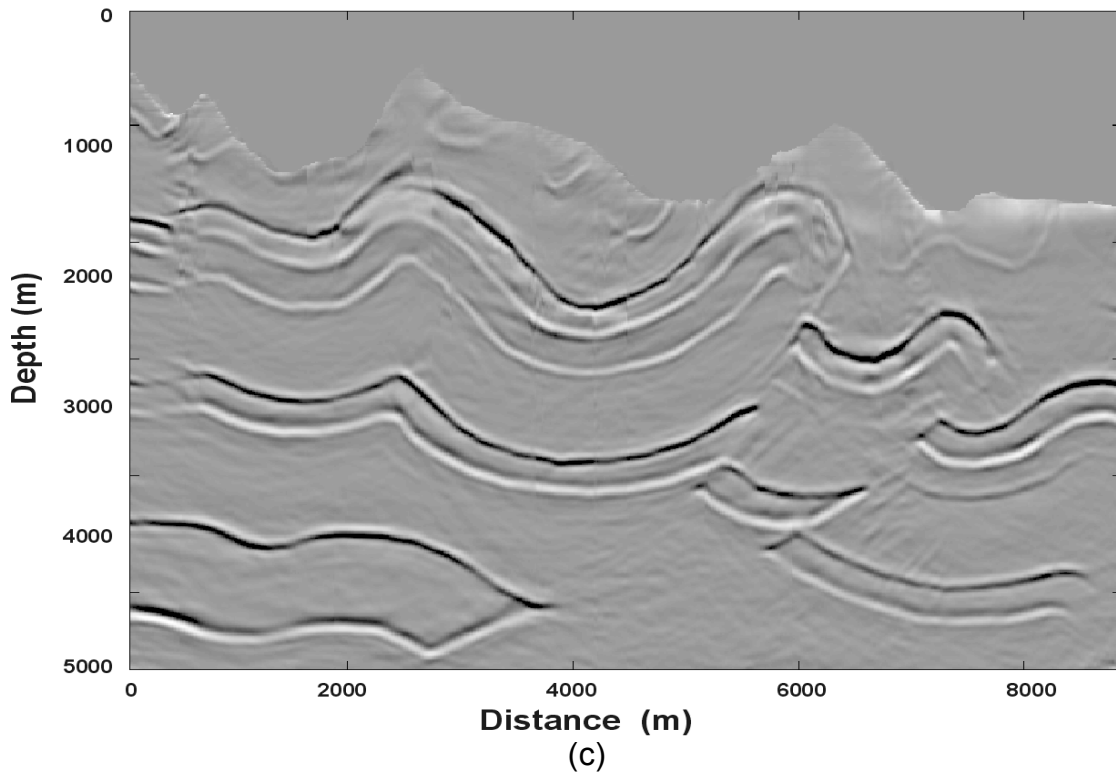


Figure 4.9 Result of depth imaging from topography with large-step PSPI algorithm. (a) A CIG in the middle of the model, (b) CIG stack and (c) a zoomed version of the region highlighted in (b).

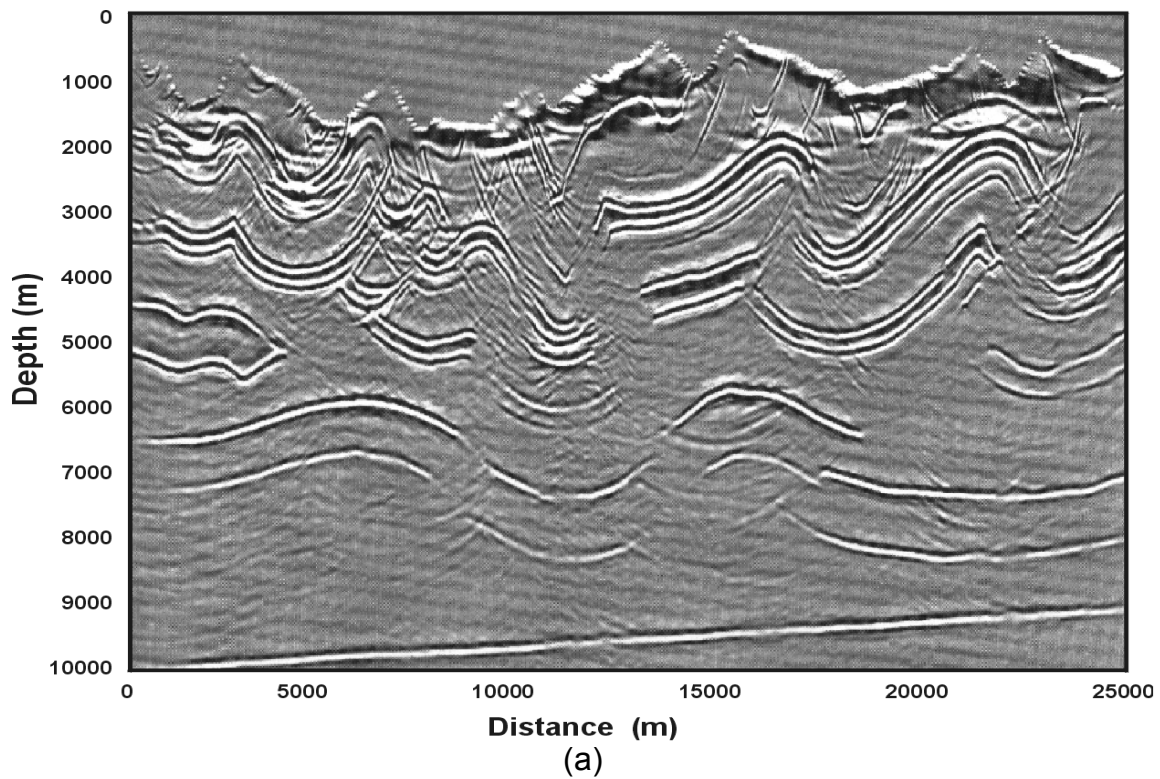


Figure 4.10 (continues)

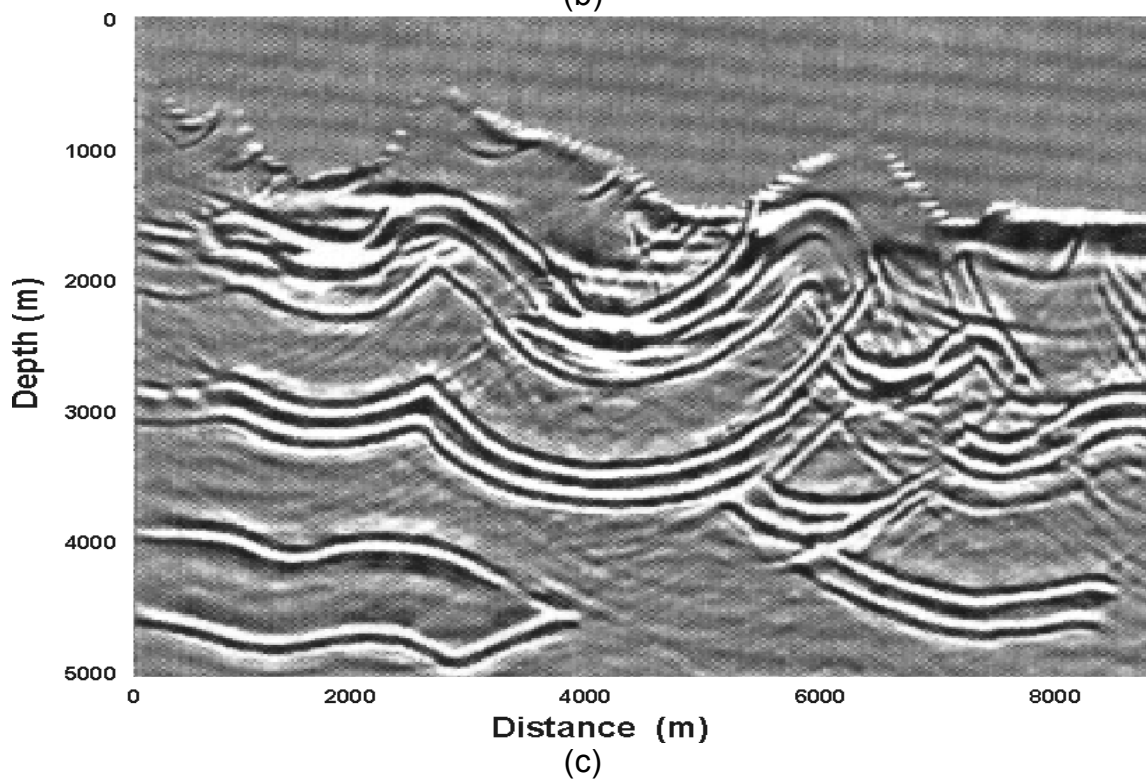
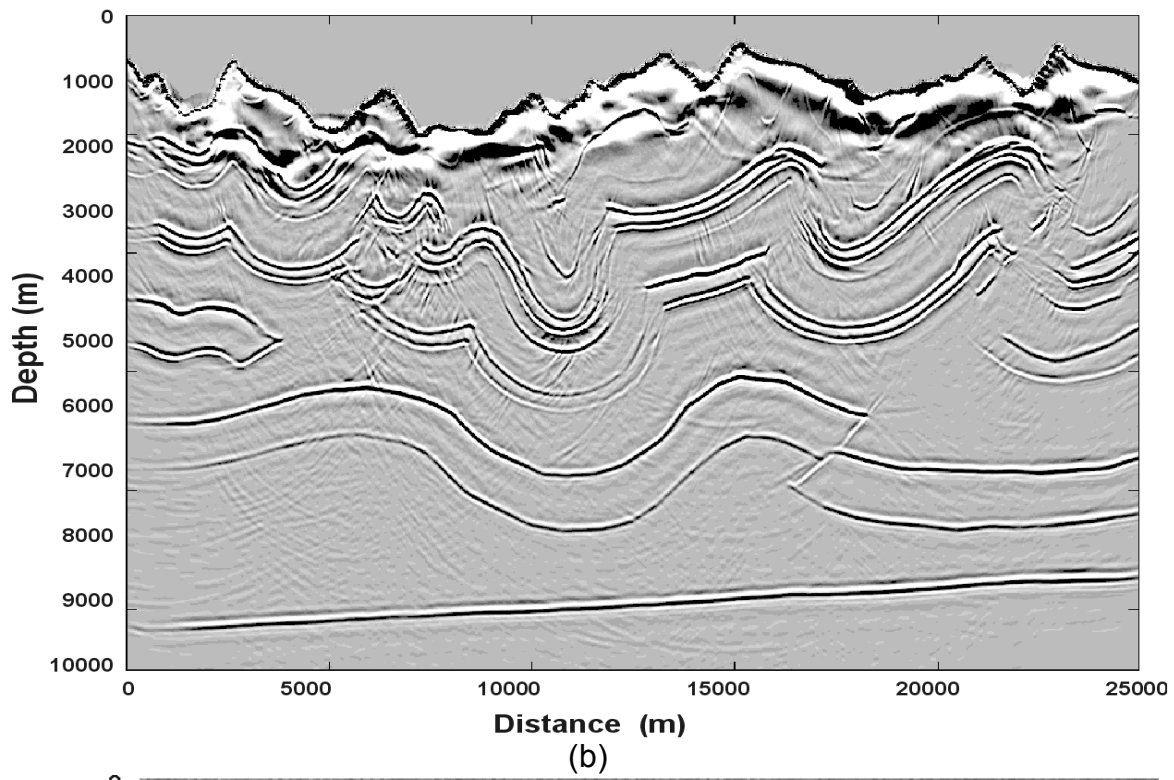


Figure 4.10 (continues)

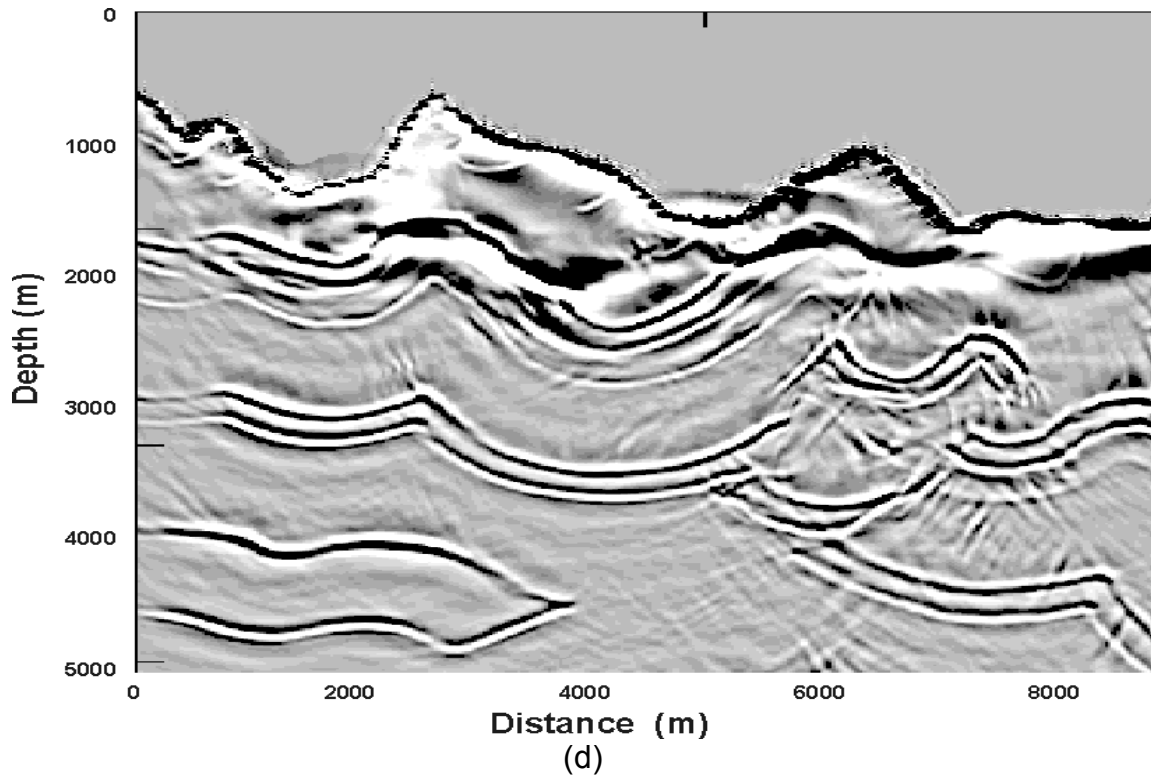


Figure 4.10 Result of prestack depth imaging by other authors. (a) Kirchhoff migration from topography, after Gray and Marfurt (1995), (b) finite-difference prestack migration from topography, by H. Lu, courtesy of the CREWES Project, University of Calgary. (c) and (d) show the upper-left corners of (a) and (b), corresponding to Figure 4.9 (c).

CHAPTER 5**FOURIER-DOMAIN CONVERTED-WAVE PRESTACK
DEPTH IMAGING****5.1 INTRODUCTION**

Shear-wave exploration has certain advantages over conventional P-wave methods. Since shear-wave propagation depends almost entirely on the rock matrix, pore fluid property has less impact on shear-wave velocity than it does on compressional-wave velocity. P-wave signal can be significantly attenuated by the presence of small amount of free gas in pore space, while shear-wave signal can pass without being attenuated much. However, shear-wave sources often have smaller energy capacity, lower frequency content and less depth-penetration, compared to conventional acoustic sources. The inclusion of horizontal components with conventional vertical-component recording leads to inexpensive acquisition of valuable mode-converted shear-wave (P-S) data with a conventional seismic source. Converted shear-wave reflections (P-S) have smaller reflection angles than P-wave reflections and more information can thus be acquired in a relatively smaller aperture. Shear waves converted from incident P-waves allow

estimation of the elastic parameters of the subsurface, which are important in many aspects of reservoir exploration, characterization and exploitation.

The major complexity in processing P-S data is asymmetry of the source-to-receiver raypaths. Conventional common-mid-point (CMP)-based processing techniques can not be used. Instead, common-conversion-point (CCP) binning-based processing should be performed. Birefringence analysis (Harrison, 1993), common-conversion-point (CCP)-binning, P-S NMO correction and velocity analysis (Slotboom and Lawton, 1989; Slotboom, 1990), P-S DMO and migration (Eaton and Stewart, 1991; Harrison, 1993) are necessary.

There has recently been an increased utilization of P-S arrivals in anisotropy analysis (Thomsen, 1999; Bale et al., 1998). Depth-migration of P-S data for subsalt imaging and in anisotropic media has been discussed by several authors (Sekulic et al., 1998; D'Agosto et al., 1998; Caldwell et al., 1998; Sollid et al., 1996). True-amplitude prestack imaging of P-S data has also been discussed (for example, Nicoletis et al., 1998). Extending from land 3C acquisition technology, ocean-bottom-cable acquisition -- which consists of 3C geophones and hydrophones -- can directly record P-S data and this technology has many advantages over marine acoustic surveys. The processing difficulties caused by water-bottom multiples can be more delicately and accurately handled by utilizing the pressure data recorded by hydrophones.

Converted-wave data acquired over complex geology presents great challenges to CCP binning that assumes a laterally invariant velocity field. Difficulties are also evident with P-S DMO and migration. These conventional processing steps are reviewed in this

chapter, followed by a review of the elastic-wave extrapolation theory. The Fourier-domain wavefield extrapolation theory, which has very successfully handled P-wave data, can be conveniently applied to converted-wave prestack depth imaging, as this chapter shows. The 3C-2D data set from the 1997 Blackfoot converted-wave survey is used for demonstration.

5.2 CONVENTIONAL CONVERTED-WAVE PROCESSING

Figure 5.1 shows a routine P-S processing flow (Harrison, 1993). The vertical-component data is routinely processed before P-S processing to provide initial velocity information and source-side statics solutions. For 2D split-spread acquisition, polarity is reversed on the recorded radial component on both sides of the source. Data on either side of the source, normally the trailing spread, must be polarity-reversed in order that the energy does not stack destructively.

Velocity anisotropy often causes shear-wave birefringence (Justice et al., 1987; Martin et al., 1986; Kramer and Davis, 1991). With converted-wave data, the presence of vertical birefringence can cause shear-wave energy to be recorded on both horizontal components (MacBeth and Crampin, 1991), resulting in a decrease in the S/N ratio of the radial channel. The fast and slow components can both contribute energy to a recorded radial or a transverse channel. This can, potentially, cause destructive interference and greater difficulty in interpretation. Various techniques have been developed for shear-wave birefringence-analysis (e.g., Schulte and Edelmann, 1988; MacBeth, 1990).

CCP binning is an important step in P-S data processing. It is easily shown that, in general, the lateral position of a conversion-point varies with depth when the offset is constant (Chung and Corrigan, 1985; Tessmer and Behle, 1988; Eaton et al., 1990). For small offset/depth ratios, the asymptotic CCP-binning approximation is usually adequate. A more accurate method of CCP-binning utilizes the depth-variant binning algorithm (Tessmer and Behle, 1988; Eaton et al., 1990).

For flat reflections, the P-S moveout curves are hyperbolic to the first order (Tessmer and Behle, 1988) and standard velocity analysis tools can be used to obtain a stacking velocity function (Taner and Koehler, 1969). With P-wave velocity obtained from the conventional P-P data, the shear-wave velocity can be calculated.

P-S dipping-moveout correction (P-S DMO) is necessary in regions of complex structure in order to reduce the destructive interference caused by dipping events (Deregowski and Rocca, 1981). The algorithm is more complicated than the conventional P-P DMO; Harrison (1993) gives a complete description.

A P-S stack section can be migrated to improve focusing. The time-coordinate of a zero-offset P-S stack section is the zero-offset traveltimes with P-wave down and S-wave up. The P-S diffraction curves on a zero-offset P-S section are approximately hyperbolic to the first order (Harrison, 1993) and this suggests that the migration can be achieved in a fashion similar to conventional P-P zero-offset migration.

Prestack-migration and migration-velocity-analysis of P-S data have been addressed by many authors, recently (e.g., Bale et al., 1998; Nicoletis et al., 1998; Zanzi, 1996; Sollid, et al., 1996; Caldwell et al., 1998; Li et al., 1998; Sekulic et al., 1998; D'Agosto et

al., 1998; Hoffe and Lines, 1998). Most approaches are Kirchhoff-summation algorithms similar to conventional P-P algorithms. P-S raytracing instead of P-P raytracing is carried out to compute the traveltimes curves. Samples along a traveltimes curve are then scaled by amplitude correction factors and then summed. In complex media, the difficulties encountered in P-P raytracing -- chaotic rays, for example -- are more likely to occur with P-S raytracing, since the P-S velocity-contrast is normally larger than P-P velocity-contrast. Fourier-domain imaging techniques, which have many advantages in the P-P cases, have similar advantages in the P-S case, especially in complex media.

5.3 P-S WAVE REFLECTION AT A SOLID-SOLID BOUNDARY

Consider an incident P and SV wavefield impinging on a solid-solid boundary between two isotropic, homogeneous media in welded contact. The parameters describing each of the media are α_j , β_j , ρ_j , λ_j and μ_j , where $j=1$ corresponds to the upper medium and $j=2$ corresponds to the lower media. α_j , β_j , ρ_j are P-wave velocity, S-wave velocity and density, respectively. λ_j and μ_j are Lamé elastic parameters. The wavefields occurring at the boundary as results of incident elastic wave-trains from both above and below the boundary, are shown in **Figure 5.2**. Mathematical description of these wave modes can be found in much of the literature of elastic wavefield propagation (e.g. Aki and Richard, 1980).

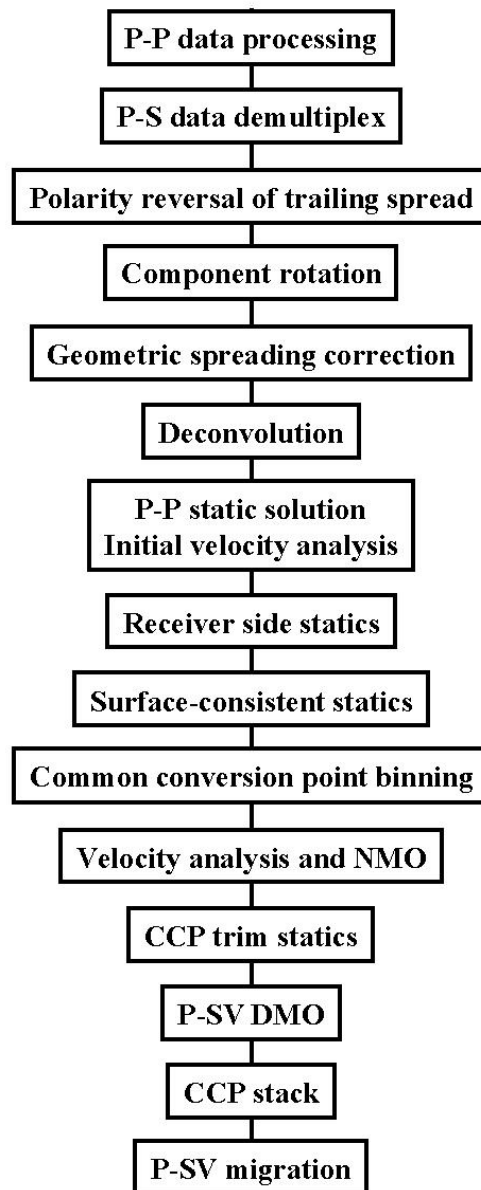


Figure 5.1 Conventional P-S data processing flow (Harrison, 1993).

Acoustic-wavefield extrapolation is a simplification of the elastic-wave propagation theory ignoring the shear wavefield. By further ignoring the multiple wavefield, the recorded primary-only acoustic wavefield can be expressed with the WRW model (Berkhout, 1981), where W represents the acoustic wave propagator and R represents the P-P reflection response. The primary-only converted-wave reflection can be expressed in a similar way. Let W_P stand for the downgoing P-wavefield propagator, C stands for the P-to-S conversion coefficients and W_S stands for the primary upgoing S-wavefield propagators, the physical process of P-S conversion can then be expressed as a $W_P C W_S$ model (**Figure 5.3**)

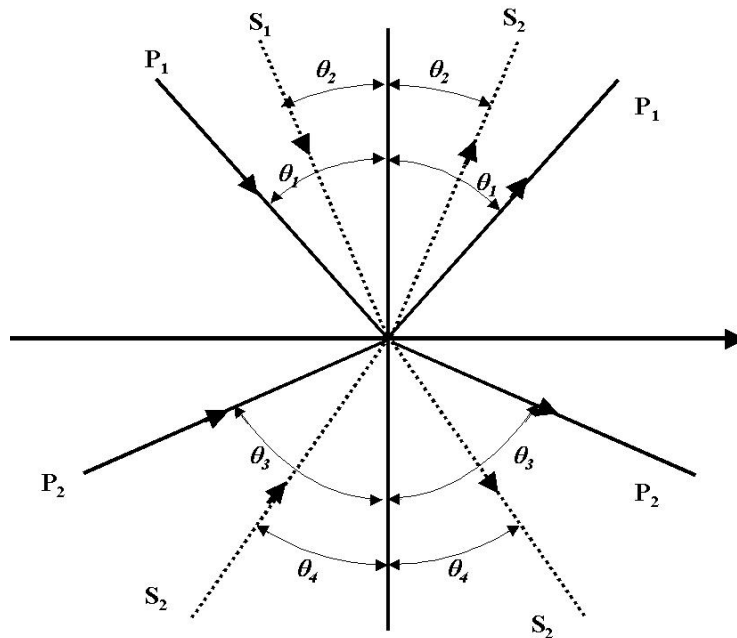


Figure 5.2 Incidence of a P- or SV-wave from medium 1 or medium 2. The angles θ_i , ($i=1, 2, 3, 4$) are related to the ray-parameter or horizontal-slowness p by the relation $p = \sin \theta_1 / \alpha_1 = \sin \theta_2 / \beta_1 = \sin \theta_3 / \alpha_2 = \sin \theta_4 / \beta_2$.

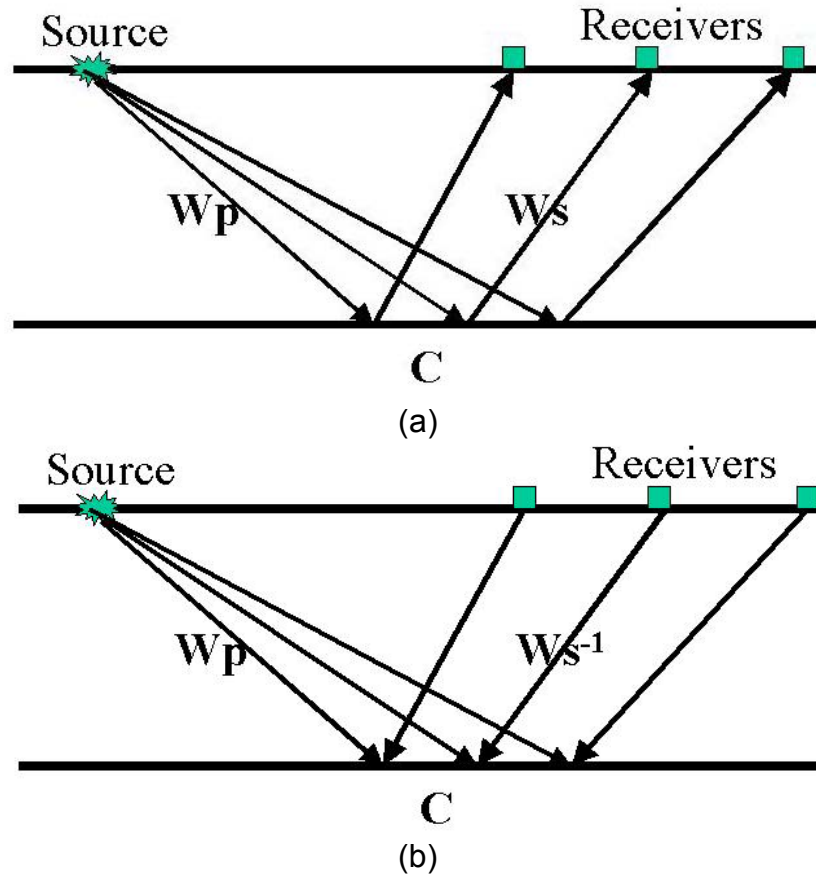


Figure 5.3 The $W_p C W_s$ model (a) for converted-wave reflection at a horizontal boundary; (b) Depth imaging of the boundary involves forward extrapolation of the source signature and inverse extrapolation of the recorded, primary-only, P-S data.

The converted-wave imaging condition has not been discussed in depth in geophysical literature. However, the formula can be expressed in a form similar to that of the P-P imaging condition. For a monochromatic plane wave, at any particular depth, the P-S conversion coefficient at a boundary can be expressed as the ratio between the S-wavefield immediately above the conversion boundary after mode conversion and the P-wavefield immediately above the boundary before mode conversion. To avoid frequency-dependence, an average of all the conversion coefficients computed from all the frequency slices is taken as an appropriate estimation of the conversion coefficients. The conversion coefficients can be written as,

$$\tilde{r}(x, z) = \frac{1}{[\omega_{\max} - \omega_{\min}]} \int_{\omega_{\min}}^{\omega_{\max}} \left\{ \frac{\psi_c^*(x, z, \omega)}{\psi_p^*(x, z, \omega)} + \frac{\psi_c(x, z, \omega)}{\psi_p(x, z, \omega)} \right\} d\omega \quad (5.1)$$

where ψ_c and ψ_p are the converted shear wavefield and the incident P wavefield. The symbol * denotes complex conjugate.

5.4 INTRODUCTION TO THE 1997 BLACKFOOT 3C-2D SURVEY

The Blackfoot 3C-2D high-resolution survey was conducted in 1997 as a joint effort between the CREWES Project at the University of Calgary, Boyd PetroSearch Consultants Ltd. and PanCanadian Petroleum Ltd. The Blackfoot field is located about 50-55 km east of Calgary, near the town of Strathmore, Alberta (**Figure 5.4**). The producing formation is Lower Cretaceous, cemented glauconitic sand deposited as incised channel-fill sediment above the Mississippian carbonates. The glauconitic sandstone lies at a depth of about 1500 m below the surface and is up to 45 m thick. The average porosity in this producing unit is about 18%. The cumulative production from this formation throughout southern Alberta exceeds 200 MMbbls oil and 400 BCF gas. **Figure 5.5** shows a typical sedimentary sequence of southern Alberta and the blocked P- and S-velocity measured from well 0908 located the middle of the 1997 3C-2D line. **Figure 5.6** shows an isopach of the reservoir and the locations of the wells and the 1997 3C-2D survey.

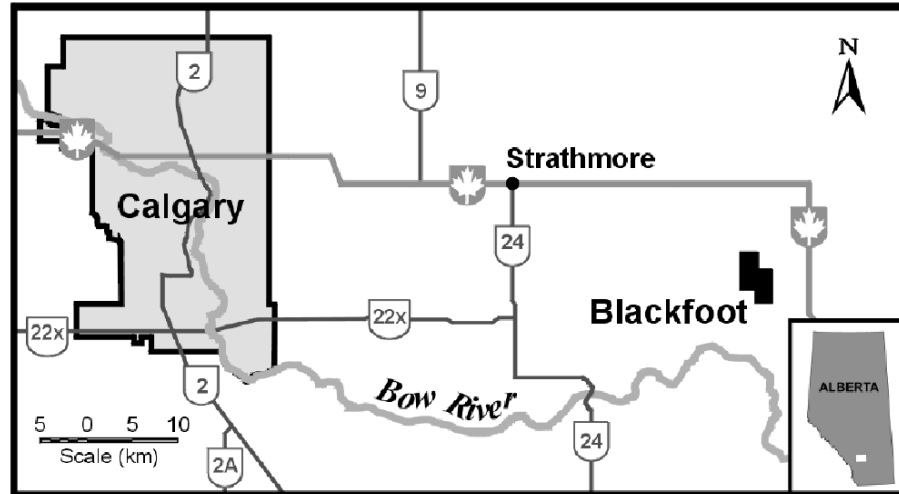


Figure 5.4 Map showing the location of the Blackfoot field where the high-resolution 3C-2D seismic survey was conducted (Courtesy of the CREWES Project, University of Calgary).

The survey involves acquisition of a 3-km 3C-2D reflection profile consisting of a combination of conventional and high-resolution receiver intervals. **Figure 5.6** is also the acquisition basemap of the region. **Figure 5.7** shows a schematic diagram of the acquisition geometry. The source interval employed for the entire 2D-profile was 20 m, shot on the half stations. The survey also involved simultaneous recording into 63 buried 3C geophones situated in 6-, 12- and 18-m holes, drilled every 50 m along the central kilometer of the profile. In addition to these buried geophones, a 48-channel vertical-hydrophone cable with a 2-m receiver interval was deployed in a 100-m cased hole located in the center of the profile. A walk-away VSP was also simultaneously recorded in PanCanadian's 100/09-08-23-23W4 well, located near the center of the spread, by recording the full range of offsets for each tool position.

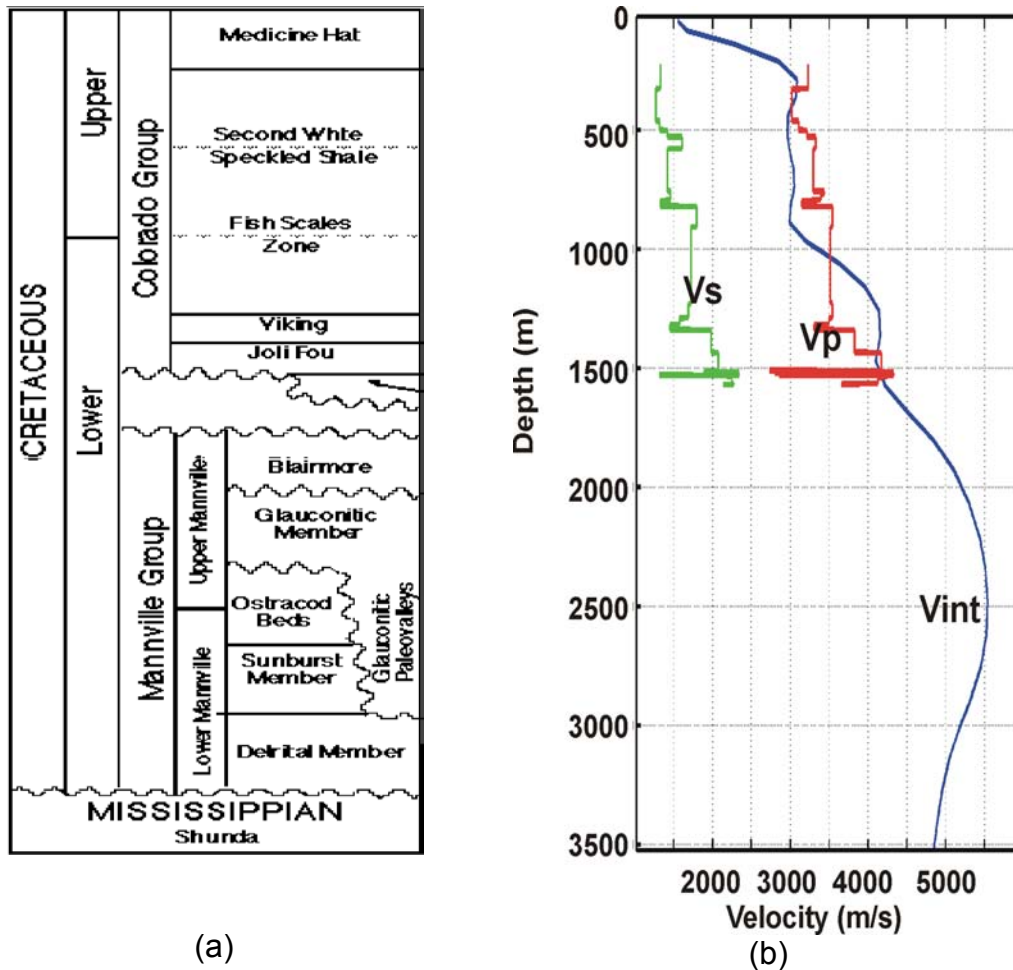


Figure 5.5 (a) The sedimentary sequence of southern Alberta (a) and the blocked V_p and V_s from well L0908. Light gray and dark gray solid lines denote the V_s and V_p , respectively. (b) Interval velocity (V_{int}) computed from seismic velocity analysis of the P-wave data is also shown as a solid black line in.

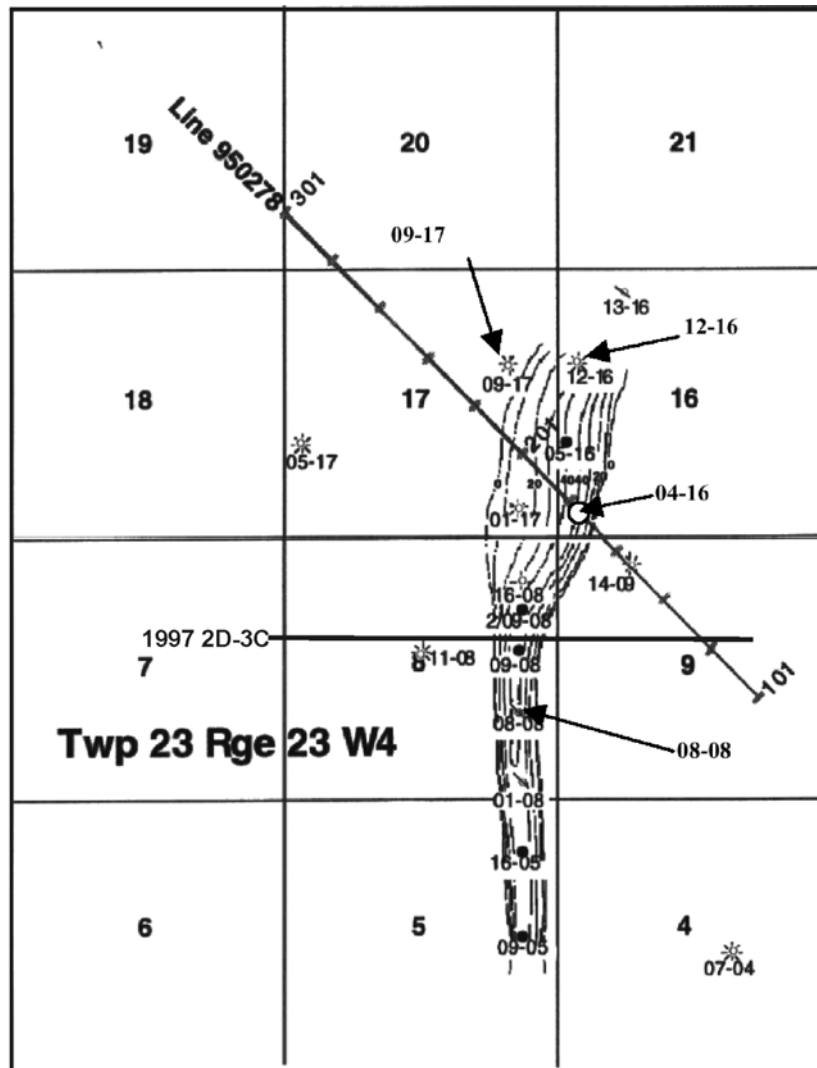


Figure 5.6 Isopach of the Blackfoot Galuconitic incised valley (Miller et al., 1995). The line of dashes represents the isopach; the contour interval is 10 m. The 1997 3C-2D line is roughly perpendicular to the glauconite channel. Line 950728 was shot in 1995.

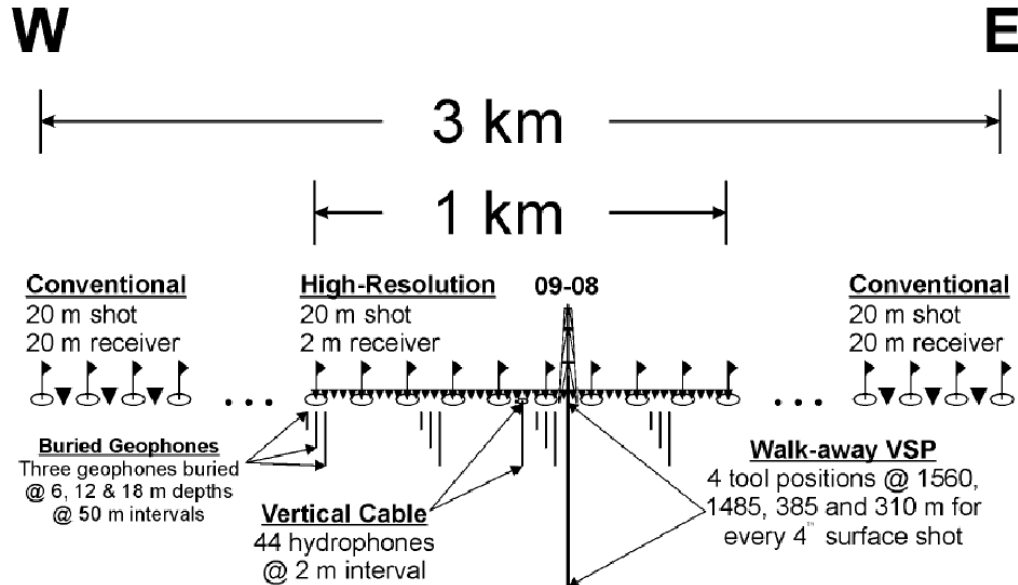


Figure 5.7 Acquisition geometry of the 1997 Blackfoot survey.

Topographic variation across the line is rather mild. The elevation difference between the highest point (west of the line) and the lowest point (roughly around 2100 m from the left end of the line) is only about 40 m (**Figure 5.8**). However, considering the low near-surface velocity and the fact that V_s is normally much lower than V_p , the receiver-elevation statics are often sufficiently large to degrade stacking. A floating datum is often used in such cases. Migration from topography or from a floating datum is thus required for converted-wave prestack depth imaging.

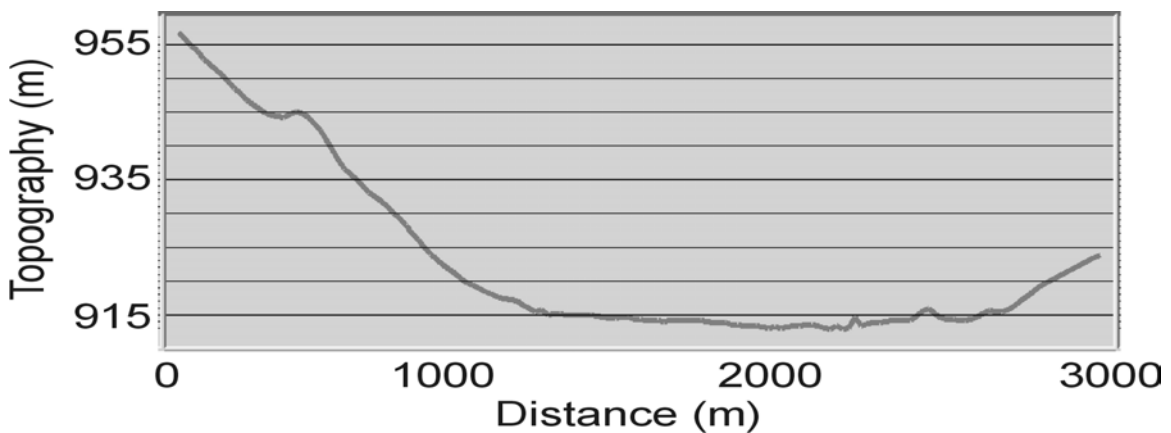


Figure 5.8 Topographic variation across the line.

5.5 PRESTACK DEPTH IMAGING FROM TOPOGRAPHY OF THE VERTICAL AND RADIAL COMPONENT

Velocity model

The 3C-2D line acquired in 1997 was previously processed by Cieslewicz and Lawton (1998) and several issues were discussed. Since the geology in the Blackfoot region lacks structural deformation and the strata are almost flat, a $v(z)$ velocity function should give a fairly good approximation to the velocity field, across the line. The log from the well 09-08 is used to determine the $v(z)$ function. Since the well log ran from about 220 m below the topography to a depth of 1560 m, the P-wave velocity function from the surface to 200 m and the velocity below 1560 m is approximated with the interval velocity computed from the stacking velocity obtained from P-P velocity analysis. The S-wave velocity function outside of the logging interval, however, is determined from a statistical relationship between the V_p and V_s within the logging interval. **Figure 5.9** shows the V_p - V_s cross-plots from the well 09-08. Note that the cross-plot of the overall logging intervals shows two V_p - V_s variation trends. The dominant trend, as plotted with a solid black line, can be written as

$$V_s = 0.9286V_p - 1592.9, \quad (5.5)$$

where the V_p and V_s are in m/s. The secondary trend is that V_s does not change much while V_p increases dramatically, as highlighted with ellipses, and appears only in the

shallow part of the well log. To illustrate this, the well log is divided into four intervals: 220 to 550 m, 550 to 900 m, 900 to 1250 m and 1250 to 1560 m. The V_p - V_s cross-plots are also shown in **Figure 5.9**. Note that this secondary trend disappears below 900 m. The S-wave velocity model outside of the logging interval can then be computed from the interval velocity as shown in **Figure 5.5**.

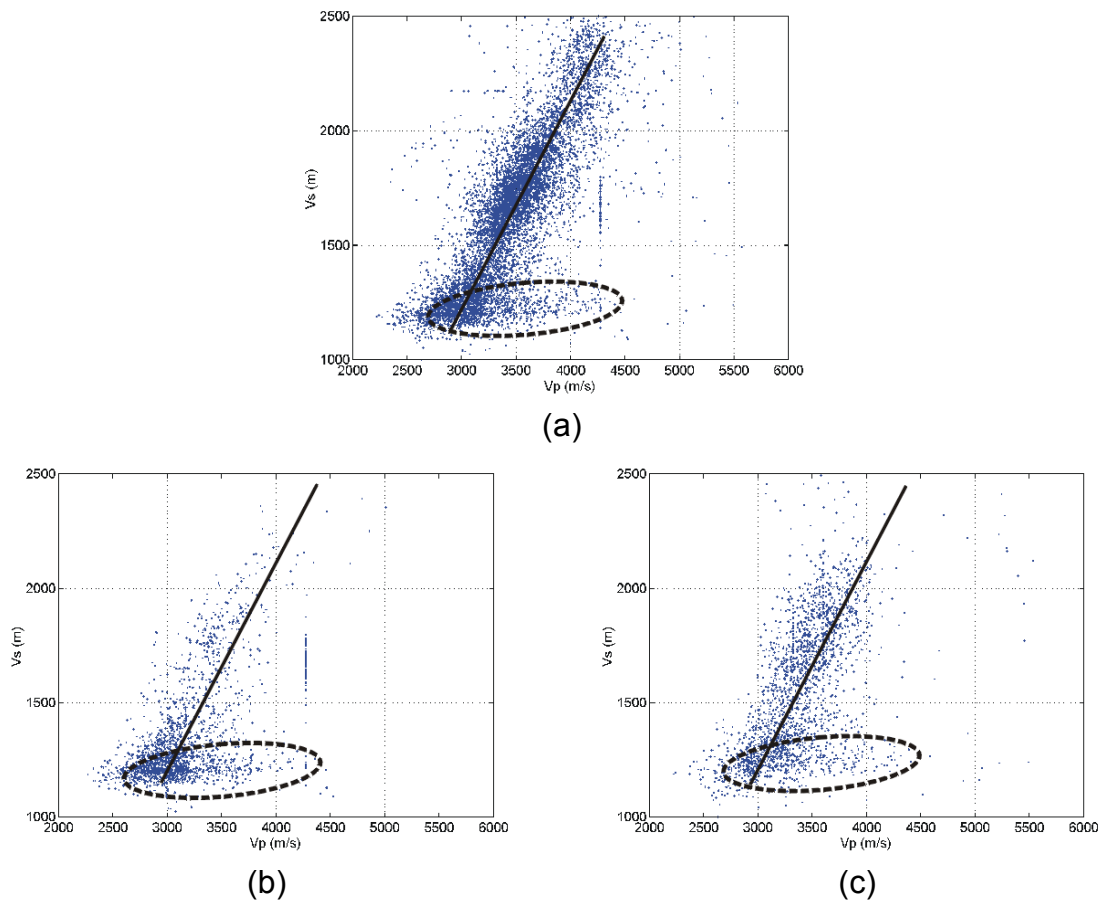


Figure 5.9 (continues)

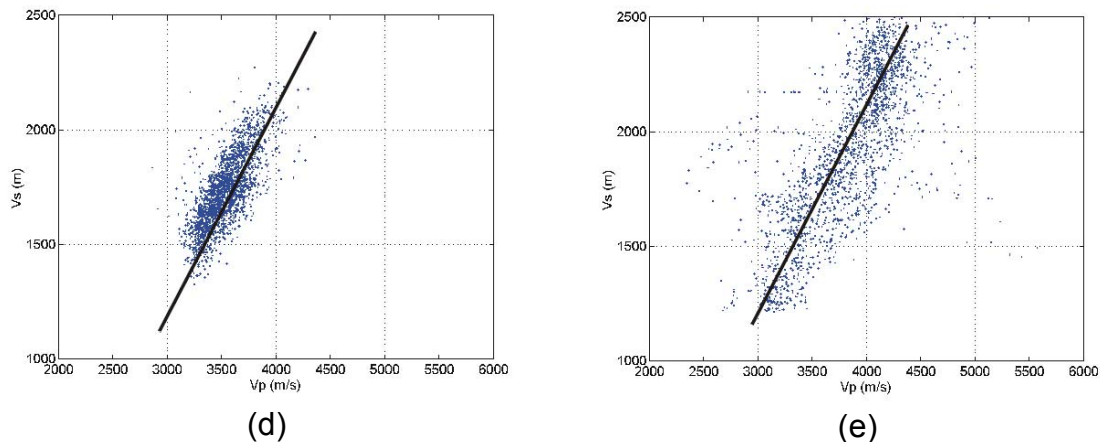


Figure 5.9 V_p - V_s cross-plots of well log 0908: (a) cross-plot of all the V_p and V_s in the logging interval, (b) cross-plot of the interval from 220 to 550 m, (c) from 550 to 900 m, (d) from 900 to 1250 m and (e) from 1250 m to 1560 m. The solid black lines depict the dominant V_p - V_s relationship. The elliptical line of dashes highlights erroneous measurements.

Figure 5.10 shows the P- and S-wave velocity-depth model built with both the L09-08 well log and the seismic interval velocities. The media are mainly $v(z)$, except for the velocities interpolated from 220 m below the well-head elevation to the topography using the V_p - V_s relationship previously discussed.

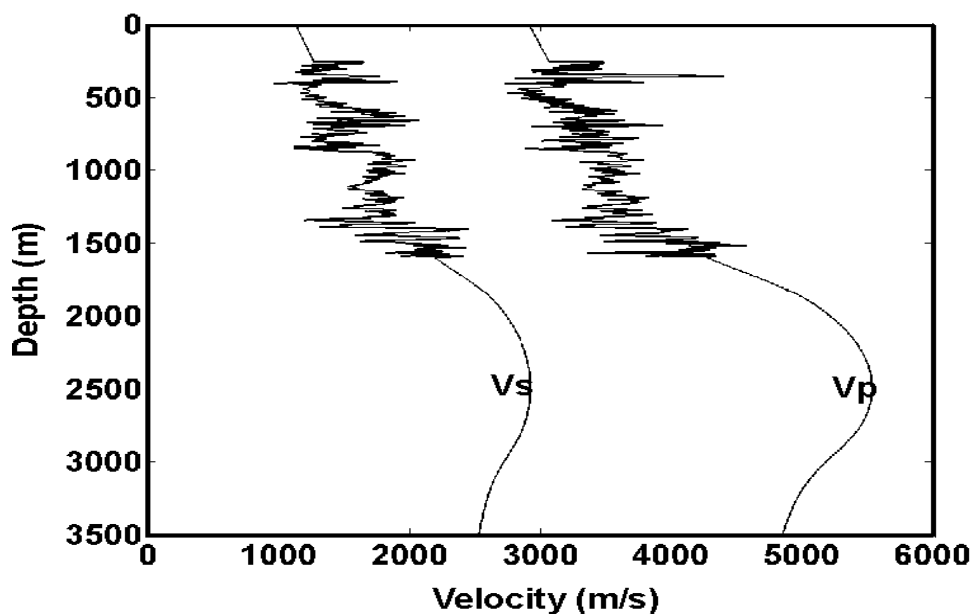


Figure 5.10 V_p and V_s velocity-depth models built by combining the log measurement, the interval seismic velocity and the statistical relationship of equation (5.5). Solid white lines denote topography.

Adjustment of source positions with linear spatial phase-shift

The source locations of the 1997 Blackfoot data acquisition are at half-stations. This created some problems since Fourier-domain algorithms require that source locations coincide with receiver stations. This problem can be approximately solved by spatially shifting the source location to an adjacent receiver location by linear spatial phase-shift before downward extrapolation of the source signature. A spatial shift is equivalent to a linear phase-shift in the wavenumber domain. This is similar to the instance of a static time-shift being equivalent to a linear phase-shift in the frequency domain. A lateral shift of a mono-frequency wavefield at the surface can be written as

$$\psi(\omega, x + \Delta x, z = 0) = \frac{1}{2\pi} \int_{-\infty}^{+\infty} \varphi(\omega, k_x, z = 0) e^{-ik_x(x+\Delta x)} dk_x, \quad (5.6)$$

where $\varphi(\omega, k_x, z = 0)$ is the spatial Fourier transform of $\psi(\omega, x + \Delta x, z = 0)$,

$$\varphi(\omega, k_x, z = 0) = \int_{-\infty}^{+\infty} \psi(\omega, x, z = 0) e^{ik_x x} dx, \quad (5.7)$$

and Δx is the distance of lateral shift. **Figure 5.11** shows a wavelet before and after a 10-m spatial shift to the right.

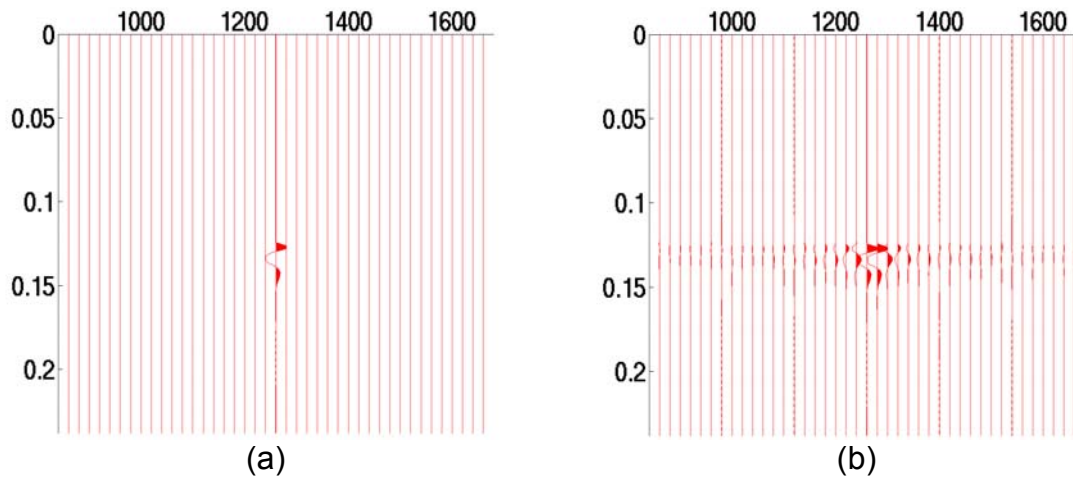


Figure 5.11 A wavelet (a) before and (b) after a 10-m spatial shift to the right. The trace interval is 20 m.

Data preparation

The vertical component has a rather good S/N ratio. **Figure 5.12a** shows shot gather 75, which is located in the middle of the line. A surface-consistent deconvolution was first applied to remove both the source wavelet and the receiver response. A forward shot-gather normal moveout correction is applied to flatten the events so that an f - k filter can be applied to remove most of the ground-roll energy. Time-variant spectral whitening is also applied to further enhance vertical resolution, especially for deep events. A surface-consistent residual-statics correction was applied to enhance the event coherency. The long-wavelength statics are removed after residual statics are applied. The data from the foregoing can be seen in **Figure 5.14**.

For P-S data, the two horizontal components are rotated first to form the radial component. Polarity of the data with a negative offset was reversed so that stacking the data with offsets of opposite signs would not cancel each other out. **Figure 5.12b** shows shot gather 75 in the middle of the line. Note the low S/N ratio and low resolution. The signal-processing flow applied to the radial component is roughly the same as the P-P flow, with parameters adjusted to fit the shear-wave data.

Since hand statics plays a crucial role in the data processing, they were selected and applied after application of the shear-wave elevation statics and refraction statics. Statics corrections bring the data to a floating datum different from the true surface topography. Migration from the floating datum, rather than from the topography, was used. The P-S data, subsequent to the above processing flow, are shown in **Figure 5.15**. As a summary,

the preprocessing flows for the vertical- and radial-components data are shown in **Figure 5.13**.

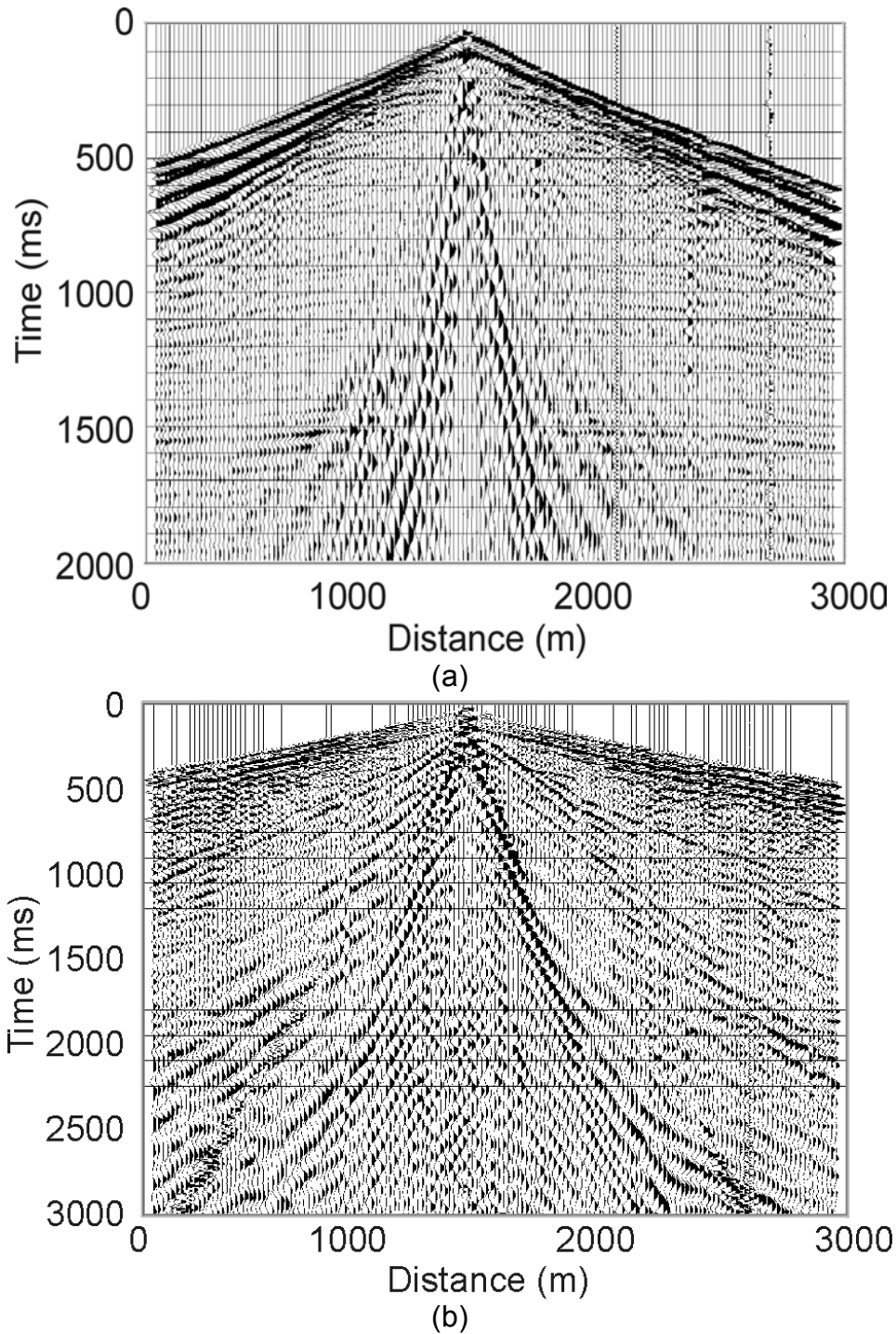


Figure 5.12 (a) Vertical-component shot gather 75 with 2000 ms AGC and (b) radial component shot gather 75 with 1000 ms AGC.

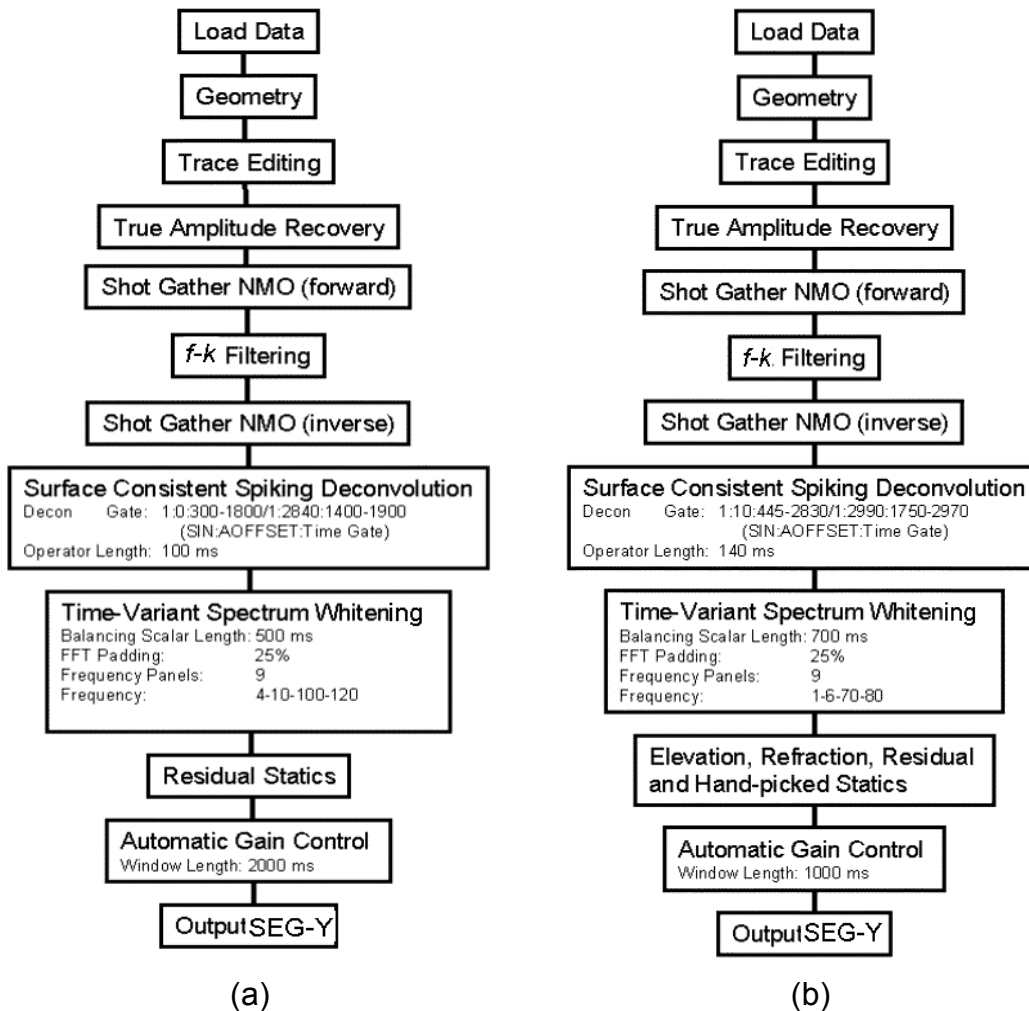


Figure 5.13 (a) Preprocessing flow and parameters for the vertical component data and (b) preprocessing flow and parameters for the radial component data.

Image processing results

A 40-m-step-size PSPI dual algorithm was used. About 30 seconds were required to migrate a shot gather to a maximum depth of 3500 m using an Alpha-XP1000 workstation with 128-MB memory. **Figure 5.14** shows vertical-component shot gathers 10, 75 and 150 after the preprocessing, and the corresponding migration results. **Figure**

5.15 shows the corresponding radial-component shot gathers after the preprocessing and migration results. **Figure 5.16** shows three vertical-component CIGs located at 500, 1500 and 2500 m of the line and **Figure 5.17** shows the corresponding radial-component CIGs. Each CIG is stacked to produce the final P-P depth image and P-S depth image. **Figure 5.18** and **5.19** show the P-P depth image and the P-S depth image, respectively.

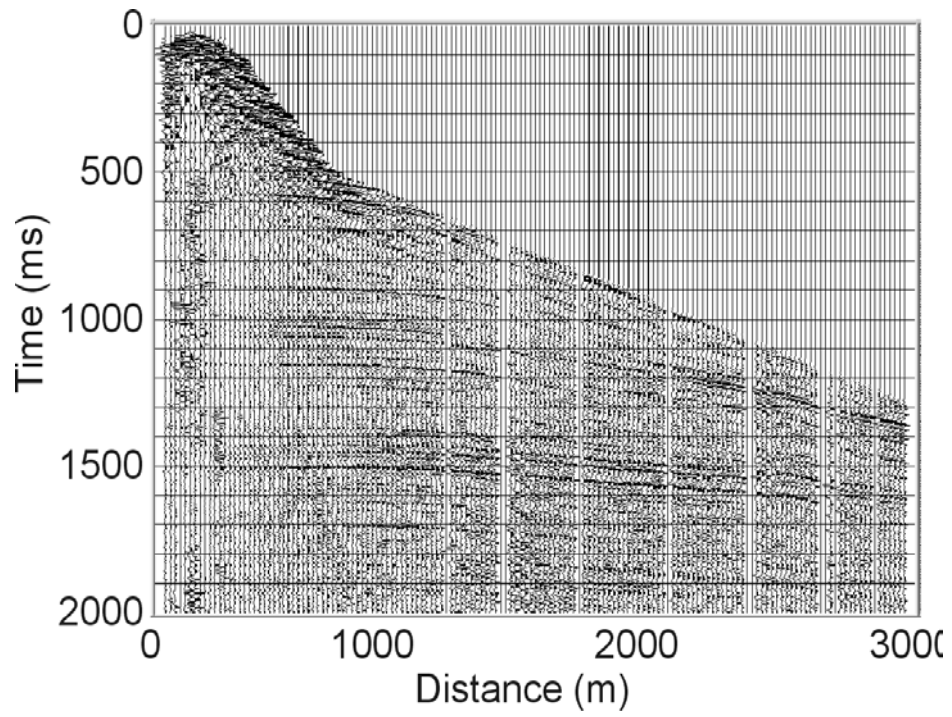
5.6 CORRELATION OF P-P AND P-S DEPTH IMAGES

It is usually difficult to correlate a P-P time-section and a P-S time-section given the uncertainty in the velocity models. The same difficulty also exists in depth-section correlation analysis because the prestack depth imaging is more sensitive to velocity errors. The events in **Figure 5.17a** and **c** still curve slightly upward, and this indicates that the modeled shear velocities are probably slower than the actual values. This can be roughly corrected by slightly increasing the shear-wave velocities; a more scientific approach is to use migration-velocity-analysis to obtain a more accurate velocity model. **Figure 5.20** shows the correlation analysis of the P-P image and P-S image. The central part of the P-P image is replaced with the P-S image. Note that the shallow part has good correlation, the events at 300, 950 and 1550 m for example, while the events in the deeper part are mistied.

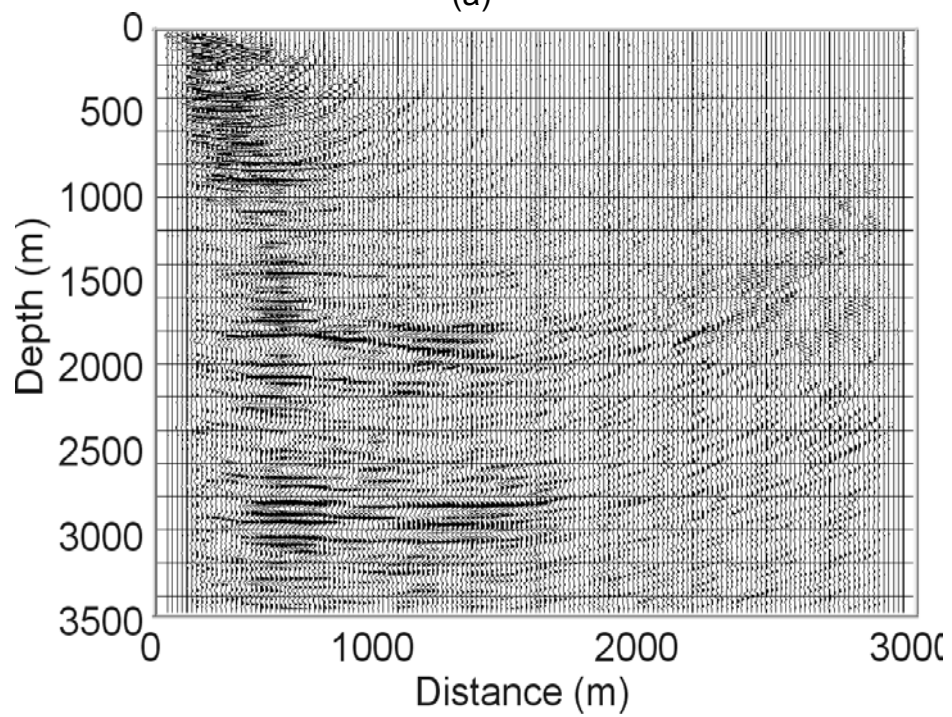
5.7 CHAPTER SUMMARY

In this chapter, the theory of elastic wave-propagation at a solid-solid boundary is reviewed. This review provides the theoretical foundation for elastic-wave extrapolation and converted-wave imaging. The W_pCW_s wave-propagation model for converted-wave imaging is proposed. Automatic common-conversion-point (CCP)-binning occurs in each step of the wavefield extrapolation so that the algorithm is very adaptable to V_p/V_s varying in both the vertical and horizontal directions at no further computational cost. This is potentially better than the raytracing-based CCP-binning with a single V_p/V_s value.

The 1997 Blackfoot 3C-2D line was used for testing. Data acquisition details are provided. A spatial phase-shift was used to adjust source positions in order to handle source geometry irregularity. Both the log from well 0908 and the interval velocity obtained from the stacking velocities were used to build the depth model. Due to different applications of statics correction, the vertical component data was migrated from the topography, while the radial component was migrated from the floating datum produced by the statics corrections. The P-P depth image-quality is rather satisfying, while the P-S depth-image quality is slightly inferior, due to poor S/N ratios in the original data and errors in the velocity model. The shallow part of the two depth-sections shows rather good correlation while the deep parts are mistied.



(a)



(b)

Figure 5.14 Vertical-component shot gather 10 (a) after the pre-migration processing and (b) after migration.

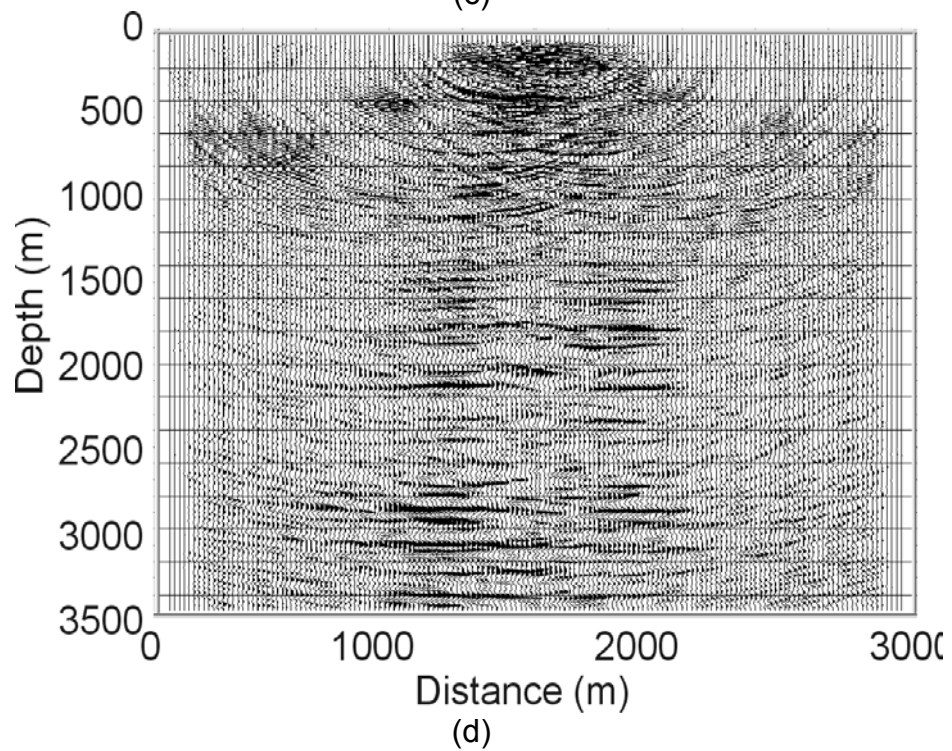
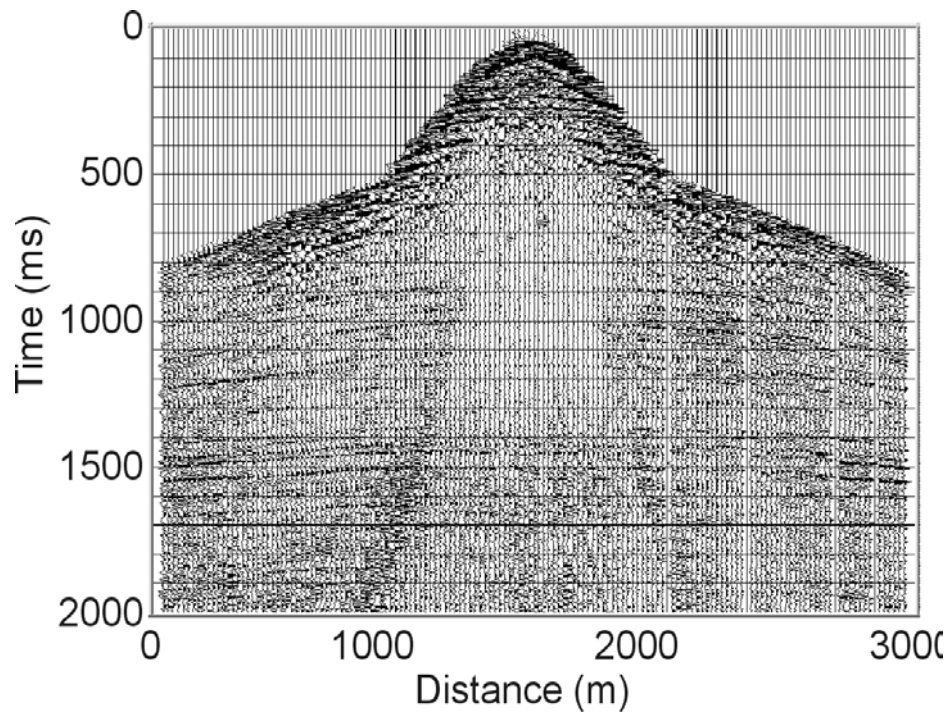
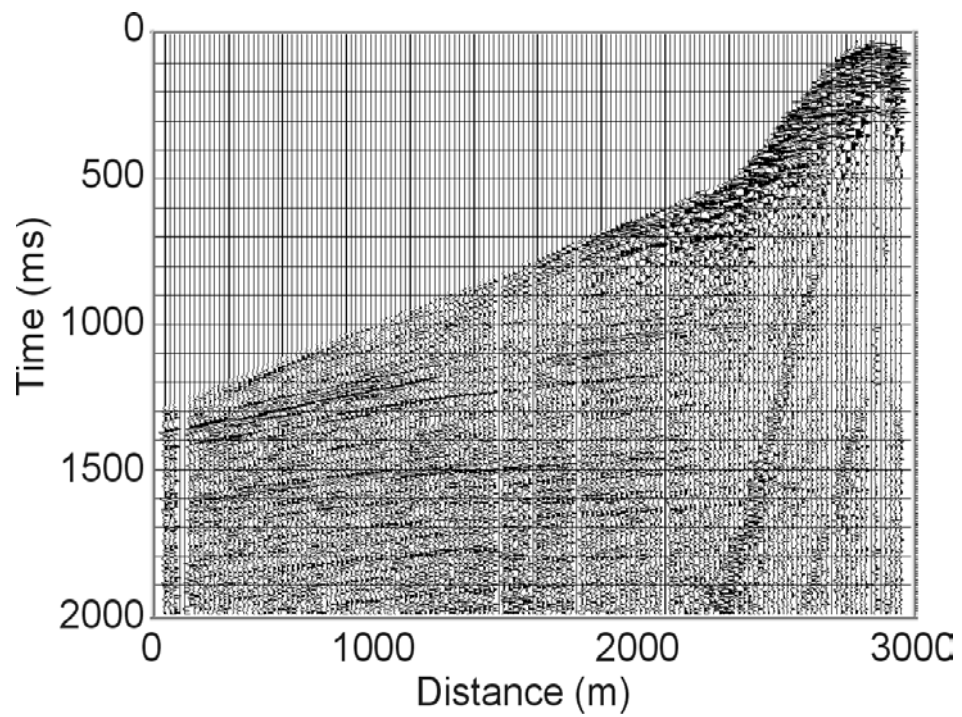
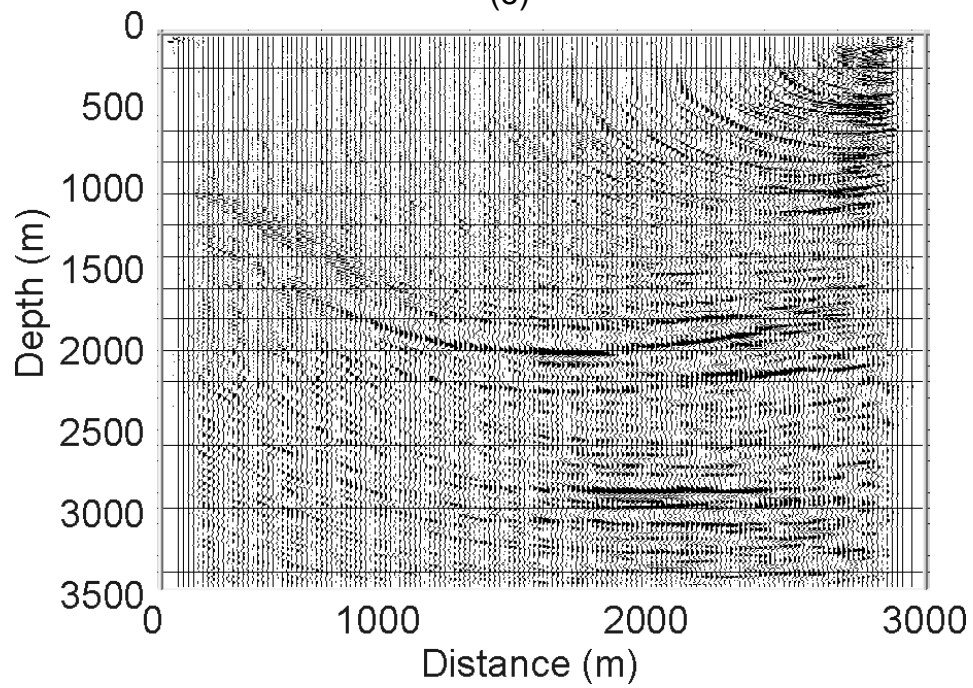


Figure 5.14 (continued) Vertical-component shot gather 75 (c) after the pre-migration processing and (d) after migration.



(e)



(f)

Figure 5.14 (continued) Vertical-component shot gather 150 (e) after the pre-migration processing and (f) after migration.

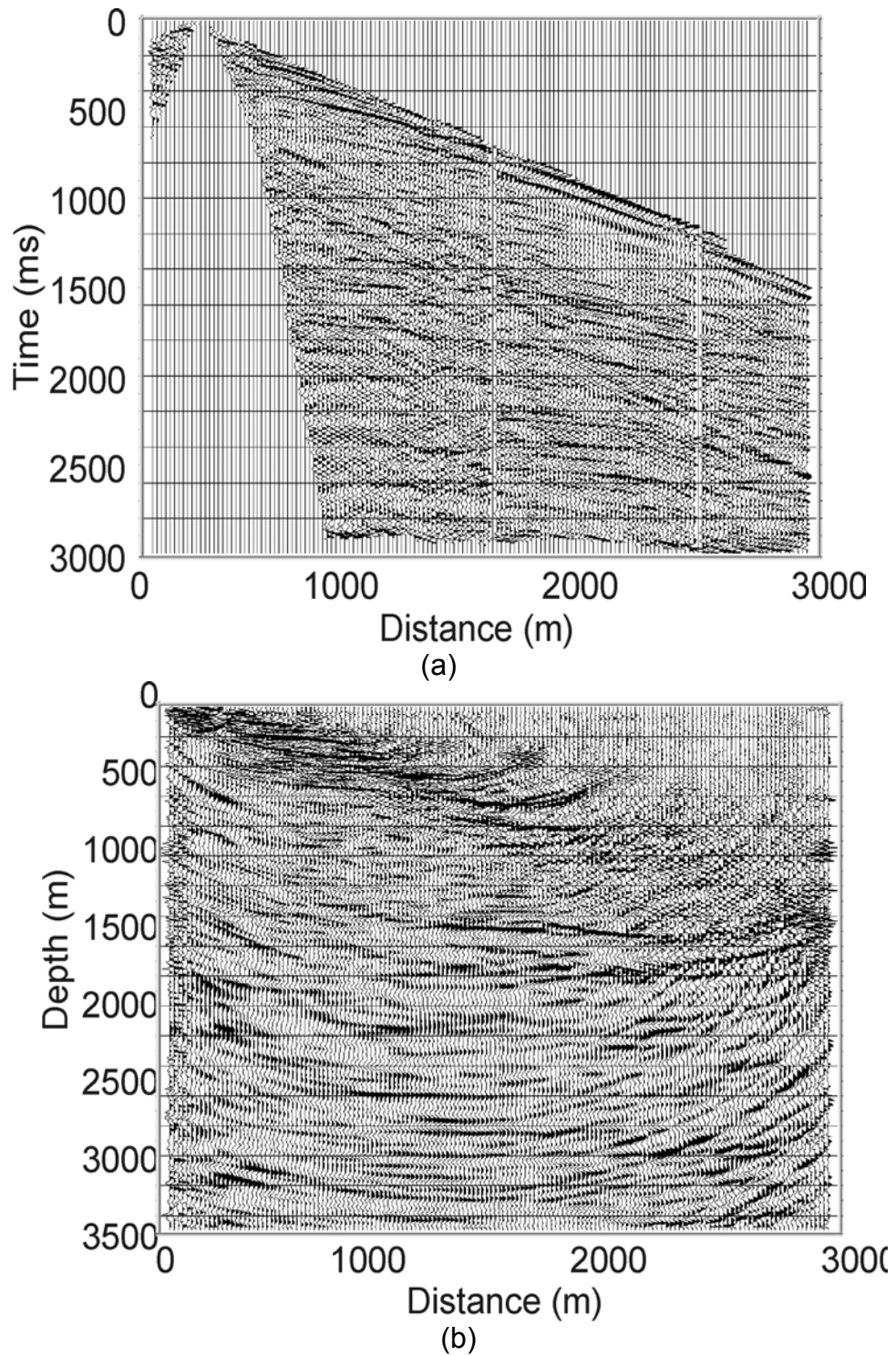
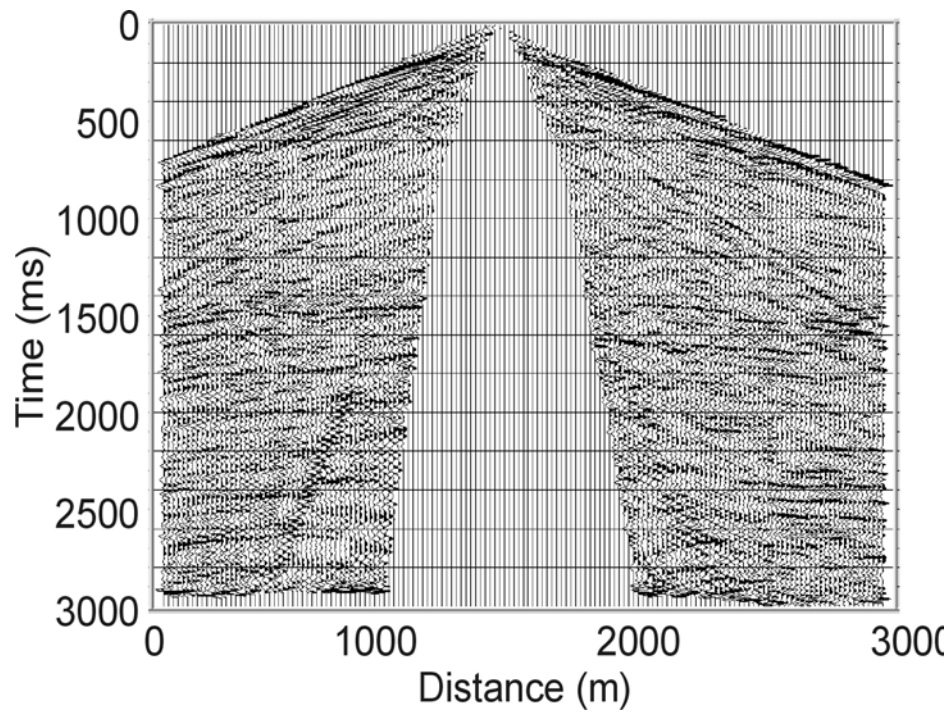
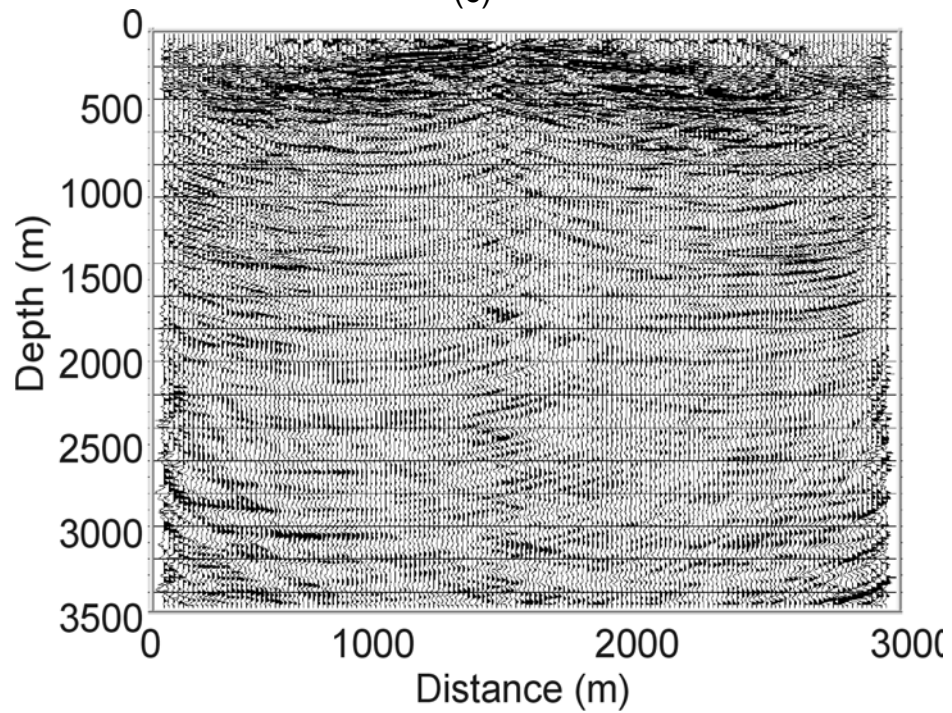


Figure 5.15 Radial-component shot gather 10 (a) after the pre-migration processing and (b) after migration.

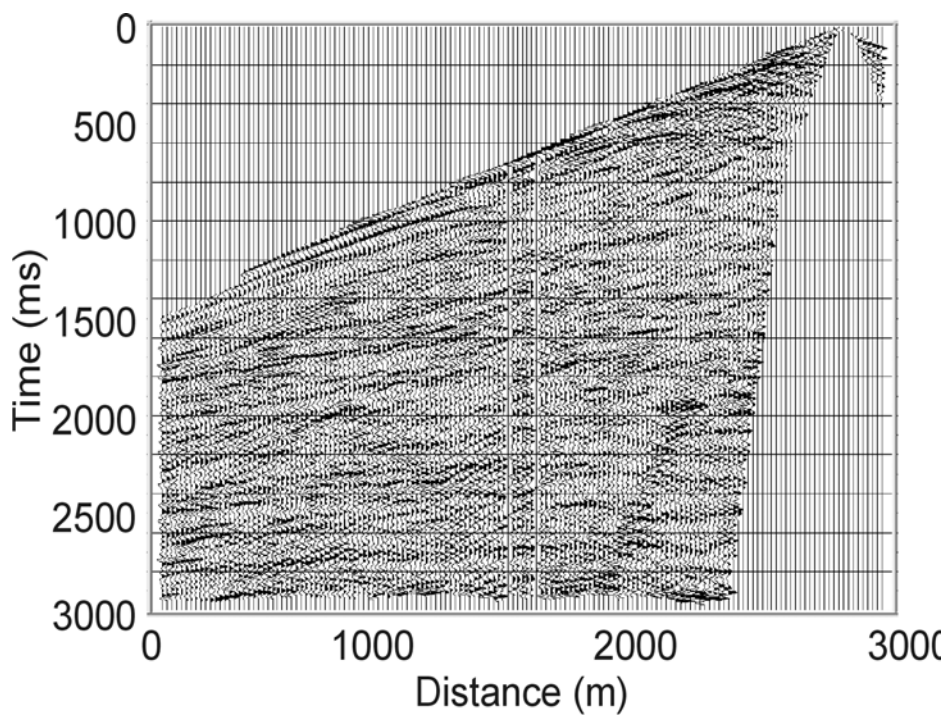


(c)

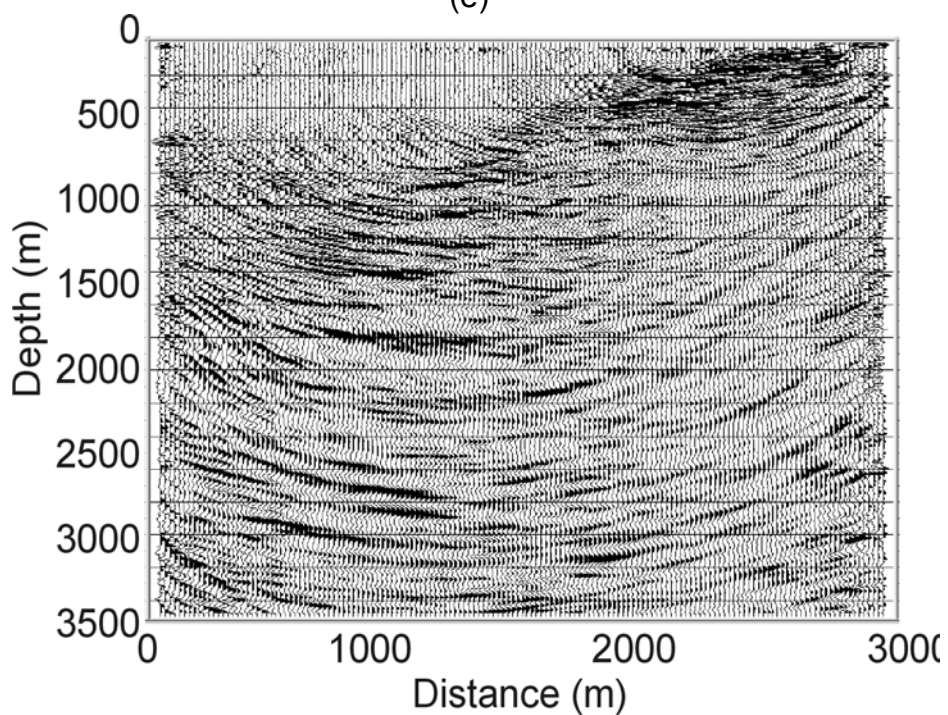


(d)

Figure 5.15 (continued) Radial-component shot gather 75 (c) after the pre-migration processing and (d) after migration.

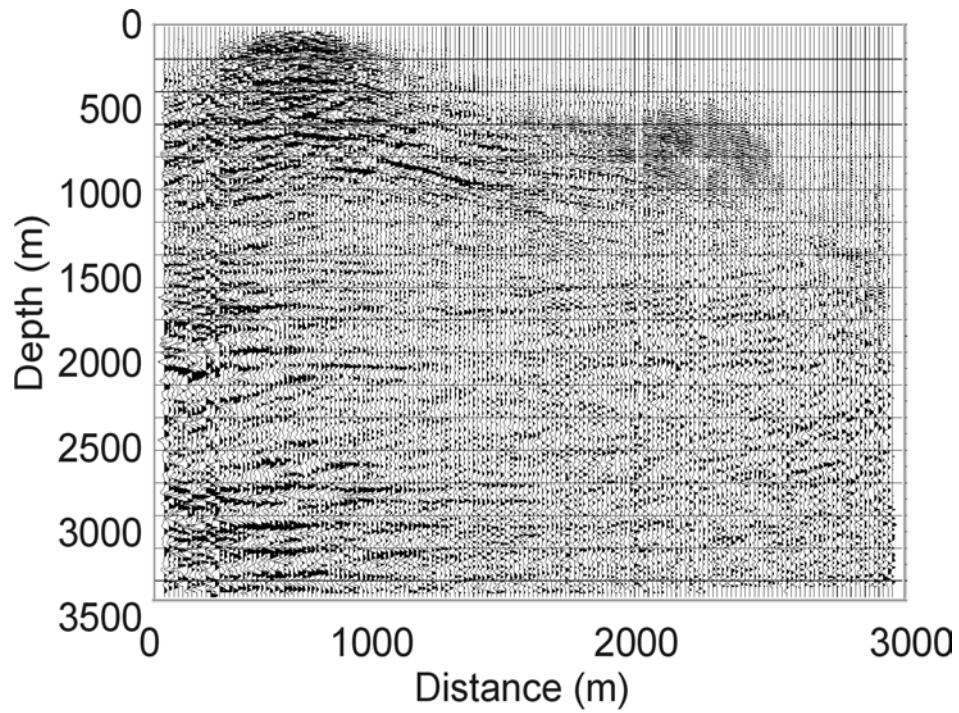


(e)

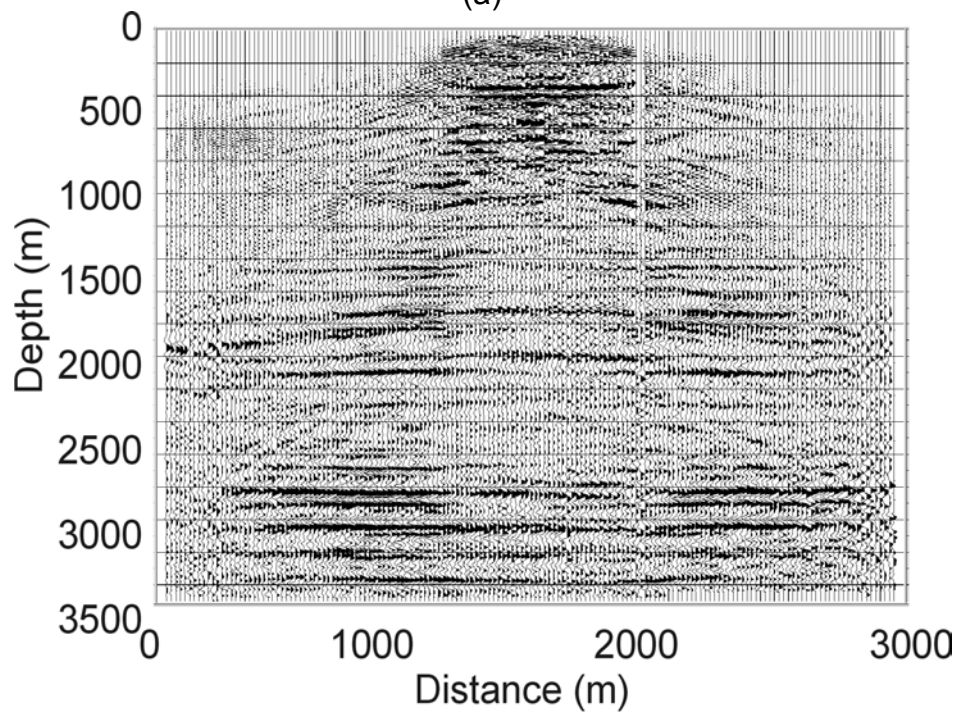


(f)

Figure 5.15 (continued) Radial-component shot gather 150 (e) after the pre-migration processing and (f) after migration.



(a)



(b)

Figure 5.16 Vertical-component CIGs located at (a) 500 m and (b) 1500 m.

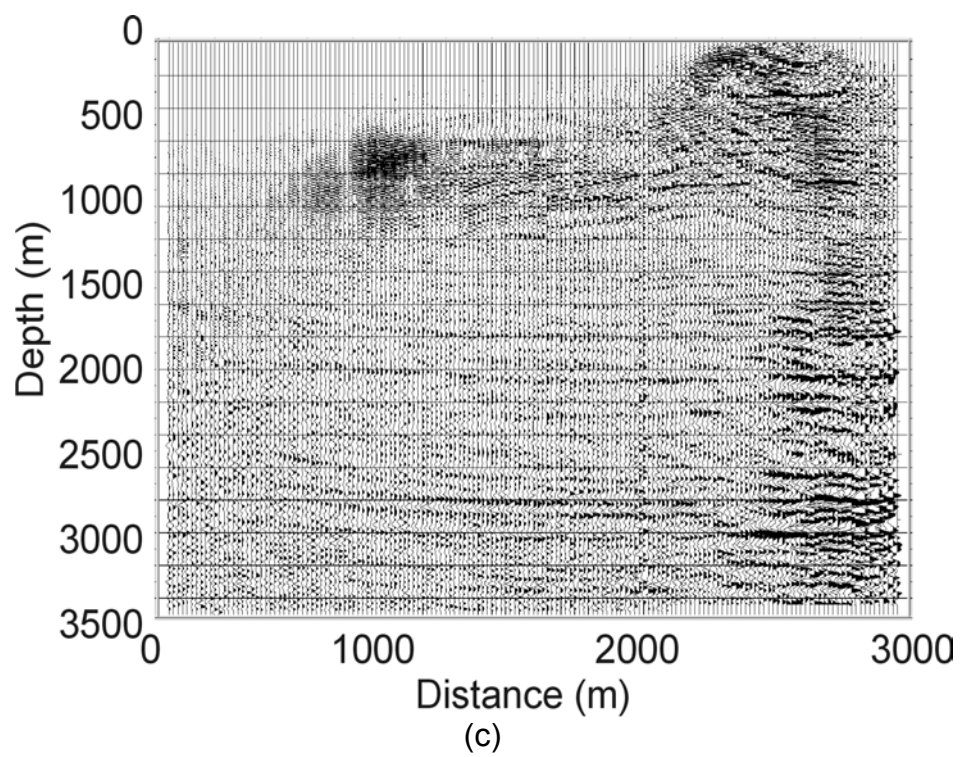


Figure 5.16 (continued) Vertical-component CIGs located at (c) 2500 m.

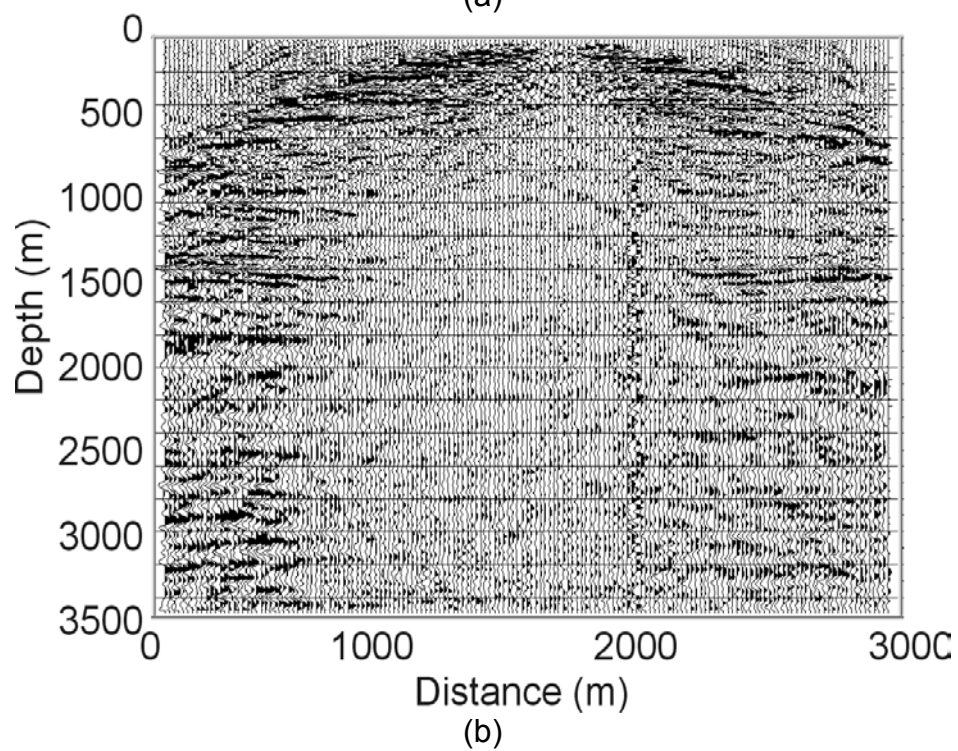
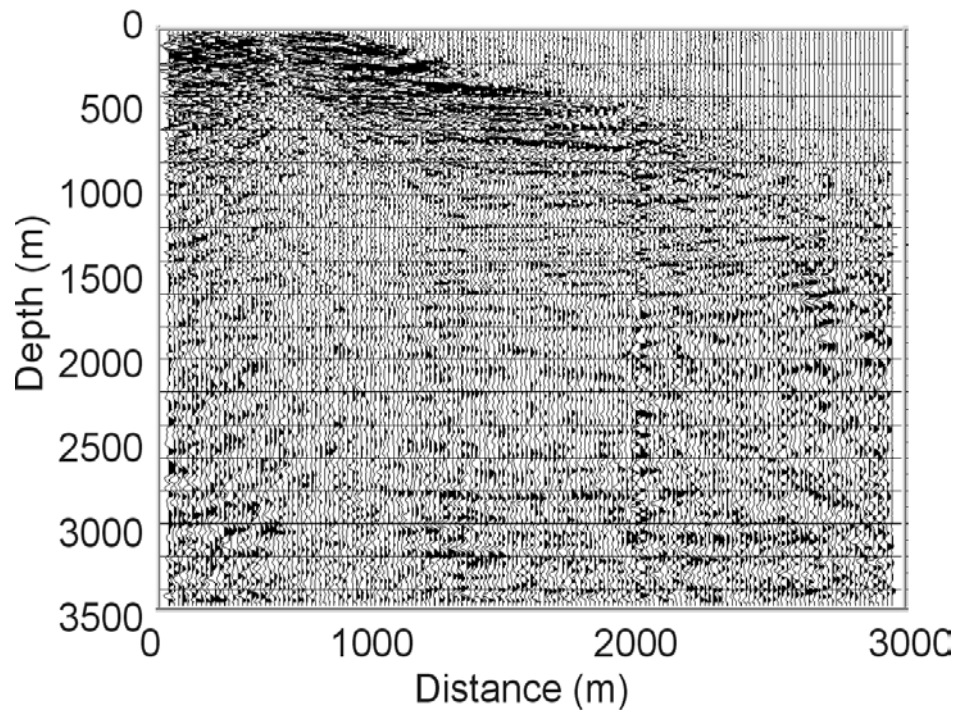


Figure 5.17 Radial-component CIGs located at (a) 500 m, (b) 1500 m.

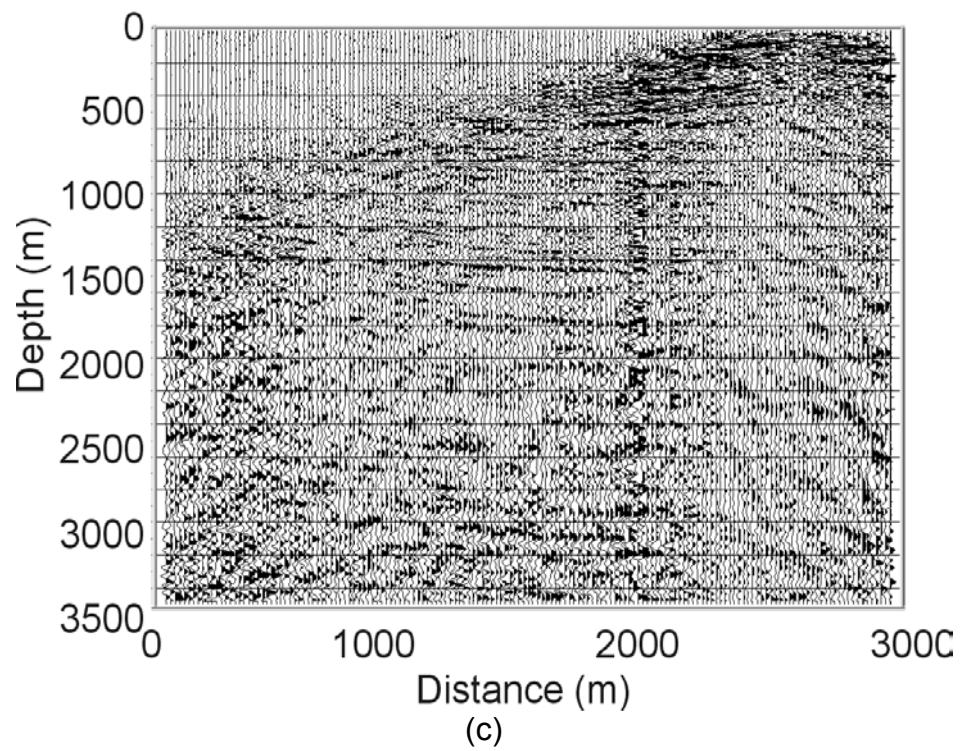


Figure 5.17 (continued) Radial-component CIGs located at (c) 2500 m.

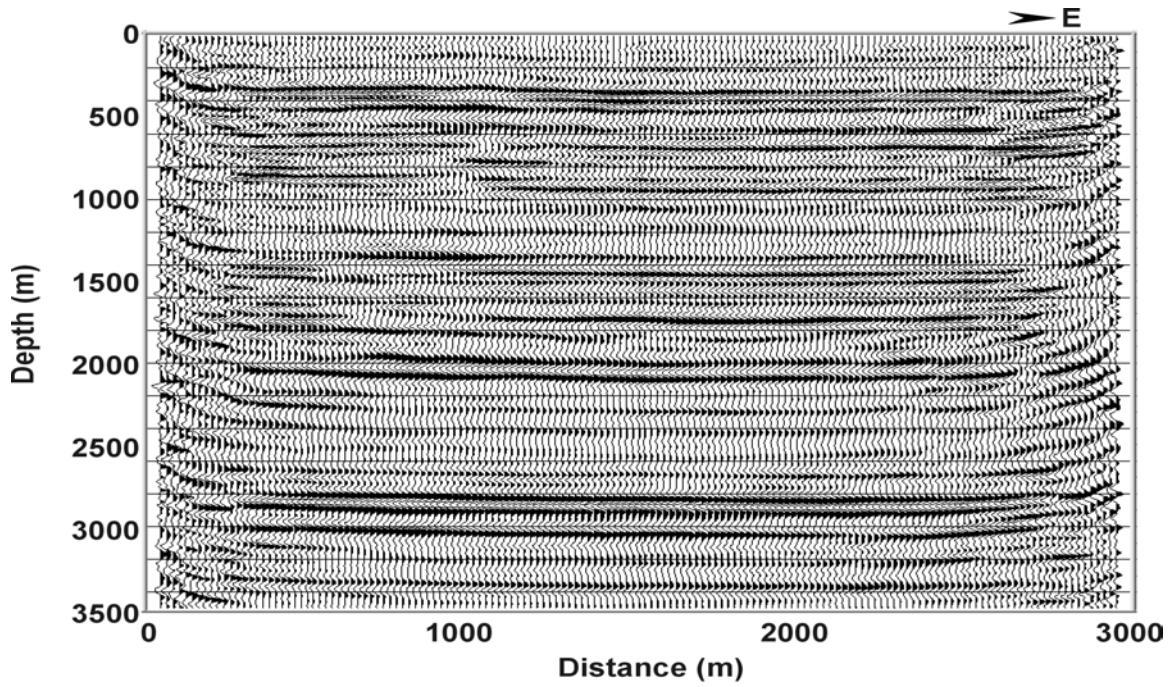


Figure 5.18 Vertical-component depth image.

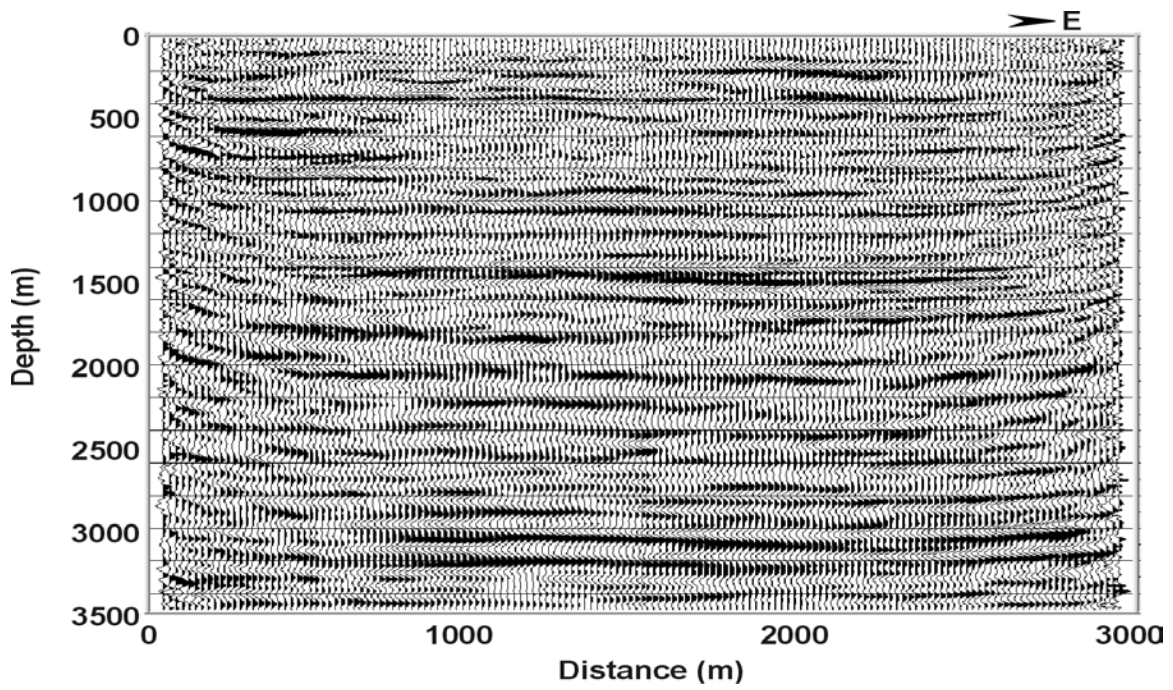


Figure 5.19 Radial-component depth image.

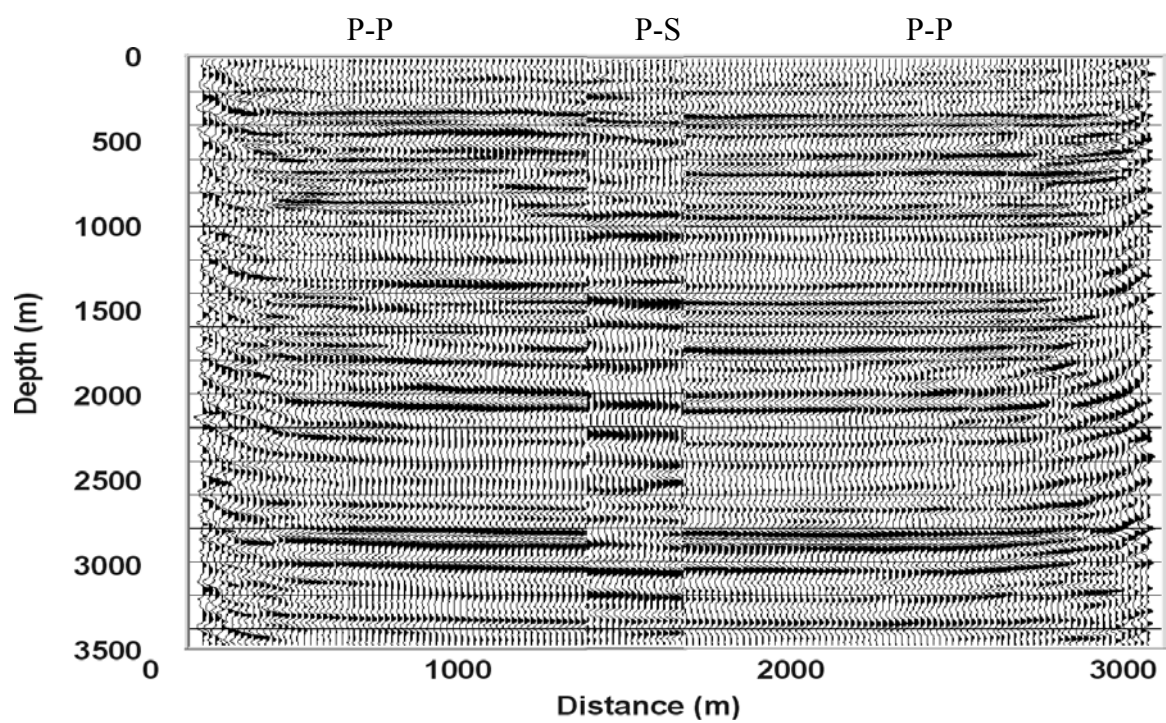


Figure 5.20 Correlation of the P-P and P-S images.

CHAPTER 6**DOWNWARD-CONTINUATION MIGRATION VELOCITY ANALYSIS****6.1 INTRODUCTION**

Seismic imaging is a two-step process of velocity analysis and migration. As the velocity function becomes more complex, the two steps become more interdependent. In complex depth-imaging problems, velocity estimation and migration are often applied iteratively. To assure that this iterative imaging process converges to a satisfactory model, it is crucial that the migration and velocity estimation procedures are consistent with each other.

Kirchhoff migration algorithms often produce unsatisfactory results in structurally complex areas since the wavefield is severely distorted by lateral velocity variations. As the shortcomings of the Kirchhoff migration have become apparent (O'Brien and Etgen, 1998), interest has been renewed in other migration methods and development of computationally efficient 3D prestack depth migration algorithms based on the recursive wavefield extrapolation (RWE) (Biondi and Palacharla, 1996; Biondi, 1997; Biondi and Sava, 1999; Mosher et al., 1997). However, there has been little corresponding progress

in the development of migration velocity analysis (MVA) that can be used in conjunction with any downward-continuation migration algorithms.

For migration, RWE-based MVA is intrinsically more robust than raytracing-based MVA since it avoids the well known problems rays encounter when the velocity model has sharp boundaries. The transmission component of finite-frequency wave propagation is mostly sensitive to the smooth variation in the velocity model. Consequently, wave-equation MVA produces smooth velocity updates and is more stable. In most cases, no smoothing constraint is necessary to assure that migration and MVA converge. On the contrary, raytracing-based MVA often need smoothing in order to avoid quick divergence.

The key issue in MVA is velocity-model updating. After each iteration of migration with a newer velocity model, ideally, the image will converge to the true subsurface. Searching for the better velocity model is intrinsically a travelttime-inversion problem (Tieman, 1995) that is normally difficult to solve and time-consuming, when the velocity field is complicated. In this chapter, a simultaneous depth imaging plus downward-continuation velocity-analysis processing flow is proposed. Beginning with the recording surface, migration velocity analysis based on common-image-point gather is carried out and large-step wavefield-extrapolation with nonstationary wavefield extrapolators is performed to downward continue the wavefield to a deeper level when the velocity model is satisfactory.

6.2 PRESTACK MIGRATION VELOCITY ANALYSIS AS A TOOL OF VELOCITY ANALYSIS

Prestack depth migration is an attractive tool for accurate velocity estimation in geologically complex regions because of its high degree of sensitivity to the velocity field. With an incorrect subsurface model, events in CIGs will exhibit curvature as a function of the offset: events curve upward at lower velocity while downward with higher velocity. With correct velocity, ideally, curvature should not be observed and events should stack coherently (Gardner et al., 1974). The velocity analysis suggests that when velocity is lower than the real velocity, the offset-dependent events should curve upward, and downward when velocity is higher than the real velocity (e.g. Lines et al., 1993).

A velocity-updating scheme is necessary to generate better estimations of the subsurface. Different authors, trying to exploit this migration property, have developed a variety of algorithms. Among these algorithms are:

I. Iterative profile migration (Al-Yahya, 1989). This algorithm updates the model parameters from event curvature and traveltimes inversion. It first migrates the data with an inaccurate subsurface model and then updates the velocity through minimization of the event curvature (Tieman, 1995). In principle, the algorithm requires manual picking of event depth. It is not only a time-consuming process, but also subject to human error. An event-picking algorithm similar to scanless velocity-analysis was proposed by Tieman (1993) and claimed to be a robust and accurate alternative to manual depth-picking.

II. Stacking power optimization (Tieman, 1984). The algorithm is analogous to conventional velocity analysis in that it uses a variety of subsurface models to migrate and stack the data to obtain a post-stack semblance spectrum. The model that results in the highest amplitude signal at a particular location and event is the most accurate model from the surface to that event. Typically, the initial models used by such a scheme are constant-velocity half-spaces. Using this type of model results in a very efficient migration scheme (Stolt, 1978). A more advanced technique of building initial subsurface models is to multiply the interface depths by a constant, u , and divide the interval slowness by the same amount. This keeps the vertical traveltime to the event unchanged. The parameter updates are computed from those models that maximize event energy to give two measurements: the velocity model that maximizes the event energy at a certain location and the depth that maximizes the event energy.

III. Focusing analysis (Yilmaz and Chambers, 1984; MacKay and Abma, 1992). This algorithm originated with Doherty and Claebout (1976) and was intended to exploit the velocity sensitivity of prestack migration by relating data-focusing to an iterative velocity-updating scheme. Yilmaz and Chambers (1984) applied this work to the prestack time-migration of field data sets. Aye and Jeannot (1986) generalized this algorithm to prestack depth migration in the form of depth-focusing analysis (DFA). MacKay and Amba (1989) showed that this algorithm can be used to produce a well-focused seismic section and their later publication (MacKay and Amba, 1992) showed the velocity limitation of DFA is suitable for up to 35° events; events of higher-angle can be analyzed by applying a damping factor to avoid velocity-analysis dispersion.

A common failure of the above algorithms is that the updating relationship is determined through restrictive assumptions about the subsurface; for example, that the subsurface velocity is constant or is a $v(z)$ media only. Any lateral-velocity variations will negatively affect the velocity-updating scheme. To remove structural distortions from the focusing analysis, Audebert and Diet (1993) introduce a new focusing-analysis algorithm.

The methods mentioned above often fail in geologically complex regions since the velocity-updating scheme is determined by the restrictive assumptions that the subsurface velocity is constant or depth-dependent only. Thus any structure or lateral velocity variation that exists in the subsurface will affect the accuracy and robustness of these methods. Several authors attempted to extend migration-velocity-analysis to the media with lateral velocity variation. Chauris et al. (1999) used differential semblance optimization (DSO) (Symes and Carazzone, 1991) formulated in the migrated-data domain with the flatness of events in common-image-gathers as a criterion for velocity quality. The use of DSO is an efficient way to converge to a local solution with a global velocity cost-function optimization. Other existing algorithms which attempt to eliminate the restrictive assumptions in established methods include layer stripping (Hadley, 1988) and tomographic inversion. The layer-stripping method recursively solves for deeper layers using the overlaying solution. Localizing the velocity analysis problem to a level close to the reflections reduces the effects of complex overburden. Reflection-tomography inversion is perhaps the best for velocity analysis/inversion on seismic data and has been advocated by many authors (Etgen, 1993; Stork, 1992). Fewer assumptions

are made about the velocity model and it therefore has the potential of rectifying problems encountered by other methods.

6.3 DOWNWARD-CONTINUATION VELOCITY ANALYSIS (DCVA)

Conventional semblance-based velocity-analysis assumes constant velocity or depth-dependent-only velocity functions, so that traveltimes curves are hyperbolic. This conventional analysis computes the stacking power within each analysis time-window with a range of velocity values. The correct velocity is the one which produces the largest semblance value (Taner, 1969). For a simple dipping reflector, this technique remains applicable; however, the velocity value obtained must be corrected with an angle factor to provide true velocity. This technique is capable in generating an optimum stacking seismic section but often fails in giving a true subsurface velocity model when structures are present.

Semblance-based velocity-analysis techniques rely on data with sufficient offset. When velocity is a function of depth only, the traveltimes curves are approximately hyperbolic and the analyzed velocity values are root-mean-square (RMS) values of the overburden velocity values. Both the shallow and deep parts of the analyzed velocity function are equally accurate. When velocity is also a function of lateral position, the traveltimes curves are non-hyperbolic and the assumptions of semblance velocity analysis are no longer strictly valid. With the increase of event depth, the traveltimes curve is more likely to be affected by lateral velocity variations. Compared with the deep events,

semblance analysis for shallow events involves less lateral velocity averaging and it therefore provides a better approximation to the local velocity function. However, sufficient offset is still required in order to resolve events close to each other.

Downward wavefield extrapolation can downward continue the recording datum to a certain depth-level when the velocity field is known, so that any deep events can be turned into shallow events and a local semblance velocity analysis can be performed. Downward-continuation velocity-analysis (DCVA) is based on this concept and can be performed by the following three steps:

- I. Semblance velocity analysis for shallow events. RMS velocities of the shallow events can be obtained.
- II. Conversion of RMS-velocity to interval-velocity, in depth, to build the velocity model for the shallow region.
- III. Downward continue the wavefields to the new recording datum with the velocity model generated from the last step. Velocity scanning by percentage variation and examination of the event curvature in the CIGs can be used to adjust the velocity model approximately. Depth image within the depth range of the velocity model can also be generated for reference.

The above three steps can be applied recursively until a desired depth is reached.

Downward continuation of the receivers and sources to a new recording datum involves a traveltimes correction. Two ways to perform traveltimes correction include:

1) Deconvolution travelttime correction.

$$\psi(x, z, \omega) = \frac{|\psi_R(x, z, \omega)|}{|\psi_S(x, z, \omega)|} e^{i(\Phi_R(x, z, \omega) - \Phi_S(x, z, \omega))}, \quad (6.1)$$

where $\psi(x, z, \omega)$, $\psi_R(x, z, \omega)$ and $\psi_S(x, z, \omega)$ are the travelttime- and amplitude-corrected data, the downward-continued receiver and source wavefields, respectively. $\Phi_R(x, z, \omega)$ and $\Phi_S(x, z, \omega)$ are the receiver and source phase spectra, from which the travelttime from the surface to the current recording datum has been removed. As both the travelttime and amplitude are corrected, this is a true-amplitude algorithm. However, it may not be very practical since it is highly sensitive to noise in the data.

2) Crosscorrelation travelttime correction.

Replacing the source amplitude spectrum with a constant (normally 1.0) in equation (6.1) leads to the crosscorrelation travelttime correction. Although it is not a true-amplitude algorithm, it is more stable than the deconvolutional travelttime correction due to its low sensitivity to the noise in the source spectrum. The method can be written as

$$\psi(x, z, \omega) = \psi_R(x, z, \omega) e^{i(\Phi_R(x, z, \omega) - \Phi_S(x, z, \omega))}. \quad (6.2)$$

The crosscorrelation travelttime correction in this chapter is used for its stability.

6.4 AN EXAMPLE – DCVA APPLIED TO THE MARMOUSI SYNTHETIC

As the Marmousi model is more complicated than most geological settings, DCVA is applied to the Marmousi synthetic data set for testing purposes. The final results of the DCMVA flow are a depth velocity model and a depth image. Due to the extensive amount of work involved in velocity picking, the recording datum was downward continued to only 600 m, with a downward-continuation step size of 200 m. At the top of the original and each extrapolated recording datum, conventional semblance velocity analysis was performed to obtain the velocity function close to the recording datum. The velocity-analysis time window was set to a value large enough to accommodate a 400-m overlapping zone with the velocity function produced from the next two recording data. This reduced the windowing effect between velocity analysis zones and human errors in velocity picking. After all velocity layers are produced, they are averaged to produce a final velocity model. The total depth of the velocity model is 1200 m.

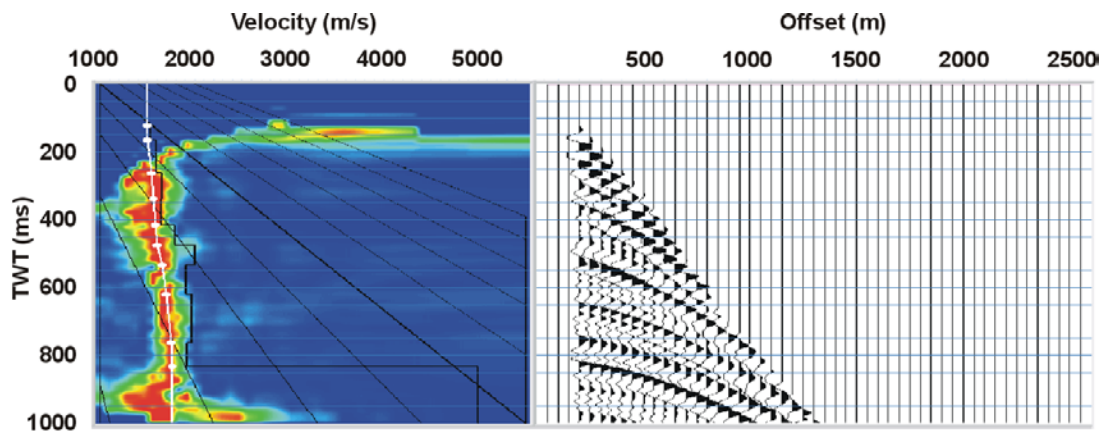
Figure 6.1 shows three velocity-analysis panels of the CDPs located at 3300 m, 5800 m and 8300 m from the surface. Distance is measured from the left of the model. The structural variation in the true velocity model is rather mild at 3300 m and at 8300 m, while it is much more complicated at 5800 m. Note that the corresponding velocity semblance is rather dispersive when structures are present in the middle of the model. **Figure 6.2** shows the 0-600 m velocity model produced by this analysis. The upper 200 m of the model is used to downward continue the recording datum to a 200-m depth.

As an example, **Figure 6.3b** shows shot gather 120 after extrapolation to the recording datum at 200 m. The corresponding shot gather recorded at the surface is shown for comparison (**Figure 6.3a**). Note that the zero-offset traveltimes of the major events has been shifted upward. The extrapolated data set can then be used for the next step of velocity analysis. **Figure 6.4** shows the velocity analysis panels of the CDPs located at 3300 m, 5800 m and 8300 m from the data extrapolated to 200-m recording datum and **Figure 6.5** shows the analyzed velocity model from 200 m to 800 m. **Figure 6.6** and **Figure 6.8** show the velocity-analysis panels of the corresponding CDPs from data extrapolated to 400- and 600-m depth. **Figure 6.7** and **Figure 6.9** show the analyzed velocity model from 400 m to 1000 m and the analyzed velocity model from 600 m to 1200 m. **Figure 6.10** shows shot gather 120 after being downward continued to the 400 m and 600 m recording datum.

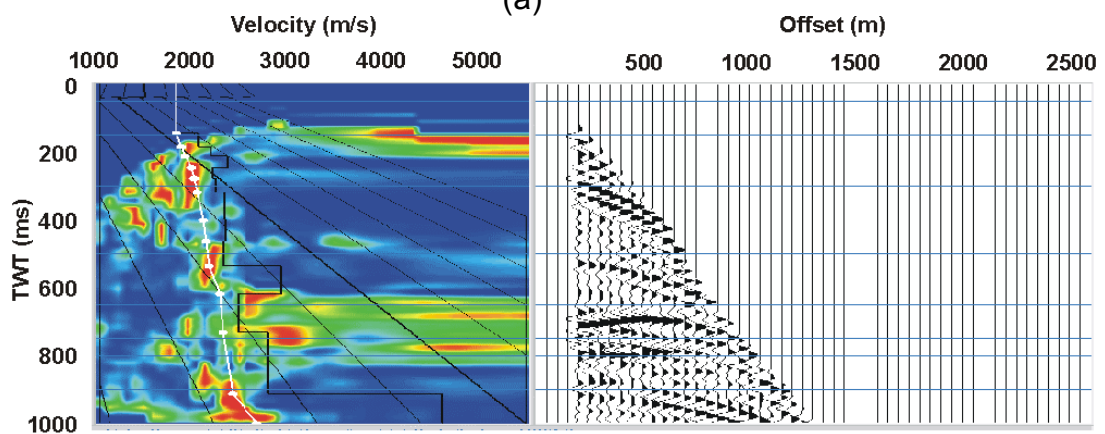
The four velocity models are then overlapped to produce the final velocity model. Velocities in the overlapping zones are averaged. For purposes of comparison, a velocity model built with direct velocity-analysis from the surface, the true velocity model after being smoothed by a 200 m x 200 m box-car and the model produced by the DCVA are shown in **Figure 6.11**. The DCVA velocity model looks more similar to the smoothed, true-velocity model.

Figure 6.12 shows three 0-1200-m images of the Marmousi migrated with the velocity model in **Figure 6.11**, accordingly. The velocity model obtained from DCVA produced a far better image than the velocity model obtained from direct velocity-analysis from surface. The improvement on the left of the image is obvious. The faulted zone in the middle of the model is also better imaged, though the fault planes are still

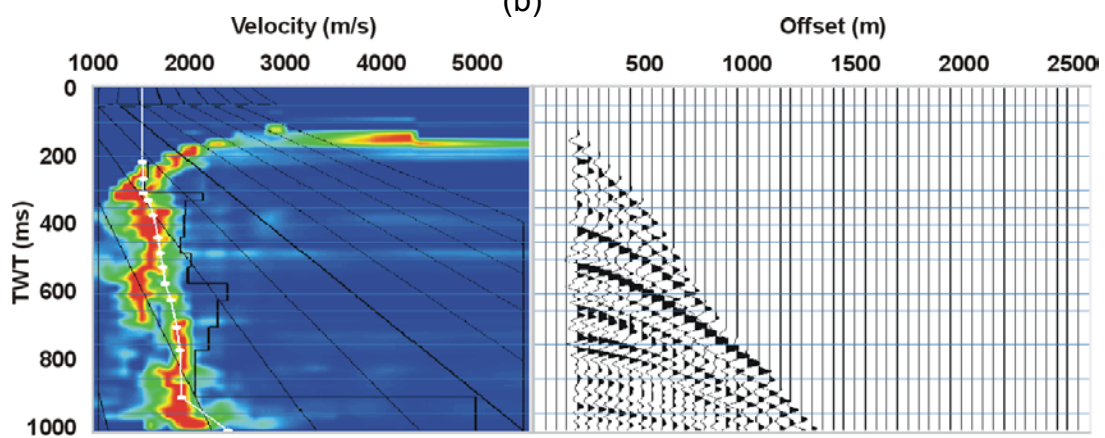
obscure compared with the image migrated with the true-velocity model. The depth and lateral locations of some the reflections are slightly incorrect and indicate that the DCVA velocity model needs further refining.



(a)



(b)



(c)

Figure 6.1 Three velocity analysis panels of the CDP gathers located at (a) 3300 m, (b) 5800 m and (c) 8300 m. Velocity-analysis datum is at $z=0$. Distance is measured from the left of the model.

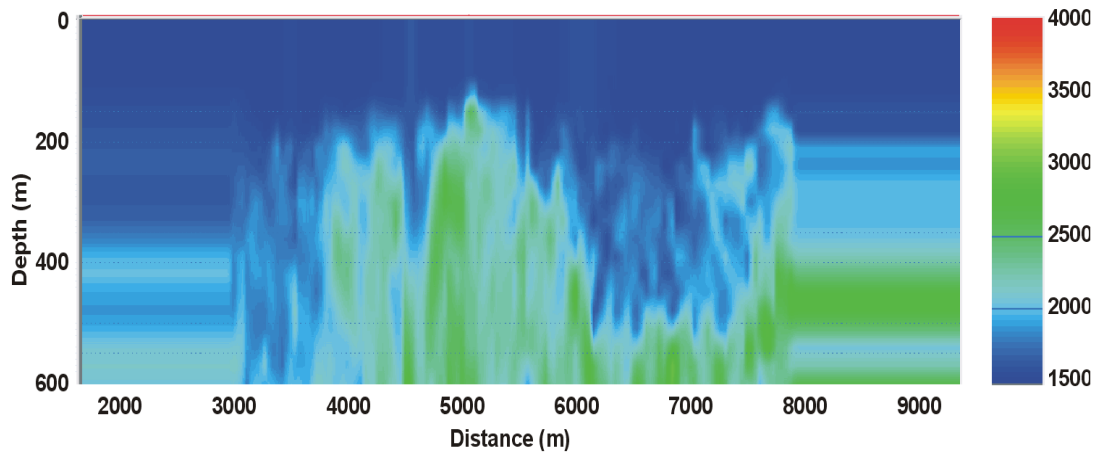


Figure 6.2 Velocity model from 0 to 600 m, built from the velocity analysis from the $z=0$ recording plane.

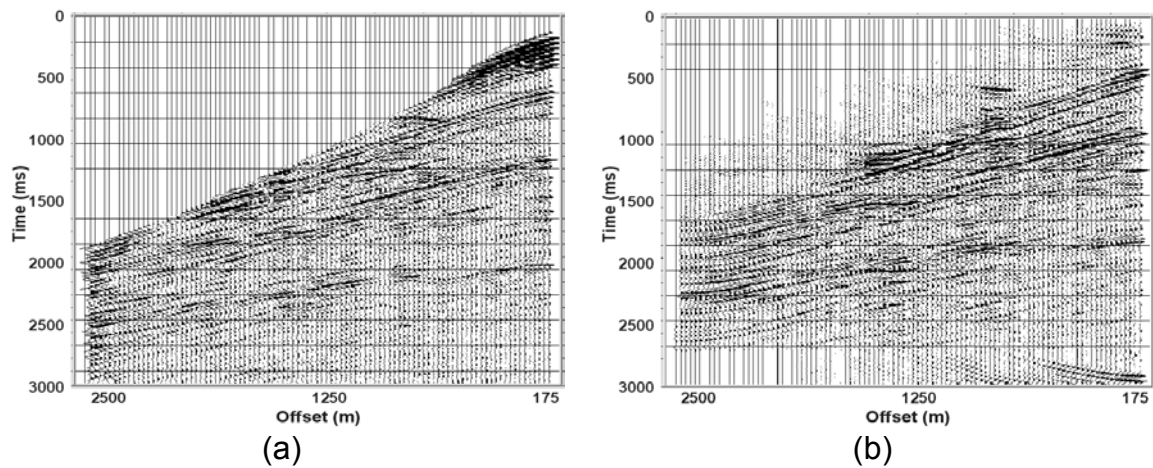
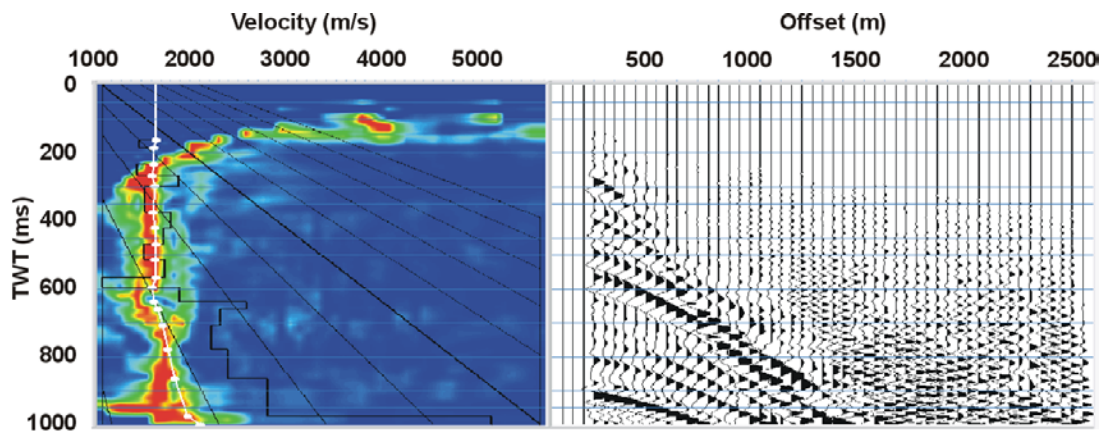
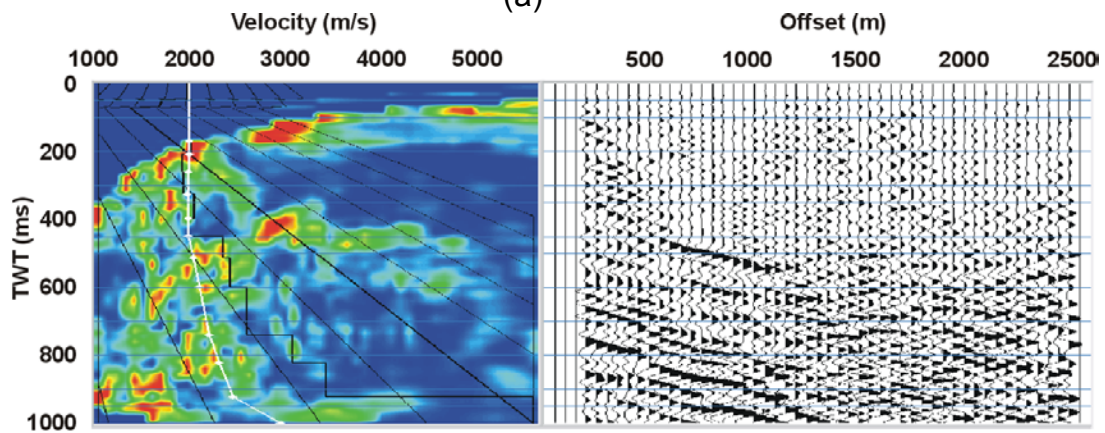


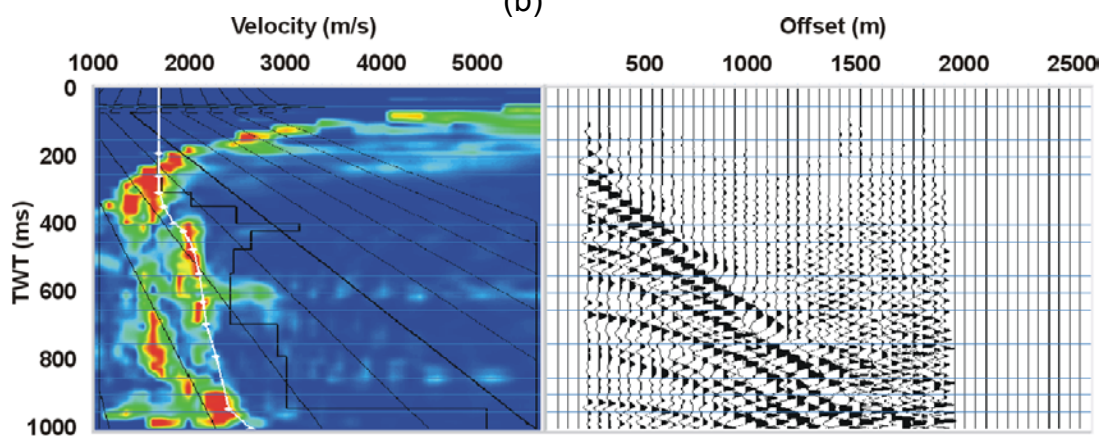
Figure 6.3 (a) Shot gather 120 recorded on the surface and (b) after being extrapolated to the recording datum at 200 m.



(a)



(b)



(c)

Figure 6.4 Three velocity-analysis panels of the CDP gathers located at (a) 3300 m, (b) 5800 m and (c) 8300 m. The data has been downward continued to the 200-m recording datum. Distance is measured from the left of the model.

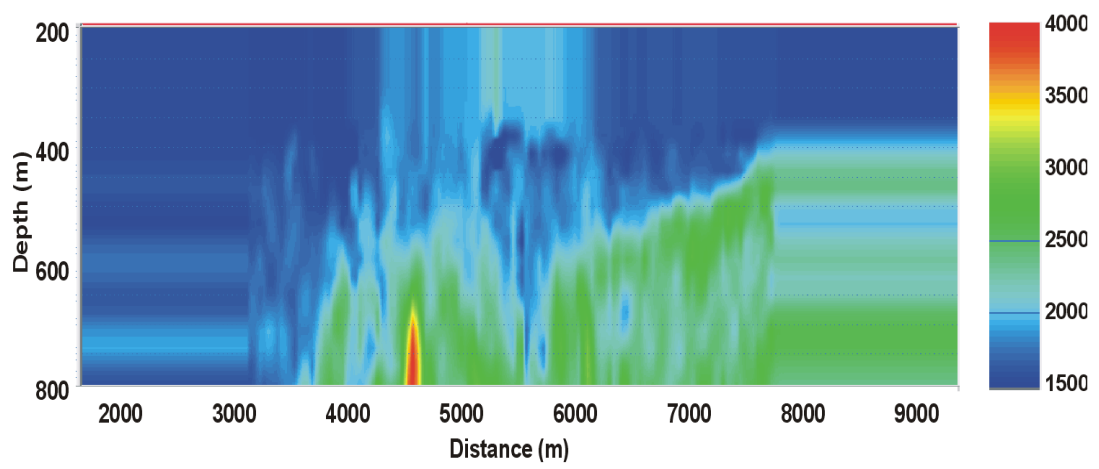
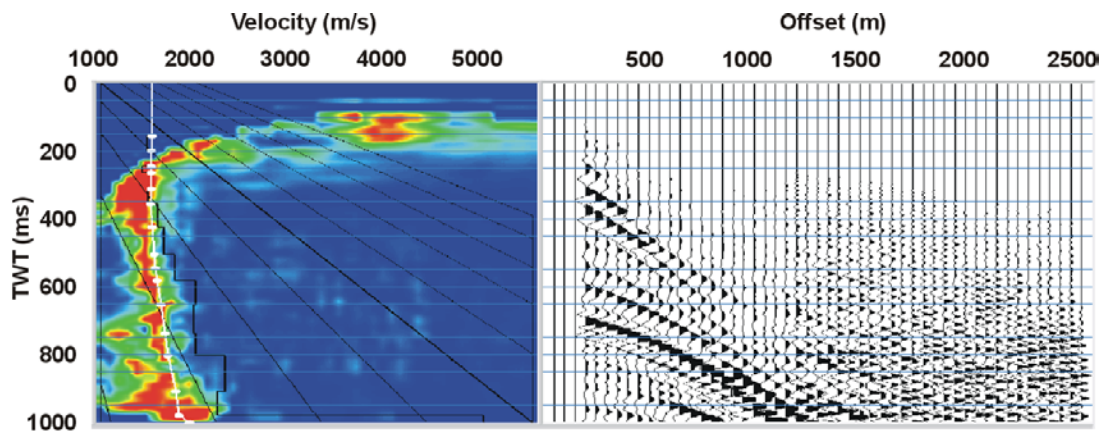
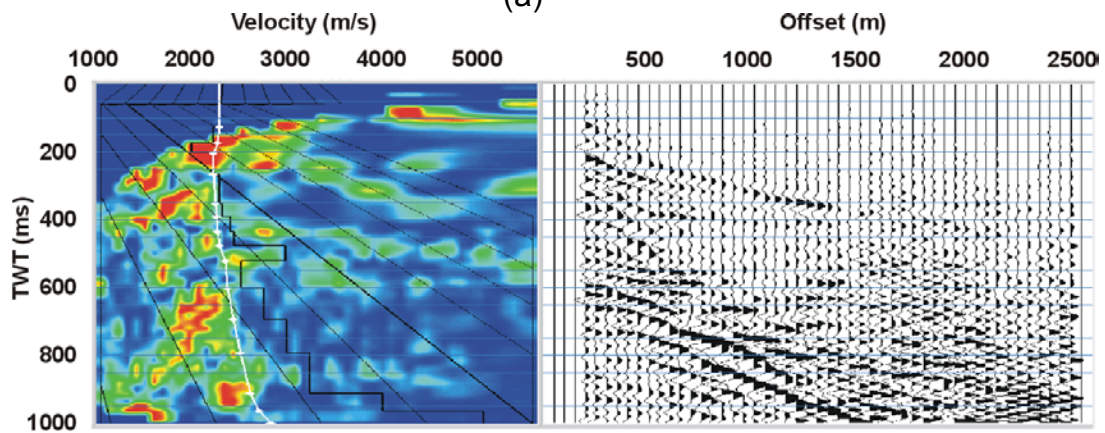


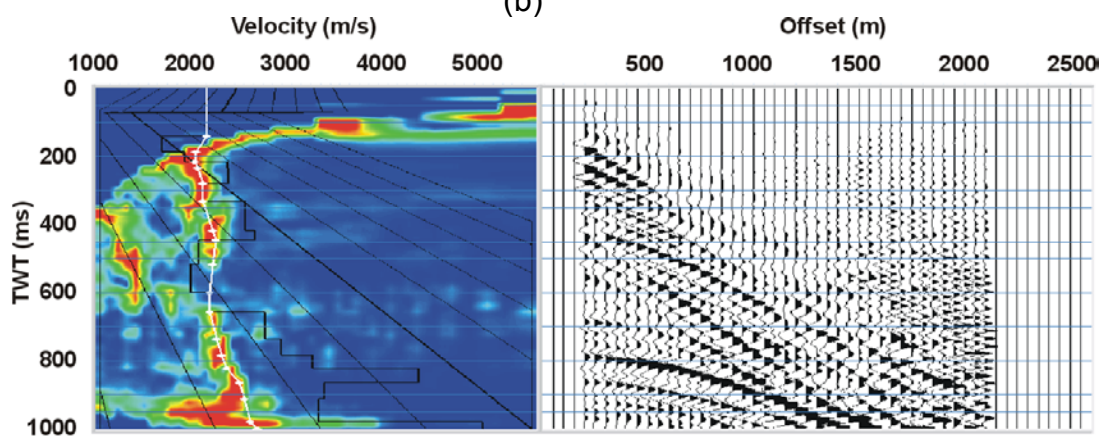
Figure 6.5 Velocity model from 200 to 800 m, built with the velocity analysis at the $z=200$ recording datum.



(a)



(b)



(c)

Figure 6.6 Three velocity-analysis panels of the CDP gathers located at (a) 3300 m, (b) 5800 m and (c) 8300 m. The data has been downward continued to the 400-m recording datum. Distance is measured from the left of the model.

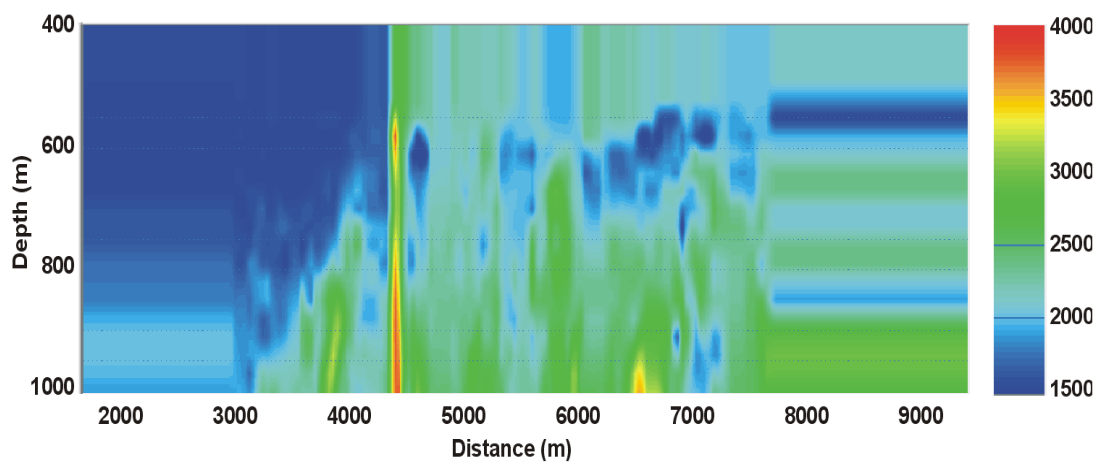
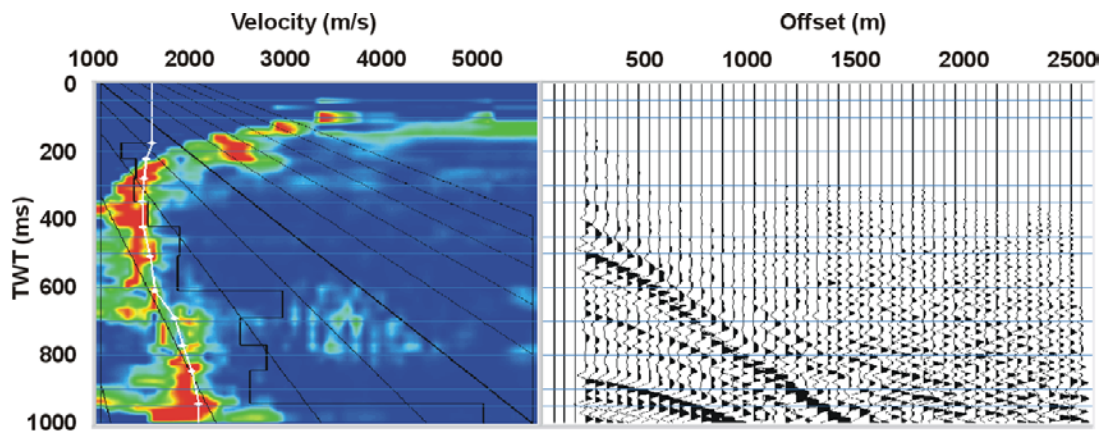
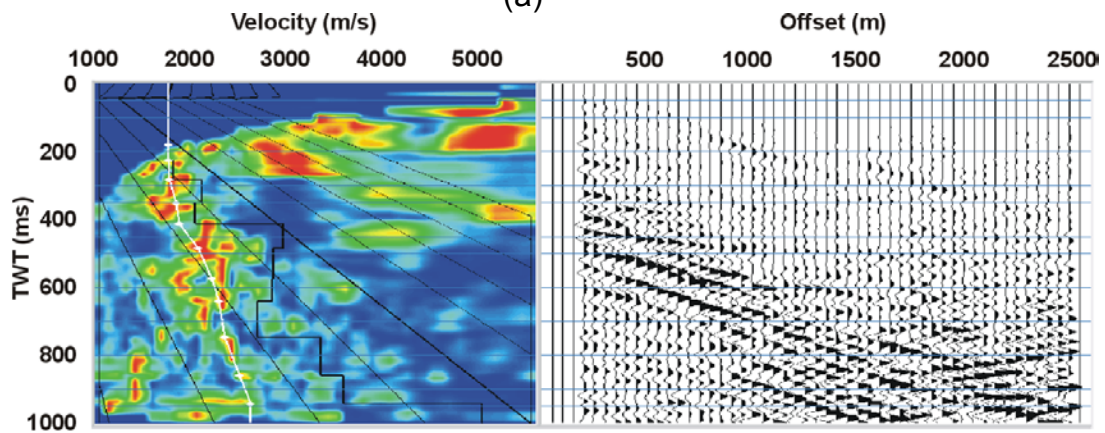


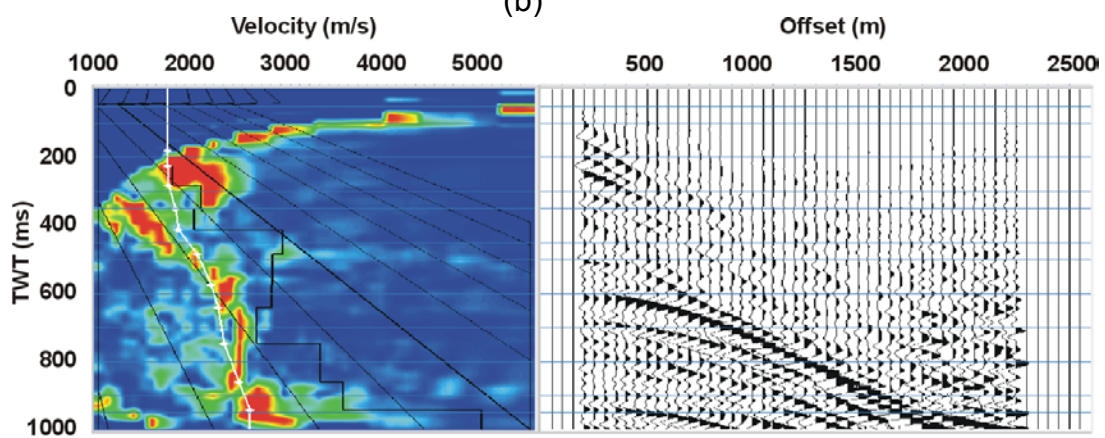
Figure 6.7 Velocity model from 400 to 1000 m built with the velocity analysis at the $z=400$ recording datum.



(a)



(b)



(c)

Figure 6.8 Three velocity-analysis panels of the CDP gathers located at (a) 3300 m, (b) 5800 m and (c) 8300 m. The data has been downward continued to the 600-m recording datum. Distance is measured from the left of the model.

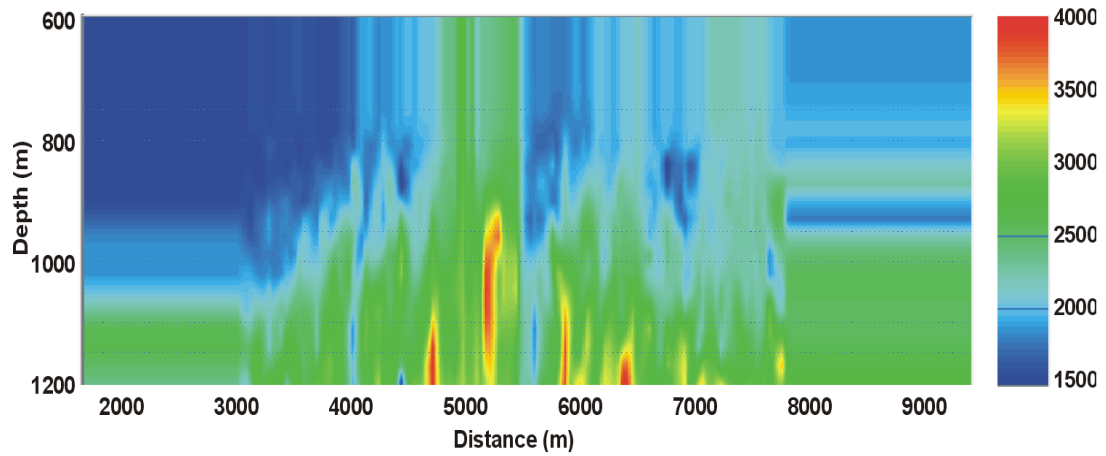


Figure 6.9 Velocity model from 600 to 1200 m built with the velocity analysis at the $z=600$ m recording datum.

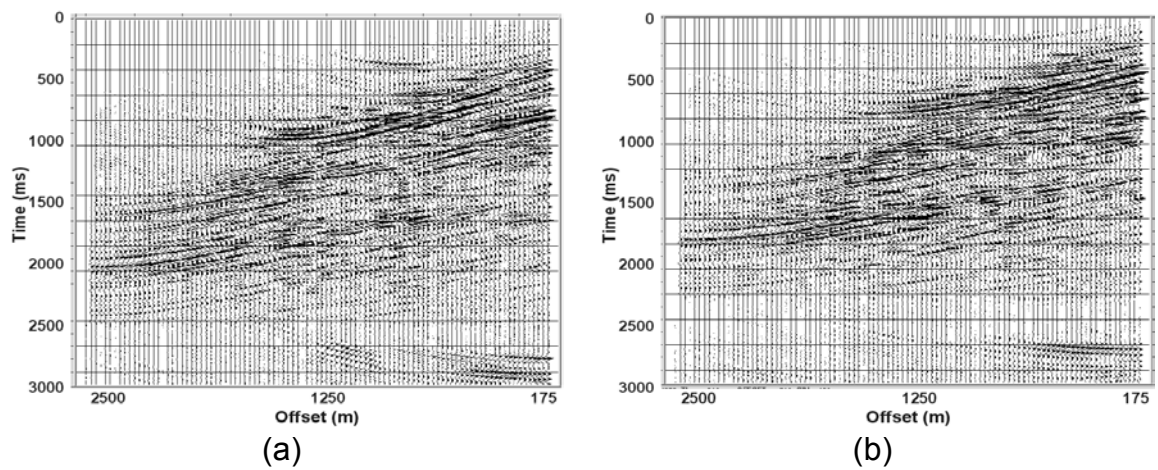


Figure 6.10 The shot gather 120 after downward-continuation to (a) the 400 m and (b) the 600 m recording datum.

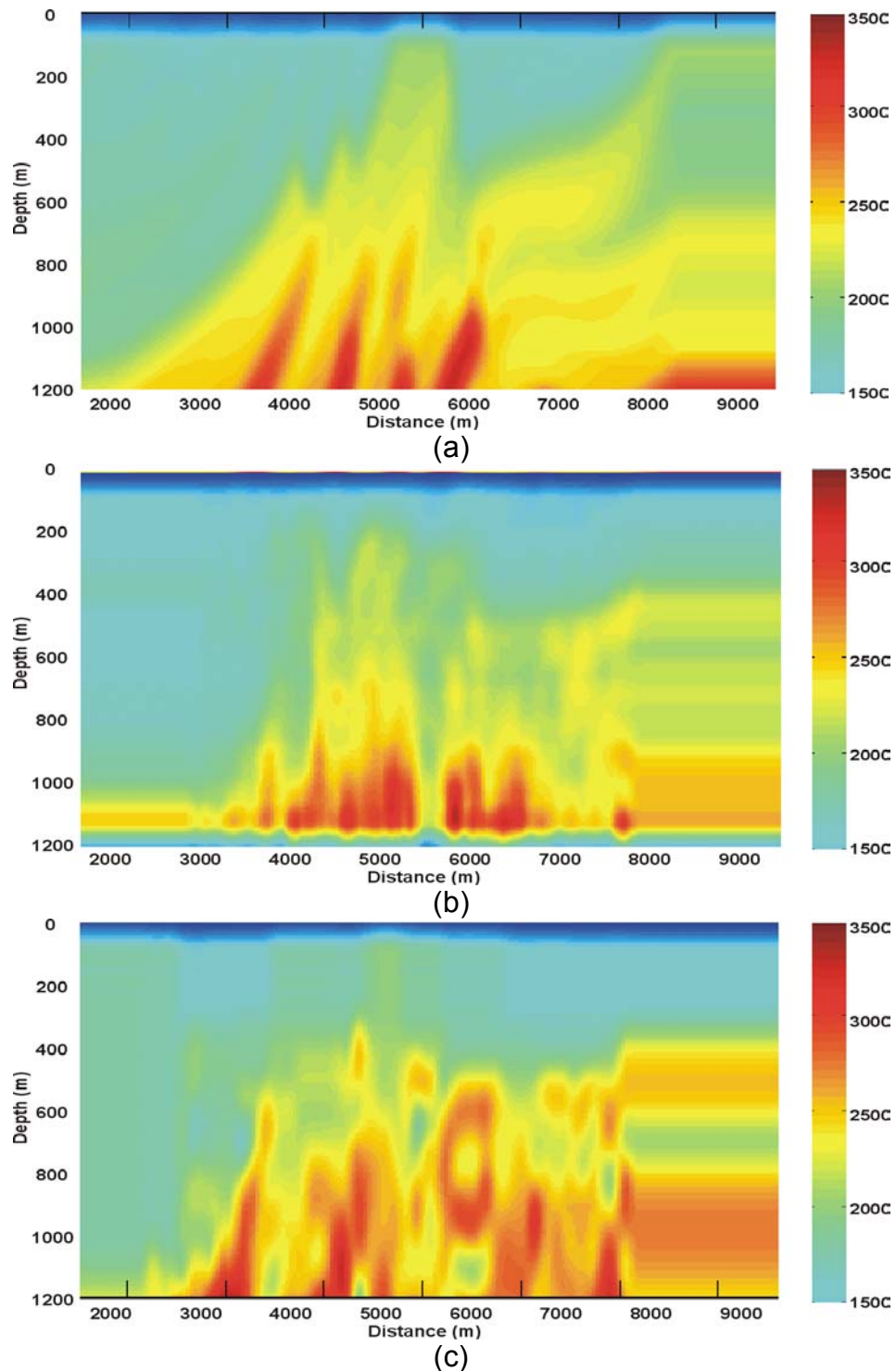


Figure 6.11 Velocity models from 0 to 1200 m of the Marmousi model. (a) True-velocity model smoothed with a 200 m x 200 m boxcar; (b) velocity model built with DCVA, and (c) velocity model built with velocity analysis from surface with conventional CMP semblance velocity analysis. Note that the model in (b) is much better than that in (c).

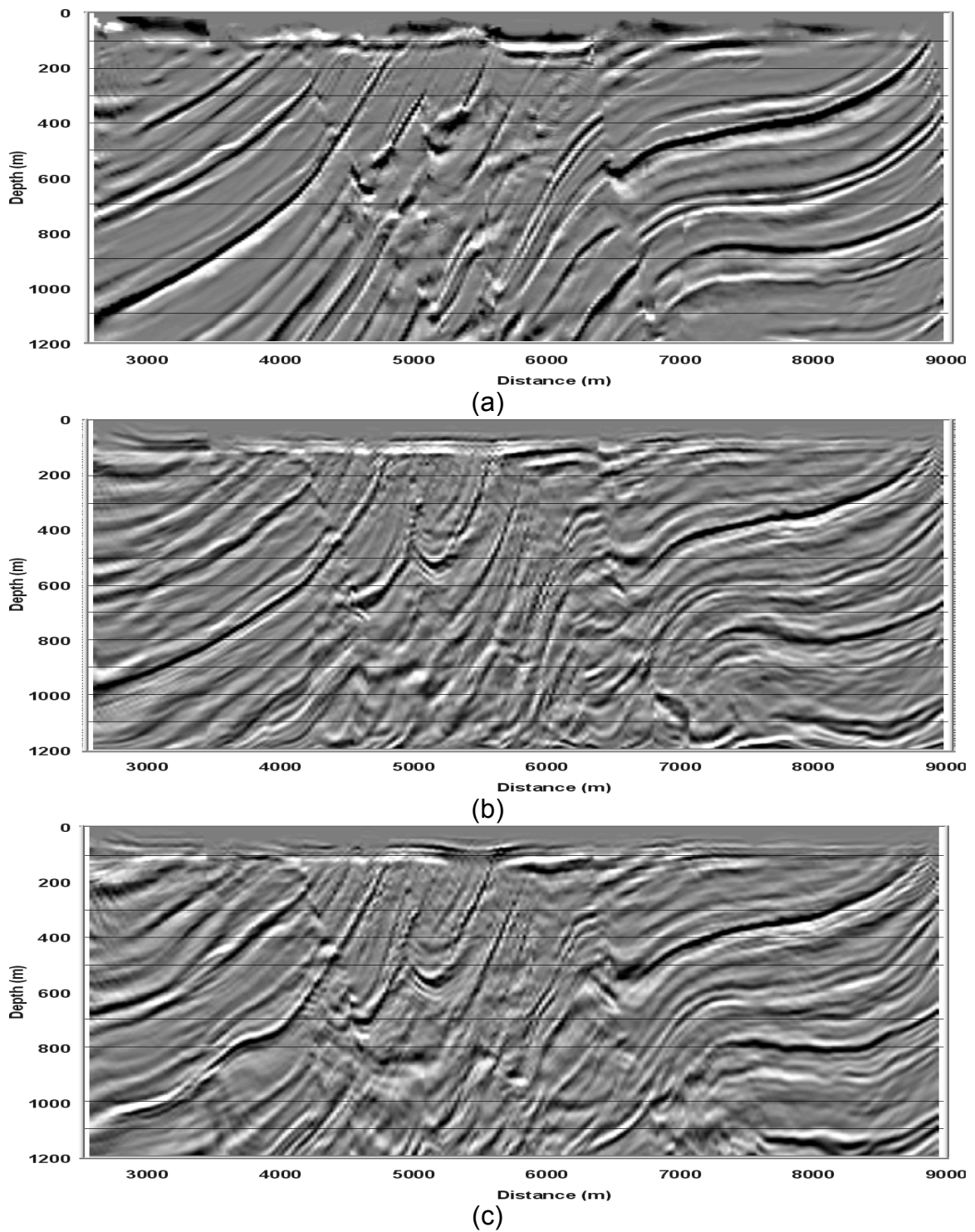


Figure 6.12 Three 0-1200-m depth images of the Marmousi produced with (a) the true velocity-model, (b) the DCVA velocity model and (c) the velocity model obtained from surface velocity analysis.

6.5 DOWNWARD-CONTINUATION MIGRATION VELOCITY ANALYSIS (DCMVA)

Although the depth image produced with the DCVA velocity model is superior in quality to that produced with the velocity model generated by surface velocity-analysis, the reflections are still not in correct spatial location. This is due to the lack of velocity-quality control when the model is built. The flatness of events in the CIGs can be used to adjust the velocity model. **Figure 6.13** shows the CIG at 3300 m after migration with 80% to 120 % of the velocity model built with the downward-continuation velocity-analysis method. The events curve upward and are shallower than the true depth when the velocity is lower than true velocity, while curves downward are deeper than true depth when the velocity is higher than true velocity. In **Figure 6.13**, with velocity percentages varying from 80% to 104%, the events gradually flatten and the image depth approaches the true depth. As the velocity further increases from 104% to 120 %, the events gradually curve downward. The correct velocity percentage should be between 104% and 108% since events curve slightly upward and downward in the two CIGs. An estimated 106% velocity scaling factor is chosen for this location. The velocity-scaling factor can be determined for other locations in a similar way.

Figure 6.14 shows the velocity-scaling function chosen for CIGs from 2000 m to 9000 m. On both sides, the scaling factor varies rather uniformly from 104% to 108%, while in the central part, where the fault zone lies, the fluctuation increases -- from 88% to 108% -- and suggests a great deal of uncertainty in the velocity model.

The model after application of the scaling factor is shown in **Figure 6.15**. It is rather similar to **Figure 6.11b**, in a general sense. **Figure 6.16** shows the CIG at 3300 m produced with (a) the true velocity model and (b) the adjusted velocity model. Note that the events continue to curve slightly upward, indicating the velocity is still slightly too slow. **Figure 6.17** shows the CIG stack migrated with the adjusted velocity model. Compared with the image produced directly with the velocity model, without the scaling factor applied, the left and right parts of the image are apparently better focused; however, in the central fault zone, the image quality does not seem to be improved. Adjusting a velocity model in a 1200-m depth-interval works rather well, on the whole, when the event dip angle is not too big; it fails, however, when structures are extremely complicated. A more delicate method involves the downward-continuation velocity-analysis and performing velocity quality control with updates to the velocity model at every downward-continuation step using velocity scanning. This procedure can effectively reduce the error in the downward-continued wavefields, so that the velocity analysis in the next step can also be improved. However, iteration of velocity-analysis and velocity-scanning takes a great deal of time and effort and is not further examined in this thesis.

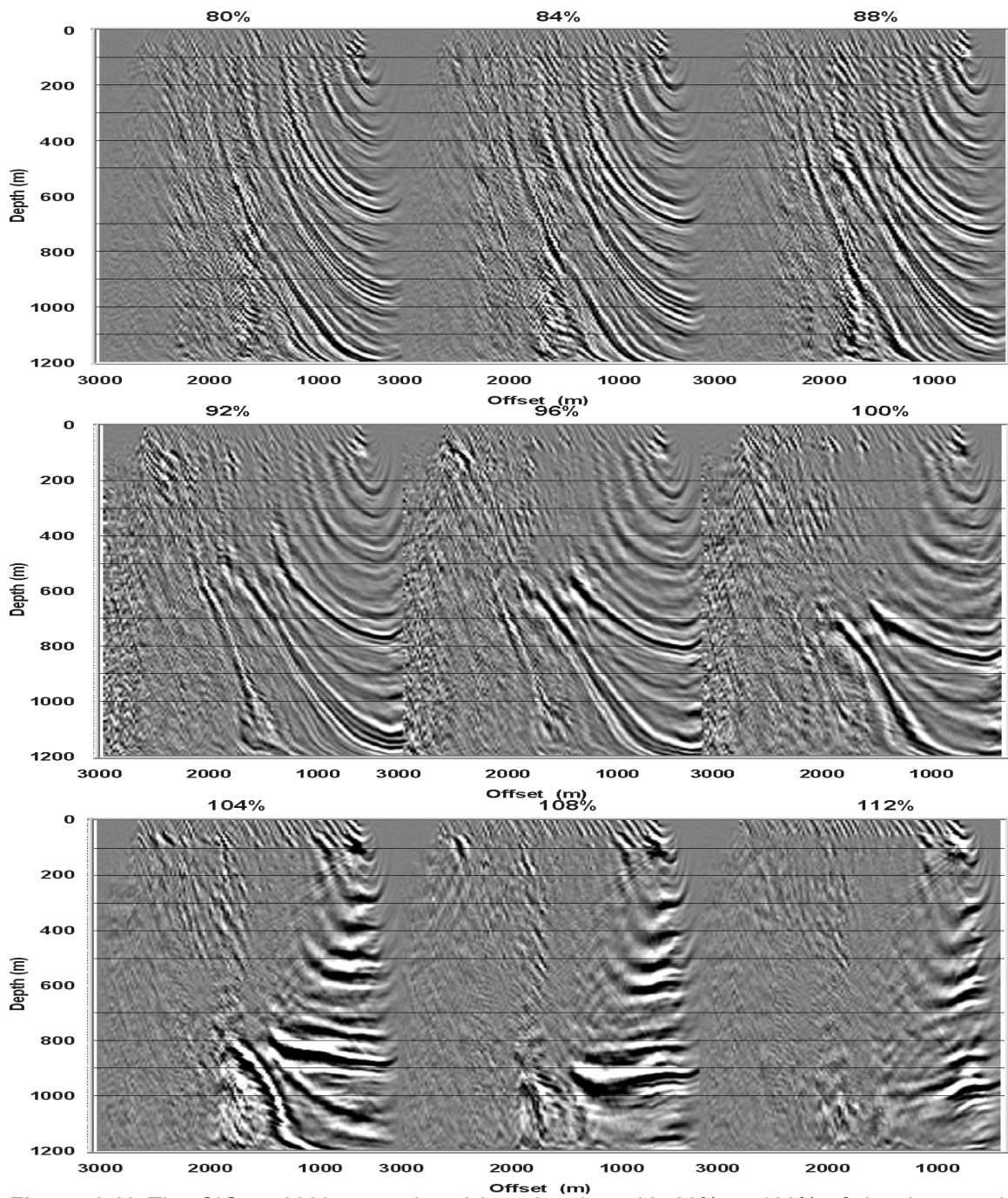


Figure 6.13 The CIG at 3300 m produced by migration with 80% to 120% of the downward-continuation velocity model (continues).

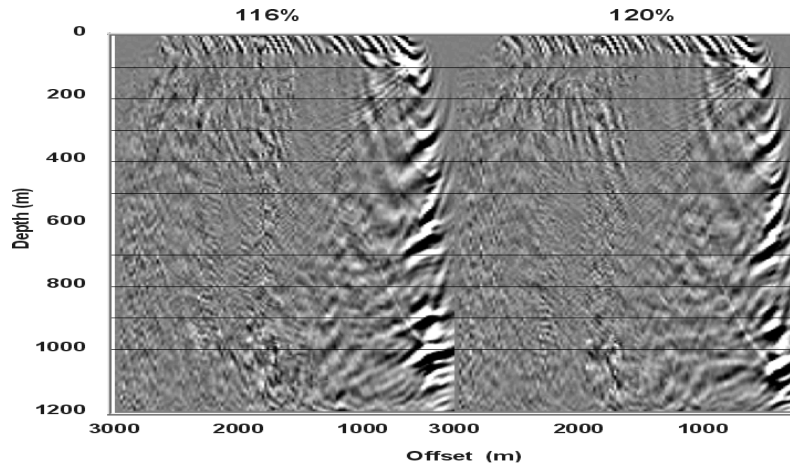


Figure 6.13 The CIG at 3300 m produced by migration with 80% to 120% of the downward-continuation velocity model. Note that the events in the image-gathers with 104%- and 108%-velocity tilt slightly upward and downward, which indicates that the correction percentage of velocity should be between 104% and 108%. A 106% velocity-scaling factor is selected at this location.

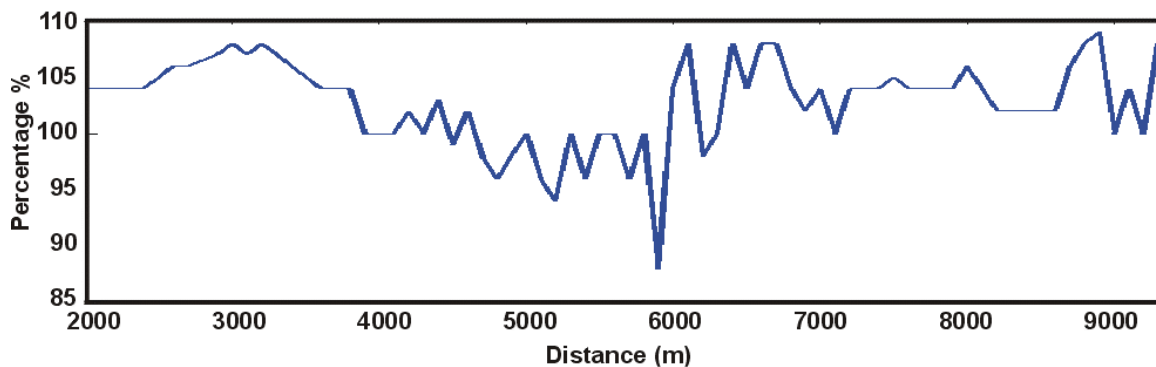


Figure 6.14 The velocity-scaling factor picked along the lines by examining the event flatness in CIGs.

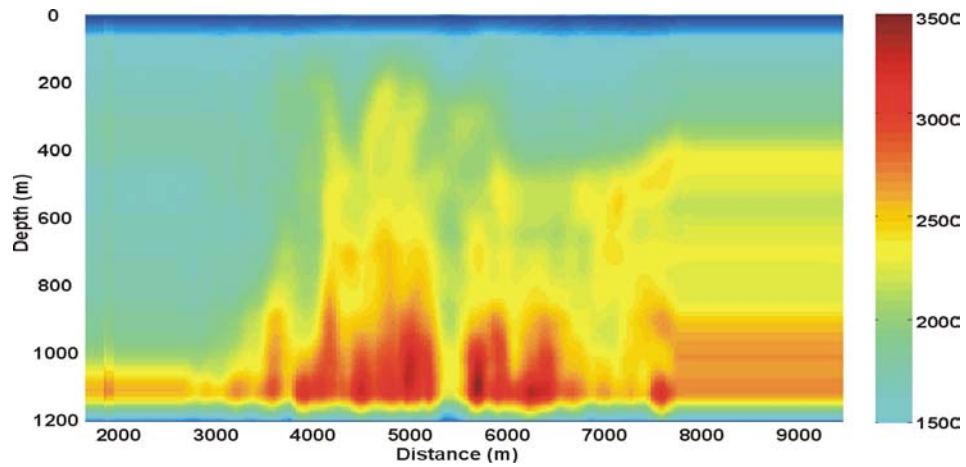


Figure 6.15 The velocity model after application of the scaling factors.

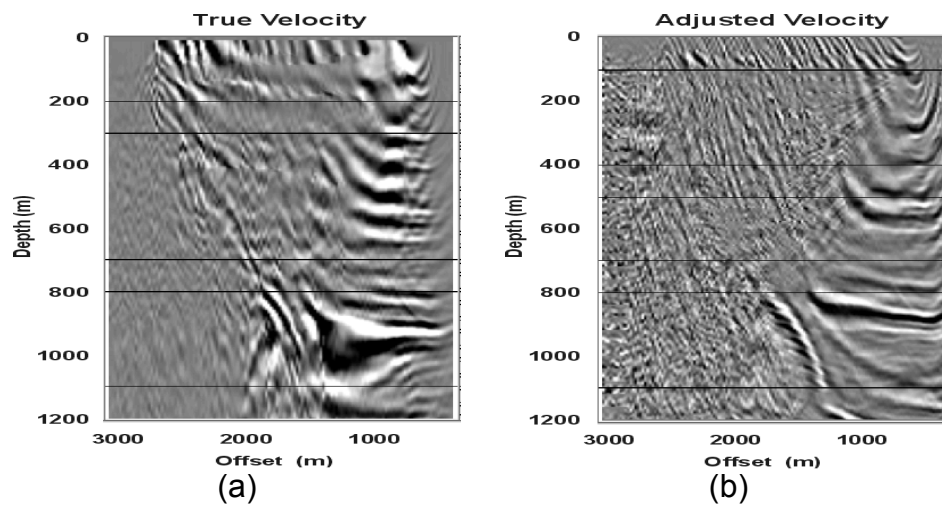


Figure 6.16 Comparison of the CIG at 3300 m migrated with (a) the true velocity model and (b) the adjusted velocity model.

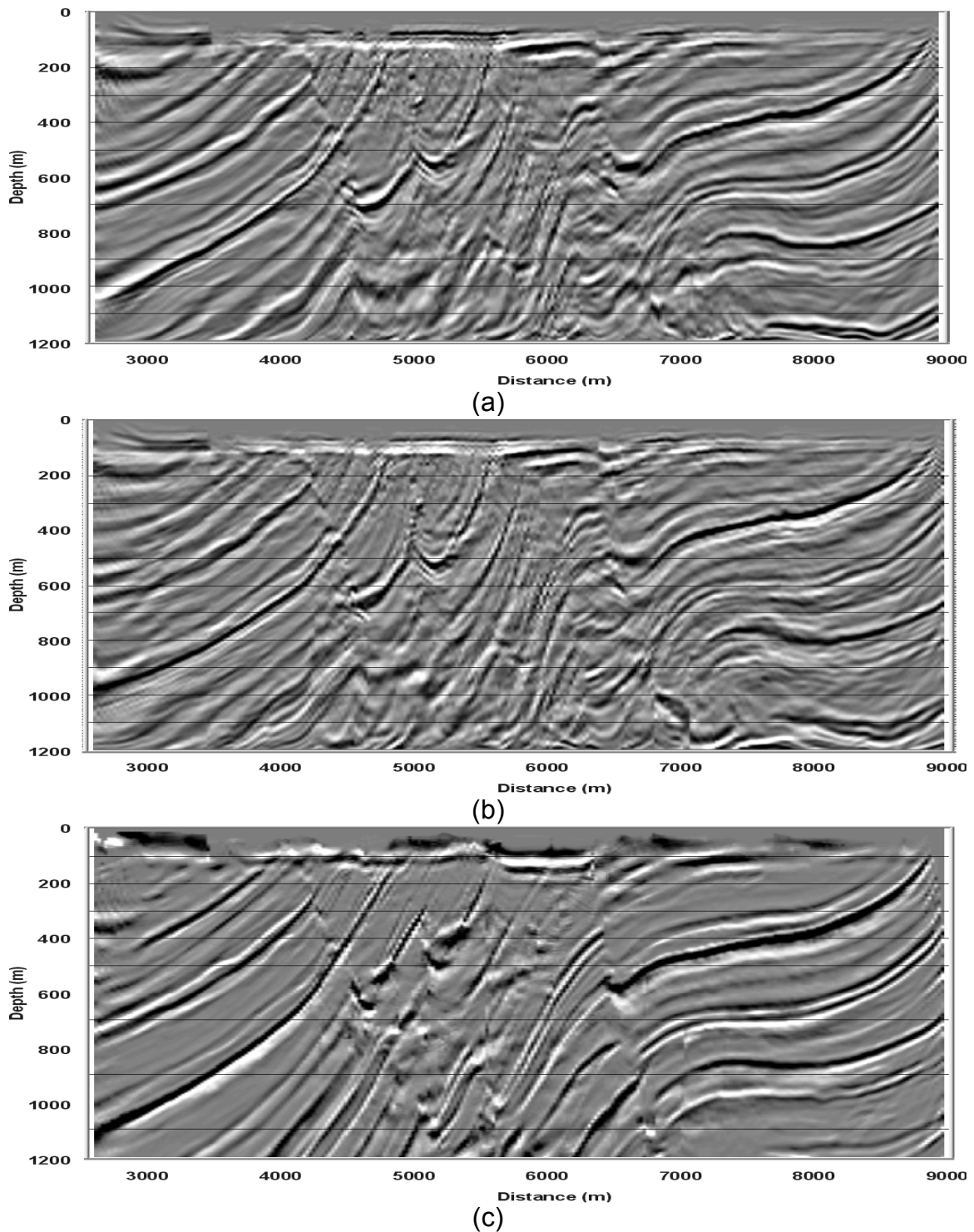


Figure 6.17 The CIG stack produced with (a) unadjusted downward-continuation velocity model, (b) adjusted downward-continuation velocity model and (c) the true velocity model. Note that the event depths at both left and right of the section are closer to the true location in (b).

6.6 CHAPTER SUMMARY

A number of established migration-velocity-analysis algorithms were reviewed. The conventional semblance velocity analysis can be combined with the wavefield downward-continuation concept and the event-curvature-based migration velocity-analysis technique to provide a new velocity-analysis method suitable for complex media. It was shown that the new velocity-analysis scheme produced a satisfactory velocity model, well able to image the left and right parts of the Marmousi model, where the dipping angle exceeds 35° . This work suggests that velocity analysis on downward-continued data can be an effective method for migration velocity analysis. However, much more research is required in order to see this as an effective and practical method.

CHAPTER 7

CONCLUSIONS

Three full integral-wavefield extrapolators based on the nonstationary filtering theory, PSPI, NSPS and SNPS were formulated. It has been shown that the split-step Fourier method can be derived from the nonstationary phase-shift operator and a better slowness-perturbation method of correction is provided. Parallel computing on the MACI Alpha-cluster computer enables implementation of the recursive integral wavefield extrapolators for prestack shot-gather depth imaging. As an example, the PSPI integral extrapolator was used to process the Marmousi synthetic and the image quality was superior. Several computing techniques, including precomputation of the Fourier-transform kernel matrix, computing the exponential functions with the Padé approximation, utilizing matrix symmetry and increasing the velocity repeatability with a small blocking factor, have significantly improved performance: the recursive integral operators have been made practical for application on prestack data.

The large-step integral wavefield-extrapolator was developed based on the integral extrapolators, by using the depth-average velocity (mean velocity) in computing the

focusing term approximately and the time-average velocity (average velocity) for vertical-traveltime correction. The dual algorithm further reduces run time of integral extrapolators by a factor of N_L , where N_L is the number of small depth-steps in a large-step extrapolation. The error in the wavefield is the result of approximation to the velocity field and a large extrapolation step; however, the error is minimal when an appropriate step size is taken. Reducing the extrapolation step enables handling of large lateral velocity gradients.

A dual algorithm for prestack depth imaging was developed. The resulting algorithm uses the large-step-extrapolation algorithm to produce reference wavefields at a depth-grid coarser than the imaging depth and linear vertical-wavefield interpolation to generate the wavefield at each imaging step. The computational cost function is of the same order as the localized split-step algorithm, while its capability in imaging steep structures is much better.

The eigenvalue-decomposition solution to the scalar wave equation was reviewed. Approximation to the velocity field is the sole source of error in this algorithm and it is more suitable for large-step extrapolation. It is not practical, however, due to its low speed. The Padé approximation to the matrix-exponential function has significantly better performance without degrading the extrapolated wavefields; however, more research is necessary to further reduce the run-time, in view of practical application.

Both the PSPI and NSPS integrals are capable of integrating a laterally varying depth-step size. Tests on zero-offset synthetics showed that both produce rather accurate results, although the NSPS is slightly superior to PSPI. However, with the typical step

size used in large-step wavefield extrapolation, the difference between the two is minimal. Algorithms for depth imaging from topography with PSPI and NSPS were formulated. A dual algorithm using PSPI for large-step extrapolation was implemented on the MACI alpha cluster. The Foothills synthetic data set was processed. The algorithm is proven to be highly capable of handling high near-surface velocity and extensive topographic variation. The image quality is superior to those processed by Kirchhoff and finite-difference algorithms.

The *WRW* wavefield-propagation model for prestack P-P depth imaging was extended to a *WCW* model for P-S prestack depth imaging. Prestack P-S depth imaging, with nonstationary wavefield extrapolators, automatically performs CCP binning and is capable of handling the case where the V_p/V_s ratio is a function of both horizontal and vertical coordinates. No extra computing effort is necessary and even the lateral V_p/V_s - ratio gradient is large. This algorithm is suitable for converted-wave depth imaging in complex regions. The 1997 Blackfoot converted-wave data set was used for demonstration purposes. Both the well log and the stacking velocities obtained from previous processing were used in building a velocity model. The P-wave velocity model turned out to be rather good, as proven by the superior P-P depth image quality. The shear-wave velocity-model, however, was not very accurate at either end of the survey line and resulted in poor images from these locations. The central part of the P-P and P-S image has rather good correlation, in general.

Downward continuation velocity analysis (DCVA) was proposed. By restricting the velocity-analysis aperture to a small offset, an average velocity near the recording surface can be estimated and used to downward continue the recorded wavefields to the next

depth level. DCVA produces a much better velocity model than conventional velocity-analysis from surface.

Velocity quality control examined the flatness of events in CIGs and provided a simple yet practical approach to migration velocity analysis in regions of complex geology. Ideally, velocity quality control and updating with event curvature in CIGs should be performed before each step of downward-continuation to the next recording datum. Even with large and coarse velocity control depth-intervals, the method is capable of generating a satisfying velocity model, which enables imaging of the left and right parts of the Marmousi data set.

REFERENCES

- Aki, K. and Richards, P. G., 1980, Quantitative seismology Volume I: W.H. Freeman and Company.
- Al-Yahya, K. M., 1989, Velocity analysis by iterative profile migration: *Geophysics*, **54**, 718-729.
- Audebert, F., Nichols, D., Rekdal, T., Biondi, B., Lumley, D. E. and Urdaneta, H., 1997, Imaging complex geologic structure with single-arrival Kirchhoff prestack depth migration: *Geophysics*, **62**, 1533-1543.
- Audebert, F. and Diet, J. P., 1993, Migrated focus panels -- focusing analysis reconciled with prestack depth migration: 63rd Ann. Internat. Mtg., Soc. Expl. Geophys., Expanded Abstract, 961-964.
- Bale, R. A., Farmer, P., Hansen, J. O., Nichols, D. E. and Palacharla, G. K., 1998, Prestack depth migration of converted wave data in anisotropic media: 68th Ann. Internat. Mtg, Soc. Expl. Geophys., Expanded Abstract, 1108-1111.
- Baysal, E., Kosloff, D. D. and Sherwood, J. W. C., 1985, Reverse time migration: *Geophysics*, **48**, 1514-1524.
- Berkhout, A. J., 1981, Wavefield extrapolation techniques in seismic migration, a tutorial: *Geophysics*, **46**, 1638-1656.
- Berkhout, A. J., 1980, Seismic migration: imaging of acoustic energy by wavefield extrapolation: Elsevier Scientific Publication Company, Amsterdam, 1985.

- Berryhill, J. R., 1979, Wave equation datuming: *Geophysics*, **44**, 1329-1344.
- Berryhill, J. R., 1984, Wave equation datuming before stack (short note): *Geophysics*, **49**, 2064-2067.
- Biondi, B. and Palacharla, G., 1996, 3-D prestack migration of common-azimuth data: *Geophysics*, **61**, 1822-1832.
- Biondi, B., 1997, Azimuth moveout + common-azimuth migration: Cost-effective prestack depth imaging of marine data: 67th Ann. Internat. Mtg., Soc. Expl. Geophys., Expanded Abstract, 1375-1378.
- Biondi, B. and Sava, P., 1999, Wave-equation migration velocity analysis: 69th Ann. Internat. Mtg., Soc. Expl. Geophys., Expanded Abstract, 1723-1726.
- Black, J. L., Su, C. B., and Wason, C. B., 1984, Steep-dip depth migration: 54th Ann. Internat. Mtg., Soc. Expl. Geophys., Expanded Abstract, 456-457.
- Bourgeois, A., Bourget, M., Lailly, P., Poulet, M., Ricarte, P., and Versteeg, R., 1991, Marmousi, model and data: in *The Marmousi experience*: 53th Ann. Internat. Mtg., Eur. Assn. Geosci. Eng., Extended Abstract, 5 - 9.
- Caldwell, J., Kristiansen, P., Beaudoin, G. J., Tollestrup, A. K., Siddiqui, S. A., Wyatt, K., Camp, W. and Raney, G. B., 1998, Marine 4-component seismic test, Gulf of Mexico: Subsalt Imaging at Mahogany Field: 68th Ann. Internat. Mtg, Soc. Expl. Geophys., Expanded Abstract, 2091-2092.

- Chauris, H., Lambare, G., Noble, M. and Podvin, P., 1999, Migration-based velocity analysis in 2-D laterally heterogeneous media: 69th Ann. Internat. Mtg, Soc. Expl. Geophys., Expanded Abstract, 1235-1238.
- Chung, W. Y. and Corrigan, D., 1985, Gathering mode-converted shear waves: A model study: 55th Ann. Internat. Mtg, Soc. Expl. Geophys., Expanded Abstract, Session: S18.7.
- Cieslewicz, D. and Lawton, D.C., 1998, Blackfoot III buried geophone experiment: 1998 CREWES Annual Report.
- Claerbout, J. F., 1971, Toward a unified theory of reflector mapping: *Geophysics*, **36**, 467-481.
- D'Agosto, Claudio, Donati, Maria Silvia and Michelena, Reinaldo Jose, 1998, Tomography + prestack depth migration of P-S converted waves, 68th Ann. Internat. Mtg, Soc. Expl. Geophys., Expanded Abstract, 1361-1364.
- De Hoop, M. V. and van Stralen, M. J. N., 1997, Exact generalized slowness surfaces: Benchmarks for one-way wave propagation: 67th Ann. Internat. Mtg, Soc. Expl. Geophys., Expanded Abstract, 1842-1845.
- Deregowski, S. M. and Rocca, F., 1981, Geometrical optics and wave theory of constant offset sections in layered media: *Geophys. Prosp.*, **29**, 374-406.
- Doherty, S. M. and Claerbout, J. F., 1976, Structure independent velocity estimation: *Geophysics*, **41**, 850-881.

- Eaton, D. W. S., Slotboom, R. T., Stewart, R. R. and Lawton, D. C., 1990, Depth-variant converted-wave stacking, 60th Ann. Internat. Mtg, Soc. Expl. Geophys., Expanded Abstract , 1107-1110.
- Eaton, D.W. S. and Stewart, R.R., 1991, Anisotropic ray-Born migration/inversion: A synthetic modeling study: 1991 CREWES Annual Report.
- Etgen, John T., 1993, Interval velocity estimation using residual prestack migration: 63rd Ann. Internat. Mtg, Soc. Expl. Geophys., Expanded Abstract, 669-672.
- Faye, J. P. and Jeannot, J. P., 1986, Prestack migration velocities from focusing depth analysis: 56th Ann. Internat. Mtg, Soc. Expl. Geophys., Expanded Abstract, Session: S7.6.
- Fei, T., Fehler, M. C., Hildebrand, S. T. and Chilcoat, S. R., 1996, Depth migration artifacts associated with first-arrival traveltimes: 66th Ann. Internat. Mtg, Soc. Expl. Geophys., Expanded Abstract, 499-502.
- Ferguson, R. and Margrave, G., 1999, A practical implementation of depth migration by nonstationary phase shift: 69th Ann. Internat. Mtg, Soc. Expl. Geophys., Expanded Abstract, 1370-1373.
- Ferguson, R., 2000, Seismic Imaging in Heterogeneous Anisotropic Media by Nonstationary Phase Shift: Ph.D thesis, Geology and Geophysics Department, the University of Calgary.

- Fishman, L., and McCoy, J. J., 1985, A new class of propagation models based on a factorization of the Helmholtz equation: *Geophys. J. Astr. Soc.*, **80**, 439-461.
- Freire, R. and Stoffa, P. L., 1986, Migration using the 'Split-step Fourier' method: 56th Ann. Internat. Mtg, Soc. Expl. Geophys., Expanded Abstract, Session: POS2.1.
- Gardner, G. H. F., French, W. S. and Matzuk, T., 1974, Elements of migration and velocity analysis: *Geophysics*, **39**, 811-825.
- Gazdag, J. and Sguazzero, P., 1984, Migration of seismic data by phase shift plus interpolation: *Geophysics*, **49**, 124-131.
- Gazdag, J., 1978, Wave equation migration with the phase-shift method: *Geophysics*, **43**, 1342-1351.
- Golub, G.H, and Van Loan, C.F., 1989, *Matrix computations*, 2nd Edition: Johns Hopkins University Press.
- Gray, S. H. and Marfurt, K. J., 1995, Migration from topography: Improving the near-surface image: *Can. J. Expl. Geophys.*, **31**, 18-24.
- Grimbergen, Joris L. T., Dessing, Frank J., Wapenaar, Kees and Kostek, Sergio, 1998, Modal expansion of one-way operators in laterally varying media: *Geophysics*, **63**, 995-1005.
- Hadley, David, Thorson, Jeff and Maher, Shannon, 1988, Increasing interpretation accuracy - A new approach to interval velocity estimation: *The Leading Edge*, **07**, no. 09, 13-16.

- Haime, G. C. and Wapenaar, C. P. A., 1989, Inverse elastic wave-field extrapolation: 59th Ann. Internat. Mtg, Soc. Expl. Geophys., Expanded Abstract, 1323.
- Hardin, R.H., and Tappert, F.D., 1973, Applications of the split-step Fourier method to the numerical solution of nonlinear and variable coefficient wave equation: SIAM Rev., 15.
- Haime, G. and Wapenaar, C. P. A., 1991, Downward extrapolation of decomposed P-wave and S-wave fields: 61st Ann. Internat. Mtg., Eur. Assn. Geosci. Eng., Extended Abstract, 226-227.
- Harrison, M.P.1993, Processing of P-S Surface-Seismic Data: Anisotropy Analysis, Dip Moveout, and Migration: Ph.D. Thesis, Department of Geology and Geophysics, the University of Calgary.
- Hoffe, B. and Lines, L., 1998, Depth imaging of elastic wavefields – where P meets S: 1998 CREWES Annual Report.
- Hubral, P., 1983, Computing true amplitude reflections in a laterally inhomogeneous earth: Geophysics, **48**, 1051-1062.
- Jin, S. and Wu, R., 1998, Depth migration using the windowed generalized screen propagators: 68th Ann. Internat. Mtg, Soc. Expl. Geophys., Expanded Abstract, 1843-1846.

- Justice, M. G., McCormack, M. D. and Lee, S. S., 1987, Anisotropy in the Morrow formation of southeast New Mexico, in Domenico, S. N., Ed., Shear-wave exploration: Soc. Expl. Geophys., 154-164.
- Kessinger, W., 1992, Extended split-step Fourier migration, 62nd Ann. Internat. Mtg, Soc. Expl. Geophys., Expanded Abstract, 917-920.
- Kramer, Darrell and Davis, Thomas L., 1991, Multicomponent vertical seismic profiles for reservoir characterization, South Casper Creek field, Natrona county, Wyoming: 61st Ann. Internat. Mtg, Soc. Expl. Geophys., Expanded Abstract, 383-386.
- Li, X. -Y., MacBeth, C., Hitchen, K. and Hanssen, P., 1998, Using converted shear-wave for imaging beneath basalt in deep water plays: 68th Ann. Internat. Mtg, Soc. Expl. Geophys., Expanded Abstract, 1369-1372.
- Lines, L. R., Rahimian, F. and Kelly, K. R., 1993, A model-based comparison of modern velocity analysis methods: The Leading Edge, **12**, no. 07, 750-754.
- Lines, L., Wu, W., Lu, H., Burton, A. and Zhu, J., 1996, Migration from topography: experience with an Alberta Foothills data set: Can. J. Expl. Geophys., **32**, no. 01, 24-30.
- MacBeth, C., 1990, Inversion of shear-wave polarizations for anisotropy using three-component offset VSPs: 60th Ann. Internat. Mtg, Soc. Expl. Geophys., Expanded Abstract, 1404-1406.

- MacBeth, C. and Crampin, S., 1991, Comparison of signal processing techniques for estimating the effects of anisotropy: *Geophys. Prosp., Eur. Assn. Geosci. Eng.*, **39**, 357-386.
- MacKay, Scott and Abma, Ray, 1989, Refining prestack depth-migration images without remigration: 59th Ann. Internat. Mtg, Soc. Expl. Geophys., Expanded Abstract, 1258.
- MacKay, S. and Abma, R., 1992, Imaging and velocity estimation with depth-focusing analysis: *Geophysics*, **57**, 1608-1622.
- Margrave, G. F. and Ferguson, R. J., 1997, Wavefield extrapolation by nonstationary phase shift: 67th Ann. Internat. Mtg, Soc. Expl. Geophys., Expanded Abstract, 1599-1602.
- Margrave, G.F., 1998, Theory of nonstationary linear filtering in the Fourier domain with application to time-variant filtering: *Geophysics*, **63**, 244-259.
- Margrave, G.F. and Ferguson, R., 1999a, An explicit, symmetric wavefield extrapolator for depth migration: 69th Ann. Internat. Mtg, Soc. Expl. Geophys., Expanded Abstract, 1461-1464.
- Margrave, G. F. and Ferguson, R. J., 1999b, Wavefield extrapolation by nonstationary phase shift: *Geophysics*, **64**, 1067-1078.

- Margrave, G.F. and Ferguson, R., 2000, Taylor series derivation of nonstationary wavefield extrapolators: 70th Ann. Internat. Mtg, Soc. Expl. Geophys., Expanded Abstract, 834-837
- Margrave, G.F. and Yao, Z., 2000, Downward extrapolation from topography with a laterally variable depth step: 70th Ann. Internat. Mtg, Soc. Expl. Geophys., Expanded Abstract, 481-484.
- Martin, M. A., Davis, T. L. and O'Rourke, T. J., 1986, An integrated three-component approach to fracture detection: 56th Ann. Internat. Mtg, Soc. Expl. Geophys., Expanded Abstract, Session:POS1.16.
- McDaniel, S.T., 1975, Parabolic approximations for underwater sound propagation: J.Acoust. Soc. Am., **58**, 1178-1185.
- Mi, Y. and Margrave, G.F., 1999, Application of homomorphic theory in nonstationary deconvolution: 1999 CREWES Annual Report.
- Mi, Y., Yao, Z. and Margrave, G.F., 2000, A Padé approximation to the scalar wavefield extrapolator for inhomogeneous media: 2000 CREWES Annual Report.
- Mi, Y. and Margrave, G.F., 2000, A Fortran 90 implementation of symmetric nonstationary phase-shift extrapolator, 2000 CREWES Annual Report.
- Mi, Y. and Margrave, G.F., 2001a, Dual extrapolation algorithms for Fourier shot record migration, 71st Ann. Internat. Mtg, Soc. Expl. Geophys., Expanded Abstract, 1021-1024.

- Mi, Y. and Margrave, G.F., 2001b, Prestack depth imaging from topography with a Fourier method, 71st Ann. Internat. Mtg, Soc. Expl. Geophys., Expanded Abstract, 1045-1048.
- Mi, Y. and Margrave, G.F., 2001c, Implementation of Symmetric Nonstationary Phase-shift Wave_eld Extrapolator on an Alpha Cluster: Proceedings of the 2001 International Conference on Computational Science.
- Miller, S. L. M., Aydemir, E. O., and Margrave, G. F., 1995, Preliminary interpretation of P-P and P-S seismic data from the Blackfoot broad-band survey: 1995 CREWES Annual Report.
- Mosher, C. C., Foster, D. J. and Hassanzadeh, S., 1997, Common angle imaging with offset plane waves: 67th Ann. Internat. Mtg, Soc. Expl. Geophys., Expanded Abstract, 1379-1382.
- Ng, M., 1994, Prestack migration of shot records using phase shift plus interpolation: Can. J. Expl. Geophys., **30**, no. 01, 11-27.
- Nicoletis, L. M., Svay-Lucas, J. and Prigent, H., 1998, True amplitude prestack imaging of converted waves: 68th Ann. Internat. Mtg, Soc. Expl. Geophys., Expanded Abstract, 734-737.
- O'Brien, M. J. and Etgen, J. T., 1998, Wavefield imaging of complex structures with sparse, point-receiver data: 68th Ann. Internat. Mtg, Soc. Expl. Geophys., Expanded Abstract, 1365-1368.

- Pann, K. and Shin, Y., 1976, A class of convolutional time-varying filters: *Geophysics*, **41**, 28-43.
- Schoepp, A.R., 1998, Nonstationary deconvolution: Master thesis, Geology and geophysics Department, the University of Calgary.
- Schulte, L. and Edelmann, H. A. K., 1988, Azimuthal anisotropy proven to be a useful approach for multicomponent shear-wave data processing: 58th Ann. Internat. Mtg, Soc. Expl. Geophys., Expanded Abstract, Session:S18.8.
- Sekulic, D. M., Gaiser, J. E. and Albertin, U. K., 1998, Role of salt base converted wave phase shift in subsalt imaging: 68th Ann. Internat. Mtg, Soc. Expl. Geophys., Expanded Abstract, 582-585.
- Sheuer, T., and Oldenburg, D.W., 1988, Aspects of time-variant filtering: *Geophysics*, **53**, 1399-1409.
- Shtivelman, V. and Canning, A., 1988, Datum correction by wave equation extrapolation: *Geophysics*, **53**, 1311-1322.
- Slotboom, R.T. and Lawton, D.C., 1989, Depth-variant mapping and moveout correction of converted-wave data: 1989 CREWES Annual Report.
- Slotboom, R. T., 1990, Converted wave (P-S) moveout estimation: 60th Ann. Internat. Mtg, Soc. Expl. Geophys., Expanded Abstract, 1104-1106.

- Sollid, A., Ekren, B. O. and Arntsen, B., 1996, Prestack time migration applied to marine P-S seismic waves: 66th Ann. Internat. Mtg, Soc. Expl. Geophys., Expanded Abstract, 1571-1574.
- Stein, E. M., 1993, Harmonic analysis: real-variable methods, orthogonality, and oscillatory integrals: Princeton University Press.
- Stoffa, P. L., Fokkema, J. T., de Luna Freire, R. M. and Kessinger, W. P., 1990, Split-step Fourier migration, *Geophysics*, **55**, 410-421.
- Stolt, R. H., 1978, Migration by Fourier transform: *Geophysics*, **43**, 23-48.
- Stork, Christof, 1992, Combining reflection tomography with migration velocity analysis: 54th Ann. Internat. Mtg., Eur. Assn. Geosci. Eng., Extended Abstract, 256-257.
- Symes, W. W. and Carazzone, J. J., 1991, Velocity inversion by differential semblance optimization: *Geophysics*, **56**, 654-663.
- Taner, M. Turhan and Koehler, Fulton, 1969, Velocity spectra - Digital computer derivation and applications of velocity functions: *Geophysics*, **34**, 859-881.
- Tessmer, G. and Behle, A., 1988, Common reflection point data-stacking technique for converted waves: *Geophys. Prosp.*, Eur. Assn. Geosci. Eng., 36, 671-688.
- Thomsen, L., 1999, Converted-wave reflection seismology over inhomogeneous, anisotropic media: *Geophysics*, **64**, 678-690.

- Tieman, H., 1984, Migration velocity analysis: Theoretical development and practical results: Ann. Internat. Mtg, Soc. Expl. Geophys., Expanded Abstract, Session:S25.7.
- Tieman, H. J., 1993, Description of a scanless method of stacking velocity analysis: Geophysics, **58**, 1596-1606.
- Tieman, H. J., 1995, Migration velocity analysis: Accounting for the effects of lateral velocity variations: Geophysics, **60**, 164-175.
- Wapenaar, C. P. A., Kinneging, N. A. and Berkhout, A. J., 1987, Principle of prestack migration based on the full elastic two-way wave equation: Geophysics, **52**, 151-173.
- Wapenaar, C. P. A. and Haime, G. C., 1990, Elastic extrapolation of primary seismic P- and S-waves: Geophys. Prosp., Eur. Assn. Geosci. Eng., **38**, 23-60.
- Wapenaar, C. P. A. and Haime, G. C., 1991, Elastic wavefield decomposition: Before or after extrapolation?: 61st Ann. Internat. Mtg, Soc. Expl. Geophys., Expanded Abstract, 1001-1004.
- Wu, R.-S. and Huang, L.-J., 1992, Scattered field calculation in heterogeneous media using phase-screen propagation: 62nd Ann. Internat. Mtg, Soc. Expl. Geophys., Expanded Abstract, 1289-1292.

Yao, Z. and Margrave, G., 2000, Wavefield extrapolation by Fourier domain eigenfunction decomposition, 70th Ann. Internat. Mtg, Soc. Expl. Geophys., Expanded Abstract, 497-500.

Yilmaz, O. and Chambers, R. E., 1984, Migration velocity analysis by wave-field extrapolation: Geophysics, **49**, 1664-1674.

Zanzi, L., 1996, Angle-velocity analysis and depth migration for P-S data: 66th Ann. Internat. Mtg, Soc. Expl. Geophys., Expanded Abstract, 1567-1570.